Optimising Coherence in Group IV Semiconductor Quantum Dot Hole Spin Qubits

Author:
Wang, Zhanning

Publication Date:
2024

DOI:
https://doi.org/10.26190/unsworks/31036

Candidate's Responses

Submit your corrected thesis and responses here

The candidate's responses to examiners' comments and corrected thesis are displayed in the tabs below.

Thesis Title and Abstract | **Declarations** | **Inclusion of Publications Statement**

Corrected Thesis and Responses

ORIGINALITY STATEMENT

☑ I hereby declare that this submission is my own work and to the best of my knowledge it contains no materials previously published or written by another person, or substantial proportions of material which have been accepted for the award of any other degree or diploma at UNSW or any other educational institution, except where due acknowledgement is made in the thesis. Any contribution made to the research by others, with whom I have worked at UNSW or elsewhere, is explicitly acknowledged in the thesis. I also declare that the intellectual content of this thesis is the product of my own work, except to the extent that assistance from others in the project's design and conception or in style, presentation and linguistic expression is acknowledged.

COPYRIGHT STATEMENT

☑ I hereby grant the University of New South Wales or its agents a non-exclusive licence to archive and to make available (including to members of the public) my thesis or dissertation in whole or part in the University libraries in all forms of media, now or here after known. I acknowledge that I retain all intellectual property rights which subsist in my thesis or dissertation, such as copyright and patent rights, subject to applicable law. I also retain the right to use all or part of my thesis or dissertation in future works (such as articles or books).

For any substantial portions of copyright material used in this thesis, written permission for use has been obtained, or the copyright material is removed from the final public version of the thesis.

AUTHENTICITY STATEMENT

☑ I certify that the Library deposit digital copy is a direct equivalent of the final officially approved version of my thesis.

Candidate's Responses

Submit your corrected thesis and responses here

The candidate's responses to examiners' comments and corrected thesis are displayed in the tabs below.

Thesis Title and Abstract | **Declarations** | **Inclusion of Publications Statement** | **Corrected Thesis and Responses**

UNSW is supportive of candidates publishing their research results during their candidature as detailed in the UNSW Thesis Examination Procedure.

Publications can be used in your thesis in lieu of a Chapter provided:

- You contributed **greater than 50%** of the content in the publication and are the "primary author", i.e. you were responsible primarily for the planning, execution and preparation of the work for publication.
- You have approval to include the publication in their thesis in lieu of a Chapter from your Supervisor and Postgraduate Coordinator.
- The publication is not subject to any obligations or contractual agreements with a third party that would constrain its inclusion in the thesis.

☑ **Some of the work described in my thesis has been published and it has been documented in the relevant Chapters with acknowledgement.**

A short statement on where this work appears in the thesis and how this work is acknowledged within chapter/s:

The results from the paper 'Optimal operation points for ultrafast, highly coherent Ge hole spin-orbit qubits' published in the journal 'npj Quantum Information' are included in Chapter 3 of this work. Additionally, findings from the paper 'Unidirectional magnetotransport of linearly dispersing topological edge states' from the journal 'Physical Review B' are incorporated in Chapter 5. Acknowledgements to the other authors of these papers have been duly made at the beginning of each respective chapter and in the acknowledgements section.

CANDIDATE'S DECLARATION

☑ I declare that I have complied with the Thesis Examination Procedure.

Optimising Coherence in Group IV Semiconductor Quantum Dot Hole Spin Qubits

Zhanning Wang

A thesis in fulfilment of the requirements for the degree of

Doctor of Philosophy

UNSW
SYDNEY

School of Physics

Faculty of Science

The University of New South Wales

February 2024

THE UNIVERSITY OF NEW SOUTH WALES
Thesis/Dissertation Sheet

Surname or Family name: **Wang**

First name: **Zhanning** Other name/s:

Abbreviation for degree as given in the University calendar: **PhD**

School: **School of Physics** Faculty: **Faculty of Science**

Title: Optimising Coherence in Group IV Semiconductor Quantum Dot Hole Spin Qubits

Abstract

This thesis presents advancements in optimising coherence for Group IV semiconductor quantum dot hole spin qubits. Given their maturity in the modern semiconductor industry, Group IV semiconductors offer an ideal platform for quantum information processing. However, the challenge of achieving high coherence in these systems remains.

Our study examines several theoretical properties of Group IV semiconductor quantum dots, focusing on the creation of high-quality hole spin qubits. We employ the $\boldsymbol{k}\cdot\boldsymbol{p}$ method as the theoretical framework to analyse spin-orbit couplings for rapid quantum state manipulation. Additionally, we investigate hole-phonon interactions to estimate relaxation times and delve into charge defect-induced dephasing time (T_2^*), aiming to understand and mitigate decoherence mechanisms. Our models incorporate environmental influences, such as magnetic field fluctuations and charge noise, to provide an overview of factors impacting coherence.

The implications of these findings extend beyond the realm of quantum computing, offering insights into general semiconductor studies and condensed matter physics.

The first chapter introduces key concepts in quantum computation and quantum information processing. It also reviews various architectures for realising scalable quantum computing and highlights the unique advantages and challenges of semiconductor quantum dot hole spin qubits. This is followed by a literature review on semiconductor quantum dot electron and hole spin qubits.

The second chapter includes the essential theoretical frameworks required to discuss the results in the following chapters, including the $\boldsymbol{k}\cdot\boldsymbol{p}$ approach in solid-state systems, mechanisms of phonon-induced relaxations, and charge defect-induced dephasings.

The third chapter presents the study of decoherence properties and the electric control of germanium semiconductor quantum dot hole spin qubits. We identified the optimal operation points where the charge-induced dephasing time is optimised, favouring fast electrical manipulations.

The fourth chapter further expands the theory developed in the third chapter. The planar silicon quantum dot hole spin qubits in a metal-oxide-semiconductor platform are studied, which can be fully integrated into industry-level solid-state device engineering. We find that fast electrical manipulations of spin states can be optimised by dot geometries and magnetic fields, and large g-factor modulations are verified, which agrees with various recent experiments.

Additionally, we dedicate a standalone chapter to study the helical edge states in a Dirac semimetal Na_3Bi system. We show that in a diffusive sample, a magnetic field can drastically increase the mean free path and drive the system into the ballistic regime with a Landauer-Büttiker conductance. A strong nonlinear nonreciprocal current emerges in the diffusive regime with opposite signs on each edge and vanishes in the ballistic limit. This chapter includes its own introduction, model and methodology, and discussion and conclusion sections.

Originality Statement

I hereby declare that this submission is my own work and to the best of my knowledge it contains no materials previously published or written by another person, or substantial proportions of material which have been accepted for the award of any other degree or diploma at UNSW or any other educational institution, except where due acknowledgement is made in the thesis. Any contribution made to the research by others, with whom I have worked at UNSW or elsewhere, is explicitly acknowledged in the thesis. I also declare that the intellectual content of this thesis is the product of my own work, except to the extent that assistance from others in the project's design and conception or in style, presentation and linguistic expression is acknowledged.

Zhanning Wang
9 February, 2024

Copyright Statement

Zhanning Wang
9 February, 2024

Authenticity Statement

I certify that the Library deposit digital copy is a direct equivalent of the final officially approved version of my thesis.

Zhanning Wang
9 February, 2024

Abstract

This thesis presents advancements in optimising coherence for Group IV semiconductor quantum dot hole spin qubits. Given their maturity in the modern semiconductor industry, Group IV semiconductors offer an ideal platform for quantum information processing. However, the challenge of achieving high coherence in these systems remains.

Our study examines several theoretical properties of Group IV semiconductor quantum dots, focusing on the creation of high-quality hole spin qubits. We employ the $\boldsymbol{k} \cdot \boldsymbol{p}$ method as the theoretical framework to analyse spin-orbit couplings for rapid quantum state manipulation. Additionally, we investigate hole-phonon interactions to estimate relaxation times and delve into charge defect-induced dephasing time (T_2^*), aiming to understand and mitigate decoherence mechanisms. Our models incorporate environmental influences, such as magnetic field fluctuations and charge noise, to provide an overview of factors impacting coherence.

The implications of these findings extend beyond the realm of quantum computing, offering insights into general semiconductor studies and condensed matter physics.

The first chapter introduces key concepts in quantum computation and quantum information processing. It also reviews various architectures for realising scalable quantum computing and highlights the unique advantages and challenges of semiconductor quantum dot hole spin qubits. This is followed by a literature review on semiconductor quantum dot electron and hole spin qubits.

The second chapter includes the essential theoretical frameworks required to discuss the results in the following chapters, including the $\boldsymbol{k} \cdot \boldsymbol{p}$ approach in solid-state systems, mechanisms of phonon-induced relaxations, and charge defect-induced dephasings.

The third chapter presents the study of decoherence properties and the electric control of germanium semiconductor quantum dot hole spin qubits. We identified the optimal operation points where the charge-induced dephasing time is optimised, favouring fast electrical manipulations.

The fourth chapter further expands the theory developed in the third chapter. The planar silicon quantum dot hole spin qubits in a metal-oxide-semiconductor platform are studied, which can be fully integrated into industry-level solid-state device engineering. We find

that fast electrical manipulations of spin states can be optimised by dot geometries and magnetic fields, and large g-factor modulations are verified, which agrees with various recent experiments.

Additionally, we dedicate a standalone chapter to study the helical edge states in a Dirac semimetal Na_3Bi system. We show that in a diffusive sample, a magnetic field can drastically increase the mean free path and drive the system into the ballistic regime with a Landauer-Büttiker conductance. A strong nonlinear nonreciprocal current emerges in the diffusive regime with opposite signs on each edge and vanishes in the ballistic limit. This chapter includes its own introduction, model and methodology, and discussion and conclusion sections.

Acknowledgement

First and foremost, I would like to express my deepest gratitude to my advisor, A.Prof. Dimitrie Culcer. His profound knowledge and professional guidance have been the solid foundation of my thesis. Throughout the research process, Dimi has not only illuminated my path with his wisdom but also supported me with infinite patience and assistance, helping me overcome numerous challenges encountered along the way. His care and guidance in life have also been immensely beneficial to me. My accomplishments would not have been possible without his guidance.

I also wish to express my sincere thanks to our group members Abhikbrata Sarkar, Sina Gholizadeh , James Cullen, and Rhonald Burgos, Scott Liles, and Wenkai Bai. The discussions with them have been immensely rewarding, enhancing my understanding of intricate details and significantly broadening my knowledge base. Their companionship has enriched my campus life and brought me great joy. Their friendship and solidarity have truly made this journey memorable and enjoyable.

Furthermore, I am deeply thankful to our faculty members, including Pankaj Bhalla, Joseph Salfi, Andrea Saraiva, Elizabeth Marcellina, Scott Liles, Alex Hamilton, Zeb Krix, and Oleg Sushkov; and co-authors Chang Liu, Mark Edmonds, and Michael Fuhrer. Their willingness to address my queries, impart valuable academic knowledge, and assist in rectifying errors in my work has been extraordinarily beneficial. Their knowledge and experience have had an immeasurable impact.

I would also like to express my gratitude to Dr. John Lambros, Dr. Phillip Van Zanden, and Nurse Maria for their excellent care in treating my heart condition and during several emergency situations. Their professional medical services and attentive care have enabled me to continue my academic pursuits. Their assistance has been crucial to me, and I am deeply thankful for their support.

Publications and Presentations

List of Publications

- Optimal operation points for ultrafast, highly coherent Ge hole spin-orbit qubits *npj Quantum Information* Zhanning Wang, Elizabeth Marcellina, Alex. R. Hamilton, James H. Cullen, Sven Rogge, Joe Salfi, and Dimitrie Culcer
- Unidirectional magnetotransport of linearly dispersing topological edge states *Phys. Rev. B* Zhanning Wang, Pankaj Bhalla, Mark Edmonds, Michael S. Fuhrer, and Dimitrie Culcer
- Electrical operation of hole spin qubits in planar MOS silicon quantum dots *Phys. Rev. B* Zhanning Wang, Abhikbrata Sarkar, S. D. Liles, Andre Saraiva, A. S. Dzurak, A. R. Hamilton, and Dimitrie Culcer
- Electrical operation of planar Ge hole spin qubits in an in-plane magnetic field *Phys. Rev. B* Abhikbrata Sarkar, Zhanning Wang, Matthew Rendell, Nico W. Hendrickx, Menno Veldhorst, Giordano Scappucci, Mohammad Khalifa, Joe Salfi, Andre Saraiva, A. S. Dzurak, A. R. Hamilton, and Dimitrie Culcer
- Theory of hole-spin qubits in strained germanium quantum dots *Phys. Rev. B* L. A. Terrazos, E. Marcellina, Zhanning Wang, S. N. Coppersmith, Mark Friesen, A. R. Hamilton, Xuedong Hu, Belita Koiller, A. L. Saraiva, Dimitrie Culcer, and Rodrigo B. Capaz
- Helical Edge Transport in Millimeter-Scale Thin Films of Na3Bi *Nano Lett.* Chang Liu, Dimitrie Culcer, Zhanning Wang, Mark T. Edmonds, and Michael S. Fuhrer
- Ultrafast coherent control of a hole spin qubit in a germanium quantum dot *Nature Communications* Ke Wang, Gang Xu, Fei Gao, He Liu, Rong-Long Ma, Xin Zhang, Zhanning Wang, Gang Cao, Ting Wang, Jian-Jun Zhang, Dimitrie Culcer, Xuedong Hu, Hong-Wen Jiang, Hai-Ou Li, Guang-Can Guo, and Guo-Ping Guo

Preprints

- A singlet-triplet hole-spin qubit in MOS silicon *preprint* S. D. Liles, D. J. Halverson, Z. Wang, A. Shamim, R. S. Eggli, I. K. Jin, J. Hillier, K. Kumar, I. Vorreiter, M. Rendell, J. H. Huang, C. C. Escott, F. E. Hudson, W. H. Lim, D. Culcer, A. S. Dzurak, and A. R. Hamilton

Contents

List of Figures

List of Tables

Abbreviations

CMOS	complementary metal-oxide-semiconductor
EDSR	Electric dipole spin resonance
HH	Heavy hole
LH	Light hole
MOS	metal–oxide–semiconductor
MOSFET	metal–oxide–semiconductor field-effect transistor
QD	Quantum dot
QW	Quantum well
SOC	Spin-orbit coupling
SQD	Semiconductor quantum dot

Chapter 1

Introduction

1.1 Concepts of quantum computations

The rapid developments in quantum information science have significantly changed the paradigm of storage, transmission, and processing of information, by leveraging the unique properties of quantum mechanics, such as quantum superpositions and entanglements. As the hardware platform to deploy quantum information processing, quantum computers have become an important research topic over the past several decades. A variety of physical systems, spanning a broad range of physics, have emerged as competitive candidates as fundamental building blocks for quantum computers. In this section, we begin by introducing the capabilities of quantum information processing and the criteria for designing a quantum computer. Then, we will provide a brief overview of several frequently studied quantum computer architectures, recognising the pioneering work and substantial efforts being made in this field.

Classical electronic devices operate on binary logic, where the basic unit of information is the *bit* [447]. A bit can be in one of two possible states, either 0 or 1, which are mutually exclusive, following the Boolean algebra [47]. These states correspond to the *on* and *off* state respectively. For instance, in electrical circuits, *on* represents a closed circuit, while

off indicates an open circuit. While this classical paradigm has significantly benefited our daily life, it inherently faces limitations in information handling capacity, predominantly restricted by the tremendous amount of energy and time required [126].

For example, a fundamental challenge in cryptography is the factorization of large integer numbers into a product of two prime numbers, which has long been a significant obstacle for computer scientists [185, 397]. The most efficient algorithms available on classical computers for this task still require exponential time. This means that the time taken for factorization increases exponentially as the size of the number grows, resulting in the consumption of excessive amount of time and energy [419]. In 1996, after correcting a critical error, Peter Shor republished his groundbreaking work titled *Polynomial-Time Algorithms for Prime Factorization and Discrete Logarithms on a Quantum Computer* [455]. In this paper, he proposed an algorithm capable of factorizing large integers in polynomial time, faster than any existing factorization algorithm on classical computers. The cornerstone of this triumphant achievement lies in the superposition state nature of the quantum bit, commonly abbreviated as *qubit*. Unlike a classical bit, a qubit can be in a quantum state of $|0\rangle$ or $|1\rangle$, or any superposition of these states, according to quantum mechanics. To illustrate quantitatively, n classical bits can encode one out of 2^n possible states. In contrast, n qubits can encode all 2^n states simultaneously, however, one measurement of a system of n qubits, will only allow one of these 2^n possible results. The challenges of performing measurement, or more broad topics related to quantum metrology, stand as a separate field of research, which is beyond the scope of this thesis, readers who are interested in these topic may find some useful information in Ref [184, 87, 171, 57, 13]. This over simplified example of qubits does not demonstrate the ingenuity of Shor's algorithm. For a more comprehensive and detailed demonstration of the large number factorization problem, please refer to [454, 455].

Computers based on quantum architectures have proven to be effective in addressing problems which are challenging for classical computers [32, 126, 399]. Another feature of quantum computers is that the interacting qubits themselves also provide a natural platform for studying quantum many-body systems. This has led to the development of

a flourishing research area known as quantum simulations, proposed by Feynman in the 1980s [157]. Understanding the complex molecular structures and their dynamics is central to condensed matter physics [162, 3]. However, incorporating the many-body interactions among electrons, nucleons, and protons presented significant challenges. While state-of-the-art computational techniques, such as density functional theory and the Hartree-Fock method, have advanced our knowledge considerably [457, 211, 15, 233], quantum simulations, with the inherent inclusion of many-body interactions among qubits, offer an alternative approach to make predictions about complex systems. It should be noted that quantum simulations also play a significant role in other fields like particle physics and quantum chemistry. Readers interested in these topics are referred to references [178, 336, 29].

Despite the insights offered by quantum computers, there are stringent criteria for physical systems to qualify as qubit candidates, making the road to commercial quantum computers arduous. In 2000, DiVincenzo systematically outlined five criteria that delineate the physical requirements for realising a fault-tolerant quantum computer [132, 133, 134]. These criteria have since become the guiding principles in the development of quantum computing technologies over the past several decades. Here, we rephrase the original statements into a shorter version.

1. The qubit of a quantum computer must be a scalable physical system, and is well-defined. This criterion implies the ability to include a large number of qubits for realistic problems.

2. The state of the qubits must be able to be initialised, e.g., all states can be written as $|0\rangle \otimes |0\rangle \otimes |0\rangle \otimes \cdots \equiv |0, 0, 0, ...\rangle$.

3. The system must maintain quantum coherence long enough to perform operations. Therefore, the qubit must have considerably long decoherence time.

4. A universal set of quantum gates can be constructed to perform all the rotations and operations.

5. The measurement can be performed on individual qubits without destroying other qubits. This requirement paves the way for the application of quantum error correction procedures on quantum circuits, which consist of many qubits.

In the engineering of quantum computers, the scalability requirement, together with defects in experimental apparatus, will introduce unwanted couplings between environments and qubits. Furthermore, these couplings will expose the information stored in qubits to various noise like electromagnetic waves, phonons, and magnetic impurities. As a result, the information will leak into environments, caused by disturbances from noise [576, 474, 272]. This leakage destroys fragile quantum superposition states and quantum entanglements between qubits, ultimately leading to faulty results [25, 86, 292]. This destructive process due to interactions between environments and qubits is known as the decoherence process [575, 351, 350]. In this process, pure quantum states eventually transition into mixed states [568, 469, 272]. In the language of density matrix formalism, which is widely used to study open quantum systems, the non-diagonal elements of the system's density matrix will vanish.

There are two particular time scales commonly used to characterize the decoherence in quantum computation, however their original concepts are established in the research of nuclear magnetic resonance [43, 44, 487]. The first time scale is known as the relaxation decoherence time, denoted by T_1. Due to interactions between environments and qubits, a higher energy state $|1\rangle$ will relax to a lower energy state $|0\rangle$, accompanied by an emission of energy. The time scale of such a transition defines the relaxation decoherence time T_1. The other important time scale is called ensemble dephasing time, denoted by T_2^*, which is typically much shorter than T_1. It measures how long the phase of a qubit will stay intact in real experiments. It is worth mentioning that there is another time scales T_2, which is known as the pure dephasing time or transverse relaxation time. T_2^* is more relevant in experimental level since it considers more interactions (like inhomogeneities of the magnetic field) that can cause a dephasing, while T_2 focus on intrinsic relaxation process, for a detailed comparison of the two dephasing times, please refer to Section 2.7.

Exclusion of decoherence in a scalable quantum computer appears to be impossible; however, various schemes have been proposed to minimise decoherence and consequent errors. At the experimental level, dynamic decoupling technology is widely used to suppress dephasing by averaging out random noise through precise pulse engineering [516, 517, 470, 248, 37]. Another widely used technique is called quantum error correction, which focuses on correcting errors by deploying extra auxiliary qubits. These auxiliary qubits monitor the operations of the working qubits in a non-destructive manner [386, 454, 72, 250, 472, 374]. Quantum error correction will further expand the scale of the quantum computer, since each logical qubit consists of many physical qubits; therefore, quantum error corrections will be less effective when the decoherence in hardware level can not be optimised [374]. Another aspect physicists are working on is the design of qubits and gates which will produce less decoherence in the first place. Consequently, the properties of the physical systems composing the qubits have been extensively examined. Thanks to advancements in theoretical understanding and developments in experimental techniques in quantum computation, scientists have identified many possible qubit schemes with only a small amount of decoherence, which will be unfolded in the following subsections [408, 322, 501, 279, 60, 160, 197, 215, 164, 122, 495, 258, 81, 120, 41, 27, 193].

1.2 Quantum computer architectures

The first qubit candidate we will introduce is the photonic qubit. Photons have many properties that can be used to encode quantum information, such as polarization, optical path, and angular momentum [60, 373, 261, 538]. We will focus on the polarization property of photons as an example. The polarization state of a photon can be easily initialized using wave-plates, which can also perform polarization rotations as one-qubit gates. Besides the mature techniques in the manipulation of polarization states, the relatively long decoherence time (up to 31 μs [310]) is another advantage, the long decoherence time is attributed to the zero rest mass of photons, which results in relatively weak interactions with other matters. However, this relatively weak interaction is a double-edged sword;

interactions with photons become very challenging, requiring strong optical nonlinearities to design a large-scale quantum computer. Over the past several decades, physicists have proposed many innovative solutions to address these shortcomings, such as the application of electromagnetically induced transparency (which uses a laser to tune the optical properties of the medium) [443], cavity quantum electrodynamics [139], and even the development of a single-photon source to achieve scalable high-coherence photonic quantum computers [254]. The advances in photonic quantum computers also stimulate further exploration in related fields such as quantum communication, solid-state physics, and quantum metrology [555, 316, 310, 210].

Trapped atoms also provide an ideal platform for quantum computations for their well-known long coherence time of a single qubit in the order of several seconds. State-of-the-art experimental techniques in the manipulation of electric and magnetic fields allow the isolation of a single atom [85]. Quantum information can be encoded in the two lowest energy levels of a trapped atom, and operations of the qubits are performed with the help of laser or microwave signals [220, 353]. Entanglements of multiple trapped atom qubits are achieved through laser-tuned collective oscillation modes, such as changes in frequency or phase [352]. Initializations of a qubit can be done by optical pumping, and the state of a qubit can be effectively determined through state-dependent optical fluorescence detection [212]. However, challenges in realizing scalable trapped atom quantum computers also exist. As the number of trapped atoms increases, the collective oscillation modes become sophisticated; the laser cooling will loss its efficiency, and the whole system is susceptible to noise. Moreover, mode crosstalk will cause the operation of one qubit to inadvertently affect a nearby qubit, resulting in errors and faults [42]. These issues are being gradually addressed by updating the laser manipulations, finer control of temperature and magnetic fields, and optimization of the distance between trapped atoms to reduce noise and eliminate crosstalk [219, 163, 96, 297, 511].

Single qubits based on nuclear magnetic resonance and nuclear spins in molecules have a comparably long decoherence time to trapped atoms. Nuclear spin systems had already been studied for many years when they were proposed as a qubit candidate in 1996 [95,

180]. Before this proposal, nuclear spin resonance technologies were already familiar in real-life applications, such as spectrum analysis and medical diagnosis [407, 385, 382, 416]. Quantum information can be encoded in the nuclear spin states (depending on the number of protons and neutrons in the nuclei), which can be identified by their Larmor frequencies. Entanglement of nuclear spin states can be realised through various methods, such as spin-spin interactions or exchange interactions via pulse engineering or nuclear spin resonance, which can be used in gate operations as well [338]. Electrons surrounding the nuclei will effectively screen out the noise, leading to a long coherence time. Furthermore, the size of a single nuclear spin qubit is relatively small, therefore favours spatial scalability [502]. However, initialisation of the nuclear spin states presented a lot of challenges [59]. In early years, pseudo-pure-state techniques were demonstrated on single nuclear spin qubits by isolating the signal of an initialised pure state from a high-entropy background [279]. Further research on nuclear spin resonance and algorithmic cooling techniques have demonstrated feasible solutions to the initialisation procedure [366, 428].

As a close analogy to classical electrical circuits, which are *on* and *off* states, encouraged scientists to propose the superconducting qubit based on superconducting circuits. A superconductor circuit includes capacitors, inductors, resistors, and most importantly, a Josephson junction [364, 16, 379]. A Josephson junction, which is made by pinching a non-superconducting material between two superconductors, can support the tunnelling of Cooper pairs. With the help of Josephson junctions, we can bring the anharmonicity into the parabolic energy band of a superconducting circuit [322]. Therefore, we can have a well seperate ground state $|0\rangle$ and the first excited state $|1\rangle$, which will be used encode the quantum information [129]. There are four widely studied qubit schemes based on superconducting circuits: the charge qubit, the phase qubit, the flux qubit, and the transmon [364, 377, 500, 80, 259, 544]. We will use the transmon as an an example. In a transmon qubit, the Hamiltonian of the superconducting circuit can be written as

$$H = 4E_c n^2 - E_J \cos\phi. \tag{1.1}$$

Where n is the number of Cooper pairs, and ϕ is the phase of the superconducting electrons. Experimentally, E_c (charging energy) and E_J (Josephson junction energy) can be

tuned individually [332, 259]. Therefore, the dynamics of the superconducting circuits are governed by the ratio E_J/E_c. When $E_J \leq E_c$, the circuit is more sensitive to charge noise, which is difficult to suppress, leading to possibly stronger decoherence. Transmons are defined in the regime where $E_J \gg E_c$, and at the same time, the energy difference between the two lowest energy levels falls within a range which is accessible to normal microwave pulses for qubit gate operations [259, 522, 544]. Entanglements between transmons are achieved through couplings via resonators, which are also used in measuring the state of the qubit due to the quantum non-destructive nature of cavity quantum electrodynamics [367, 314, 191]. Superconducting qubits are highly integrable with industry-level solid-state platforms, which favours its scalability. However, short decoherence times and precise temperature dependencies are still obstacles towards commercialization [460]. Future investigations will focus on mitigating virous electrical and magnetic noises.

Understanding complex energy band structures requires a significant amount of efforts, as we have seen in trapped atom qubits, nuclear spin qubits, and superconducting qubits. It would be ideal to fabricate an artificial atom, who has well-defined discrete energy levels, which is analogous to an electron or a nuclei in natural atoms, but with simpler structures [239]. Such an artifical atom could potentially be integrated into the well-developed solid-state industry [501, 197, 68, 580]. This spirit has inspired many new schemes, including electron or hole spin qubits (Loss-DiVincenzo spin qubit) [308], exchange-only qubits [131], resonant-exchange qubit [426], donor-acceptor type qubits [236], and the singlet-triplet transition qubits [282, 390]. The hole spin qubit is the major focus of this thesis, which will have its own seperate introductory subsections. In this subsection, we only focus on donor-accepter type qubits as an example. Similarly to the nuclear spins in molecules, spin-1/2 nucleus of a ^{31}P donor in silicon can also be used to construct a qubit. While in natural atoms, the noise from other nuclear spins are hard to manager, in artificial atoms, the host material, silicon, can be isotopically purified, reducing the noise significantly [226, 227]. Qubit gates can be realized using electrical gate confinement to pull the donor electron into the silicon host, which controls the nuclear spin resonance frequency [234]. Entanglements between qubits are achieved by changing the overlap of the electron wave-functions between two donors, which can also be used in the measurement and initialization of a qubit [203].

The most significant challenge on donor-accepter type qubits is the precise placement of the donors, which requires further efforts to improve the precision of fabrication and donor implementation [319].

These five types qubits we introduced above only spans a small portion of the current range of qubit schemes. There are many other talented ideas and competitive candidates, such as spins in point defects, anyons in fractional quantum statistics [365, 429, 11, 75], Majorana fermions [223, 554, 513], neutrinos [18, 422], and so on. These schemes are not covered in our brief introductions, which are only intended to provide a quick overview of the rapid growing field of quantum computation research. At the end of this introductory subsection, profound reverence should be expressed to all the theorists and experimentalists who have carried us into an exciting quantum world.

1.3 Literature review: semiconductor quantum dot electron spin qubits

In this section and the next, we present a brief literature review of semiconductor quantum dot spin qubits and its sub-category - the semiconductor quantum dot hole spin qubits, tracing their developments in chronological order. Semiconductor quantum dot spin qubits, a competitive hardware platform for realizing quantum computing, have witnessed significant advancements over the past several decades.

It's noteworthy that while our review is concentrated on semiconductor quantum dot spin qubits, the broader field of quantum dot research, semiconductor research, and quantum information research encompasses a vast variety of research topics. Each of them is rich enough to deserve its own detailed literature review. Subjects such as quantum metrology [183, 184, 391], quantum cryptography [185, 397], and quantum simulations [162, 353] represent the frontier of research in quantum matters and quantum information. Kondo effects [100, 228, 403], spin-orbit couplings (SOCs) [546, 548, 224], and hyperfine interactions [444, 19, 442] are all important topics for understanding low-dimensional electronic systems like quantum wells, nanowires, and quantum dots. Experimentally, the challenges of semiconductor fabrication techniques, laser manipulations, and resonance technologies are also integrated into industry-level designs [83, 372, 235, 463].

However, limited by the scope of this thesis, many of the areas mentioned above have been omitted from this particular review. Again, it is worth noting that the development of semiconductor quantum dot spin qubits cannot stand by itself; rather, it is deeply rooted in those areas. The methodologies for qubit state preparation, the complex gate manipulation techniques, and the qubit state read-out schemes all owe their advancements to the foundational work done in these allied fields. Therefore, while they are not the primary focus of this review, some related works will permeate throughout.

The initial consideration of using spin as a qubit to encode quantum information is difficult to trace, as it may have appeared in colloquial discussions before being formally presented

in a research article. A starting point might be the pioneering theoretical work of David P. DiVincenzo in 1995 in Ref.[132]. In this work, the spin of electrons, a natural two-level system, is used to construct the basic Boolean logics. Moreover, this article considered an isolated spin in the presence of a static magnetic field B_z and an oscillating magnetic field B_x, which can be described by the following Hamiltonian:

$$H = \frac{1}{2} g\mu_B B_z \sigma_z + \frac{1}{2} g\mu_B B_y \sigma_y P(t) \sin(\omega t)\,, \tag{1.2}$$

where g is the g-factor of the particle, either electron or protons, as mentioned in his original work, μ_B represents the magnetic moment. $P(t)$ is the pulse used to generate various state operations. This Hamiltonian established the fundamental theoretical framework for spin qubits in semiconductor quantum dot systems. Many semiconductor quantum dot spin qubit architectures developed in the following years can be effectively described by this Hamiltonian. This article also included some examples of quantum gates and circuits realized by the relevant modifications of the Hamiltonian.

Encouraged by the successful experimental demonstration of two-qubit gates in ion trap systems, cavity quantum electrodynamics systems, and earlier theoretical speculations on coupled quantum dots as quantum gates, Loss and DiVincenzo published the first mature proposal on semiconductor quantum dot spin qubits in 1997 [308]. This proposal used the localized spin of carriers in semiconductor systems to encode quantum information. In this groundbreaking work, they pointed out that a full set of universal operations is possible using auxiliary spins in quantum dots, achieving both single-qubit and two-qubit gate operations. As an initial attempt to implement two-qubit operations, Loss and DiVincenzo considered the height of tunnelling barrier, via electrostatic gate engineering. They examined the decoherence issue within the framework of quantum master equations, treating the qubits in a magnetic environment as an open quantum system. Over the subsequent 26 years, various spin qubit architectures, including exchange qubits [136, 337], singlet-triplet transition qubits [232, 268], hole spin qubits [63, 64], and many hybrids [512, 202], have been proposed based on this work.

In 1998, Burkard et al. in Ref. [66] discussed quantum gates in semiconductor quantum dots, which can be used to create entanglements between different qubits. They explored

how the Coulomb exchange interaction, combined with the Pauli exclusion principle, leads to the formation of a spin singlet as the ground state of coupled electrons. In this scenario, the spin-spin interaction can be described by Heisenberg-type exchange interactions:

$$H_{\mathrm{s}}(t) = J(t)\mathbf{S}_1 \cdot \mathbf{S}_2 \,, \tag{1.3}$$

where $J(t)$, representing the exchange interaction strength, is controlled by external magnetic fields, electric field, and geometry of the quantum dot. Furthermore, this work highlights that dephasing due to nuclear spins in gallium arsenide, a major platform for semiconductor quantum dot electron spin qubits, is a significant concern. Another finding of Ref. [66] is that the dephasing time can be optimised through dynamical nuclear spin polarization with appropriate magnetic field angles.

A year later, Burkard et al. in Ref. [67] began working on quantum error corrections, aiming to protect quantum computations at the software level. This represents the first tentative step towards implementing quantum algorithms on spin qubit systems. In the same year, Imamoğlu et al. in Ref. [225] proposed a scheme to tune the interactions between two spin qubits using the cavity quantum electrodynamics method. In this framework, parallel controlled NOT gates and arbitrary SU(2) rotations of the spin state were achieved using conduction band-to-valence band hole Raman transitions induced by laser fields. Notably, a year prior, in 1998, Sherwin et al. in Ref. [451] had theoretically proposed using circularly polarized light in cavity quantum electrodynamics to couple quantum dots for the entanglement of qubits. However, their focus was primarily on the orbital levels of the quantum dots. This article also posed a critical issue that became a major topic in subsequent years: the gate operation time should be much shorter than the spin relaxation and decoherence time. How to evaluate the realistic decoherence time became a question. In previous experiments, coherence times of up to 1 μs for conduction band electrons had been observed in doped quantum wells and bulk semiconductor structures. However, in 1998, Gupta et al. in Ref. [194] reported a much shorter relaxation time, only 3 ns in chemically prepared CdSe quantum dots, posing a challenge. More details on this relaxation problem will be introduced in other literature in the following text.

In 2000, Hu et al. in Ref. [217] used GaAs as the platform to study the electron spin

qubits, adopting several experimental-relevant parameters from single-electron transistor designs. They demonstrated that achieving a substantial exchange coupling for fast gate operations is not compatible with a vanishing double occupation probability, which is necessary for maintaining a low error rate. The Hilbert space structure was examined in detail to understand decoherence, magnetic control, and error correction mechanisms.

In 2000, Hu et al. in Ref. [217] used GaAs as the platform to study electron spin qubits, adopting several experimental-relevant parameters from single-electron transistor designs. They demonstrated that achieving substantial exchange coupling for fast gate operations is not compatible with a vanishing double occupation probability, which is necessary for maintaining a low error rate. The Hilbert space structure was examined in detail to understand decoherence, magnetic control, and error correction mechanisms.

Parallel to the developments of spin qubits in semiconductor quantum dot systems, spintronics has emerged as a competitive candidate for the next generation of solid-state devices. Research in spintronics has revealed that SOCs in semiconductors can lead to anisotropic exchange interactions among a pair of localized conduction-band electrons, i.e., the spins of electrons in quantum dots. In this context, Kavokin in Ref. [242] found that the Heisenberg-type exchange Hamiltonian, considered in coupled quantum dots, exhibits anisotropic exchange interactions. Furthermore, SOC is present due to the lack of inversion symmetry in GaAs. It was also pointed out that the anti-symmetric SOC, known as Dzyaloshinskii-Moriya interactions, significantly contributes to spin relaxation and decoherence. The role of SOC in semiconductor quantum dot systems is further explored in work done by Khaetskii et al. in Ref. [246], which considers the Bulk inversion asymmetry-induced Dresselhaus SOC:

$$H = \beta(\sigma_y p_y - \sigma_x p_x)\,. \tag{1.4}$$

This work indicates that SOC is the dominant mechanism for phonon-assisted spin-flip transitions between two relevant Zeeman sub-levels of a spin qubit in SQDs. Another study by Merkulov et al. in Ref. [340] examined electron spin relaxation due to nuclear interactions, determined by electron spin-nuclear spin interactions and the nuclear spin in the dipole field of its nuclear neighbours.

In 2001, Salis et al. in Ref. [435] successfully demonstrated electrical control of spin coherence in semiconductor nanostructures, verifying the potential of using quantum dots as a spin qubit platform. Their experiments showed that the spin coherence time T_2^* could reach up to 450 ps, while the coherent spin precession frequency could reach 13 GHz for a fixed magnetic field of 6 T in $Al_xGa_{1-x}As$ quantum wells, where x varies across the sample. In these experiments, the applied electric field could alter the wave-function shape and electronic g-factors, thereby changing the spin splittings. In the same year, Gupta et al. in Ref. [195] demonstrated all-optical control over electron spins on a femtosecond timescale. Their work involved time-resolved Faraday rotation experiments, using ultrafast laser pulses to produce coherent rotations of electron spins. The study also examined the effects of below-band-gap *tipping* pulses in creating an effective magnetic field through the optical Stark effect, crucial for rotating the electron spins.

In 2002, Khaetskii et al. in Ref. [247] theoretically calculated that spin decoherence of an electron in a semiconductor quantum dot is due to coupling between the electron spin and nuclei at different atomic sites, with a decoherence time scale of several milliseconds. Furthermore, they found that the decay of the electron spin correlation follows a power law or an inverse logarithmic law. In another work, Erlingsson et al. further explored this nature and pointed out that decoherence time due to nuclear spin is determined by the flipping of spin, therefore, a standard Markovian approach is not applicable [147]. Woods et al. in Ref. [550] discussed how, at low temperatures, the size of the quantum dot is another crucial factor in improving relaxation time, and that two-phonon relaxation processes become significant at higher temperatures. For quantum gate operations, Burkard et al. in Ref. [65] pointed out that in an ideal case, where the CNOT gate operation may cancel the SOC effects due to similar pulse shapes, the gate error can be significantly mitigated by designing the pulse shape.

Experimentally, Petta et al. in Ref. [388] measured the full angular dependence of the Zeeman splitting in copper nanoparticles at a constant magnetic field. This work revealed highly anisotropic g-factors, supported by considering the SOCs in the context of random matrix theory. Although copper nanoparticles are not a platform for spin qubits, this

research still provides important insights into g-factor modulation and the effects of SOCs. Another achievement of Ref. [388] is the demonstration of tuning electron-spin-nuclear-spin interactions using only gate voltages in two-dimensional electron gas systems, paving the way for more advanced manipulation of spin states.

In 2003, Golovach et al. in Ref. [187] theoretically examined the phonon-induced decay of the electron spin in GaAs quantum dots. This article considered an effective Hamiltonian that includes the spin qubit, phonons, confinement potentials, and both the Rashba SOC and the Dresselhaus SOC; it predicted that the dephasing time T_2 can be comparable with spin relaxation T_1. Another work done by Sousa et al. in Ref. [121] further discussed the interactions between the electronic wave-functions and the gate electric field and the interface electric field, pointing out that due to the presence of the SOCs, g-factors and the T_1 relaxation time are very sensitive to the dot geometry and the magnetic field applied. These SOCs and g-factors can be tuned by the gate electric field, which is a possible way to scale up the computations.

The electron spin relaxation time was experimentally determined in GaAs quantum dots by Hanson et al. this year [196]. The Zeeman energy splitting was measured by electronic transport experiments directly. In the experiments, a magnetic field up to 7.5 T was applied, resulting in a spin relaxation time of more than 50 μs, which is much longer than the spin relaxation time measured in bulk n-type GaAs, GaAs quantum wells, and InAs quantum dots.

In 2004, Pryor et al. studied the Landé g-factors in GaAs semiconductor quantum dots [401]. They highlighted that in quantum dot structures, the electronic g-factors can vary significantly (the bare value is far beyond the bulk material's values as previous experiments suggested), influenced by the dot geometries, the strain, and the confinements. These variations in g-factors can lead to rich spin dynamics, emphasizing the role of quantum confinements and strains in tuning spin splitting and anisotropic exchange interactions. The electrical control of g-factors, which is a probe of the qubit Zeeman splitting, started to become an important topic.

Kroutvar et al. in Ref. [265] demonstrated a novel technique for optically programming electron spin in semiconductor quantum dots. Their work shows that a single electron spin could be programmed and read out optically, with spin lifetimes extending up to 20 ms at a temperature of 1 K. Elzerman et al. in Ref. [146] demonstrated the readout of the state of an individual electron spin in a quantum dot. Their approach, characterized by a visibility of about 65%, leverages the differences in tunnel rates for different spin states. This visibility is significant in the context of quantum measurement and indicates a high degree of accuracy in detecting spin states. The method's success hinges on the spin-to-charge conversion mechanism and the sensitivity of the quantum point contact used as a charge detector. Another experimental advance is using strain to create spin splittings. Kato et al. in Ref. [240] demonstrated coherent spin manipulation in strained semiconductor quantum wells without an external magnetic field, owing to the SOCs. They used electric fields only to induce spin precession in GaAs quantum wells. A key feature of their experiment was achieving Rabi frequencies up to 30 MHz, measured by optical techniques, demonstrating precise control over the spin states. The role of strains is further explored, which is the main reason for the spin splitting.

In 2005, Stano et al. in Ref. [464] presented a detailed theoretical analysis of phonon-induced spin relaxation in coupled lateral quantum dots in the presence of SOC, including the Bychkov-Rashba term, the linear Dresselhaus term, and the cubic Dresselhaus term. This work highlights that spin relaxation in coupled quantum dots is highly anisotropic as a result of the interplay between Bychkov-Rashba and Dresselhaus spin-orbit terms and is limited by the in-plane inversion symmetry. Another discovery is the identification of *spin-hot spots*, which are really the anti-crossings caused by SOC that significantly enhance spin relaxation under certain conditions. Stepanenko et al. in Ref. [467] introduced a novel approach theoretically to enhance the electron spin coherence in quantum dots using optical preparation of the nuclear spins. This work showed that light can be used as a probe to measure the nuclear spins and hyperfine field, to make better preparation of the electron spin coherence. From this method, one can improve the electron coherence time from 5 ns to 10 μs. Bulaev et al. in Ref. [62] explored both the Rashba SOC and the Dresselhaus SOC of electrons in two-dimensional QDs under a perpendicular magnetic

field, calculated that the two SOCs will lead to anti-crossings and spin mixings. A key finding is that Rashba SOC leads to level anti-crossing and a cusp-like structure in the spin relaxation rate as a function of the magnetic field, which is present in Dresselhaus SOCs. A theoretical prediction of long single-spin relaxation times in GaAs quantum dot is given up to 0.85 ms, and up to 20 ms in GaInAs quantum dots.

In experiments, Johnson et al. in Ref. [232] investigated the spin relaxation mechanisms in confined electron systems within a GaAs double quantum dot (forming a triplet-singlet state). The study reveals that spin flips, which cause an electron to lose its spin orientation memory, are primarily dominated by interactions with nuclear spins, as predicted in single spin qubit in semiconductor quantum dot. It's noted that these spin flips are significantly slowed down when a magnetic field of a few millitesla is applied. Petta et al. in Ref. [389] demonstrated the coherent control of a quantum two-level system based on two-electron spin states in semiconductor quantum dots. Using GaAs as the platform, the researchers developed techniques for rapid electrical control of the exchange interaction between electron spins, enabling them to prepare, manipulate, and read out the spin states. The dephasing time was measured to be about 10 ns, which was limited by hyperfine interactions with the GaAs host nuclei. Rabi oscillations in two-spin space, and 180 ps SWAP operation between two electron spins were demonstrated. Moreover, Spin-echo pulse sequences were implemented to suppress hyperfine-induced dephasing, extending the spin coherence time beyond 1 ms.

In 2006, Flindt et al. in Ref. [161] proposed that SOCs can be a route to control electron spins in quantum dots for quantum computing applications. This approach allows for both single-qubit and two-qubit operations. Compared to the exchange coupling method, the spin-orbit-induced coupling is less sensitive to random electrical fluctuations, making it a potentially more robust option. For two-qubit operations, the coupling mechanism involves a combination of SOC and the long-range Coulomb interaction. This approach differs from traditional methods that use exchange coupling, offering a potentially more stable alternative that is less affected by electrical noise. The study focuses on a simplified one-dimensional model with electrons localized in quantum dots, considering a perpendic-

ular magnetic field and SOC of a specific form. San-Jose et al. in Ref. [437] studied the spin-orbit mediated relaxation and dephasing of electron spins in quantum dots. The study reveals that higher-order contributions, often overlooked in literature, provide a dominant relaxation mechanism in low magnetic fields and have a geometrical origin. In the low-field limit, relaxation is mainly due to couplings to electron-hole excitations and possibly $1/f$ noise, rather than phonons. The researchers show that in the low magnetic field regime, relaxation processes related to the diffusion of the Berry phase become significant. These processes are analogs to Elliott's spin relaxation in bulk semiconductors and metals and have a geometric interpretation. The study emphasizes that spin relaxation is induced by any fluctuating electric field, not just phonons, and can include Ohmic fluctuations from electrodes and quantum point contacts, shot noise, and $1/f$ background charge fluctuations common in mesoscopic systems. Witzel et al. in Ref. [549] studied the decoherence of a single localized electron spin due to its coupling to the lattice nuclear spin bath in semiconductor quantum computer architectures. This complex quantum decoherence problem involves spectral diffusion of the electron spin resonance frequency, arising from temporally fluctuating nuclear magnetic fields caused by dipolar interaction-induced flip-flops of nuclear spin pairs. The study provides a formally exact solution to this non-Markovian quantum decoherence problem and numerically calculated accurate spin decoherence at short times, which is particularly relevant.

In 2007, Trif et al. in Ref. [488] theoretically studied the electron spins in nanowire quantum dots within a transmission line resonator. Calculations showed that SOCs enable coherent manipulation, storage, and read-out of quantum information in an all-electrical manner. The study discussed both cases of strong longitudinal and transverse confinements, focusing on the potential for longitudinal confinement.

Fasth et al. in Ref. [153] experimentally demonstrated the control of electron numbers down to the last electron in tunable few-electron quantum dots in InAs nanowires. The researchers developed a method to directly determine the magnitude of SOC in a two-electron quantum dot. They observed that due to a large effective g-factor, the transition between the singlet state and the triplet state is dominated by the Zeeman energy rather

than by orbital effects. This argument is supported by an experimentally measured avoided crossing with a magnitude of 0.25 meV. The experiment, conducted using low-temperature transport spectroscopy in the Coulomb blockade regime, allowed the creation of highly tunable quantum dot systems with significant SOC. Amasha et al. in Ref [14] demonstrated electrical control over the spin relaxation time between Zeeman splitting in a lateral quantum dot. The key result is that the spin relaxation, mediated by the spin-orbit interaction, can be varied by over an order of magnitude through manipulation of the orbital states using gate voltages (up to 1 s). Further, the spin relaxation rate depends only on the confinements of the electron wave function along the direction of the applied in-plane magnetic field. This observation verified the theoretical expectations introduced above in GaAs. Another experimental advance is the mitigation of the dephasing in quantum dot spin qubits due to the Larmor precession around a random effective field from the nuclear spins in GaAs by Koppens et al. in Ref. [263] The authors demonstrated the suppression of this dephasing to a large extent via a spin-echo pulse, achieving a spin-echo decay time of about 0.5 μs at 70 mT. This result is within the range of theoretical predictions for the electron spin coherence time governed by electron-nuclear dynamics. The researchers used a two-quantum dot system, where one electron always resides in the right dot, and a second electron can flow through the two dots only if the spins are antiparallel. By manipulating the electron spins with a sequence of radio-frequency pulses, they could control the spin states and study their dynamics. This experiment also verified that the spin-echo decay time T_2 is much longer than the dephasing time T_2^*, which will be further explored in Chapter 2-Section 2.7.

In 2008, Cywiński et al. in Ref. [111] theoretically investigated the pure dephasing decoherence (free induction decay and spin echo) of a spin qubit interacting with a nuclear spin bath. Focusing on the hyperfine-mediated interactions between nuclear spins, the decoherence at higher magnetic fields has a small oscillation superimposed on the spin echo signal due to spectral diffusion, while at lower fields, the coherence decays to zero in characteristic times of about 0.1-1 μs in gated GaAs dots.

In experiments, Hu et al. in Ref. [216] presented a novel quantum non-demolition method

for measuring a single-electron spin in a quantum dot inside a microcavity using a giant optical Faraday rotation near the resonant regime, where different phase shifts for left-circularly and right-circularly polarized lights reflected from the cavity result in significant Faraday rotation. This rotation, caused by cavity quantum electrodynamics and the optical spin selection rule, can be easily detected experimentally. The paper proposes a photon-spin entangling gate and a scalable scheme for creating remote spin entanglement via a single photon. The study considers a singly charged quantum dot, such as a self-assembled In(Ga)As quantum dot or a GaAs interface quantum dot inside an optical resonant cavity. It details how the optical transitions of a negatively charged exciton in the quantum dot show spin-dependent behavior. The interaction between the cavity field and the charged exciton results in a significant Faraday rotation, which can be exploited for quantum non-demolition measurement of a single-electron spin. Reilly et al. addressed the challenge of spin dephasing caused by fluctuating nuclear spins in GaAs. The study introduces a method for preparing the nuclear spin environment that remarkably suppresses the relevant component of nuclear spin fluctuations by a factor of approximately 70%. This suppression made the inhomogeneous dephasing time for the two-electron spin state extend beyond 1 μs.

By 2009, it was becoming clear that obtaining high coherence using GaAs quantum dots as the platform for fabricating electron spin qubits was challenging due to the strong hyperfine interactions, which are a built-in problem arising from the magnetic moments of the Ga and As nuclei. Alternative materials like Silicon or Germanium have been extensively studied after 2009, either using the donor-acceptor type architecture or quantum dots. These materials were very appealing for spin qubits due to the low concentration of magnetic nuclei, allowing for the overcoming of the hyperfine-induced dephasing present in GaAs semiconductors. There have been many exciting advances, both theoretically and experimentally [243]. A reconfigurable gate architecture in the Silicon/Germanium system has been demonstrated [566]. In Silicon systems, various milestones have been achieved, including a two-qubit logic gate [507], a fault-tolerant addressable spin qubit [478], circuit quantum electrodynamics manipulations [341], a resonantly driven CNOT gate [567], a spin-photon interface [342], a programmable two-qubit quantum processor [535], and the

measurement of spin lifetime and charge noise [387].

1.4 Literature review: semiconductor quantum dot hole spin qubit

As we introduced in the last section, the decoherence issue due to the nuclear spin in III-V semiconductor quantum dot electron spin qubit is hard to address. Scientists started looking at using holes in the valence band to encode quantum information. Firstly, hole systems possess strong SOC [412, 545, 546, 114, 103, 325, 251, 252, 79, 140, 356, 38, 347, 348, 329, 483, 2, 291], which enables pure electrical manipulation of spin states via EDSR [188, 64, 413, 414]. Secondly, the absence of valley degeneracy avoids complications associated with the increase in Hilbert space that occurs for electrons [190, 167, 106, 107, 166, 199, 432, 48, 56, 155, 519, 462, 520]. Thirdly, the hyperfine interaction is a strong decoherence source in other materials such as III-V group semiconductors [226, 247, 90, 389, 271, 159, 89, 158, 77, 20, 78, 252, 398, 526], some materials which had been studied in p-type devices like silicon can be isotopically purified. In this section, we will explored how the hole spin qubits becomes to an important candidate in solid-state quantum computations.

Hole devices have been studied in various semiconductor contexts before being considered as candidates for qubits [354, 12, 249, 278, 119, 160, 197, 441]. However, the focus on hole systems for quantum information processing, particularly in the context of semiconductor quantum dot spin qubits, gained significant momentum after the seminal proposal by Loss and DiVincenzo in 1997 [308].

The early discussions on using holes in the valence band for quantum information processing primarily revolved around the spin relaxation time. The relaxation time in III-V semiconductor quantum dot electronic spin qubits is limited by nuclear spins via hyperfine interactions. This limitation can be mitigated in hole systems because the hole wave functions exhibit p-like orbital symmetry near each atom in the crystal. As a result, the holes do not experience the contact-type hyperfine interactions that are a significant source of decoherence in electron spin qubits.

This characteristic of hole systems makes them particularly attractive for quantum computing applications. The reduced interaction with nuclear spins potentially leads to longer coherence times, making hole spin qubits a promising platform for quantum information processing. The exploration of hole spin qubits has thus been driven by the quest to overcome the decoherence challenges faced by electron spin qubits in semiconductor quantum dots, paving the way for more stable and reliable quantum computing technologies.

Woods et al. in 2003 presented a theoretical analysis of hole spin relaxation in quantum dots [551]. While there were many articles on hole spin relaxation in quantum wells and bulk semiconductors, quantum dots present distinct characteristics. The research focused on acoustic phonon-assisted spin flips at low temperatures with a magnetic field. A detailed numerical diagonalization of the Luttinger Hamiltonian with the Bir-Pikus Hamiltonian is discussed, alongside the perturbation treatment of the magnetic field. Key findings include the decoherence time for hole spins in quantum dots, with a size around 20 nm, the decoherence time is estimated to be on the order of 100 ns, which is actually shorter than the decoherence time for electron spins mentioned before. This difference is attributed to the stronger phonon scattering in hole systems. Furthermore, the relaxation rate is influenced by the diameter of the quantum dot and the mass of the hole, providing possibilities to design qubits using other materials.

In 2004, Lu et al. in Ref. [309] expanded on the relaxation problem of hole spins in GaAs quantum dots. This research improved the previous result by adding more terms such as strain, magnetic field, quantum dot diameter, quantum well width, and temperatures. The study reveals that strain impacts quantum dot spin relaxation differently based on the quantum well's growth direction. For instance, in quantum dots within [001]-oriented quantum wells, strain alters the energy levels of heavy and light holes, whereas in [111]-oriented wells, it introduces additional spin mixing and subsequent relaxation. This work also highlights the significance of both piezoelectric interaction and deformation potential in hole-phonon scattering, marking a contrast to electron spins in quantum dots where relaxation is mainly due to piezoelectric interactions, which is different from [551]. The research also delves into the effects of quantum dot diameter and magnetic field on spin

relaxation, showing that relaxation time can increase with quantum dot diameter at lower temperatures and exhibit a peak at higher temperatures. Additionally, the temperature dependence of spin relaxation is analyzed, demonstrating a reduction in relaxation time with rising temperature due to increased phonon activity.

In 2005, Bulaev et al. in Ref. [63] investigated the heavy-hole spin relaxation and decoherence in quantum dots subjected to perpendicular magnetic fields. This study shows that at low temperatures, the spin decoherence time is twice as long as the spin relaxation time. Additionally, it is found that the spin relaxation time for heavy holes can be comparable to, or even longer than, that for electrons in strongly two-dimensional quantum dots. The research explores two primary spin relaxation mechanisms for electron spins in quantum dots: interaction with phonons and hyperfine interaction with surrounding nuclear spins. Due to the valence band's p-type symmetry, the hyperfine interaction of holes with lattice nuclei is reduced compared to that of electrons, making hole spins potentially more suitable for long-lived quantum information carriers. The paper also investigates the effect of SOCs (Rashba and Dresselhaus) and the coupling between heavy-hole and light-hole sub-bands on spin relaxation and decoherence, using an effective Hamiltonian for two-dimensional heavy holes in a perpendicular magnetic field.

In 2006, Sleiter et al. in Ref. [458] raised a question regarding the use of holes in GaAs quantum dots as qubits for quantum computing. This research estimated the Rabi frequency for coherent quantum state manipulations, finding the Rabi frequency for holes in these quantum dots to be notably low, around 10 kHz, primarily due to the minor coupling between the heavy-hole states and the light-hole states ($|M = 3/2\rangle$ and $|M = -3/2\rangle$ states in the original article). This finding is crucial for achieving effective qubit operations through external radio-frequency magnetic fields. It also points out the dependency of the Rabi frequency on the specific nature of the quantum dot's confining potential and the orientation of the magnetic field. This question is later addressed by considering the electrical control of the spin qubits using strong SOCs, which will be further explained in subsequent discussions.

In the same year, Bulaev et al. in Ref. [64] proposed an innovative approach for manipu-

lating the spin of heavy holes in quantum dots called EDSR, distinguished from electron spin resonance used in electron spin qubits. EDSR uses the SOC between states of different orbital momentum and opposite spin orientations, enabling the use of an applied electric radio-frequency field to induce transitions between spin-up and spin-down states. The study pointed out the potential of using heavy-hole spins, instead of electron spins, as carriers of quantum information due to their reduced hyperfine interaction with lattice nuclei owing to the valence band's p-symmetry. It suggests that the spin relaxation and decoherence times for holes could be comparable to, or even longer than, those for electrons, making them attractive for quantum computing applications. This approach offers a solution to the challenge of manipulating hole spins, which do not couple to magnetic fields in the leading dipole approximation. By demonstrating that an applied electric field can induce transitions between hole spin states due to spin-orbit interaction, the paper opens up a new window for detecting heavy-hole spin resonance signals and controlling spin dynamics in two-dimensional systems. The method can also be used to determine parameters of heavy holes such as the g-factor, effective mass, SOC constants, and spin relaxation and decoherence times.

In 2008, Fischer et al. in Ref. [159] conducted a theoretical study on the interaction of a heavy-hole state with nuclear spins in a quasi-two-dimensional III-V semiconductor quantum dot and its implications for spin decoherence. Contrary to previous conclusions that heavy-hole states have negligible interaction with nuclear spins, the study reveals that the interaction can be quite strong and potentially dominant in some cases. The paper pointed out that, for unstrained quantum dots, the interaction is Ising-like, leading to unique decoherence properties that could be advantageous for using dot-confined hole spins in quantum information processing. The nuclear-spin interactions were derived, leading to an effective spin Hamiltonian for quantum-dot-confined heavy-hole states. The dynamics of the transverse heavy-hole spins were calculated for different external magnetic field directions, and the coupling strengths were estimated for a GaAs quantum dot. This work also explored the interactions in both an atom and a quantum dot, noting that the strong coupling of the HH to the nuclear spins is not due to confinement but is also present in bulk crystals, while the Ising-type interaction is a feature of quasi-

two-dimensional systems. In the same year, Rashba in Ref. [413] presented a detailed theoretical discussion for understanding EDSR in quantum dots in a mean field theory view (this is not only aimed at hole spin qubits; experimental demonstration of EDSR in electron spin qubits can be found in Ref. [362]). This paper discussed three mechanisms of EDSR: SOCs, inhomogeneous Zeeman coupling, and hyperfine interaction with nuclear spins. This approach allows the replacement of the nuclear spin reservoir with a classical field, facilitating the analysis of electron-spin dynamics. Another finding was that the hyperfine interaction between electron and nuclear spins can be strong and plays a critical role in the dynamics of EDSR. This interaction is particularly important in low magnetic fields, where it becomes the dominant mechanism for EDSR.

Experimentally, Gerardot et al. in Ref. [179] demonstrated the initialization of a single hole spin in a semiconductor quantum dot using optical pumping techniques. This research achieves a remarkably high fidelity (about 99%) in initializing the hole spin in a self-assembled quantum dot even at zero magnetic field. The experimental approach involves using an S_z-polarized laser to drive a single hole within the quantum dot to an exciton state, achieving high-fidelity initialization. This is the first experimental demonstration of the valence hole in the quantum dot. Experiments also verified that in a quantum dot, with strong strain and quantization, the heavy hole, which typically has a spin-3/2, can be effectively described by a pseudo-spin-1/2 system, contributing to the observed weak spin decoherence mechanisms. Furthermore, the researchers observed a hole spin relaxation time at a low field of about 1 ms, which is comparable to electron spin relaxation times under similar conditions. These findings support the development of quantum computing and spintronic devices, as they suggest a route to realizing solid-state quantum networks capable of intra-converting the spin state with the polarization of a photon.

In the same year, Eble et al. in Ref. [142] provided an experimental investigation of hole spin dynamics in p-doped InAs/GaAs quantum dots, and the hyperfine interactions between hole and nuclear spins. The study considers pump-probe and time-resolved photoluminescence experiments to observe the dynamics and interactions of spins in these quantum dots. A key finding of the research is the experimental evidence of the existence

of hyperfine interactions between hole spins and nuclear spins, even though the contact hyperfine is declared not to be present. The paper also reports that in the absence of an external magnetic field, calculations based on dipole-dipole coupling between the hole and the quantum dot nuclei yield a hole-spin dephasing time for an ensemble of dots of approximately 14 ns. The quantum dots used are based on self-assembled InAs, separated by GaAs spacer layers, with a surface density of about $10^{10}\,\mathrm{cm}^{-2}$. These structures are p-modulation doped with carbon; the circularly polarized pump beams are used to generate spin-polarized electrons, and the spontaneous decay of the trion state leads to efficient hole-spin cooling. Unlike the perpendicular magnetic field considered in previous experiments, this study considers the external magnetic field parallel to the growth axis of the sample.

In 2009, Trif et al. in Ref. [489] explored the spin relaxation in heavy-hole quantum dots at low external magnetic fields, focusing on the role of two-phonon processes combined with spin-orbit interaction in explaining the observed saturation of spin-relaxation rates in heavy-hole quantum dots at small magnetic fields. A major finding of the paper is the theoretical demonstration that two-phonon processes are experimentally relevant and provide a quantitative explanation for the recently observed behaviours in heavy-hole quantum dots. The study proposes further experiments to identify the relevant spin-relaxation mechanisms at low magnetic fields. The model considered a heavy hole confined to a quantum dot interacting with the surrounding phonon bath with various elements, including the dot Hamiltonian, Zeeman energy, spin-orbit Hamiltonian, and the interaction of the heavy hole charge with the phonon field. In the absence of an external magnetic field, the hole-spin dephasing time for an ensemble of quantum dots is approximately 14 ns, which is about the same as the experimental result. In the same year, Testelin et al. in Ref. [485] provided detailed calculations of the spin interaction of a hole confined in a quantum dot with surrounding nuclei. The study primarily focuses on the effective magnetic field resulting from the hyperfine interaction and its impact on the dephasing time of hole spins. In contrast to electrons, the hyperfine interaction for holes is predominantly dipole-dipole in nature due to the p-symmetry of valence-band states. This interaction is anisotropic for both pure and mixed hole states, with the coupling constants of the hole-nuclear in-

teraction being only one order of magnitude smaller than those of the electron-nuclear interaction. An important finding is that the ensemble dephasing time for hole spins in III-V quantum dots is of the order of 10 ns, which is significantly longer than that for electrons due to the weaker nature of the hole-nuclear interaction.

Experimentally, Crooker et al. in Ref. [101] measured spin noise spectroscopy and probed the dynamical properties of spins localized in semiconductor quantum dot ensembles. They analyzed the frequency spectra of random spin fluctuations in ensembles of InAs/GaAs quantum dots at low temperatures. Both electron and hole spin fluctuations generate distinct noise peaks that shift and broaden with magnetic field, serving as a direct probe to test their g-factors and dephasing rates within the ensemble. The paper reports a large, energy-dependent anisotropy of the in-plane hole g-factor, reflecting variations in the average quantum dot confinement potential. The experimental setup involved a sensitive optical Faraday rotation magnetometer, coupled to a digitizer and field-programmable gate array, to measure and average noise spectra from 0-1 GHz continuously in real time with sub-nano sensitivity. This is the first spin noise spectroscopy of fully quantum-confined electrons and holes in quantum dots. The research provides direct measurements of g-factors and dephasing times.

In 2010, Fischer et al. in Ref. [158] theoretically investigated the spin dynamics of a heavy hole confined in an unstrained III-V semiconductor quantum dot, interacting with a narrowed nuclear-spin bath. The study focused on the band hybridization-induced exponential decay of hole-spin superpositions due to hyperfine-mediated nuclear pair flips. Calculations demonstrate that the single-hole-spin decoherence time T_2 can be significantly manipulated by varying external parameters, including the formation of band hybridization non-Ising (transverse) terms in the hyperfine Hamiltonian. The magnitude of these terms depends on the quantum dot's geometry, leading to fluctuations in the Overhauser field and consequently causing exponential single-hole-spin decoherence. This contrasts with the predominantly Ising-like coupling of heavy holes to nuclear spins. The paper also shows that under certain experimentally accessible conditions, hyperfine-mediated nuclear-pair-flip processes can be significantly suppressed, thereby extending the coherence times

of hole spins. The hole-nuclear spin interactions within the quantum dot are estimated by considering the contributions of conduction band and light-hole states to the hybridized heavy-hole states. This paper also explores the impact of various factors, such as magnetic field strength and quantum dot dimensions, on the hole-spin decoherence rate. Roloff et al. in Ref. [423] investigated high-fidelity single-qubit operations on a hole spin in a quantum dot through electric g-tensor control. This paper verified the increased dephasing time due to reduced interaction with nuclear spins and efficient g-tensor control. It discusses the optimization of pulse shapes for various qubit operations using process-tomography-based optimal control, revealing that these operations can be performed with minimal fidelity loss despite decoherence and dissipation arising from interactions with host-lattice nuclear spins and phonons. Another finding is that gate operation times of approximately 10 ns can achieve a fidelity loss of only about 1%, highlighting the robustness of the proposed scheme against decoherence factors.

Experimentally, Fallahi et al. in Ref. [150] performed measurements of the hyperfine interaction strength and sign of a heavy hole with nuclear spins in single self-assembled quantum dots. This study used quantum dot resonance locking to an incident laser frequency for generating nuclear spin polarization. By monitoring the resulting Overhauser shift in optical transitions split by electron or exciton Zeeman energy, determining the ratio of the heavy-hole to electron hyperfine interactions becomes possible. This ratio was found to be approximately 0.09 ± 0.02 in three different quantum dots. The study was conducted using charge-tunable InGaAs self-assembled quantum dots embedded in a Schottky-diode structure. The experiments were carried out at a temperature of 4.2 K with an external field in the Faraday geometry. Circularly polarized pump beams were used to generate spin-polarized electrons, and the spontaneous decay of the trion state led to efficient hole-spin cooling. The experimental results indicate that the hyperfine interactions for heavy holes are not only significant but also have an opposite sign to those of electrons.

In 2011, Kloeffel et al. in Ref. [251] theoretically studied the low-energy hole states in Germanium/Silicon core/shell nanowires, highlighting that the low-energy valence band

in these nanowires is quasi-degenerate, formed by two doublets with different orbital angular momentum. These holes can be controlled through the relative shell thickness and external fields. A direct coupling to a moderate electric field is possible, leading to a notably large Rashba-type spin-orbit interaction, resulting in pronounced helical states that enable electrical spin control. The nanowires, which are sensitive to external magnetic fields, exhibit g-factors dependent on the field orientation and the hole momentum. Another important term of the study is the direct Rashba spin-orbit interaction, arising from direct dipolar coupling to an external electric field. This interaction is substantially larger than the conventional Rashba spin-orbit interaction for holes, appearing in the third order. The direct Rashba SOC scales linearly with the core diameter, ensuring that spin-orbit interaction remains strong even in larger nanowires. The study demonstrates that Germanium/Silicon nanowires can act as a unique platform for helical hole states and potentially for Majorana fermions.

This theoretical proposal was immediately followed by an experimental study in the same year. Hu et al. in Ref. [218] measured hole spin relaxation in Germanium–Silicon core–shell nanowire-based quantum dots. Experiments demonstrated a series of state preparation, pulsed gate control, and charge-sensing spin read-out of hole spins. T_1 spin relaxation times of up to 0.6 ms in coupled quantum dots at zero magnetic field were reported. Furthermore, the spin relaxation time was found to increase as the magnetic field was reduced, consistent with the spin–orbit mechanism.

In 2012, Szumniak et al. in Ref. [475] presented a new hole-based nano-device, which can control the spin state of heavy holes. This device uses the Dresselhaus spin-orbit interaction, which can convert the spatial motion of the hole into a spin rotation. The manipulation of the heavy-hole spin is achieved by moving the hole around closed loops defined by metal gates. The process does not require the application of microwave radiation, radio-frequency electric fields, or magnetic fields. Instead, the quantum gate operations are on sub-nanosecond timescales and rely on the application of a weak static voltage (gate field). Theoretically, the proposal is supported by the four-band Luttinger-Kohn model.

Experimentally, Godden et al. in Ref. [186] demonstrated the coherent optical control of a

single heavy-hole spin confined in an InAs/GaAs quantum dot using an in-plane magnetic field. The creation of a coherent superposition of hole-spin states through the ionization of a spin-polarized electron-hole pair enabled the hole to be left in a spin-polarized state as the electron tunnelled from the dot. From the hole spin precesses about the applied magnetic field, and from the decay of this precession, a dephasing time of approximately 15.4 ns was measured, which is longer than that for an electron. The rotation of the hole spin about the optical axis was realized using a circularly polarized laser pulse resonant with the hole-trion transition. This process induced a geometric phase shift on the selected spin, allowing for arbitrary rotations of the hole spin by combining rotations about two axes.

In 2013, Kloeffel et al. in Ref. [320] proposed the integration of circuit quantum electrodynamics with hole spins in Germanium/Silicon core/shell nanowire quantum dots. The work theoretically highlighted how single-qubit gates can be driven through electric-dipole-induced spin resonance, achieving spin-flip times shorter than 100 ps. Furthermore, the study discusses the possibility of realizing long-distance qubit-qubit coupling via the cavity electric field of a superconducting transmission line resonator, with operation times below 20 ns for the entangling iSWAP gate. This scheme relies on the absence of Dresselhaus spin-orbit interaction and the presence of strong Rashba-type SOCs, enabling precise control over transverse qubit coupling through an externally applied perpendicular electric field, which can act as a switch for quantum gates and provides control over the g-factor, thereby allowing the independent operation of single- and two-qubit gates.

In experiments, Pribiag et al. in Ref. [400] realized electrical control of single hole spins in InSb nanowire quantum dots. The study shows that hole spins in III-V semiconductors, due to their strong spin-orbit interaction and weak coupling to nuclear spins, can offer longer coherence times and enhanced spin control compared to electron spins. This work demonstrated the gate-tunable hole quantum dots in InSb nanowires, which allow for a direct comparison of hyperfine interaction strengths, g-factors, and spin blockade anisotropies in both hole and electron quantum dot regimes. Secondly, Pauli spin blockade is observed in spin-dependent transport in hole quantum dots, which is an essential

technique for initializing and reading out spin states in quantum computing. This research establishes InSb nanowires as a promising platform for tunable hole quantum dots.

In 2014, Dahbashi et al. in Ref. [112] explored the spin dynamics of a single heavy hole in a flat (InGa)As quantum dot using advanced spin noise spectroscopy (SNS). The experiments demonstrated that even at low magnetic fields, there is a strong magnetic field dependence of the longitudinal heavy hole spin relaxation time, with a long T_1 relaxation time of 180 μs at 31 mT and 5 K. The platform for this experiment was a single-layer self-assembled InAs/GaAs quantum dots within an antinode of a λ-Bragg cavity. This configuration enhanced the Faraday rotation noise signal without increasing optical shot noise. The random fluctuations of spin polarization at thermal equilibrium were detected. The SNS technique was used to observe the magnetic field and light intensity-dependent spin dynamics. This discovery actually contradicts previous assumptions about saturation at zero magnetic fields, indicating a much stronger magnetic field dependence.

In 2015, Li et al. in Ref. [287] performed a series of hole transport measurements in a planar silicon MOS based double quantum dot, demonstrating Pauli spin blockade in the few-hole regime and mapping the spin relaxation induced leakage current as a function of inter-dot level spacing and magnetic field. In this experiment, the application of a strong out-of-plane magnetic field led to an avoided singlet-triplet level crossing. Therefore, the authors can deduced the heavy hole g-factor of approximately around 0.93 and the strength of spin-orbit interaction of around 110 μeV, which is direct evidence of strong spin-orbit interaction of heavy holes, promising fast local spin manipulation using only electric fields. The platform is a highly flexible multi-gate silicon p-MOS structure, allowing varied operational modes from single to few-hole double quantum dots.

Voisin et al. in Ref. [518] demonstrated the possibility of using silicon nanowire metal-oxide semiconductor field-effect transistors as p-type quantum dots in the few-hole regime, and the electrical control of the g-factor in these silicon quantum dots, reported Rabi frequencies exceeding several hundred MHz. The experimental work was carried out on devices fabricated on a complementary metal-oxide semiconductor platform starting from undoped silicon-on-insulator wafers. This precise control provided by complementary metal-oxide

semiconductor technology is in line with the industry. The magneto-transport measurements at low temperatures were performed to probe the Zeeman splitting of the first accessible hole level, which indicated a spin doublet with predominant heavy-hole character. Furthermore, the anisotropy and gate dependence of the hole g-factor were confirmed, revealing that the system meets all the requirements to be used as a spin qubit electrically manipulated by g-tensor modulation resonance. The findings of this research were particularly exciting for the development of quantum computing and spintronics. They demonstrated the feasibility of using silicon-based p-type quantum dots for spin qubit applications, combining the benefits of reduced hyperfine interaction, expected from the p-symmetry valence band states, with full compatibility with mainstream microelectronics technology.

In 2016, Marcellina et al. in Ref. [329] provided a comprehensive study of spin-orbit interactions in inversion-asymmetric two-dimensional hole gases at semiconductor heterointerfaces, focusing on common semiconductors like GaAs, InAs, InSb, Germanium, and Silicon. The research adopted a semi-analytical variational method to quantify spin-orbit interactions, accounting for both structure inversion asymmetry and bulk inversion asymmetry. This work established a method to calculate the spin-dependent dispersion of ground state heavy hole sub-bands. It used the Schrieffer-Wolff approximation to calculate the Rashba spin splitting, pointing out the dispersion is proportional to k^3. However, it is limited in some common hetero-structures like Silicon devices. The study identifies the parameter regimes where this occurs for the materials in focus and offers an alternative semi-analytical method to obtain the correct spin splitting, effective masses, Fermi level, and sub-band occupancy. The results align well with both numerical calculations and experimental findings.

In experiments, Maurand et al. in Ref. [335] further developed their platform, realizing a silicon qubit using industry-standard complementary metal–oxide–semiconductor technology, updated from the silicon nanowire field-effect transistors at low temperatures. The device is based on a 300 mm silicon-on-insulator wafer and consists of a 10 nm-thick and 20 nm-wide undoped silicon channel with p-doped source and drain contact regions, and

two parallel top gates. The first gate defines a quantum dot encoding a hole spin qubit, and the second one is used for qubit read-out. A series of experiments, including all-electrical, two-axis control of the spin qubit by applying phase-tunable microwave modulation to the first gate, was performed. Spin lifetimes, including T_2^* and T_2 (T_{echo} in the original text), were determined through Ramsey and spin echo manipulation sequences. For the read-out, the Pauli spin blockade was used. Prechtel et al. in Ref. [398] performed important experiments to reduce the dephasing in hole spin qubits caused by interactions with nuclear spins. These experiments, still using InGaAs quantum dots, demonstrated the decoupling of the hole spin from the nuclear spins by creating a large transverse nuclear spin polarization and measuring the hole Zeeman energy with a precision of 10 neV through dark-state spectroscopy. The hole hyperfine interaction is highly anisotropic, with the transverse coupling being less than 1% of the longitudinal coupling. This finding implies that for unpolarized, randomly fluctuating nuclei, the ideal heavy-hole limit can be achieved down to nano-electron-volt energies, equivalent to dephasing times up to a microsecond. The experiments used a transverse magnetic field and monitored the polarization via the lone electron spin in the exciton. The hole hyperfine interaction was probed in a self-assembled InGaAs quantum dot, uncovering an extremely high anisotropy that is close to the ideal heavy-hole limit. From 2016, attention increasingly focused on group IV semiconductor quantum dot hole spin qubits.

In 2017, Kloeffel et al. in Ref. [253] systematically analyzed Germanium and Germanium/Silicon core/shell nanowires with rectangular cross sections. The work considered the presence of a direct Rashba spin-orbit interaction in these nanowires, finding that the dominant contribution to the spin-orbit interaction is these direct Rashba terms, particularly in Germanium and Germanium/Silicon core/shell nanowires. For Silicon nanowires, the spin-orbit energies and the effects of direct Rashba terms depend significantly on the orientation of the crystallographic axes. The theoretical framework is still based on the Luttinger-Kohn Hamiltonian and the gate electric fields. The research shows that the direct Rashba SOC in Silicon nanowires allows for spin-orbit energies of the order of milli-electron-volts, which are controllable with moderate electric fields. The study also considers the impact of varying nanowire dimensions, orientation of crystallographic axes.

In experiments, Ono et al. in Ref. [375] explored the use of a p-channel silicon MOSFET to study sub-threshold transport and electrically driven spin resonance (EDSR) in a double quantum dot system. The research focuses on the effects of spin-orbit interaction and EDSR in lifting the spin blockade, a condition where spin symmetries restrict the movement of charge carriers. The paper reports on microwave-induced transitions between mixed singlet-triplet states in the double dot, with the observed EDSR spectra and the magnetic field dependence of the resonances providing clear evidence of spin-orbit-coupling-induced anti-crossing. Near the anti-crossing point, a suppressed EDSR signal is observed. Crippa et al. in Ref. [99] experimentally investigated the physical mechanisms underlying coherent spin rotations in semiconductor spin qubits with significant SOC. This experiment examined the angular dependence of the Rabi frequency, the gate-voltage dependence of g-factor, and the anisotropy of the hole g-factor. In their experiment, the authors used a silicon quantum dot to induce Rabi oscillations of a pseudo-spin-1/2 hole state through gate-voltage radio-frequency modulation. The research highlights that the electrical driving of a spin-orbit qubit can be fully characterized by measuring the g-factors and Rabi frequencies for different magnetic-field orientations. In the same year, Huthmacher et al. in Ref. [221] used InGaAs as a platform to study the dynamical decoupling of a heavy hole, which can offer a stable spin and optical coherence, potentially forming an ideal, high-bandwidth spin-photon interface. With the help of this dynamical decoupling, the longest ground-state coherence time T_2 reported was $4.0\,\mu$s. This improvement in coherence is supported by an independent analysis of the local electrical environment. The research also investigates the dependence of T_2^* and T_2 on the external magnetic field, revealing significant coupling to the nuclear-spin ensemble at low fields and to electrical noise at high fields. The study also indicates that strain-induced mixing with light-hole states enables hyperfine interactions that bound the coherence time for external magnetic fields up to a few Tesla.

In 2018, Venitucci et al. in Ref. [510] presented a theoretical analysis of the full electrical manipulation of semiconductor quantum dot hole spin qubits. The study introduces a generalised g-matrix formalism, which combines the bare g-factor and its derivative with respect to the electric field. This formalism efficiently maps the Larmor and Rabi fre-

quencies as a function of the magnetic field orientation, offering a robust model for qubit control. The research highlights the possibility of switching the qubit between two bias points for efficient manipulation and coherence. Additionally, the role of residual strains in such devices is discussed, emphasizing their potential impact on device performance.

In experiments, Marcellina et al., in Ref. [329], explored the use of semiconductor holes with strong SOC in a GaAs quantum well, aiming to demonstrate a new mechanism for controlling the Zeeman splitting through an electrical field. A significant advancement of this study is the observation of a three-fold enhancement in the in-plane g-factor. To measure the in-plane g-factor, the work introduced a novel methodology based on magnetotransport in crossed magnetic fields, allowing for successful detection of variations in the spin splitting. Li et al. in Ref. [289] conducted experiments on Ge quantum dots, leveraging its strong SOC to achieve coupling between the superconducting resonator and the quantum dot. This design enables the extraction of the charge stability diagram of the quantum dot independent of direct current transport measurements. The hole-resonator coupling rate in the single quantum dot-resonator system is measured to be 148 MHz, with the spin-resonator coupling rate measured to be in the range of 2-4 MHz, substantially larger than the rate obtained by directly coupling a single spin magnetic dipole to the magnetic field of a resonator. This advance paved the way for coupling between photons and hole spin qubits. Vukušic et al., in Ref. [521], demonstrated the first single-shot readout of hole spins in a germanium quantum dot by integrating a charge sensor into a high-bandwidth radiofrequency reflectometry setup. In these experiments, hole spin relaxation times were measured to be around 90 μs at a magnetic field of 0.5 T. The study achieved a remarkable total readout visibility of about 70%. Watzinger et al. in Ref. [537] demonstrated two-axis control of the germanium hole spin qubit using the Pauli spin blockade and EDSR, with fast Rabi frequencies exceeding 100 MHz reported. Additionally, the study measured dephasing times of approximately 130 ns, notably longer than those previously reported for holes in silicon. Liles et al. in Ref. [294] conducted a detailed study on valence band holes confined in silicon quantum dots, focusing on characterising the spin and orbital states of the first six holes in a planar silicon MOS-based quantum dot device. The study demonstrates number shell filling consistent with the Fock-Darwin

states of a circular two-dimensional quantum dot, revealing a spin filling sequence for the first six holes consistent with Hund's rule. Using pulse-bias spectroscopy, the orbital spectrum is found to be heavily influenced by strong hole-hole interactions. Furthermore, a stable single-hole quantum dot operating in the planar geometry is also demonstrated, connecting silicon MOS technology with current industrial technology and providing a path towards scalable silicon hole-spin qubits.

In 2019, Venitucci et al. in Ref. [509] provided a theoretical analysis of a hole spin qubit in semiconductor quantum dots subjected to various fields: static magnetic and electric fields, and a radio-frequency electric field in different materials and orientations. The calculations demonstrate that [110]-oriented quantum dots on [001] substrates are more efficient than [001]-oriented dots, attributed to the anisotropy of the valence band of the host material. Furthermore, despite its relatively small SOC, Silicon's advantage lies in its highly anisotropic valence band, making it a favourable candidate for hole spin qubit applications. Philippopoulos et al. in Ref. [392] offers a theoretical analysis of hole spin-echo envelope modulation and its application in extracting hyperfine parameters for semiconductor qubits. The study finds that in unstrained silicon, both the hyperfine and Zeeman Hamiltonians are approximately isotropic, leading to negligible envelope modulations. However, in strained silicon, where light-hole spin qubits can be energetically isolated, the hyperfine Hamiltonian and g-tensor are sufficiently anisotropic to give significant spin-echo envelope modulations. The researchers demonstrated that there is an optimal magnetic-field orientation for maximising the visibility of envelope modulations in strained silicon, estimating that the maximum modulation depth can reach about 10% at a moderate laboratory magnetic field of approximately 200 mT.

In experiments, Lodari et al. in Ref. [305] performed measurements of the effective hole mass across a wide range of densities, spanning from 2.0 to $11 \times 10^{11}\mathrm{cm}^{-2}$ in undoped germanium quantum wells. This light mass is attributed to the compressive strain in the quantum well, leading to a phenomenon known as mass inversion, where the topmost band develops a lighter mass compared to the lower-lying band. This light effective hole mass has significant implications for spin qubits in quantum computing. It facilitates larger

energy level spacing in quantum dots, enabling enhanced tunnel rates and relaxing the requirements for lithographic fabrication. The findings position strained Ge/SiGe quantum wells as an ideal planar platform for spin qubit devices, given their lightest effective mass among similar platforms. Crippa et al. in Ref. [98] demonstrated gate-coupled radiofrequency reflectometry for the dispersive readout of a fully functional spin qubit device. The device, a p-type double-gate transistor, was fabricated using standard silicon technology. It features a unique configuration with one gate confining a hole quantum dot to encode the spin qubit and the other serving as a helper dot for readout. This included conducting magneto-spectroscopy of the double quantum dot and observing behaviour indicative of an inter-dot charge transition.

In 2020, Bosco et al. in Ref. [53] theoretically studied hole spin qubits in silicon fin field-effect transistors. A key aspect of the study is the identification of operational sweet spots in silicon fin field-effect transistors, where charge noise can be largely reduced. These sweet spots are consequences of the anisotropy of the material and the unique triangular shape of the fin field-effect transistors' cross-section. Additionally, the study considers the effects of moderate strain on the spin-orbit switch and examines the charge noise, showing that working near the spin-orbit sweet spots greatly suppresses the charge noise and significantly improves the dephasing time. Mutter et al. in Ref. [360] studied the flopping mode in germanium hole spin qubits. This work finds that these natural flopping mode qubits exhibit highly tunable spin coupling strengths. This tunability enables qubit gate operation times in the nanosecond range. The work also finds that the dynamics of these qubits are affected by various factors such as the applied magnetic field, inter-dot distance, strength of Rashba SOI, and dot detuning.

In experiments, Hendrickx et al. in Ref. [206] demonstrated a fully electrically controlled germanium hole spin qubit by employing gate-defined quantum dots in high-mobility germanium quantum wells, integrated into silicon substrates using standard manufacturing techniques. Single-qubit rotations with frequencies exceeding 100 MHz, and two-qubit logic operations within just 75 ns were demonstrated, marking a significant improvement in qubit operation speed. Furthermore, high control fidelity was achieved, with single-

qubit control reaching a fidelity of 99.3%. The coherence times of the hole spin qubits in germanium were found to be longer compared to other semiconductor systems, indicating robustness suitable for quantum computing applications. Lawrie et al. in Ref. [276] investigated hole spin relaxation in single- and multi-hole regimes in a 2×2 germanium quantum dot array. They found spin relaxation times as high as 32 ms for quantum dots with single-hole occupations and 1.2 ms for five-hole occupations, setting benchmarks for spin relaxation times in hole quantum dots. Additionally, the study explored qubit addressability and electric field sensitivity by measuring the resonance frequency dependence of each qubit on gate voltages. This approach allows for significant tuning of the resonance frequency for both single and multi-hole qubits while maintaining minimal dependence on neighbouring gates.

In 2021, Adelsberger et al. in Ref. [6] examined the strong spin-orbit interaction inherent in germanium hole systems. A key focus of the study was the observation that orbital effects will lead to a substantial renormalisation of the g-factor. The strain and cross-sectional geometry of the nanowire are also discussed, with an identification of a *sweet spot* for the nanowire g-factor, where charge noise is strongly suppressed.

In experiments, Liles et al. in Ref. [295] studied single holes confined in silicon planar MOS quantum dots, with a particular focus on how electrode-induced strain affects the heavy-hole–light-hole splitting and the g-tensor of these holes. A critical finding of the study was the observation that nonuniform electrode-induced strain leads to variations in heavy-hole-light-hole splitting across the quantum dot. This variation, which can reach up to 50%, can significantly impact the hole-spin physics and the behaviour of the g-tensor. The researchers also demonstrated the capacity to electrically modulate the hole g-tensor by displacing the hole relative to the nonuniform strain profile, achieving substantial tuning of the hole g-factor by up to 500%. The study also identified a potential *sweet spot* for the g-factor, where the differential of g-factor with respect to voltage is zero. It is worth mentioning that the search for the *sweet spot* is receiving more and more attention.

Hendrickx et al. in Ref. [205] demonstrated the first quantum processor using hole spins in germanium quantum dots. This processor, designed in a 2×2 array, which can integrate

circuits of one-, two-, three-, and four-qubit operations, all controlled electrically. It is an exhibition of modern advanced semiconductor manufacturing techniques, paving the way towards scalable quantum computations. The quantum dots are formed in a strained germanium quantum well on a silicon substrate, which have high mobility of holes and low effective mass. The manipulation and readout of qubits are based on the Pauli spin blockade mechanism, incorporating a latched readout process for enhanced efficiency and accuracy. This study also demonstrated the successful execution of a quantum logic circuit that generates a four-qubit Greenberger–Horne–Zeilinger state, coherent evolution, and the potential for dynamical decoupling in such systems. Froning et al. in Ref. [169] demonstrated the manipulation of a hole spin qubit in a germanium/silicon nanowire. This study demonstrated an exceptionally strong and electrically tunable spin–orbit interaction in hole spins. In the experiments, the Rabi frequency of the hole spin qubit can be tuned between 31 to 219 MHz, with coherence times between 7 to 59 ns, and varying the Landé g-factor from 0.83 to 1.27 through small changes in gate voltage. The experiment involves a few-hole double quantum dot formed inside the nanowire. The readout was done by Pauli spin blockade, and the spin manipulation was done by microwave burst durations and gate voltages. Jirovec et al. in Ref. [230] demonstrated a singlet-triplet hole spin qubit operating at fields below 10 mT in a germanium quantum dot. The qubit achieved tunable Rabi frequencies exceeding 100 MHz and extended dephasing times of 1 μs, which were further enhanced beyond 150 μs using spin echo techniques. This advance indicates the advantage of a large g-factor and strong SOCs in germanium, supported by record-breaking long dephasing times.

In 2022, Bosco et al. in Ref. [54] proposed fully tunable longitudinal spin-photon interactions in hole spin qubits. In this study, the interactions change from transversal to longitudinal depending on the magnetic field direction, offering a novel way to control and measure these interactions electrically. An advantage of this approach is the feasibility of high-fidelity two-qubit entangling gates at high temperatures, significantly advancing the implementation of large-scale quantum processors. The longitudinal nature of these interactions eliminates backaction on the qubit and avoids residual qubit-qubit couplings. These interactions do not require multiple quantum dots or parametric driving and can

be harmonically modulated by AC electric fields.

In experiments, Camenzind et al. in Ref. [73] demonstrated the operation of hole spin qubits at temperatures above 4 Kelvin using silicon fin field-effect transistors. This study is particularly significant as it addresses one of the greatest challenges in quantum computing: scalability and integration with classical control electronics on the same chip. The researchers achieved fast electrical control of hole spins with driving frequencies up to 150 MHz. Another achievement is the high single-qubit gate fidelities, with a Rabi oscillation quality factor greater than 87. The devices were fabricated using standard CMOS techniques, ensuring industry compatibility and quality. Wang et al. in Ref. [530] demonstrated ultrafast single-spin manipulation within a hole-based double quantum dot in a germanium hut wire, achieving a record-setting Rabi frequency exceeding 540 MHz at a magnetic field of 100 mT. The research employed a two-hole model to accurately describe the resonances, pointing out the distinct g-factors for the two dots. Piot et al. in Ref. [395] demonstrated a spin–orbit qubit made of a single hole in a natural silicon MOS device, further improving the spin coherence and qubit control. Operational sweet spots were identified, leading to a large Hahn-echo coherence time up to 88μs, with the help of isotopically purified silicon.

In 2023, Vecchio et al. in Ref. [123] studied the light-hole spin-orbit qubit, demonstrating the selective confinement of light-hole states in a tensile-strained germanium quantum well. This confinement allows for the design of an ultrafast gate-defined spin qubit under EDSR. The qubit size-dependent g-factor and dipole moment are mapped, revealing that the dipole moment of light-hole spin qubits is considerably higher than that of the canonical heavy-hole qubits. This is attributed to the significant spin splitting caused by the combined action of large cubic and linear Rashba spin-orbit interactions, which are unique to light-hole states. An important finding is the relaxation rate, which is influenced by the strong spin-orbit interaction, typically following a B^7 behaviour. Michal et al. in Ref. [343] presented a study on the interactions between a single hole in a semiconductor quantum dot and microwave photons in a resonator, demonstrating the modulation of the g-factor via electrical control. The gate voltages and the orientation of the magnetic field are ex-

amined, which can act as a knob to tune the spin-photon interaction, allowing it to switch from fully transverse to fully longitudinal. The study estimates coupling rates reaching approximately 10 MHz in realistic settings. Moreover, the anisotropic Zeeman interaction, device setup, and potential circuit-QED applications are also discussed. Abadillo-Uriel et al. in Ref. [2] discussed the inhomogeneous strain fields in hole spin qubits, which give rise to linear Rashba spin-orbit interactions and g-factor modulations, enabling fast Rabi oscillations without requiring additional magnetic fields. An important finding is that shear strain gradients as small as $3 \times 10^{-6}\,\mathrm{nm}^{-1}$ within quantum dots can increase Rabi frequencies by an order of magnitude.

Yu et al. in Ref. [564] experimentally demonstrated strong coupling between a microwave photon in a superconducting resonator and a hole spin within a silicon-based double quantum dot, developed via a foundry-compatible metal–oxide–semiconductor process, reporting a spin–photon coupling rate surpassing 330 MHz. The investigation extends into the domain where a spin is confined within a single quantum dot, recording a spin–photon coupling rate around 1 MHz. Lawrie et al in Ref. [277] demonstrated the achievement of high-fidelity operations above 99.9% for individual qubits and addresses the challenge of maintaining this performance when driving multiple qubits simultaneously. Prior to this work, simultaneous driving of two qubits had been limited to a fidelity of 98.67%. The experiment is performed on a two-dimensional array of spin qubits, using a novel benchmarking technique, N-copy randomised benchmarking, designed for simple experimental implementation and accurate estimation of simultaneous gate fidelity. Through this method, they achieve two- and four-copy randomised benchmarking fidelities of 99.905% and 99.34% respectively.

Chapter 2

Methodology

In this chapter, we will introduce the necessary theoretical frameworks to understand the discussions about semiconductor quantum dot germanium hole spin qubits and silicon hole spin qubits. We first present time-independent perturbation theory, which is the tool used to obtain the effective Hamiltonian in hole spin qubits. Then, we introduce the valence band structures and the famous Luttinger-Kohn Hamiltonian, followed by the Bir-Pikus Hamiltonian to include strains. Electric dipole spin resonance, phonon-induced relaxation time, and charge dephasing are studied, paving the way to quantitatively characterize the coherence properties of a hole spin qubit.

2.1 Time-independent perturbation theory

In quantum mechanics, exactly solvable models are very limited; thus, perturbative approaches are widely used across various disciplines. The aim of the perturbation approach is to understand the global behaviors of solutions to differential equations. In standard time-dependent perturbation problems, a Hamiltonian can be expressed as:

$$H = H_0 + H' \tag{2.1}$$

where H_0 is a solvable Hamiltonian, and $H'$is the perturbation that renders the full model unsolvable. Assuming the energy scale of the perturbation is small, we can use the eigen-basis of H_0 to extrapolate the influence of H' on the energy spectra and eigen-states.

2.1.1 Non-degenerate perturbation theory

Focusing on a non-degenerate Hermitian physical system, the term *non-degenerate* implies that for our solvable Hamiltonian, each eigenenergy is associated with a one-dimensional eigenspace (i.e., both algebraic and geometric multiplicities are equal to one). In this context, we consider the eigenvalue problem:

$$H\left|\psi_n\right\rangle = E_n\left|\psi_n\right\rangle \tag{2.2}$$

where

$$H = H_0 + H' \quad \text{with} \quad \left\|H'\right\| \leq \left\|H_0\right\| \tag{2.3}$$

To solve this problem, we begin with the solvable unperturbed Hamiltonian:

$$H_0\left|\psi_n^{(0)}\right\rangle = E_n^{(0)}\left|\psi_n^{(0)}\right\rangle \tag{2.4}$$

Here, the subscript n denotes the energy level of interest, and the superscript (0) indicates the order of perturbation, which, in this case, is the zeroth-order perturbation. $E_n^{(0)}$ represents the unperturbed energy, and $\left|\psi_n^{(0)}\right\rangle$ is the corresponding unperturbed eigenstate. As our solvable model is Hermitian (self-adjoint), its eigen-states provide a complete orthonormal set in accordance with the spectral theorem:

$$\left\langle\psi_n^{(0)}\middle|\psi_m^{(0)}\right\rangle = \delta_{n,m} \tag{2.5}$$

where $\delta_{n,m}$ denotes the Kronecker delta. The perturbed eigen-states are anticipated to closely align with the unperturbed states, attributed to the relative magnitude between H' and H_0. The perturbed states are expanded using the orthonormal set as:

$$\left|\psi_n\right\rangle = \sum_l \left|\psi_l^{(0)}\right\rangle \tag{2.6}$$

Consequently, the original problem is reformulated as:

$$\sum_l a_l(H_0 + H')\left|\psi_l^{(0)}\right\rangle = \sum_l a_l(E_l^{(0)} + H')\left|\psi_l^{(0)}\right\rangle = E_n \sum_l a_l \left|\psi_l^{(0)}\right\rangle \tag{2.7}$$

Subsequent simplifications lead to:

$$\sum_l a_l(E_n - E_l^{(0)})\left|\psi_n^{(0)}\right\rangle = \sum_l a_l H' \left|\psi_l^{(0)}\right\rangle \tag{2.8}$$

To analyze the perturbation at level m (an arbitrary level), we project the unperturbed state $\left|\psi_m^{(0)}\right\rangle$ onto both sides, yielding:

$$a_m(E_n - E_m^{(0)}) = \sum_l \left\langle\psi_m^{(0)}\middle|H'\middle|\psi_l^{(0)}\right\rangle \tag{2.9}$$

For simplicity, we denote:

$$\left\langle\psi_m^{(0)}\middle|H'\middle|\psi_l^{(0)}\right\rangle = H'_{m,l} \tag{2.10}$$

From Eq. (2.9), an iterative relationship emerges, indicating that a_m is related to all other a_n:

$$a_m = \frac{1}{En - E_m^{(0)}} \sum_l H'_{m,l} \tag{2.11}$$

equivalent to:

$$am(E_n - E_m^{(0)}) = a_m H'_{m,m} + \sum_{l \neq m} a_l H'_{m,l} \tag{2.12}$$

The coefficient can thus be expressed as:

$$a_m = \frac{1}{En - E_m^{(0)} - H'_{m,m}} \sum_{l \neq m} a_l H'_{m,l} \tag{2.13}$$

This formula delineates a_m as a function of all other coefficients. With minimal perturbation, E_n closely approximates $E_m^{(0)}$, enabling first-order corrections by setting an to zero and altering the index to $n' = m$. To deduce second-order corrections, we transpose a_n to the left and iterate the right-hand side with a distinct index:

$$a_l = \frac{1}{E_{n'} - E_n^{(0)} - H'_{n,n}} \sum_{l' \neq l} a_{l'} H'_{l,l'} \tag{2.14}$$

This expression can be substituted into Eq. (2.13) to compute the expansion coefficients a_m. For enhanced precision, this iterative process can be reiterated for third-order corrections, necessitating a triple summation. Now, we proceed to calculate the exact expression for a specific example.

In the first-order perturbation problem, we start from:

$$a_m = \frac{1}{E_n - E_m^{(0)} - H'_{m,m}} \sum_{l \neq m} a_l H'_{m,l} \tag{2.15}$$

As we discussed before, the perturbation is small; therefore, we are left with:

$$a_m(E_m - Em^{(0)} - H'_{m,m}) = 0 \tag{2.16}$$

where a_m is a constant, we have:

$$E_m = Em^{(0)} + H'_{m,m} \tag{2.17}$$

Since we did not iterate Eq. (2.13), there are no corrections to the wave-functions in this order.

For the second order, we need to iterate Eq. (2.13) once, which means:

$$a_m(E_m - E_m^{(0)} - H'_{m,m}) = \sum_{n \neq m} \left[\frac{1}{E_m - E_n^{(0)} - H'_{n,n}} \sum_{n'' \neq n} \left[a_{n''} H'_{n,n''} H'_{m,n} \right] \right] \tag{2.18}$$

For the right-hand side, if we pick out the case $n'' = m$, and truncate our perturbation, we will have:

$$a_m \left[\left(E_m - E_m^0 - H'_{m,m} \right) - \sum_{n \neq m} \frac{H'_{n,m} H'_{m,n}}{E_m - E_n^0 - H'_{nn}} \right] = 0 \tag{2.19}$$

Now we can write down our second-order energy corrections:

$$E_m = E_m^{(0)} + H'_{m,m} + \sum_{n \neq m} \frac{\left\| H'_{m,n} \right\|^2}{E_m - E_n^{(0)} - H'_{n,n}} \tag{2.20}$$

Since we have iterated the coefficient once, there will be a correction to the eigenstate as well:

$$|\psi_m\rangle = \sum_n \left| \psi_n^{(0)} \right\rangle = \left| \psi_m^{(0)} \right\rangle + \sum_{n \neq m} a_n \left| \psi_m^{(0)} \right\rangle \tag{2.21}$$

Recall that:

$$a_n = \frac{1}{E'_n - E_n^0 - H'_{n,n}} \sum_{n'' \neq n} a_{n''} H'_{n,n''} \tag{2.22}$$

For the lowest order correction to the eigen-states, we only care about the case $n'' = m$ (by setting $a_m = 1$, and disregard all the other corrections):

$$a_n = \frac{H'_{n,m}}{E_m - E_n^0 - H'_{n,n}} \tag{2.23}$$

The eigen-states become:

$$|\psi_m\rangle = \left|\psi_m^{(0)}\right\rangle + \sum_{n \neq m} \frac{H'_{n,m} \left|\psi_n^{(0)}\right\rangle}{E_m - E_n^0 - H'_{n,n}} \tag{2.24}$$

From this equation, we should realize that the wavefunction depends on E_m itself, which is still not an explicit expression. To tackle this problem, the first approach is to ignore the energy difference temporarily between the unperturbed state and the perturbed state when calculating the corrections. This approach is known as the Rayleigh-Schrödinger perturbation method. The second approach is using an iterative method; we substitute the first-order energy expression after corrections into the denominator in Eq. (2.24), and repeat the procedures until the value of E_m is convergent. This iterative approach is known as the Brillouin-Wigner perturbation method.

2.1.2 Degenerate perturbation theory

When the geometric multiplicity is greater than one, multiple eigen-states will correspond to one single eigen-energy, indicating a degenerate energy level. In such cases, it is essential to identify a linear combination of eigen-states that can evolve out of the degeneracy under perturbations. Consider a system with an f-fold degeneracy of energy levels. We can partition all eigen-states into two groups. The first, group is the degenerate set in the eigen-subspace of the degenerate energy level:

$$\left|\psi_1^{(0)}\right\rangle, \left|\psi_2^{(0)}\right\rangle, \left|\psi_3^{(0)}\right\rangle, \ldots, \left|\psi_f^{(0)}\right\rangle \tag{2.25}$$

The second group contains eigen-states belonging to other non-degenerate energy levels:

$$\left|\psi_{f+1}^{(0)}\right\rangle, \left|\psi_{f+2}^{(0)}\right\rangle, \ldots \tag{2.26}$$

In this degenerate case, our iterative relation Eq. (2.13) still applies with some extra modifications. Starting from our iterative relation:

$$a_m = \frac{1}{E_n - E_m^{(0)} - H'_{m,m}} \sum_{l \neq m} a_l H'_{m,l} \tag{2.27}$$

In the right-hand side of this equation, we isolate all coefficients corresponding to the degenerate energy levels and transfer them to the left-hand side. To calculate perturbation-induced changes in the energy spectrum, we consider all a_n in the degenerate set to be significant, while those outside are minor, indicating the primary contributions arise from the eigen-subspace. At the first order, we neglect all couplings external to the eigen-subspace. Consequently, we obtain f linear homogeneous equations:

$$\begin{array}{cccc} a_1\left(E_1^0 + H'_{11} - E\right) & +a_2 H'_{12} & +\ldots & +a_f H'_{1f} \quad = 0 \\ a_1 H'_{21} & +a_2\left(E_2^0 + H'_{22} - E\right) & +\ldots & +a_f H'_{2f} \quad = 0 \\ \vdots & \vdots & \vdots & \vdots \\ a_1 H'_{f1} & +a_2 H'_{f2} & +\ldots & +a_f\left(E_f^0 + H'_{ff} - E\right) = 0 \end{array} \tag{2.28}$$

Solving this linear system by evaluating the secular equations yields corrections to the degenerate eigen-energy spectrum and eigen-states. Higher-order corrections can be obtained by modifying the sets of linear equations. In general, perturbations can lift the degeneracy; however, if the degeneracy persists at the first order, higher-order perturbations may be necessary.

2.1.3 Löwdin partitioning

The exact diagonalization of a Hermitian Hamiltonian is a central topic in quantum mechanics. The spectrum theory reveals that for a self-adjoint operator, diagonalization through unitary transformation is alway formidable. The essence of this approach lies in identifying a change of basis matrix that recasts the Hamiltonian into a diagonal form. However, this process is challenging. Notably, no general algorithm exists for finding the roots of higher-order characteristic polynomials, necessitating the alternative perturbative approaches like the Löwdin partitioning method.

The Löwdin partitioning method has been developed in various disciplines, adopting different forms. It is recognized as the Foldy-Wouthuysen transformation in the relativistic theory of quantum mechanics, the Fröhlich transformation in phonon-electron interaction problems, and the Nakajima transformation in superconductivities. Within the realm of solid-state physics, this technique is also referred to as the Schrieffer-Wolff transformation. Schrieffer and Wolff demonstrated that for a localized magnetic moment in a dilute alloy, the Anderson Hamiltonian can be related to the Kondo Hamiltonian, particularly their equivalence in the limit of small s-d mixing.

Our thesis will extensively employ the Löwdin partitioning method to derive several important effective Hamiltonians in the context of $\boldsymbol{k}\cdot\boldsymbol{p}$ theory. We will introduce this formalism through the language of matrix algebra and, subsequently, discovering the renormalization nature embedded in this unitary transformation techniques.

Consider a standard perturbation problem:

$$H = H_0 + H' \tag{2.29}$$

The spectrum of the unperturbed Hamiltonian H_0 is well-understood, and its eigen-states are denoted as

$$\left|\psi_1^{(0)}\right\rangle, \left|\psi_2^{(0)}\right\rangle, \left|\psi_3^{(0)}\right\rangle, \ldots \tag{2.30}$$

We categorize the wave-functions into two weakly interacting sets: set A and set B. Assuming our primary interest lies in set A, we then introduce the following unitary transformation:

$$\tilde{H} = e^{-S} H e^{S} \tag{2.31}$$

This transformation ensures that the matrix elements $\left\langle \psi_m \middle| \tilde{H} \middle| \psi_l \right\rangle$ between states $|\psi_m\rangle$ from set A and $|\psi_l\rangle$ from set B vanish up to the desired order of H'. Without loss of generality, the total Hamiltonian can be decomposed into three components:

$$H = H_0 + H' = H_0 + H_1 + H_2 \tag{2.32}$$

Here, H_1 has all the non-zero elements of H' solely between the eigen-states within either set A or B. H_2 contains non-zero elements of H_0 between sets A and B, representing the

$$\begin{pmatrix} H_{11} & 0 & V_{13} & V_{14} \\ 0 & H_{22} & V_{23} & V_{24} \\ V_{31} & V_{32} & H_{33} & 0 \\ V_{41} & V_{42} & 0 & H_{44} \end{pmatrix} = \begin{pmatrix} H_{11} & 0 & 0 & 0 \\ 0 & H_{22} & 0 & 0 \\ 0 & 0 & H_{33} & 0 \\ 0 & 0 & 0 & H_{44} \end{pmatrix} + \begin{pmatrix} 0 & 0 & V_{13} & V_{14} \\ 0 & 0 & V_{23} & V_{24} \\ V_{31} & V_{32} & 0 & 0 \\ V_{41} & V_{42} & 0 & 0 \end{pmatrix}$$

Figure 2.1: **Löwdin partitioning** A demonstartion of a simple Löwdin partitioning, the total Hamiltonian is seperated into thwo parts: the diagnal part indicating the eigen-energies of the system, from where we can check the renormalization gap; and the off-digonal part descrbing the interactions between different sets.

coupling terms. To obtain a block diagonal form with respect to sets A and B, we need to determine the matrix S. Given that e^S is unitary, S must be anti-Hermitian:

$$S^\dagger = -S \tag{2.33}$$

The expansion of S is given by:

$$e^S = 1 + S + \frac{1}{2!}S^2 + \frac{1}{3!}S^3 + \frac{1}{4!}S^4 + \cdots \tag{2.34}$$

Consequently, our Eq. (2.31) is expanded as follows:

$$\begin{aligned} \tilde{H} =& \left[1 - S + \frac{1}{2!}S^2 + \cdots\right] H \left[1 + S + \frac{1}{2!}S^2 + \cdots\right] \\ =& H + [H, S] + \frac{1}{2!}[[H, S], S] + \cdots \\ =& \sum_\alpha^\infty \left[\frac{1}{\alpha!}[H, S]^{(\alpha)}\right] \\ =& \sum_\alpha^\infty \left[\frac{1}{\alpha!}[H_0, S]^{(\alpha)}\right] + \sum_\alpha^\infty \left[\frac{1}{\alpha!}[H_1, S]^{(\alpha)}\right] + \sum_\alpha^\infty \left[\frac{1}{\alpha!}[H_2, S]^{(\alpha)}\right] \end{aligned} \tag{2.35}$$

Considering that S is anti-Hermitian, it must be block-off-diagonal. It follows that the product of two block-off-diagonal matrices results in a diagonal matrix, whereas the product of two diagonal matrices remains a diagonal matrix. Furthermore, the product of a block-diagonal matrix with a block-off-diagonal matrix yields an off-diagonal matrix. Based on these observations, the diagonal part of $\tilde{H}$ must incorporate terms like $[H_0 + H_1, S]^{(j)}$ where j is even, and terms like $[H_2, S]^{(j)}$ where j is odd. The resultant form of the diagonal component $\tilde{H}_d$ is given by:

$$\tilde{H}d = \sum_{j=0}^\infty \left[\frac{1}{(2j)!}[H_0 + H_1, S]^{(2j)}\right] + \sum_{j=0}^\infty \left[\frac{1}{(2j+1)!}[H_2, S]^{(2j+1)}\right] \tag{2.36}$$

Similarly, the block-off-diagonal part, $\tilde{H}_n$, can be expressed as:

$$\tilde{H}n = \sum_{j=0}^{\infty}\left[\frac{1}{(2j+1)!}[H_0+H_1,S]^{(2j+1)}\right] + \sum_{j=0}^{\infty}\left[\frac{1}{(2j)!}[H_2,S]^{(2j)}\right] \tag{2.37}$$

To ensure the only term left is $\tilde{H}_d$, S must satisfy:

$$\tilde{H}_n = \sum_{j=0}^{\infty}\left[\frac{1}{(2j+1)!}[H_0,S]^{(2j+1)}\right] + \sum_{j=0}^{\infty}\left[\frac{1}{(2j+1)!}[H_1,S]^{(2j+1)}\right] + \sum_{j=0}^{\infty}\left[\frac{1}{(2j)!}[H_2,S]^{(2j)}\right] \tag{2.38}$$

Expand the matrix S by orders:

$$S = S^{(1)} + S^{(2)} + S^{(3)} + S^{(4)} + \cdots \tag{2.39}$$

Similarly, we can expand the Eq. (2.38) by orders:

$$\begin{aligned}
\tilde{H}_n =& [H_0,S] + [H_1,S] + H_2 + \frac{1}{3!}[H_0,S]^3 + \frac{1}{3!}[H_1,S]^3 + \frac{1}{2!}[H_2,S]^2 + \cdots \\
=& + \left[H_0,S^{(1)}\right] + \left[H_0,S^{(2)}\right] + \left[H_0,S^{(3)}\right] + \left[H_0,S^{(4)}\right] + \left[H_0,S^{(5)}\right] \\
&+ \left[H_1,S^{(1)}\right] + + \left[H_1,S^{(2)}\right] + \left[H_1,S^{(2)}\right] + \left[H_1,S^{(4)}\right] \\
&+ H_2 + \frac{1}{3!}\left[H_0,S^{(1)}\right]^3 + \frac{1}{3!}\left[H_0,S^{(2)}\right]^3 + \frac{1}{3!}\left[H_1,S^{(1)}\right]^3 + \frac{1}{3!}\left[H_1,S^{(2)}\right]^3 \\
&+ \frac{1}{2!}\left[H_2,S^{(1)}\right]^2 + \frac{1}{2!}\left[H_2,S^{(2)}\right]^2 + \frac{1}{2!}\left[H_2,S^{(3)}\right]^2 + \cdots
\end{aligned} \tag{2.40}$$

Solve the equations above for the matrix S, we have:

$$\left[H_0,S^{(1)}\right] + H_2 = 0 \tag{2.41}$$

$$\left[H_0,S^{(2)}\right] + \left[H_1,S^{(1)}\right] = 0 \tag{2.42}$$

$$\left[H_0,S^{(3)}\right] + \frac{1}{3!}\left[H_0,S^{(1)}\right]^3 + \frac{1}{2!}\left[H_2,S^{(1)}\right]^2 + \left[H_1,S^{(2)}\right] = 0 \tag{2.43}$$

$$\left[H_0,S^{(4)}\right] + \left[H_1,S^{(3)}\right] + \frac{1}{3!}\left[H_1,S^{(1)}\right]^3 = 0 \tag{2.44}$$

$$\left[H_0,S^{(5)}\right] + \left[H_1,S^{(4)}\right] + \frac{1}{2!}\left[H_2,S^{(2)}\right]^2 + \frac{1}{4!}\left[H_2,S^{(1)}\right]^4 = 0 \tag{2.45}$$

$$\cdots \tag{2.46}$$

The matrix element will read:

$$S^{(1)}_{m,l} = -\frac{H'_{m,l}}{E_m - E_l} \tag{2.47}$$

$$S^{(2)}_{m,l} = \frac{1}{E_m - E_l}\left[\sum_{m'}\left(\frac{H'_{m,m'}H'_{m',l}}{E_{m'} - E_l}\right) - \sum_{l'}\left(\frac{H'_{m,l'}H'_{l',l}}{E_m - E_{l'}}\right)\right] \tag{2.48}$$

$$\cdots \tag{2.49}$$

Here, the subscripts m, m', m'' correspond to states in set A, the subscripts l, l', l'' correspond to states in set B, $H_{m,l} = \langle \psi_m | H | \psi_l \rangle$. Put these expression for S into our transformations of the diagonal blocks:

$$\tilde{H}_{\mathrm{d}} = \sum_{j=0}^{\infty} \frac{1}{(2j)!} [H_0 + H_1, S]^{(2j)} + \sum_{j=0}^{\infty} \frac{1}{(2j+1)!} [H_2, S]^{(2j+1)} \tag{2.50}$$

This will be the effective Hamiltonian after the Lowdin partitioning perturbation. Here we only list the block-diagonal part up to third orders:

$$H^{(1)}_{m,m'} = H'_{m,m'} \tag{2.51}$$

which is we have obtained in Eq. (2.24). The second order result is

$$H^{(2)}_{m,m'} = \frac{1}{2} \sum_{l} \left[H'_{m,l} H'_{l,m'} \left(\frac{1}{E_m - E_l} - \frac{1}{E_l - E_{m'}} \right) \right] \tag{2.52}$$

The third order result is

$$\begin{aligned} H^{(3)}_{m,m'} = &- \frac{1}{2} \sum_{l,m''} \left[\frac{H'_{m,l} H'_{l,m''} H'_{m'',m'}}{(E_{m'} - E_l)(E_{m''} - E_l)} + \frac{H'_{m,m''} H'_{m'',l} H'_{l,m'}}{(E_m - E_l)(E_{m''} - E_l)} \right] \\ &+ \frac{1}{2} \sum_{l,l'} H'_{m,l} H'_{l,l'} H'_{l',m'} \left[\frac{1}{(E_m - E_l)(E_m - E_{l'})} + \frac{1}{(E_{m'} - E_l)(E_{m'} - E_{l'})} \right] \end{aligned} \tag{2.53}$$

As a summary, we note that the primary requirement is to define the sets A and B, which are weakly interacting with each other. In other words, sets A and B must be separated by a large energy gap. By reordering the series in Eq. (2.31), we 'transform out' the high-energy part of the Hamiltonian, leaving an effective Hamiltonian. This renormalization is assured by the natural energy gap between sets A and B.

The Löwdin partitioning method is also valid when the Hamiltonian is a combination of a matrix of operators and some diagonal energies $E_n \delta_{n,n}$ like:

$$\hat{H}_{n,n'} = \begin{bmatrix} E_1 & 0 & \cdots \\ 0 & E_2 & \cdots \\ \cdots & \cdots & \cdots \end{bmatrix} + \begin{bmatrix} \hat{H}_{1,1} & \hat{H}_{1,2} & \cdots \\ \hat{H}_{2,1} & \hat{H}_{2,2} & \cdots \\ \cdots & \cdots & \cdots \end{bmatrix} \tag{2.54}$$

We have put a hat on top of the elements to emphasize that they are operators. Operators and matrices will not be further distinguished unless specified. In this case, the matrix

S will become operators as well, but their expression will not be altered, as assured by the formal power series. Therefore, in expressions like Eq. (2.53), the order of the matrix elements must be followed.

2.2 Holes in valence band: $\boldsymbol{k}\cdot\boldsymbol{p}$ theory

In this section, we provide the essential background on holes in the valence band within semiconductor systems. Understanding this foundation is crucial for the work presented in Chapters 3.1, 4.1, where we further explore and apply these concepts.

A perfect crystal can be described by the following Hamiltonian:

$$\begin{aligned} H = &\sum_i \frac{\boldsymbol{p}_i^2}{2m_i} + \sum_j \frac{\boldsymbol{P}_j^2}{2M_j} + \frac{1}{2}\sum_{j,j'} \frac{Z_j Z_{j'} e^2}{4\pi\varepsilon_0 \left|\boldsymbol{R}_j - \boldsymbol{R}_{j'}\right|} \\ &- \sum_{j,i} \frac{Z_j e^2}{4\pi\varepsilon_0 \left|\boldsymbol{r}_i - \boldsymbol{R}_j\right|} + \frac{1}{2}\sum_{i,i'} \frac{e^2}{4\pi\varepsilon_0 \left|\boldsymbol{r}_i - \boldsymbol{r}_{i'}\right|} \end{aligned} \tag{2.55}$$

where $\boldsymbol{r}_i$ and $\boldsymbol{p}_i$ represent the position and momentum operators of the i-th electron, respectively, $\boldsymbol{R}_j$ and $\boldsymbol{P}_j$ denote those of the j-th nucleus. Z_j is the atomic number of the j-th nucleus, and $-e$ (where $e = 1.602 \times 10^{-19}\,\mathrm{C}$) represents the electron charge. This Hamiltonian encapsulates the kinetic energy of electrons and nuclei, the inter-nuclear repulsions, electron-electron interactions, and electron-nucleus attractions.

A central problem in condensed matter physics is to understand the energy spectrum of the Hamiltonian in Eq. (2.55). To address this, several approximations are necessary. First, we categorize the electrons into two groups: core and valence. Core electrons (e.g., the $1s^2$, $2s^2$, $2p^6$ electrons in silicon) are localized around the nuclei and can be treated collectively with their nucleus as an ion core. This approach significantly reduces the computational complexity by limiting the considerations to valence electrons and ion cores. Furthermore, we apply the Born-Oppenheimer (adiabatic) approximation, presuming the ion cores are stationary relative to the valence electrons. The Hamiltonian simplifies to:

$$H = H_{\text{ion}}(\boldsymbol{R}_j) + H_{\text{ve}}(\boldsymbol{r}_i, \boldsymbol{R}_{j,0}) + H_{\text{e-i}}(\boldsymbol{r}_i, \delta\boldsymbol{R}_j) \tag{2.56}$$

The first term describes the motion of ion cores, the second term describes the valence electrons around the nuclei at their equilibrium positions (denoted by $\boldsymbol{r}_{j,0}$), and the last term describes the interactions between valence electrons and ion cores due to the displacement $\delta\boldsymbol{R}_j$ of the ion cores, which is also known as the electron-phonon interaction. For simplicity, we will henceforth refer to valence electrons simply as electrons. Focusing on the Hamiltonian for these electrons, we obtain:

$$H_e = \sum_i \frac{p_i^2}{2m_i} + \frac{1}{2}\sum_{i,i'} \frac{e^2}{4\pi\varepsilon_0 \left|\boldsymbol{r}_i - \boldsymbol{r}_{i'}\right|} - \sum_{i,j} \frac{Z_j e^2}{4\pi\varepsilon_0 \left|\boldsymbol{r}_i - \boldsymbol{r}_{j0}\right|} \tag{2.57}$$

Solving this many-body problem presents difficulties due to the correlations between electrons. To address this challenge, we consider the Hartree-Fock mean-field approximation. In this framework, a single electron experiences an effective potential which includes all interactions between itself and the remaining electrons. The effective potential can be written as:

$$v_e(\boldsymbol{r}_i) = \sum_{i \neq i'} \frac{e^2}{4\pi\epsilon_0 \left|\boldsymbol{r}_i - \boldsymbol{r}_{i'}\right|}, . \tag{2.58}$$

Now, for a single electron, the Hamiltonian becomes

$$H_{1e} = \frac{\boldsymbol{p}^2}{2m} + V(\boldsymbol{r}), , \tag{2.59}$$

where

$$V(\boldsymbol{r}) = v_e(\boldsymbol{r}) - \sum_j \frac{Z_j e^2}{4\pi\varepsilon_0 \left|\boldsymbol{r} - \boldsymbol{R}_{j0}\right|}, . \tag{2.60}$$

Due to the long-range order nature of crystals, we observe that this effective potential is invariant under the translation by any Bravais lattice vector, i.e., $V(\boldsymbol{r}) = V(\boldsymbol{r} + \boldsymbol{R}_l)$. Our discussion will extend to the behaviors of holes in the valence band from Eqs. (2.60) and (2.59). First, we will introduce the relevant concepts of the $\boldsymbol{k}\cdot\boldsymbol{p}$ method in semiconductor systems, then discuss how the Luttinger-Kohn Hamiltonian, which characterizes the valence band structure, is derived based on the $\boldsymbol{k}\cdot\boldsymbol{p}$ approach. Finally, we will examine several important features of the Luttinger-Kohn Hamiltonian.

2.2.1 Bloch theorem

The energy spectrum of an electron in a crystal can be derived from

$$\frac{p^2}{2m}\Psi_n(\boldsymbol{r}) + V(\boldsymbol{r})\Psi_n(\boldsymbol{r}) = E_n\Psi_n(\boldsymbol{r}),, \tag{2.61}$$

under the condition

$$V(\boldsymbol{r}+\boldsymbol{R}) = V(\boldsymbol{r}),, \tag{2.62}$$

where n labels the eigen-states. The solution, $\Psi_n(\boldsymbol{r})$, is known as the Bloch electron wave function. Bloch theorem states that these wave functions can be expressed as plane waves modulated by a periodic function of the form:

$$\Psi_n(\boldsymbol{r}) = \exp(i\boldsymbol{k}\cdot\boldsymbol{r})u_{\boldsymbol{k}}(\boldsymbol{r}),, \tag{2.63}$$

where $u_{\boldsymbol{k}}(\boldsymbol{r})$ is the periodic function satisfying $u_{\boldsymbol{k}}(\boldsymbol{r}) = u_{\boldsymbol{k}}(\boldsymbol{r}+\boldsymbol{R}_l)$, and $\boldsymbol{k}$ is the wave vector of the plane wave. By plotting the eigen-energy E_n as a function of $\boldsymbol{k}$, we obtain the electronic band structure of the crystal. It is important to note that the Bloch wave function is not an eigen-function of the wave-vector operator; therefore, $\hbar\boldsymbol{k}$ should not be interpreted as the mechanical momentum of an electron but rather as the crystal momentum.

2.2.2 $\boldsymbol{k}\cdot\boldsymbol{p}$ theory

To calculate the band structure explicitly, earlier attention focused on several pseudopotential approaches, which usually require parameters (especially energy gaps) obtained from experimental results. As developments in experimental techniques advanced, optical measurements began to play an important role in the semiconductor industry, determining both the energy gap and formidable optical transitions between different states. Therefore, using transition matrix elements as a starting point to calculate band structures became an alternative approach to the pseudopotential method. The $\boldsymbol{k}\cdot\boldsymbol{p}$ theory then becomes particularly convenient against this backdrop since the entire Brillouin zone can be extrapolated from the center, determinable by optical measurements.

Starting with Bloch theorem, we re-expressed it using the unit cell periodic function $u_{n,\boldsymbol{k}}(\boldsymbol{r})$

$$\left(\frac{p^2}{2m} + \frac{\hbar}{m}\boldsymbol{k}\cdot\boldsymbol{p} + \frac{\hbar^2 k^2}{2m} + V\right) u_{n,\boldsymbol{k}} = E_{n,\boldsymbol{k}} u_{n,\boldsymbol{k}},. \tag{2.64}$$

At the center of the Brillouin zone, i.e., when $\boldsymbol{k} = \boldsymbol{k}_0 = (0,0,0)$, we have

$$\left(\frac{p^2}{2m} + V\right) u_{n,\mathbf{0}} = E_{n,\mathbf{0}} u_{n,\mathbf{0}} \quad (n = 1,2,3,\ldots) \tag{2.65}$$

The solutions of Eq. (2.65) form a complete orthonormal set of basis functions. Once the $E_{n,\mathbf{0}}$ are known, we can treat the $\boldsymbol{k}\cdot\boldsymbol{p}$ term and the term $\hbar^2k^2/(2m_0)$ as perturbations, forming a standard time-independent perturbation problem.

This $\boldsymbol{k}\cdot\boldsymbol{p}$ method yields highly accurate results without intensive computations when $\boldsymbol{k}$ does not deviate too much from the zone center. The entire Brillouin zone band structure is also accessible when we include sufficiently many basis functions, requiring only a limited number of energy gaps and optical transition matrix elements from experimental results. We will use the $\boldsymbol{k}\cdot\boldsymbol{p}$ method to discuss the top valence bands in many semiconductors with diamond structures.

2.2.3 Luttinger-Kohn Hamiltonian

Considering the Group IV elements, their highest energy point of the valence band is at the center of the Brillouin zone. The valence band wave-functions resemble p-orbitals, which exhibit a three-fold degeneracy, represented by $|X\rangle$, $|Y\rangle$, and $|Z\rangle$. Later, we will demonstrate how these can be expressed using spherical harmonics. We should also include the spin degree of freedom, denoted by $|s\rangle$ for spin-up states and $|\downarrow\rangle$ for spin-down states, which are the eigenstates of the S_z operator.

From atomic physics, we understand that electron spins can be coupled with their orbital degree of freedom via the spin-orbit coupling mechanism, a relativistic effect proportional to $1/c^2$. This coupling is particularly strong in elements with heavier atomic masses, such as germanium, gallium, and arsenide. Generally, the spin-orbit coupling Hamiltonian is given by:

$$H_{\mathrm{SO}} = \frac{\hbar^2}{4c^2m^2}(\nabla V \times \boldsymbol{p})\cdot\boldsymbol{\sigma} \tag{2.66}$$

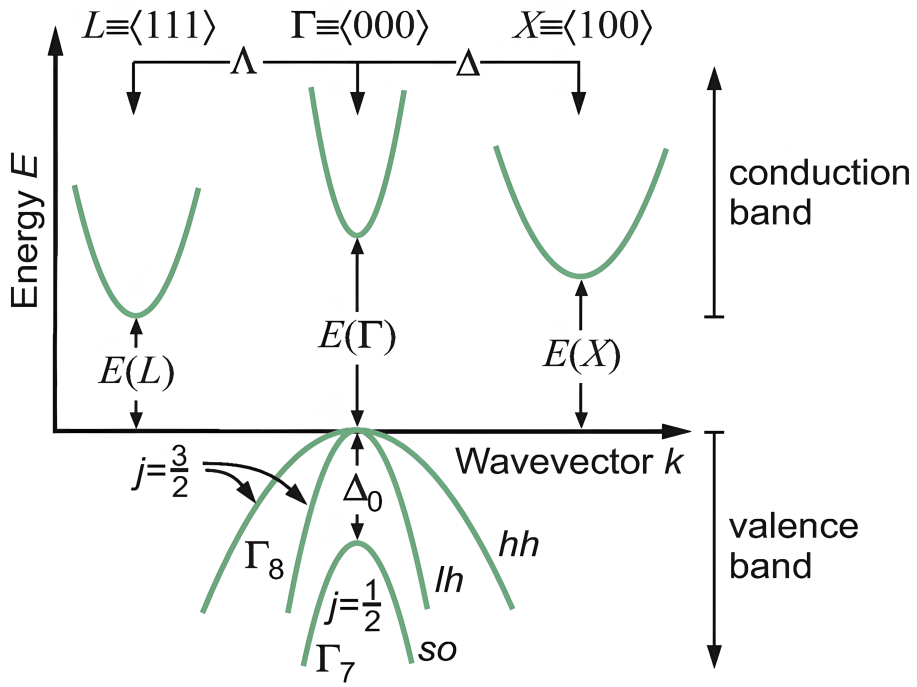

Figure 2.2: **Band structure** A demontration of a simplifed band structure diagram of a typical semiconductor. The center of the Brillouin zone is marked as Γ point, which is not necessary the lowest energy of the conduction band. In our thesis, we focus on the valence band, where we have demonstrated that the heavy-hole band (hh in the figure) and the light-hole band (lh in the figure) will have a finite split away from the Γ point. The split-off band is denoted as SO in the figure, the energy splitting between the split-off band and the heavy-hole band at Γ point is denoted as Δ_0. The original source of this figure is Ref. [45].

where V is the electric potential experienced by the electrons, and $\boldsymbol{\sigma}$ represents the Pauli spin matrices:

$$\sigma_x = \begin{bmatrix} 0 & 1 \\ 1 & 0 \end{bmatrix} \quad \sigma_y = \begin{bmatrix} 0 & -i \\ i & 0 \end{bmatrix} \quad \sigma_z = \begin{bmatrix} 1 & 0 \\ 0 & -1 \end{bmatrix} \tag{2.67}$$

The presence of spin-orbit coupling implies that neither the orbital angular momentum operators nor the spin operators form a complete set of commuting observables. Instead, we should consider the total angular momentum operators $\boldsymbol{J} = \boldsymbol{L} + \boldsymbol{S}$. Then, the new complete set of commutable observables is J^2 and J_z:

$$\boldsymbol{J}^2 \left|J, M\right\rangle = \hbar J(J+1) \left|J, M\right\rangle \quad J_z \left|J, M\right\rangle = \hbar M \left|J, M\right\rangle \tag{2.68}$$

The total angular momentum Hilbert space can be spaned by $\left|\frac{3}{2}, \frac{3}{2}\right\rangle$, $\left|\frac{3}{2}, -\frac{3}{2}\right\rangle$, $\left|\frac{3}{2}, \frac{1}{2}\right\rangle$, $\left|\frac{3}{2}, -\frac{1}{2}\right\rangle$, $\left|\frac{1}{2}, \frac{1}{2}\right\rangle$, $\left|\frac{1}{2}, \frac{1}{2}\right\rangle$. We can use Clebsh-Gordon tables to translate expressions in $|J, M\rangle$ basis into the $|L, S; l, m\rangle$ basis:

$$\left|\frac{3}{2}, \frac{3}{2}\right\rangle = \left|1, \frac{1}{2}; 1, +\right\rangle \tag{2.69}$$

$$\left|\frac{3}{2}, \frac{1}{2}\right\rangle = \sqrt{\frac{2}{3}} \left|1, \frac{1}{2}; 0, +\right\rangle + \frac{1}{\sqrt{3}} \left|1, \frac{1}{2}; 1, -\right\rangle \tag{2.70}$$

$$\left|\frac{3}{2}, -\frac{1}{2}\right\rangle = \frac{1}{\sqrt{3}} \left|1, \frac{1}{2}; -1, +\right\rangle + \sqrt{\frac{2}{3}} \left|1, \frac{1}{2}; 0, -\right\rangle \tag{2.71}$$

$$\left|\frac{3}{2}, -\frac{3}{2}\right\rangle = \left|1, \frac{1}{2}; -1, -\right\rangle \tag{2.72}$$

$$\left|\frac{1}{2}, \frac{1}{2}\right\rangle = \sqrt{\frac{2}{3}} \left|1, \frac{1}{2}; 1, -\right\rangle - \frac{1}{\sqrt{3}} \left|1, \frac{1}{2}; 0, +\right\rangle \tag{2.73}$$

$$\left|\frac{1}{2}, -\frac{1}{2}\right\rangle = \frac{1}{\sqrt{3}} \left|1, \frac{1}{2}; 0, -\right\rangle - \sqrt{\frac{2}{3}} \left|1, \frac{1}{2}; -1, +\right\rangle \tag{2.74}$$

As observed, spin-orbit coupling terms divide the entire Hilbert space into the $J = 3/2$ and $J = 1/2$ sub-manifolds. This gap, denoted by Δ_0 is known as the spin-orbit splitting of the valence band at Γ_4, also known as the split-off energy.

To obtain the orbital angular momentum basis, we consider the spherical harmonics, which satisfy the following conditions:

$$L^2 Y_l^m = \hbar^2 l(l+1) Y_l^m \quad L_z Y_l^m = \hbar m Y_l^m \tag{2.75}$$

We express the p-orbital spherical harmonics as follows:

$$\langle \boldsymbol{r}|1,-1\rangle = Y_1^{-1} = +\sqrt{\frac{3}{8\pi}}\sin\theta e^{-i\phi} = +\sqrt{\frac{3}{8\pi}}\frac{x-iy}{\sqrt{x^2+y^2+z^2}} \tag{2.76}$$

$$\langle \boldsymbol{r}|1,1\rangle = Y_1^{1} = -\sqrt{\frac{3}{8\pi}}\sin\theta e^{+i\phi} = -\sqrt{\frac{3}{8\pi}}\frac{x+iy}{\sqrt{x^2+y^2+z^2}} \tag{2.77}$$

$$\langle \boldsymbol{r}|1,0\rangle = Y_1^{0} = \sqrt{\frac{3}{4\pi}}\cos\theta = \sqrt{\frac{3}{4\pi}}\frac{z}{\sqrt{x^2+y^2+z^2}} \tag{2.78}$$

Therefore, we have

$$|X\rangle = \frac{1}{\sqrt{2}}(|1,-1\rangle - |1,1\rangle) \quad |Y\rangle = \frac{i}{\sqrt{2}}(|1,-1\rangle + |1,1\rangle) \quad |Z\rangle = |1,0\rangle \tag{2.79}$$

We define this $1/\sqrt{2}$ to ensure that the terms $|X\rangle, |Y\rangle$, and $|Z\rangle$ each have a consistent coefficient of $\sqrt{3/4\pi}$. With this nornalization, we can now inversely solve the equations:

$$|1,-1\rangle = |X\rangle - i\,|Y\rangle \quad |1,1\rangle = -\,|X\rangle - i\,|Y\rangle \quad |1,0\rangle = |Z\rangle \tag{2.80}$$

The $|J,M\rangle$ basis can be written into the $|X\rangle, |Y\rangle, |Z\rangle, |\uparrow\rangle, |\downarrow\rangle$ basis:

$$\left|\frac{3}{2},\frac{3}{2}\right\rangle = -\frac{1}{\sqrt{2}}|X\rangle|\uparrow\rangle - i\frac{1}{\sqrt{2}}|Y\rangle|\uparrow\rangle \tag{2.81}$$

$$\left|\frac{3}{2},-\frac{3}{2}\right\rangle = \frac{1}{\sqrt{2}}|X\rangle|\downarrow\rangle - i\frac{1}{\sqrt{2}}|Y\rangle|\downarrow\rangle \tag{2.82}$$

$$\left|\frac{3}{2},\frac{1}{2}\right\rangle = -\sqrt{\frac{1}{6}}|X\rangle|\downarrow\rangle - i\sqrt{\frac{1}{6}}|Y\rangle|\downarrow\rangle + \sqrt{\frac{2}{3}}|Z\rangle|\uparrow\rangle \tag{2.83}$$

$$\left|\frac{3}{2},-\frac{1}{2}\right\rangle = \sqrt{\frac{1}{6}}|X\rangle|\uparrow\rangle - i\sqrt{\frac{1}{6}}|Y\rangle|\uparrow\rangle + \sqrt{\frac{2}{3}}|Z\rangle|\downarrow\rangle \tag{2.84}$$

Now, we perform degenerate perturbations around the Γ_4 point of the valence band. Initially, we assume the eigenstates of our unperturbed Hamiltonian can be expressed as follows:

$$\left|u_{n,1}^{(0)}\right\rangle, \left|u_{n,2}^{(0)}\right\rangle, \cdots \left|u_{n,g_n}^{(0)}\right\rangle, \left|v_{n+1}^{(0)}\right\rangle, \left|v_{n+1}^{(0)}\right\rangle \cdots \tag{2.85}$$

Where the n-th energy level is g_n-fold degenerate, we have employed the letter v to emphasize the eigenstates outside the degenerate energy levels. We now use linear combinations of the degenerate states to construct a new group of eigenstates, the degeneracy of which can be lifted by perturbations.

$$\left|\phi_{n,\alpha}^{(0)}\right\rangle = \sum_{i=1}^{g_n}\left\langle u_{n,i}^{(0)}\middle|\phi_{n,\alpha}^{(0)}\right\rangle\left|u_{n,i}^{(0)}\right\rangle \tag{2.86}$$

Utilizing the Rayleigh-Schrödinger perturbation method, the problem can be formulated as follows:

$$\begin{aligned}&(H_0+H')\left(\left|\phi_{n,\alpha}^{(0)}\right\rangle+\lambda\left|\phi_{n,\alpha}^{(1)}\right\rangle+\lambda^2\left|\phi_{n,\alpha}^{(0)}\right\rangle+\cdots\right)\\=&(E_{n,\alpha}^{(0)}+\lambda E_{n,\alpha}^{(1)}+\lambda^2E_{n,\alpha}^{(2)}+\cdots)\left(\left|\phi_{n,\alpha}^{(0)}\right\rangle+\lambda\left|\phi_{n,\alpha}^{(1)}\right\rangle+\lambda^2\left|\phi_{n,\alpha}^{(0)}\right\rangle+\cdots\right)\end{aligned}\tag{2.87}$$

where H_0 is the unperturbed Hamiltonian and H' denotes the $\boldsymbol{k}\cdot\boldsymbol{p}$ Hamiltonian, we have neglected the spin-orbit coupling Hamiltonian due to its relatively small magnitude. The zeroth-order equation is then given by:

$$H_0\left|\phi_{n,\alpha}^{(0)}\right\rangle=E_{n,\alpha}^{(0)}\left|\phi_{n,\alpha}^{(0)}\right\rangle\tag{2.88}$$

The first order perturabtion is:

$$H_0\left|\phi_{n,\alpha}^{(1)}\right\rangle+H'\left|\phi_{n,\alpha}^{(0)}\right\rangle=E_{n,\alpha}^{(0)}\left|\phi_{n,\alpha}^{(1)}\right\rangle+E_{n,\alpha}^{(1)}\left|\phi_{n,\alpha}^{(0)}\right\rangle\tag{2.89}$$

If we project a state from the degenerate energy level:

$$\sum_i^{g_n}\left[\left\langle u_{n,j}^{(0)}\right|H'\left|u_{n,i}^{(0)}\right\rangle\left\langle u_{n,i}^{(0)}\right|\left.\phi_{n,\alpha}^{(0)}\right\rangle-E_{n,\alpha}^I\delta_{\alpha,j}\left\langle u_{n,i}^{(0)}\right|\left.\phi_{n,\alpha}^{(0)}\right\rangle\right]=0\tag{2.90}$$

The second-order corrections can be obtained by evaluating the eigenvalues of the coefficient matrix. Setting the degeneracy g_n to 3, which corresponds to the x,y,z orbits, we obtain:

$$H_{i,j}=E_0\delta_{i,j}+\frac{\hbar^2k^2}{2m_0}\delta_{i,j}+\sum_{k>3}\frac{\left\langle u_{n,j}^{(0)}\right|H'\left|u_{n,i}^{(0)}\right\rangle\left\langle u_{n,i}^{(0)}\right|H'\left|u_{n,k}^{(0)}\right\rangle}{E_0-E_k}\tag{2.91}$$

where we have ignore the order superscriptions for $E_k^{(0)}$, now the E_0 is the unperturbed energy of the level we are interested in, E_m is the unperturbed energy of the remote bands (outside the degenerate manifold). Evaluate the matrix element terms by terms, in the basis of $|X\rangle, |Y\rangle, |Z\rangle$, we have:

$$\begin{pmatrix}E_0+Ak_x^2+B\left(k_y^2+k_z^2\right)&Ck_xk_y&Ck_xk_z\\Ck_xk_y&E_0+Ak_y^2+B\left(k_x^2+k_z^2\right)&Ck_yk_z\\Ck_xk_z&Ck_yk_z&E_0+Ak_z^2+B\left(k_x^2+k_y^2\right)\end{pmatrix}\tag{2.92}$$

where

$$A=\frac{\hbar^2}{2m_0}+\frac{\hbar^2}{m_0^2}\sum_{k>3}\frac{\left|\langle X\left|p_x\right|k\rangle\right|^2}{E_0-E_k}\tag{2.93}$$

$$B = \frac{\hbar^2}{2m_0} + \frac{\hbar^2}{m_0^2}\sum_{k>3}\frac{|\langle X|p_y|k\rangle|^2}{E_0 - E_k} \tag{2.94}$$

$$C = \frac{\hbar^2}{m_0^2}\sum_{k>3}\frac{\langle X|p_x|k\rangle\langle k|p_y|Y\rangle + \langle X|p_y|k\rangle\langle k|p_x|Y\rangle}{E_0 - E_k} \tag{2.95}$$

Here, we can refer to certain optical transition measurements and introduce the Luttinger parameters:

$$\gamma_1 = -\frac{2m_0}{3\hbar^2}(A+2B) \quad \gamma_2 = -\frac{m_0}{3\hbar^2}(A-B) \quad \gamma_3 = -\frac{m_0}{3\hbar^2}C \tag{2.96}$$

solve them inversely:

$$A = -(\gamma_1 + 4\gamma_2)\frac{\hbar^2}{2m_0} \quad B = -(\gamma_1 - 2\gamma_2)\frac{\hbar^2}{2m_0} \quad C = -6\gamma_3\frac{\hbar^2}{2m_0} \tag{2.97}$$

In terms of the Luttinger-Kohn parameters, and transform the Eq. (2.92) into the $|J, M\rangle$ basis, we have, for example,

$$H_{1,1} = E_0 - \frac{\hbar^2 k_z^2}{2m_0}(\gamma_1 - 2\gamma_2) - \frac{\hbar^2\left(k_x^2 + k_y^2\right)}{2m_0}(\gamma_1 + \gamma_2) \tag{2.98}$$

Note that since Luttinger parameters are obtained for holes in a filled valence band, which inherently have negative energy, if we flip the bands to make the energy positive, we have:

$$H_{1,1} = \frac{\hbar^2 k_z^2}{2m_0}(\gamma_1 - 2\gamma_2) + \frac{\hbar^2\left(k_x^2 + k_y^2\right)}{2m_0}(\gamma_1 + \gamma_2) \tag{2.99}$$

By repeating the procedures outlined above, we are able to write down the four-band Luttinger-Kohn Hamiltonians ($\mu, \nu \in \{x, y, x\}$):

$$H_{\mathrm{LK}} = \frac{\hbar^2}{2m_0}\left[\left(\gamma_1 + \frac{5}{2}\gamma_2\right)k^2\boldsymbol{I} - 2\gamma_2\delta^{\mu,\nu}k_\mu^2 J_\nu^2 - 4\gamma_3\bar{\delta}^{\mu,\nu}\{k_\mu, k_\nu\}\{J_\mu, J_\nu\}\right] \tag{2.100}$$

where $\delta^{\mu,\nu}$ is the kronecker delta, $\bar{\delta}^{\mu,\nu}$ is the anti-kronecker delta define by $\bar{\delta}^{\mu,\nu} = (1 - \delta^{\mu,\nu})/2$, and the Einstein summation notation is used. The expansion of Eq. (2.100) will be:

$$\begin{aligned} H_{\mathrm{LK}} =& \frac{\hbar^2}{2m_0}\left(\gamma_1 + \frac{5}{2}\gamma_2\right)(k_x^2 + k_y^2 + k_z^2)\boldsymbol{I}_{4\times4} - 2\frac{\hbar^2}{2m_0}\gamma_2(k_x^2 J_x^2 + k_y^2 J_y^2 + k_z^2 J_z^2) \\ & - 4\frac{\hbar^2}{2m_0}\gamma_3[\{k_x, k_y\}\{J_x, J_y\} + \{k_x, k_z\}\{J_x, J_z\} + \{k_y, k_z\}\{J_y, J_z\}] \end{aligned} \tag{2.101}$$

The symmetrization of operators is done by:

$$\{k_x, k_y\} = \frac{k_x k_y + k_y k_x}{2} \tag{2.102}$$

If we want to include the two split-off bands, we have the six-band model:

$$H_{\mathrm{LK}} = \begin{bmatrix} P+Q & 0 & -S & R & -\frac{1}{\sqrt{2}}S & \sqrt{2}R \\ 0 & P+Q & R^* & S^* & -\sqrt{2}R^* & -\frac{1}{\sqrt{2}}S^* \\ -S^* & R & P-Q & 0 & -\sqrt{2}Q & \sqrt{\frac{3}{2}}S \\ R^* & S & 0 & P-Q & \sqrt{\frac{3}{2}}S^* & \sqrt{2}Q \\ -\frac{1}{\sqrt{2}}S^* & -\sqrt{2}R & -\sqrt{2}Q^* & \sqrt{\frac{3}{2}}S & P+\Delta & 0 \\ \sqrt{2}R^* & -\frac{1}{\sqrt{2}}S & \sqrt{\frac{3}{2}}S^* & \sqrt{2}Q^* & 0 & P+\Delta \end{bmatrix} \tag{2.103}$$

$$P = \frac{\hbar^2}{2m_0}\gamma_1 k_z^2 + \frac{\hbar^2}{2m_0}\gamma_1(k_x^2+k_y^2) \tag{2.104}$$

$$Q = -2\frac{\hbar^2}{2m_0}\gamma_2 k_z^2 + \frac{\hbar^2}{2m_0}(k_x^2+k_y^2) \tag{2.105}$$

$$P+Q = \frac{\hbar^2}{2m_0}\left(\gamma_1-2\gamma_2\right)k_z^2 + \frac{\hbar^2}{2m_0}\left(\gamma_1+\gamma_2\right)\left(k_x^2+k_y^2\right) \tag{2.106}$$

$$P-Q = \frac{\hbar^2}{2m_0}\left(\gamma_1+2\gamma_2\right)k_z^2 + \frac{\hbar^2}{2m_0}\left(\gamma_1-\gamma_2\right)\left(k_x^2+k_y^2\right) \tag{2.107}$$

$$R = \sqrt{3}\frac{\hbar^2}{2m_0}\left[-\gamma_2\left(k_x^2-k_y^2\right)+2i\gamma_3 k_x k_y\right] \tag{2.108}$$

$$S = 2\sqrt{3}\frac{\hbar^2}{2m_0}\gamma_3\left(k_x k_z - i k_y k_z\right) \tag{2.109}$$

Another commonly used notations for the R and S terms are:

$$R = \sqrt{3}\frac{\hbar^2}{2m_0}\left(\gamma k_+^2 + \delta k_-^2\right) \quad S = 2\sqrt{3}\frac{\hbar^2}{2m_0}\gamma_3 k_- k_z \tag{2.110}$$

where

$$k_+ = k_x + ik_y \quad k_- = k_x - ik_y \quad \gamma = \frac{\gamma_3-\gamma_2}{2} \quad \delta = -\frac{\gamma_2+\gamma_3}{2} \tag{2.111}$$

This matrix is written under the basis $\left|\frac{3}{2},\frac{3}{2}\right\rangle$, $\left|\frac{3}{2},-\frac{3}{2}\right\rangle$, $\left|\frac{3}{2},\frac{1}{2}\right\rangle$, $\left|\frac{3}{2},-\frac{1}{2}\right\rangle$, $\left|\frac{1}{2},\frac{1}{2}\right\rangle$, $\left|\frac{1}{2},\frac{1}{2}\right\rangle$, noting that the order of this basis will be maintained throughout the thesis. The total

angular momentum matrices in the x, y, and z directions are:

$$J_{x,6\times6} = J_{x,4\times4} \oplus \sigma_{x,2\times2} = \frac{1}{2}\begin{bmatrix} 0 & 0 & \sqrt{3} & 0 & 0 & 0 \\ 0 & 0 & 0 & \sqrt{3} & 0 & 0 \\ \sqrt{3} & 0 & 0 & 2 & 0 & 0 \\ 0 & \sqrt{3} & 2 & 0 & 0 & 0 \\ 0 & 0 & 0 & 0 & 0 & 1 \\ 0 & 0 & 0 & 0 & 1 & 0 \end{bmatrix} \tag{2.112}$$

$$J_{y,6\times6} = J_{y,4\times4} \oplus \sigma_{y,2\times2} = \frac{1}{2}i\begin{bmatrix} 0 & 0 & -\sqrt{3} & 0 & 0 & 0 \\ 0 & 0 & 0 & \sqrt{3} & 0 & 0 \\ \sqrt{3} & 0 & 0 & -2 & 0 & 0 \\ 0 & -\sqrt{3} & 2 & 0 & 0 & 0 \\ 0 & 0 & 0 & 0 & 0 & -1 \\ 0 & 0 & 0 & 0 & 1 & 0 \end{bmatrix} \tag{2.113}$$

$$J_{z,6\times6} = J_{z,4\times4} \oplus \sigma_{z,2\times2} = \frac{1}{2}\begin{bmatrix} 3 & 0 & 0 & 0 & 0 & 0 \\ 0 & -3 & 0 & 0 & 0 & 0 \\ 0 & 0 & 1 & 0 & 0 & 0 \\ 0 & 0 & 0 & -1 & 0 & 0 \\ 0 & 0 & 0 & 0 & 1 & 0 \\ 0 & 0 & 0 & 0 & 0 & -1 \end{bmatrix} \tag{2.114}$$

The effective mass of the hole in the valence band can be written down immediately from Eq. (2.104) and Eq. (2.105):

$$m_{\mathrm{HH}} \equiv \frac{m_0}{\gamma_1 - 2\gamma_2} \quad m_{\mathrm{LH}} \equiv \frac{m_0}{\gamma_1 + 2\gamma_2} \tag{2.115}$$

$$m_{\mathrm{HP}} \equiv \frac{m_0}{\gamma_1 + \gamma_2} \quad m_{\mathrm{LP}} \equiv \frac{m_0}{\gamma_1 - \gamma_2} \tag{2.116}$$

where m_{HH} is the out-of-plane heavy-hole mass, m_{LH} is the out-of-plane light-hole mass, m_{HP} is the in-plane heavy-hole mass, m_{LP} is the in-plane light-hole mass. These different masses indicates a strong anisotropy in hole systems, which is weak in electron systems. The Luttinger-Kohn Hamiltonian gives a detailed description of the valence band behaviours including the effective mass of the diamond structure material like silicon and

germanium, which set up the foundations of semiconductor quantum dot hole spin qubits [484].

2.3 Bir-Pikus Hamiltonian

In the semiconductor industry, strain engineering is an important topic. Firstly, strains are unavoidable in the fabrication processes. Strains can be induced by dislocations, mismatches, and thermal expansions, which will lead to local deformations of crystals. Secondly, the application of strains is a well-developed technique to engineer the band structure of crystals. This can enhance the mobility of carriers or increase the emission or absorption rate in many optical devices. Nowadays, strain has also become an important factor in improving the coherence properties of semiconductor spin qubits, which will be the main focus of this section.

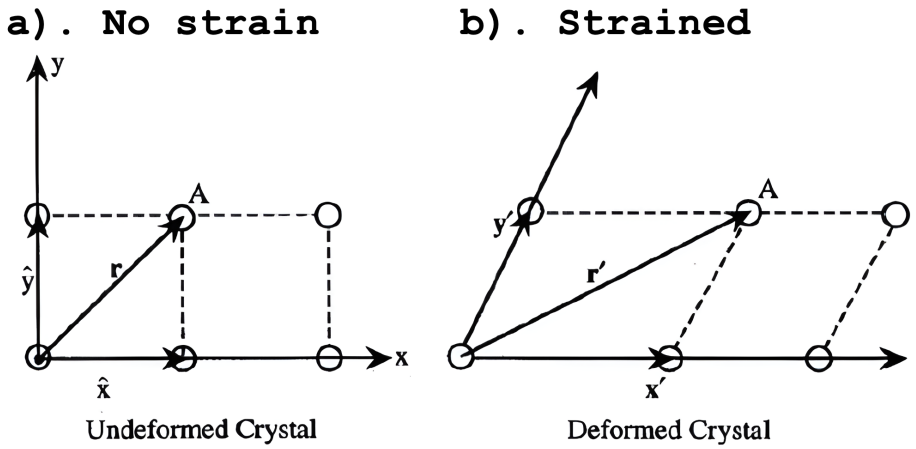

Figure 2.3: **Strain and deformation of a lattice.** a.) A lattice without strain. When there is no strain, the local coordinate frame is just an orthogonal Cartesian coordinate frame. b.) A lattice with strain. When there is strain, the coordinate frame is distorted, to descrbe such a distortion, we introduce the coordinate transformation. The original source of this figure is Ref. [473].

The local deformation of a crystal is equivalent to the coordinate transformation of the crystal. Therefore, we can introduce the strain and stress tensors, which are invariant

under coordinate transformations, to quantify the deformations. Deformations in one direction can be affected by displacements along the other two directions; therefore, the strain tensor is a rank-two tensor with nine components. In the limit of small elongation, the strain tensor can be further assumed to be symmetrical (whereas in the large elongation or even deflection limit, the strain tensor is usually non-symmetrical). To derive the invariant quantity, we can consider the transformation of the unit vectors of the crystal:

$$\hat{\boldsymbol{x}}' = (1+\varepsilon_{xx})\,\hat{\boldsymbol{x}} + \varepsilon_{xy}\hat{\boldsymbol{y}} + \varepsilon_{xz}\hat{\boldsymbol{z}} \tag{2.117}$$

$$\hat{\boldsymbol{y}}' = \varepsilon_{yx}\hat{\boldsymbol{x}} + (1+\varepsilon_{yy})\,\hat{\boldsymbol{y}} + \varepsilon_{yz}\hat{\boldsymbol{z}} \tag{2.118}$$

$$\hat{\boldsymbol{z}}' = \varepsilon_{zx}\hat{\boldsymbol{x}} + \varepsilon_{zy}\hat{\boldsymbol{y}} + (1+\varepsilon_{zz})\,\hat{\boldsymbol{z}} \tag{2.119}$$

where ϵ_{ij} is the strain along the direction i due to deformation along the direction j. We have added a hat on top of the variables to indicate it is a unit vector. A demonstration of this transformation can be found from Fig. 2.3 The strain tensor can be written as:

$$\Xi = \begin{bmatrix} \varepsilon_{xx} & \varepsilon_{xy} & \varepsilon_{xz} \\ \varepsilon_{yx} & \varepsilon_{yy} & \varepsilon_{yz} \\ \varepsilon_{zx} & \varepsilon_{zy} & \varepsilon_{zz} \end{bmatrix} \tag{2.120}$$

with conditions:

$$\varepsilon_{xy} = \varepsilon_{yx} \quad \varepsilon_{xz} = \varepsilon_{zx} \quad \varepsilon_{yz} = \varepsilon_{zy} \tag{2.121}$$

Considering the Luttinger-Kohn Hamiltonian, we have to perform the local coordinate transformation as well:

$$\boldsymbol{r}' = (1+\Xi)\boldsymbol{r} \Rightarrow r_i = (1-\Xi)r_i' \tag{2.122}$$

hence, $\boldsymbol{k}\cdot\boldsymbol{p}$ Hamiltonian:

$$\left(\frac{p'^2}{2m} + \frac{\hbar}{m}\boldsymbol{k}\cdot\boldsymbol{p} + \frac{\hbar^2 k^2}{2m} + V'\right) u_{n,\boldsymbol{k}'} = E_{n,\boldsymbol{k}'} u_{n,\boldsymbol{k}'} \tag{2.123}$$

We also have to perform the coordinate transformation on our differential operators:

$$\frac{\partial}{\partial r'} = \frac{\partial}{\partial r_i} - \varepsilon_{ji}\frac{\partial}{\partial r_j} \Rightarrow \boldsymbol{p}' = \boldsymbol{p}(1-\Xi) \tag{2.124}$$

where we have used Einstein summation notations. Further, we have

$$p'^2 = p^2 - 2p_i\varepsilon_{ij}p_j \tag{2.125}$$

The potential can be expanded in the small elongation limit:

$$V((1+\Xi)\boldsymbol{r}) = V_0 + \frac{\partial V}{\partial \varepsilon_{ij}}\epsilon_{ij} \tag{2.126}$$

We can introduce similar expansions on the unit-cell wavefunction as well. Now our $\boldsymbol{k}\cdot\boldsymbol{p}$ Hamiltonian is re-written as:

$$\left(\frac{p^2}{2m_0} + V_0 + \frac{\hbar}{m_0}\boldsymbol{k}\cdot\boldsymbol{p} + H_{\text{strain}} + H_{\text{strain}-\boldsymbol{kp}}\right)\tilde{u}_{n,\boldsymbol{k}}(\boldsymbol{r}) = \left(E - \frac{\hbar^2 k^2}{2m_0}\right)\tilde{u}_{n,\boldsymbol{k}}(\boldsymbol{r}) \tag{2.127}$$

where

$$H_{\text{strain}} = D_{\alpha\beta}\varepsilon_{\alpha\beta} \quad H_{\text{strain}-\boldsymbol{kp}} = -2\frac{\hbar^2}{m_0}k_\alpha \varepsilon_{\alpha\beta} p_\beta \tag{2.128}$$

The term $H_{\text{strain}-\boldsymbol{kp}}$ is disregarded since it is a higher order term. The term H_{strain} is known as Bir-Pikus Hamiltonian, which has a similar structure like Luttinger-Kohn Hamiltonian:

$$H_{\text{BP}} = \begin{bmatrix} P_\varepsilon + Q_\varepsilon & 0 & -S_\varepsilon & R_\varepsilon & -\frac{1}{\sqrt{2}}S_\varepsilon & \sqrt{2}R_\varepsilon \\ 0 & P_\varepsilon + Q_\varepsilon & R_\varepsilon^* & S_\varepsilon^* & -\sqrt{2}R_\varepsilon^* & -\frac{1}{\sqrt{2}}S_\varepsilon^* \\ -S_\varepsilon^* & R_\varepsilon & P_\varepsilon - Q_\varepsilon & 0 & -\sqrt{2}Q_\varepsilon & \sqrt{\frac{3}{2}}S_\varepsilon \\ R_\varepsilon^* & S_\varepsilon & 0 & P_\varepsilon - Q_\varepsilon & \sqrt{\frac{3}{2}}S_\varepsilon^* & \sqrt{2}Q_\varepsilon \\ -\frac{1}{\sqrt{2}}S_\varepsilon^* & -\sqrt{2}R_\varepsilon & -\sqrt{2}Q_\varepsilon^* & \sqrt{\frac{3}{2}}S_\varepsilon & P_\varepsilon & 0 \\ \sqrt{2}R_\varepsilon^* & -\frac{1}{\sqrt{2}}S_\varepsilon & \sqrt{\frac{3}{2}}S_\varepsilon^* & \sqrt{2}Q_\varepsilon^* & 0 & P_\varepsilon \end{bmatrix} \tag{2.129}$$

where

$$P_\varepsilon = -a_v\left(\varepsilon_{xx} + \varepsilon_{yy} + \varepsilon_{zz}\right) \tag{2.130}$$

$$Q_\varepsilon = -\frac{b_v}{2}\left(\varepsilon_{xx} + \varepsilon_{yy} - 2\varepsilon_{zz}\right) \tag{2.131}$$

$$R_\varepsilon = \frac{\sqrt{3}}{2}b_v\left(\varepsilon_{xx} - \varepsilon_{yy}\right) - id_v\varepsilon_{xy} \tag{2.132}$$

$$S_\varepsilon = -d_v\left(\varepsilon_{xz} - i\varepsilon_{yz}\right) \tag{2.133}$$

$$P_\varepsilon + Q_\varepsilon = -\left(a_v + \frac{b_v}{2}\right)\varepsilon_{xx} - \left(a_v + \frac{b_v}{2}\right)\varepsilon_{yy} - (a_v - b_v)\varepsilon_{zz} \tag{2.134}$$

$$P_\varepsilon - Q_\varepsilon = -\left(a_v - \frac{b_v}{2}\right)\varepsilon_{xx} - \left(a_v - \frac{b_v}{2}\right)\varepsilon_{yy} - (a_v + b_v)\varepsilon_{zz} \tag{2.135}$$

We added a subscript ϵ for strains. The D matrices in Eq. (2.129) can be extracted from the Bir-Pikus Hamiltonian, and further, the deformation potentials can be experimentally determined. The material-specific parameters a_v, b_v, and d_v are known as the hydrostatic deformation potential constant, the uniaxial deformation potential constant, and the shear deformation potential constant, respectively.

To demonstrate the influence on the band structures due to the Bir-Pikus Hamiltonians, we ignore the shear strain $(\varepsilon_{xy}, \varepsilon_{xz}, \varepsilon_{yz})$ first. Then, we can see that when we apply a tensile strain, we may be able to push the LH states into the ground states at the Brillouin Zone center. By applying compressive strains, we can push the LH states into the excited states at the Brillouin center. Similar to the S and R terms in the Luttinger-Kohn Hamiltonian, the shear strains can further enhance the HH-LH mixing, which is an active research topic to improve the coherence properties of the semiconductor quantum dot hole spin qubits.

2.4 Spin-orbit couplings in 2D system

The study of spin-orbit coupling effects originates from understanding the fine structure of the hydrogen atom spectra [224]. A direct expansion of the Dirac equation in the weak relativistic limit will give us the following terms:

$$H = m_e c^2 + \frac{\boldsymbol{P}^2}{2m_e} + V(R) - \frac{\boldsymbol{P}^4}{8m_e^3 c^2} + \frac{1}{2m_e^2 c^2}\frac{1}{R}\frac{\mathrm{d}V(R)}{\mathrm{d}R}\boldsymbol{L}\cdot\boldsymbol{S} + \frac{\hbar^2}{8m_e^2 c^2}\Delta V(R) + \cdots \quad (2.136)$$

The first term is the rest mass energy, the second and third terms are the normal kinetic energy and potential energy, which are the major contributions to the Hamiltonian. The fourth term is the first-order correction to the kinetic energy, which depends only on the momentum. The fourth term is the central topic of our discussion, which is the spin-orbit coupling (spin-orbit coupling) term. The fifth term is the so-called Darwin term, which is related to the spatial variation of the potential. Historically, even though we can solve the hydrogen energy spectrum analytically without doing this expansion using Dirac equations, it is still necessary to understand the possible interactions hidden in the Dirac equation. Furthermore, the form of these interactions can be used to study many-electron

systems as well, e.g., many crystals.

Symmetry analysis is a powerful tool to study the spin-orbit couplings in crystal systems, since long-range ordered crystals possess numerous natural geometrical symmetries. Let us start the symmetry analysis from the energy dispersion point of view. Considering that the dispersion is invariant under spatial inversion operation, we have:

$$E(\boldsymbol{k},\uparrow) = E(-\boldsymbol{k},\uparrow) \tag{2.137}$$

under time-reversal symmetry, we will have:

$$E(\boldsymbol{k},\uparrow) = E(-\boldsymbol{k},\downarrow) \tag{2.138}$$

Then we can see that for a crystal which is invariant under spatial inversion and time-reversal, we have at least a two-fold degeneracy:

$$E(\boldsymbol{k},\uparrow) = E(\boldsymbol{k},\downarrow) \tag{2.139}$$

Now, let us maintain the time-reversal symmetry; if we break this inversion symmetry by applying an asymmetric electric potential, we will no longer have equation Eq. (2.139). On the other hand, without introducing any magnetic field, the spin degeneracy is also lifted by this potential. Now we have two dispersion branches:

$$E_+(\boldsymbol{k}) \quad E_-(\boldsymbol{k}) \tag{2.140}$$

It is worth noting that the two dispersion branches are not due to spin splitting, which is different from the spin-momentum locking mechanism in the quantum spin hall effect. Therefore, we have used the signs $+$ and $-$ respectively.

In quasi-2D structures, like quantum wells or heterostructures, the inversion asymmetry can be the consequence of bulk inversion asymmetry in certain crystal structures, such as zinc-blende crystals, which do not have a well-defined inversion center. Many familiar semiconductors are in this category, like GaAs, InAs, and InSb. Another possibility to obtain inversion asymmetry, as mentioned above, is by adding an asymmetric electric potential. This will induce spin-orbit couplings in crystals with inversion centers, such

as those with a diamond structure. Group four elements like silicon, germanium, and carbon are all in this category. Interface inversion asymmetries are another important source of spin-orbit couplings, which present challenges to estimate; however, it requires a detailed analysis of the semiconductor architectures. Therefore, we have ignored this type of spin-orbit couplings in our work.

It is important to note that breaking the inversion symmetry while maintaining time-reversal symmetry is a crucial feature distinguishing spin-orbit couplings from magnetic fields, even though both can cause band splitting. This feature plays an important role in topological insulators. Since the major focus of our work is on diamond structure crystals like silicon or germanium, we will only discuss the Rashba spin-orbit couplings, which are the structure inversion asymmetries due to asymmetric electric potentials. The current well-developed experimental techniques can already precisely tune the Rashba spin-orbit couplings by applying gate electrodes, enabling many new designs of spin-orbit coupling devices [143, 475, 252, 360, 156, 231].

Consider a perpendicular electric field applied along the z-direction (the growth direction):

$$V(z) = eF_z z \tag{2.141}$$

As introduced earlier, it is a standard quantum well design. We can solve the corresponding Schrödinger equation in the z-direction:

$$-\frac{\hbar^2}{2m^*}\frac{\partial^2\psi(z)}{\partial z^2} + V(z)\psi(z) = E\psi(z) \tag{2.142}$$

Now we are dealing with a quasi-2D system. To illustrate some basic features of spin-orbit couplings in this quasi-2D system, we introduce the spin-orbit coupling term in electron systems first, and then we will discuss spin-orbit couplings in hole systems.

In 1984, Bychkov and Rashba proposed that in the Γ_6 conduction band, the spin-orbit coupling is given by the following form:

$$H_{\mathrm{SO}} = \alpha(\boldsymbol{\sigma}\cdot\boldsymbol{k})\times\boldsymbol{F} \tag{2.143}$$

where the components of $\boldsymbol{\sigma}$ are Pauli matrices, α is a material-specific coefficient, and $\boldsymbol{F}$ is the gate electric field. Considering $\boldsymbol{F} = (0, 0, F_z)$, we have:

$$H_{\mathrm{SO}} = \alpha F_z(k_-\sigma_+ - k_+\sigma_-) = \alpha F_z \begin{bmatrix} 0 & ik_- \\ -ik_+ & 0 \end{bmatrix} \tag{2.144}$$

where

$$k_+ = k_x + ik_y, \quad k_- = k_x - ik_y, \quad \sigma_+ = (\sigma_x + i\sigma_y)/2, \quad \sigma_- = (\sigma_x - i\sigma_y)/2 \tag{2.145}$$

Considering the normal parabolic dispersion, we can plot the dispersion for two different branches as shown in Fig. 2.4

The evaluation of the Rashba coefficient can be obtained by performing Löwdin partitioning perturbation calculations on the Kane Hamiltonian, which includes the conduction band and the valence band.

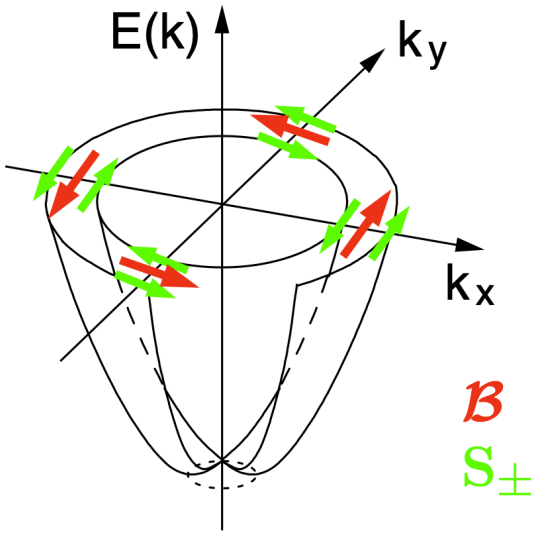

Figure 2.4: **Rashba spin-orbit coupling splitting** There are two branches of dispersions as a function of k_x and k_y, the read arrow in the figures indicated the effective magnetic field, which is alway tangential to the dispersion surface counter-clockwisely. The expectation of the spin polarization is indicated in the figure as well, denoted by green arrows. We can notice that the spin polarization is opposite for the two dispersions. The original source of this figure is Ref. [548].

In 2D hole systems, strong confinement in the z-direction creates a finite gap between HH states and LH states. The magnitude of this finite gap is material-specific and usually

depends on their out-of-plane effective mass. A rough estimation of the HH-LH splitting in a silicon 2D hole system is around 10 meV. Note that we have not included any strains yet. The existence of shear strain will further renormalize the HH-LH splitting gap, which is another important topic in current hole spin qubit research. Typically, the HH-LH splitting gap is very large, providing a natural energy gap for performing Lowdin partitioning renormalizations of our system. We can write down an effective Hamiltonian to capture both the manifold we are interested in and the HH-LH mixing physics.

In our work, we focus on the HH manifold, which consists of the two lowest eigen-energy states without deliberate application of strains. Performing Lowdin partitioning up to the second order on our Hamiltonian, we get:

$$H_{\mathrm{SO}} = \alpha_2 \left(k_+^3 \sigma_- - k_-^3 \sigma_+\right) + \alpha_3 \left(\left\{k_+^2, k_-\right\} \sigma_+ - \left\{k_+, k_-^2\right\} \sigma_-\right) \tag{2.146}$$

The asymmetrical nature is hidden in the shape of the wave-functions like ψ_{HH} and ψ_{LH}, which are the solutions of Eq. (2.142). Thus, the spin-orbit coupling coefficients can be tuned electrically via the external electric field. These cubic k terms have been measured experimentally, demonstrating that the $k_+ k_- k_+$ term winds around the Fermi surface once, while the k_+^3 term winds around the Fermi surface three times. These spin-orbit couplings will be further discussed in the electrical dipole spin resonance sections.

2.5 Electric dipole spin resonance

Following the introductions above, we have known that the qubit is based on the lowest two HH states. The next step is to understand which mechanism is available to allow the transition of the qubit between these two states. Thanks to advanced solid-state experimental techniques, the manipulations of quantum states in a two-level system using resonances were demonstrated on various platforms, such as nuclear magnetic resonance (NMR) in nuclear spin systems, electron cyclotron resonance (ECR) in plasma etchings, electron spin resonance (ESR, also known as electron paramagnetic resonance, EPR) in electron qubits.

The central idea of these resonance techniques is based on the couplings between external fields (electric field, magnetic fields) and the orbital degree of freedom or the spin degree of freedom. In crystals, due to the existence of the spin-orbit couplings, the resonance is even more complicated [51, 149, 411, 144, 188, 64, 413, 99]. In this section, we will firstly introduce some general concepts, including Larmor frequency formulism and Rabi oscillations. Then we will introduce how the electron qubit state is manipulated by the ESR technology and why it would not be effective in hole spin qubits. Finally, we will introduce the electric dipole spin resonance mechanism in Group IV semiconductor quantum dot hole spin qubits.

2.5.1 Larmour frequency

To understand the behaviors of the spin degree of freedom, we initially omit the orbital motions, rendering our Hilbert space purely two-dimensional. It is essential to define the gyromagnetic ratio, which is the ratio between the magnetic moment and the angular momentum:

$$\gamma = \frac{\mu}{L} \tag{2.147}$$

The magnetic moment of an electron spin can be calculated as follows:

$$\mu = g_e \mu_B s \tag{2.148}$$

where s is the spin quantum number of the particle (which is 1/2 for electrons), q is the charge, m_e is the bare electron mass, and g_e is the Landé g-factor, which is assumed to be 2 in our thesis, and we did not consider any interactions between the electrons and vacuum electromagnetic fluctuations. μ_B is the well-known Bohr magneton:

$$\mu_B = \frac{e\hbar}{2m_e} \approx 5.788 \times 10^{-5}\, eV/T \tag{2.149}$$

Now we can write down the Hamitonian for an electron in a magnetic field:

$$H = -\boldsymbol{\mu} \cdot \boldsymbol{B} = -\gamma \boldsymbol{B} \cdot \boldsymbol{S} \tag{2.150}$$

To simplify the algebra, we only consider the magnetic field component along the B_z axis:

$$\mathbf{H} = -\gamma B_z S_z = -\frac{\gamma B_z \hbar}{2} \begin{bmatrix} 1 & 0 \\ 0 & -1 \end{bmatrix} \tag{2.151}$$

The eigen-energies are $E_+ = -(\gamma B_z \hbar)/2$ and $E_- = (\gamma B_z \hbar)/2$, corresponding to the eigen-states $|\uparrow\rangle$ and $|\downarrow\rangle$ respectively. The result indicates that when the magnetic dipole moment is parallel to the magnetic field, the system has lower energy. Since the Hamiltonian is time-independent, can solve the time evolution of the eigen-states (denoted by $|\chi\rangle$, which can be either $|\uparrow\rangle$ or $|\downarrow\rangle$):

$$i\hbar \frac{\partial |\chi\rangle}{\partial t} = H |\chi\rangle \tag{2.152}$$

The solution is

$$|\chi; t\rangle = a|\uparrow\rangle \exp\left(-\frac{i}{\hbar} E_+ t\right) + b|\uparrow\rangle \exp\left(-\frac{i}{\hbar} E_- t\right) = \begin{bmatrix} a \exp\left(\frac{i}{2}\gamma B_z t\right) \\ b \exp\left(-\frac{i}{2}\gamma B_z t\right) \end{bmatrix} \tag{2.153}$$

where the constants a and b are determined by the initial states of the spinor:

$$|\chi; 0\rangle = \begin{bmatrix} a \\ b \end{bmatrix} \tag{2.154}$$

Using the trigonometric identities and the normalization condition, we can express our spinor at time t as:

$$|\chi; t\rangle = \begin{bmatrix} \cos\left(\frac{\alpha}{2}\right) \exp\left(\frac{i}{2}\gamma B_z t\right) \\ \sin\left(\frac{\alpha}{2}\right) \exp\left(-\frac{i}{2}\gamma B_z t\right) \end{bmatrix} \tag{2.155}$$

The expectation values of the spin polarizations can be calculated using the given spinor expression:

$$\langle S_x \rangle = \frac{\hbar}{2} \sin(\alpha) \cos(\gamma B_z t) \tag{2.156}$$

$$\langle S_y \rangle = -\frac{\hbar}{2} \sin(\alpha) \sin(\gamma B_z t) \tag{2.157}$$

$$\langle S_z \rangle = \frac{\hbar}{2} \cos(\alpha) \tag{2.158}$$

The results indicate that the angle between the spin polarization $\langle \boldsymbol{S} \rangle$ and the $\hat{z}$-axis is invariant, but it follows a precessional motion with Larmor frequency $\omega = -\gamma B_z$. Meanwhile, we notice that the energy gap of the two-level system is $\gamma \hat{B}_z$, if we are able to generate a signal whose frequency matches this energy gap, we will observe Rabi oscillations.

2.5.2 Rabi oscillations

Rabi oscillations were first studied in atomic physics when coherent light acts on an atom. In this process, the atom periodically absorbs and re-emits photons, a phenomenon known as Rabi oscillation. Now, let us derive the important Rabi frequency formula. Consider a non-degenerate two-level system; without loss of generality, the Hamiltonian can be spanned by Pauli matrices:

$$H = E_0 \cdot \sigma_0 + W_1 \cdot \sigma_1 + W_2 \cdot \sigma_2 + \Delta \cdot \sigma_3 = \begin{bmatrix} E_0 + \Delta & W_1 - iW_2 \\ W_1 + iW_2 & E_0 - \Delta \end{bmatrix} \tag{2.159}$$

where E_0 can be thought of as the energy scale of the system, Δ is the major energy gap of the two-level system, and W_1 and W_2 are the hopping energies. The eigenvalues of the problem are:

$$E_+ = E_0 + \sqrt{\Delta^2 + W_1^2 + W_2^2} = E_0 + \sqrt{\Delta^2 + \|W\|^2} \tag{2.160}$$

$$E_- = E_0 - \sqrt{\Delta^2 + W_1^2 + W_2^2} = E_0 - \sqrt{\Delta^2 + \|W\|^2} \tag{2.161}$$

For E_+, the eigenstate is

$$|u_+\rangle = \left[a, -\frac{a\,(E_0 + \Delta - E_+)}{W_1 - iW_2}\right]^T \tag{2.162}$$

Useing the normalization condition, we can express the entries of the E_+ eigenstate as follows:

$$a = \exp\left(\frac{i}{2}\phi\right)\cos\left(\frac{\theta}{2}\right) \quad b = \exp\left(-\frac{i}{2}\phi\right)\sin\left(\frac{\theta}{2}\right) \tag{2.163}$$

where

$$\sin\theta = \frac{\|W\|}{\sqrt{\Delta^2 + \|W\|^2}} \quad \cos\theta = \frac{\Delta}{\sqrt{\Delta^2 + \|W\|^2}} \tag{2.164}$$

The E_+ eigen-state becomes to

$$|u_+\rangle = \begin{bmatrix} \cos\left(\frac{\theta}{2}\right) \\ \exp(i\phi)\sin\left(\frac{\theta}{2}\right) \end{bmatrix} = \cos\left(\frac{\theta}{2}\right)|0\rangle + \exp(i\phi)\sin\left(\frac{\theta}{2}\right)|1\rangle \tag{2.165}$$

Similarly, we have

$$|u_-\rangle = \cos\left(\frac{\theta}{2}\right)|0\rangle - \exp(i\phi)\sin\left(\frac{\theta}{2}\right)|1\rangle \tag{2.166}$$

$$|0\rangle = \cos\left(\frac{\theta}{2}\right)|u_+\rangle + \sin\left(\frac{\theta}{2}\right)|u_-\rangle \tag{2.167}$$

$$|1\rangle = \exp(-i\phi)\cos\left(\frac{\theta}{2}\right)|u_+\rangle - \exp(-i\phi)\sin\left(\frac{\theta}{2}\right)|u_-\rangle \tag{2.168}$$

Assuming that the system starts evolving in the state $|0\rangle$ at time $t = 0$:

$$|\psi; t=0\rangle = |0\rangle = \cos\left(\frac{\theta}{2}\right)|E_+\rangle + \sin\left(\frac{\theta}{2}\right)|E_-\rangle \tag{2.169}$$

The time-evoluation of the state can be written as:

$$|\psi; t\rangle = \exp\left(\frac{-i\hat{H}t}{\hbar}\right)|\psi; t=0\rangle = \cos\left(\frac{\theta}{2}\right)\exp\left(\frac{-iE_+t}{\hbar}\right)|E_+\rangle + \sin\left(\frac{\theta}{2}\right)\exp\left(\frac{-iE_-t}{\hbar}\right)|E_-\rangle \tag{2.170}$$

We can evaluate the probability amplitude at time t for the state $|1\rangle$:

$$\langle 1|\psi; t\rangle = \exp(i\phi)\sin\left(\frac{\theta}{2}\right)\cos\left(\frac{\theta}{2}\right)\left(\exp\left(\frac{-iE_+t}{\hbar}\right) - \exp\left(\frac{-iE_-t}{\hbar}\right)\right) \tag{2.171}$$

The probability is:

$$P_{0\to1}(t) = \frac{\sin^2\theta}{4}\left(2 - 2\cos\left(\frac{(E_+ - E_-)\,t}{\hbar}\right)\right) \tag{2.172}$$

which can be futher simplified to:

$$P_{0\to1}(t) = \sin^2(\theta)\sin^2\left(\frac{(E_+ - E_-)\,t}{2\hbar}\right) = \frac{\|W\|^2}{\Delta^2 + \|W\|^2}\sin^2\left(\frac{(E_+ - E_-)\,t}{2\hbar}\right) \tag{2.173}$$

The result shows that the probability is periodic, with a frequency:

$$\omega = \frac{\sqrt{\Delta^2 + \|W\|^2}}{\hbar} \tag{2.174}$$

In the case of a single spin in a magnetic field, this Rabi frequency is the same as the precession frequency we derived in Subsection. 2.5.1.

2.5.3 Electron spin resonance

We have observed that with a perpendicular magnetic field B_z, the energy undergoes splitting, causing the spin to precess along the $\hat{z}$-direction. Now, when an additional oscillating magnetic field $B_x \cos(\omega t)\hat{x}$ is introduced into the system, the total Hamiltonian will be:

$$H(t) = \frac{1}{2}\hbar\gamma(B_z\sigma_z + B_x \cos(\omega t)\sigma_x) \tag{2.175}$$

It is a time-dependent Hamiltonian, which means:

$$\big[H(t), H(t')\big] \neq 0 \tag{2.176}$$

Therefore, we cannot simply use time evolution operators to evolve the quantum state. To solve this Hamiltonian, we can introduce the time-ordering operator T, or we can change the frame of reference. We will now translate our problem into a frame of reference rotating at the Larmor frequency. The new state, which is called unwound states, is:

$$|\psi'; t\rangle = \exp\left(\frac{i}{2}\omega_L\sigma_z t\right)|\psi; t\rangle \tag{2.177}$$

Here, we use the dashed variable to indicate it is in the rotating frame, and we have added a subscript L to indicate it is the Larmor frequency. The evolution of these states is still governed by the Schrödinger equation:

$$i\hbar\frac{\mathrm{d}}{\mathrm{d}t}|\psi'; t\rangle = -\frac{1}{2}\hbar\omega_L\sigma_z|\psi'; t\rangle + \exp\left(\frac{i}{2}\omega_L\sigma_z t\right)i\hbar\frac{\mathrm{d}}{\mathrm{d}t}|\psi; t\rangle \tag{2.178}$$

The last term can be written as:

$$\exp\left(\frac{i}{2}\omega_L\sigma_z t\right)i\hbar\frac{\mathrm{d}}{\mathrm{d}t}|\psi; t\rangle = \exp\left(\frac{i}{2}\omega_L\sigma_z t\right)H(t)|\psi; t\rangle \tag{2.179}$$

then the total euqation can be expressed as:

$$i\hbar\frac{\mathrm{d}}{\mathrm{d}t}|\psi'; t\rangle = \left(-\frac{1}{2}\hbar\omega_L\sigma_z + \exp\left(\frac{i}{2}\omega_L\sigma_z t\right)H(t)\exp\left(-\frac{i}{2}\omega_L\sigma_z t\right)\right)|\psi'; t\rangle \tag{2.180}$$

which defines the Hamiltonian in the rotating frame:

$$H'(t) = -\frac{1}{2}\hbar\omega_L\sigma_z + \exp\left(\frac{i}{2}\omega_L\sigma_z t\right)H(t)\exp\left(-\frac{i}{2}\omega_L\sigma_z t\right) \tag{2.181}$$

The last term can be calculated explicitly:

$$\exp\left(\frac{i}{2}\omega_L\sigma_z t\right)H(t)\exp\left(-\frac{i}{2}\omega_L\sigma_z t\right)=\frac{\hbar}{2}\gamma\left(B_z\sigma_z+\exp\left(\frac{i}{2}\omega_L\sigma_z t\right)B_x\cos(\omega t)\exp\left(-\frac{i}{2}\omega_L\sigma_z t\right)\right) \tag{2.182}$$

Notice the following relation:

$$\cos(\omega t)\sigma_x=\left(\left(e^{-i\omega t}\sigma_+ + e^{i\omega t}\sigma_-\right)+\left(e^{i\omega t}\sigma_+ + e^{-i\omega t}\sigma_-\right)\right) \tag{2.183}$$

Where we have decomposed the σ_x into two counter-rotating circular waves. Now the total Hamiltonian can be expressed as:

$$H'(t)=\frac{\hbar\gamma}{2}B_1\left(\left(e^{i(\omega_L-\omega)t}\sigma_+ + e^{i(\omega-\omega_L)t}\sigma_-\right)+\left(e^{i(\omega+\omega_L)t}\sigma_+ + e^{-i(\omega+\omega_L)t}\sigma_-\right)\right) \tag{2.184}$$

If we apply a signal identical to the Larmor frequency, i.e., $\omega=\omega_L$ (resonance condition), our Hamiltonian becomes:

$$H'(t)=\frac{\hbar\gamma}{2}B_1\left((\sigma_+ + \sigma_-)+\left(e^{2i\omega_L t}\sigma_+ + e^{-2i\omega_L t}\sigma_-\right)\right) \tag{2.185}$$

Now, we need to introduce the rotating wave approximation (RWA) to ignore the second term since it is oscillating so fast that its effect on the spin dynamics is negligible. The Hamiltonian left has a very simple form:

$$H'(t)=\frac{\hbar\gamma}{2}B_1\left(\sigma_+ + \sigma_-\right)=\frac{\hbar\gamma}{2}B_x\sigma_x \tag{2.186}$$

Which describes a spin rotation in the $\hat{x}$-direction, with frequency $\omega_R=\gamma B_x/2$, which is called the Rabi frequency of ESR.

ESR technology finds extensive use in manipulating the spin states of electron qubits [541, 28]. In experimental setups, a micromagnet is often integrated with the sample, allowing the emission of oscillating magnetic signals into the system. ESR is particularly effective for unpaired electrons, as the Pauli Exclusion Principle prevents a pair of electrons from yielding zero magnetic momentum. Unpaired electrons, which contribute to the paramagnetism of electrons, also give ESR another name: Electron Paramagnetic Resonance (EPR) [480, 542, 12]. It serves as a powerful tool for controlling the spin states of electron qubits. However, integrating micromagnets into semiconductor systems during fabrication is a complex task [389, 479, 498]. Additionally, generating a sufficiently large

magnetic field using micromagnets poses a significant challenge, raising concerns about the scalability of electron qubits. Then, physicists were seeking an alternative approach, using an electric field to control the spin states.

2.5.4 Electric dipole spin resonance

Magnetic dipole transitions are not the sole method for manipulating spin states. In hole systems, the electric dipole spin resonance (electric dipole spin resonance) technique is also widely employed. Instead of relying on magnetic dipole transitions induced by an oscillating magnetic field, electric dipole spin resonance relys on the spin-orbit couplings in semiconductor systems to facilitate electric dipole transitions driven by an oscillating electric field [537, 530, 73]. Using an electric field offers several advantages. Firstly, the magnitude of an electric field can be much larger, leading to faster Rabi oscillation frequencies. Secondly, integrating electric circuits with semiconductor quantum dot hole spin qubits is relatively straightforward. In this subsection, we first focus on electric dipole spin resonance using an alternating in-plane electric field. Subsequently, we briefly discuss some important features of electric dipole spin resonance.

Focusing on the HH submanifold, the effective Hamiltonian of the quantum dot will read:

$$H = H_0 + H_{\text{SO}} + V_0 + H_{\text{Zeeman}} + H_{Eac} \tag{2.187}$$

The first term represents the kinetic energy, the second term corresponds to the effective Hamiltonian we derived in Sec. 2.4, the third term accounts for parabolic confinement, the fourth term introduces an out-of-plane magnetic field that induces spin quantization along the $\hat{z}$-direction, and the last term is an in-plane alternating electric field capable of inducing electric dipole transitions. Since the magnetic field is applied along the $\hat{z}$-direction, the primary contribution to the energy of this Hamiltonian is exactly solvable:

$$(H_0 + V_0)\,|\phi\rangle = E\,|\phi\rangle \tag{2.188}$$

When applying a magnetic field, we need to perform a Peierls substitution for all the

wave-vectors in Equation (2.187):

$$\boldsymbol{k} \to -i\nabla - \frac{e}{\hbar}\boldsymbol{A} \tag{2.189}$$

A carrier in an out-of-plane magnetic field is known as the Fock-Darwin problem. The in-plane wave function is obtained by solving the Fock-Darwin Hamiltonian:

$$H = -\frac{\hbar^2}{2m_{\mathrm{HP}}}\left(\frac{\partial^2}{\partial x^2} + \frac{\partial^2}{\partial y^2}\right) + \frac{1}{2}m_{\mathrm{HP}}\left(\omega_0^2 + \frac{1}{4}\omega_c^2\right)(x^2+y^2) - \frac{1}{2}\omega_c l_z \tag{2.190}$$

Here, we define the cyclotron frequency as:

$$\omega_c = \frac{eB_z}{m_{\mathrm{HP}}} \tag{2.191}$$

The ground state of the Hamiltonian is:

$$\phi_0(x,y) = \frac{1}{R_{a,0}\sqrt{\pi}}\exp\left(-\frac{x^2+y^2}{2R_0^2}\right) \tag{2.192}$$

Here, we introduce an important quantity known as the effective dot size, denoted as $R_{a,0}$:

$$R_{a,0} = \sqrt{\frac{\hbar}{m_{\mathrm{HP}}\Omega_0}} \quad \Omega_0 = \sqrt{\omega_0^2 + \frac{1}{4}\omega_c^2} \tag{2.193}$$

The ground state energy is

$$E_0 = \hbar\Omega_0 \tag{2.194}$$

The excisted state wave-functions are:

$$\phi_{\pm 1}(x,y) = \frac{2}{R_0^2\sqrt{\pi}}(x \pm iy)\exp\left(-\frac{x^2+y^2}{2R_0^2}\right) \tag{2.195}$$

Their eigen-energies are:

$$E_{\pm} = \hbar\Omega_0 \pm \frac{\hbar}{2}\omega_c \tag{2.196}$$

Now we can treat all the other Hamiltonians in Eq. (2.187) as perturbations. Then we revert to our standard Lödin partitioning problem once again, yielding two sets of states: the ground state $|\phi_0\rangle$ and the first excited states $|\phi_{+1}\rangle$ and $|\phi_{-1}\rangle$. It is worth noting that there is one more hidden degeneracy, which is the pseudospin of the HH manifolds, denoted by $|\uparrow\rangle$ and $|\downarrow\rangle$. The renormalization gap is $\hbar\Omega_0$, which is the largest energy scale. Then, we need to project the perturbation Hamiltonians H_{SO}, H_{Zeeman}, H_{Eac} onto our basis to obtain their matrix forms.

Determining which matrix elements will be left is important for understanding electric dipole spin resonance. Then, the matrix elements of the Zeeman Hamiltonian will only appear along the diagonal elements, which are not listed. Several important features should be noted here. First, in a circular quantum dot (where the confinement frequency is the same for both the $\hat{x}$-direction and the $\hat{y}$-direction), only the α_2 linear Rashba term is responsible for electric dipole transitions. On the other hand, the α_3 Rashba term winds the Fermi surface three times, enabling a $\Delta n = 3$ orbital transition, whereas the α_3 Rashba term winds the Fermi surface only once, inducing a $\Delta n = 1$ Rashba term. Notably, as mentioned in Sec. 2.4, the α_2 Rashba spin-orbit coupling coefficient can be electrically tuned through the gate electric field, serving as the foundation for achieving purely electrical control of the spin states [439]. Finally, it is worth noting that elliptical quantum dots can activate the α_3 Rashba spin-orbit coupling coefficients, offering possibilities to enhance the spin-orbit coupling effects through anisotropic geometry designs.

In the small magnetic field limit, we can expand the electric dipole spin resonance frequency in the first order of B_z, which takes the following form:

$$|f_R| = \frac{eE_{\text{ac}}\alpha_2 g_z \mu_B B_z m_x^2 R_0^2}{2\pi\hbar^5} \tag{2.197}$$

The situation becomes more complicated when the magnetic field is oriented along the in-plane directions (i.e., perpendicular to the gate electric field directions). Firstly, we no longer have analytical expressions for $H_0 + V_0$, necessitating a detailed numerical scheme. Additionally, the Löwdin partitioning method may not be accurate since the in-plane magnetic field results in a smaller orbital splitting. This means that the two interacting sets may not be weakly separated. In such cases, we can only evaluate the Rabi frequency numerically:

$$f_{\text{Rabi}} = \frac{1}{h}\|\langle \mathbb{1}|H|\mathbb{0}\rangle\| \tag{2.198}$$

where $|\mathbb{1}\rangle$, $|\mathbb{0}\rangle$ is the excited state and the ground state respectively, in the qubit HH submanifold. Here we only present a superficial analysis and the Rabi frequency, in practice, there are many other quantities can play a role, such as strain profiles, anisotropic dot geometries, growth directions, and external fields applied. Acheiving ultrafast Rabi oscillations is a central topic in improving the coherence of the quantum computations.

2.6 Phonon-hole interaction

Our electric dipole spin resonance Rabi frequency calculations demonstrated that in semiconductor quantum dot hole spin qubits, the spin manipulation times can reach tens of nanoseconds. However, the electric dipole spin resonance Rabi time cannot solely characterize the quality of the qubit; we also need to consider the relaxation decoherence time and dephasing time (which will be introduced in the next section). The phonon-induced relaxation is a dominant source of decoherence, particularly at high temperatures or in large magnetic fields. The interactions between holes and phonons are unavoidable in solid-state devices and difficult to mitigate with external fields.

In this section, we will first introduce the properties of phonons, followed by a discussion of the phonon-hole interaction Hamiltonian. Then, we will establish a formalism to estimate the phonon-induced relaxation time. Finally, we will examine several important aspects of phonon relaxations.

2.6.1 Phonons

In the context of condensed matter physics, the complex intermolecular interactions determine the macroscopic behavior of a many-body system. A solid is formed when molecules are organized in an ordered manner, and the collective motion of these molecules yields low-energy excitations. These low-energy excitations are known as sound waves on the macroscopic scale. From a quantum mechanical perspective, these sound waves correspond to a quasi-particle called phonons. The nature of phonon collective excitations can be illustrated using a classical model: a one-dimensional atomic chain with N atoms, with periodic boundary conditions [15, 370, 130, 471, 26, 490, 283]. The unit atom, assumed to have a mass m, are connected by springs with a spring constant k_0, analogous to chemical bonds. The interatomic distance at equilibrium is a_0.

The Lagrangian of this chain can be expressed as:

$$L = T - V = \sum_{n=1}^{N} \left[\frac{m}{2} \dot{x}_n^2 - \frac{k_0}{2} \left(x_{n+1} - x_n - a_0 \right)^2 \right] \tag{2.199}$$

where x_n represents the position of the atom at the n-th site. Focusing on low-energy physics, we have disregarded the anharmonicities. To further investigate the dynamics of the system, we now rewrite the Lagrangian in terms of the displacements, defined as

$$x_n(t) = n a_0 + \phi_n(t) \tag{2.200}$$

where $\phi_n(t)$ denotes the displacement from the equilibrium position at the n-th site. The Lagrangian now will read:

$$L = \sum_{n=1}^{N} \left[\frac{m}{2} \dot{\phi}_n^2 - \frac{k_0}{2} \left(\phi_{n+1} - \phi_n \right)^2 \right] \tag{2.201}$$

The periodical boundary condition is translated to:

$$\phi_{N+1} = \phi_1 \tag{2.202}$$

We can write the Euler-Lagrange equation for each atom; for instance, let us consider the case of the n-th atom:

$$m \ddot{\phi}_n = -k_s \left(\phi_n - \phi_{n+1} \right) - k_s \left(\phi_n - \phi_{n-1} \right) \tag{2.203}$$

Taking $\phi_n(t) = e^{i\omega t} \phi_n$, we have:

$$\left(-m\omega^2 + 2k_s \right) \phi_n - k_0 \left(\phi_{n+1} + \phi_{n-1} \right) = 0 \tag{2.204}$$

The solution is plane-wave like:

$$\phi_n = \frac{1}{\sqrt{N}} e^{ikna} \quad k = \frac{2\pi m}{Na} \quad N/2 \leq m < N/2 \tag{2.205}$$

We can get the dispersion relations:

$$\omega_k = 2\sqrt{\frac{k_s}{m}} |\sin(ka/2)| \tag{2.206}$$

In the low energy limit, which corresponds to the long wavelength limit, the system exhibits linear dispersion as follows:

$$\omega_k = a\sqrt{\frac{k_0}{m}} k \tag{2.207}$$

Here, v represents the sound wave velocity, which is a result from the collective excitations of the vibrating atomic chain. In the continuum limit, our theoretical framework can be updated with the following transformations:

$$\phi_n = \phi(x), \quad \frac{\phi_{n+1} - \phi_n}{a} = \frac{\partial \phi(x)}{\partial x}, \quad \sum_n \to \frac{1}{a}\int_0^L \mathrm{d}x \tag{2.208}$$

Subsequently, we immediately obtain our Lagrangian density for the displacement field:

$$\mathcal{L}(\dot{\phi}, \phi) = \frac{\rho}{2}\left(\frac{\partial \phi}{\partial t}\right)^2 - \frac{1}{2}\kappa_0 a^2 \frac{\partial^2 \phi}{\partial x^2} \tag{2.209}$$

where $\rho = m/a$ and $\kappa = k/a$. Applying the Euler-Lagrange equation again yields:

$$\rho \frac{\partial^2 \phi}{\partial t^2} - \kappa_0 a^2 \frac{\partial^2 \phi}{\partial x^2} = 0 \tag{2.210}$$

This equation is a standard wave-type partial differential equation. The wave speed is given by:

$$v = a\sqrt{\frac{\kappa_0}{\rho}} = a\sqrt{\frac{k_0}{m}} \tag{2.211}$$

Performing Legendre transformations of the Lagrangian density, we have:

$$\mathcal{H}(\phi, \pi) = \pi\dot{\phi} - \mathcal{L}(\dot{\phi}, \phi) = \frac{1}{2\rho}\pi^2 + \frac{\kappa_s a^2}{2}\left(\partial_x \phi\right)^2 \tag{2.212}$$

where the canonical momentum is:

$$\pi = \partial_{\dot{\phi}} \mathcal{L}(\dot{\phi}, \phi) = \rho\dot{\phi} \tag{2.213}$$

In the canonical quantization method, we preserve the commutation relation:

$$\left[\hat{\pi}(x), \hat{\phi}\left(x'\right)\right] = -i\hbar\delta\left(x - x'\right) \tag{2.214}$$

The Hamiltonian will read:

$$\hat{H} = \int_0^L dx \left[\frac{1}{2\rho}\hat{\pi}^2 + \frac{\kappa_s a^2}{2}\left(\partial_x \hat{\phi}\right)^2\right] \tag{2.215}$$

Now we introduce the Fourier transformation for our field operators:

$$\hat{\phi}_k = \frac{1}{\sqrt{L}}\int_0^L \exp(-ikx)\hat{\phi}(x)\,\mathrm{d}x \quad \hat{\pi}_k = \frac{1}{\sqrt{L}}\int_0^L \exp(ikx)\hat{\pi}(x)\,\mathrm{d}x \tag{2.216}$$

and their inverse Fourier transformation (since the wave-vectors are discrete):

$$\hat{\phi}(x) = \frac{1}{\sqrt{L}} \sum_k e^{ikx} \hat{\phi}_k \quad \hat{\pi}(x) = \frac{1}{\sqrt{L}} \sum_k e^{-ikx} \hat{\pi}_k \tag{2.217}$$

From Eq. (2.6.1), we can see that:

$$\left[\hat{\pi}_k, \hat{\phi}_{k'}\right] = -i\hbar\delta_{kk'} \tag{2.218}$$

If we now write the Hamiltonian in Fourier space, we need to solve:

$$\int_0^L (\partial\hat{\phi})^2 \, \mathrm{d}x = \sum_{k,k'} \left(ik\hat{\phi}_k\right)\left(ik'\hat{\phi}_{k'}\right) \frac{1}{L} \int_0^L e^{i(k+k')x} \, \mathrm{d}x = \sum_k k^2 \hat{\phi}_k \hat{\phi}_{-k} \tag{2.219}$$

Then our Hamiltonian will read:

$$\hat{H} = \sum_k \left[\frac{1}{2\rho}\hat{\pi}_k\hat{\pi}_{-k} + \frac{1}{2}\rho\omega_k^2\hat{\phi}_k\hat{\phi}_{-k}\right] \tag{2.220}$$

where the linear dispersion is preserved:

$$\omega_k = vk \tag{2.221}$$

From this Hamiltonian, as expressed in Eq. (2.220), we observe that the one-dimensional atomic chain can be equivalently described by a series of harmonic oscillators, each with a distinct frequency. This model reveals that each oscillator mode encompasses all N atoms in the chain, thereby highlighting the collective excitation nature of the system.

Drawing from the idea of using ladder operators to represent momenta and positions, we can write down our creation and annihilation operators for phonons:

$$\hat{a}_k \equiv \sqrt{\frac{m\omega_k}{2\hbar}}\left(\hat{\phi}_k + \frac{i}{m\omega_k}\hat{\pi}_{-k}\right) \tag{2.222}$$

$$\hat{a}_k^\dagger \equiv \sqrt{\frac{m\omega_k}{2\hbar}}\left(\hat{\phi}_{-k} - \frac{i}{m\omega_k}\hat{\pi}_k\right) \tag{2.223}$$

where:

$$\left[\hat{a}_k, \hat{a}_{k'}^\dagger\right] = \delta_{kk} \quad [\hat{a}_k, \hat{a}_{k'}] = \left[\hat{a}_k^\dagger, \hat{a}_{k'}^\dagger\right] = 0 \tag{2.224}$$

Then our phonon Hamiltonian will become to:

$$\hat{H} = \sum_k \hbar\omega_k \left(\hat{a}_k^\dagger\hat{a}_k + \frac{1}{2}\right) \tag{2.225}$$

The canonical commutation relations indicate that phonons are bosons, as they obey Bose-Einstein statistics. Their number states can be written as:

$$|\Psi\rangle = \frac{1}{\sqrt{\prod_i n_i!}} \left(\hat{a}^\dagger_{k_1}\right)^{n_1} \left(\hat{a}^\dagger_{k_2}\right)^{n_2} \cdots |0\rangle \tag{2.226}$$

From Eq. (2.222) and Eq. (2.223), we can work out the displacement field operators in position space:

$$\hat{\phi}(x) = \sqrt{\frac{\hbar}{2\rho V\omega}} \left(\hat{a}_k \exp(ikx - i\omega t) + \hat{a}^\dagger_{-k} \exp(ikx + i\omega t)\right) \tag{2.227}$$

Which will be used again when we derive the hole-phonon interactions. Our derivations above have shown that the vibrations of our solids can be conceptualized as particles called phonons. Therefore, any changes in electronic properties related to lattice vibrations can be translated into a problem of phonon interactions. The well-established many-body theory of phonons allows us to treat them as quasi-particles, thereby avoiding complicated reasoning about microscopic degrees of freedom in a low-energy regime. There are several important features to notice. Firstly, at low energies with long phonon wavelengths, when $k \to 0$, phonon excitations can have vanishingly small energy, referred to as massless particles. This is a generic consequence of the Nambu-Goldstone theorem, where breaking a continuous symmetry (as per Bloch theorem) generates massless collective excitations. However, it is important to note that since our discussion is limited to a mono-atomic system, we did not encounter optical phonons, which are not Nambu-Goldstone bosons. They are consequences of the diatomic structure in the atomic chain. A typical phonon spectrum is shown in the Fig. 2.5

2.6.2 Hole-phonon interactions

To derive the hole-phonon interactions in Group IV elements, we must consider several features of phonons in these elements to simplify the calculations. Firstly, since Group IV semiconductor systems are mono-atomic, we do not need to consider any hole-phonon interactions in the optical branch. Secondly, as germanium and silicon systems are non-polar

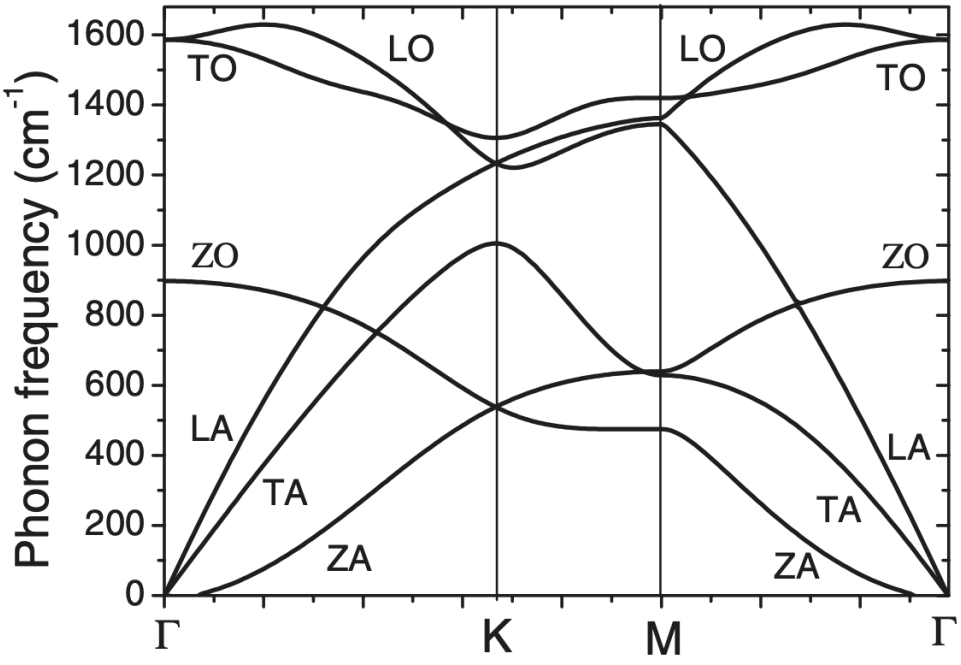

Figure 2.5: **Phonon spectrum of the 2D graphene** The phonon spectrum of the 2D graphene. We have labelled the three different acoutisc phonon branches in the figure, the longitudinal phonon dipsersion is denoted as LA, the first transversal phonon dispersion is denoted as TA, the second transveral phonon dipsersion is denoted as ZA. They are the consequence of the Nambu-Goldstone theorem, which will be the main focus of our work. There are also three branches of optical phonons labelled by TO, LO, and ZO respectively. The original source of this figure is Ref. [559].

molecules, they will not induce any piezoelectric phonons. This simplifies the estimation of relaxation decoherence times [56]. Based on these two features, our hole-phonon interactions will solely involve the local displacements of the lattice. In the last subsection, we did not discuss anything in a three-dimensional lattice. Now, we will include all three polarization directions a phonon can have in such a lattice. Firstly, to determine the direction of polarizations, we select the longitudinal polarization, which is parallel to the phonon wave-vector (To distinguish between the wave-vector $\boldsymbol{k}$ and the phonon wave-vector $\boldsymbol{q}$, we will use $\boldsymbol{q}$ to denote the phonon in the following derivations, unless specified deliberately):

$$\hat{\boldsymbol{e}}_l = q^{-1}\left(q_x, q_y, q_z\right) = \left(\sin\theta\cos\varphi, \sin\theta\sin\varphi, \cos\theta\right) \tag{2.228}$$

In this context, θ is the azimuthal angle, and φ is the polar angle. We use q to denote the magnitude of the phonon wave-vector. The components of a phonon wave-vector in Cartesian coordinates are q_x, q_y, and q_z. To obtain the other two transverse branches, we rotate the frame by $\pi/2$, yielding two orthogonal directions. For the Transverse Acoustic Branch 1, this involves a rotation of θ by $\pi/2$.

$$\hat{\boldsymbol{e}}_{t_1} = q^{-1}\left(q_x^2+q_y^2\right)^{-\frac{1}{2}}\left(q_x q_z, q_y q_z, -\left(q_x^2+q_y^2\right)\right) = \left(\cos\theta\cos\varphi, \cos\theta\sin\varphi, -\sin\theta\right) \tag{2.229}$$

Transverse Acoustic Branch 2 is obtained by rotating the ϕ by $\pi/2$:

$$\hat{\boldsymbol{e}}_{t_2} = \left(q_x^2+q_y^2\right)^{-\frac{1}{2}}\left(q_y, -q_x, 0\right) = \left(-\sin\varphi, \cos\varphi, 0\right) \tag{2.230}$$

$$\hat{\boldsymbol{e}}_{t_2} = \left(q_x^2+q_y^2\right)^{-\frac{1}{2}}\left(q_y, -q_x, 0\right) = \left(-\sin\varphi, \cos\varphi, 0\right) \tag{2.231}$$

The form of the hole-phonon interaction is analogous to the Bir-Pikus Hamiltonian. This similarity arises because both are derived from the $\boldsymbol{k}\cdot\boldsymbol{p}$ theory, which describes the local deformation of the lattice. However, a key distinction should be noted: while the Bir-Pikus Hamiltonian focuses on the strain applied by the external environment, the hole-phonon Hamiltonian is intrinsic to the solid, characterized by local deformations as detailed in

Eq. (2.227). The structure of the hole-phonon interaction Hamiltonian is:

$$H_{\mathrm{hp},\alpha} = \begin{bmatrix} P_{\varepsilon,\alpha}+Q_{\varepsilon,\alpha} & 0 & -S_{\varepsilon,\alpha} & R_{\varepsilon,\alpha} & -\frac{1}{\sqrt{2}}S_{\varepsilon,\alpha} & \sqrt{2}R_{\varepsilon,\alpha} \\ 0 & P_{\varepsilon,\alpha}+Q_{\varepsilon,\alpha} & R_{\varepsilon}^{\alpha *} & S_{\varepsilon}^{\alpha *} & -\sqrt{2}R_{\varepsilon}^{\alpha *} & -\frac{1}{\sqrt{2}}S_{\varepsilon}^{\alpha *} \\ -S_{\varepsilon}^{\alpha *} & R_{\varepsilon,\alpha} & P_{\varepsilon,\alpha}-Q_{\varepsilon,\alpha} & 0 & -\sqrt{2}Q_{\varepsilon,\alpha} & \sqrt{\frac{3}{2}}S_{\varepsilon,\alpha} \\ R_{\varepsilon}^{\alpha *} & S_{\varepsilon,\alpha} & 0 & P_{\varepsilon,\alpha}-Q_{\varepsilon,\alpha} & \sqrt{\frac{3}{2}}S_{\varepsilon}^{\alpha *} & \sqrt{2}Q_{\varepsilon,\alpha} \\ -\frac{1}{\sqrt{2}}S_{\varepsilon}^{\alpha *} & -\sqrt{2}R_{\varepsilon,\alpha} & -\sqrt{2}Q_{\varepsilon}^{\alpha *} & \sqrt{\frac{3}{2}}S_{\varepsilon,\alpha} & P_{\varepsilon,\alpha} & 0 \\ \sqrt{2}R_{\varepsilon}^{\alpha *} & -\frac{1}{\sqrt{2}}S_{\varepsilon,\alpha} & \sqrt{\frac{3}{2}}S_{\varepsilon}^{\alpha *} & \sqrt{2}Q_{\varepsilon}^{\alpha *} & 0 & P_{\varepsilon,\alpha} \end{bmatrix} \tag{2.232}$$

We use the subscript α to denote the considered polarization, where $\alpha \in l, t_1, t_2$. Having determined the form of each element in Eq. (2.6.1), our next step is to evaluate the strains. For instance:

$$P_{\varepsilon,\alpha} = -a_v\left(\varepsilon_{xx}+\varepsilon_{yy}+\varepsilon_{zz}\right) \tag{2.233}$$

Where a_v represents the hydrostatic deformation potential constant, the local deformation is described by the derivative of the displacement field $\boldsymbol{u}(\boldsymbol{r})$:

$$\varepsilon_{i,j} = \frac{1}{2}\left(\frac{\partial u_i(\boldsymbol{x})}{\partial x_j}+\frac{\partial u_j(\boldsymbol{x})}{\partial x_i}\right) \tag{2.234}$$

The displacement field operator was previously introduced in Eq. (2.227). Now, we simply need to use its three-dimensional version and multiply it with a polarization vector.

$$\boldsymbol{u}_\alpha = \hat{\phi}(x)_\alpha(\boldsymbol{x},t)\hat{\boldsymbol{e}}_\alpha = \sqrt{\frac{\hbar}{2\rho V\omega_\alpha}}\left(\hat{a}_{\alpha,\boldsymbol{q}}\exp(i\boldsymbol{q}\cdot\boldsymbol{x}-i\omega t)+\hat{a}^\dagger_{\alpha,-\boldsymbol{q}}\exp(i\boldsymbol{q}\cdot\boldsymbol{x}+i\omega t)\right)\hat{\boldsymbol{e}}_\alpha \tag{2.235}$$

To evaluate the strain, we simply insert Eq. (2.235) into Eq. (2.234). This substitution yields the following expression:

$$\varepsilon_\alpha(\boldsymbol{x},t) = iq\sqrt{\frac{\hbar}{2\rho V\omega_\alpha}}\left(\hat{a}_{\alpha,\boldsymbol{q}}\exp(i\boldsymbol{q}\cdot\boldsymbol{x}-i\omega t)+\hat{a}^\dagger_{\alpha,-\boldsymbol{q}}\exp(-i\boldsymbol{q}\cdot\boldsymbol{x}+i\omega t)\right)\epsilon_\alpha \tag{2.236}$$

where ϵ is a matrix, in Cartesian coordinates with $\hat{\boldsymbol{q}} = (q_x/q, q_y/q, q_z/q)$, we enumerate all the possible ϵ matrices for different polarization directions:

$$\epsilon_l = \frac{1}{2}\begin{bmatrix} 2\frac{q_x^2}{q^2} & 2\frac{q_xq_y}{q^2} & 2\frac{q_xq_z}{q^2} \\ 2\frac{q_yq_x}{q^2} & 2\frac{q_y^2}{q^2} & 2\frac{q_yq_z}{q^2} \\ 2\frac{q_zq_x}{q^2} & 2\frac{q_zq_y}{q^2} & 2\frac{q_z^2}{q^2} \end{bmatrix} = \begin{bmatrix} \frac{q_x^2}{q^2} & \frac{q_xq_y}{q^2} & \frac{q_xq_z}{q^2} \\ \frac{q_yq_x}{q^2} & \frac{q_y^2}{q^2} & \frac{q_yq_z}{q^2} \\ \frac{q_zq_x}{q^2} & \frac{q_zq_y}{q^2} & \frac{q_z^2}{q^2} \end{bmatrix} \tag{2.237}$$

$$\epsilon_{t_1} = \frac{1}{2}\begin{bmatrix} 2\dfrac{q_x^2 q_z}{q^2\sqrt{q_x^2+q_y^2}} & 2\dfrac{q_x q_y q_z}{q^2\sqrt{q_x^2+q_y^2}} & \dfrac{q_x q_z^2 - q_x q_x^2 - q_x q_y^2}{q^2\sqrt{q_x^2+q_y^2}} \\ 2\dfrac{q_x q_y q_z}{q^2\sqrt{q_x^2+q_y^2}} & 2\dfrac{q_y^2 q_z}{q^2\sqrt{q_x^2+q_y^2}} & \dfrac{q_y q_z^2 - q_y q_x^2 - q_y q_y^2}{q^2\sqrt{q_x^2+q_y^2}} \\ \dfrac{q_x q_z^2 - q_x q_x^2 - q_x q_y^2}{q^2\sqrt{q_x^2+q_y^2}} & \dfrac{q_y q_z^2 - q_y q_x^2 - q_y q_y^2}{q^2\sqrt{q_x^2+q_y^2}} & -2\dfrac{q_z(q_x^2+q_y^2)}{q^2\sqrt{q_x^2+q_y^2}} \end{bmatrix} \tag{2.238}$$

$$\epsilon_{t_2} = \frac{1}{2}\begin{bmatrix} -2\dfrac{q_x q_y}{q\sqrt{q_x^2+q_y^2}} & \dfrac{q_x^2-q_y^2}{q\sqrt{q_x^2+q_y^2}} & -\dfrac{q_y q_z}{q\sqrt{q_x^2+q_y^2}} \\ \dfrac{q_x^2-q_y^2}{q\sqrt{q_x^2+q_y^2}} & 2\dfrac{q_x q_y}{q\sqrt{q_x^2+q_y^2}} & \dfrac{q_x q_z}{q\sqrt{q_x^2+q_y^2}} \\ -\dfrac{q_y q_z}{q\sqrt{q_x^2+q_y^2}} & \dfrac{q_x q_z}{q\sqrt{q_x^2+q_y^2}} & 0 \end{bmatrix} \tag{2.239}$$

Using spherical coordinates can be beneficial for certain calculations, so we have also listed them here:

$$\epsilon_l = \frac{1}{2}\begin{bmatrix} 2\sin^2\theta\cos^2\varphi & \sin^2\theta\sin 2\varphi & \sin 2\theta\cos\varphi \\ \sin^2\theta\sin 2\varphi & 2\sin^2\theta\sin^2\varphi & \sin 2\theta\sin\varphi \\ \sin 2\theta\cos\varphi & \sin 2\theta\sin\varphi & 2\cos^2\theta \end{bmatrix} \tag{2.240}$$

$$\epsilon_{t_1} = \frac{1}{2}\begin{bmatrix} \sin 2\theta\cos^2\varphi & \frac{1}{2}\sin 2\theta\sin 2\varphi & \cos 2\theta\cos\varphi \\ \frac{1}{2}\sin 2\theta\sin 2\varphi & \sin 2\theta\sin^2\varphi & \cos 2\theta\sin\varphi \\ \cos 2\theta\cos\varphi & \cos 2\theta\sin\varphi & -\sin 2\theta \end{bmatrix} \tag{2.241}$$

$$\epsilon_{t_2} = \frac{1}{2}\begin{bmatrix} -\sin\theta\sin 2\varphi & \sin\theta\cos 2\varphi & -\cos\theta\sin\varphi \\ \sin\theta\cos 2\varphi & \sin\theta\sin 2\varphi & \cos\theta\cos\varphi \\ -\cos\theta\sin\varphi & \cos\theta\cos\varphi & 0 \end{bmatrix} \tag{2.242}$$

Taking the longitudinal polarization direction as an example, we have:

$$\varepsilon_{xx} = i\frac{q_x^2}{q}\sqrt{\frac{\hbar}{2\rho V\omega_\alpha}}\left(\hat{a}_{\alpha,\boldsymbol{q}}\exp(i\boldsymbol{q}\cdot\boldsymbol{x}-i\omega t) + \hat{a}^\dagger_{\alpha,-\boldsymbol{q}}\exp(i\boldsymbol{q}\cdot\boldsymbol{x}+i\omega t)\right) \tag{2.243}$$

We are now in a position to reformulate the hole-phonon interaction Hamiltonian as follows:

$$H_{hp,\alpha} = D_{xx}\varepsilon_{\alpha,xx} + D_{xy}\varepsilon_{\alpha,xy} + D_{xz}\varepsilon_{\alpha,xz} + D_{yy}\varepsilon_{\alpha,yy} + D_{yz}\varepsilon_{\alpha,yz} + D_{zz}\varepsilon_{\alpha,zz} \tag{2.244}$$

We have omitted the polarization indices for the D matrices, as they remain identical across different polarization directions.

$$D_{11} = \begin{bmatrix} -\left(a_v + \frac{b_v}{2}\right) & 0 & 0 & \frac{\sqrt{3}}{2}b_v & 0 & \sqrt{\frac{3}{2}}b_v \\ 0 & -\left(a_v + \frac{b_v}{2}\right) & \frac{\sqrt{3}}{2}b_v & 0 & -\sqrt{\frac{3}{2}}b_v & 0 \\ 0 & \frac{\sqrt{3}}{2}b_v & -\left(a_v - \frac{b_v}{2}\right) & 0 & \frac{b_v}{\sqrt{2}} & 0 \\ \frac{\sqrt{3}}{2}b_v & 0 & 0 & -\left(a_v - \frac{b_v}{2}\right) & 0 & -\frac{b_v}{\sqrt{2}} \\ 0 & -\sqrt{\frac{3}{2}}b_v & \frac{b_v}{\sqrt{2}} & 0 & -a_v & 0 \\ \sqrt{\frac{3}{2}}b_v & 0 & 0 & -\frac{b_v}{\sqrt{2}} & 0 & -a_v \end{bmatrix} \tag{2.245}$$

$$D_{12} = \begin{bmatrix} 0 & 0 & 0 & -id_v & 0 & -i\sqrt{2}d_v \\ 0 & 0 & id_v & 0 & -i\sqrt{2}d_v & 0 \\ 0 & -id_v & 0 & 0 & 0 & 0 \\ id_v & 0 & 0 & 0 & 0 & 0 \\ 0 & i\sqrt{2}d_v & 0 & 0 & 0 & 0 \\ i\sqrt{2}d_v & 0 & 0 & 0 & 0 & 0 \end{bmatrix} \tag{2.246}$$

$$D_{13} = \begin{bmatrix} 0 & 0 & d_v & 0 & \frac{d_v}{2} & 0 \\ 0 & 0 & 0 & -d_v & 0 & \frac{d_v}{\sqrt{2}} \\ d_v & 0 & 0 & 0 & 0 & -\sqrt{\frac{3}{2}}d_v \\ 0 & -d_v & 0 & 0 & -\sqrt{\frac{3}{2}} & 0 \\ \frac{d_v}{\sqrt{2}} & 0 & 0 & -\sqrt{\frac{3}{2}} & 0 & 0 \\ 0 & \frac{d_v}{\sqrt{2}} & -\sqrt{\frac{3}{2}}d_v & 0 & 0 & 0 \end{bmatrix} \tag{2.247}$$

$$D_{22} = \begin{bmatrix} -\left(a_v + \frac{b_v}{2}\right) & 0 & 0 & -\frac{\sqrt{3}}{2}b_v & 0 & -\sqrt{\frac{3}{2}}b_v \\ 0 & -\left(a_v + \frac{b_v}{2}\right) & -\frac{\sqrt{3}}{2}b_v & 0 & \sqrt{\frac{3}{2}}b_v & 0 \\ 0 & -\frac{\sqrt{3}}{2}b_v & -\left(a_v - \frac{b_v}{2}\right) & 0 & \frac{b_v}{\sqrt{2}} & 0 \\ -\frac{\sqrt{3}}{2}b_v & 0 & 0 & -\left(a_v - \frac{b_v}{2}\right) & 0 & -\frac{b_v}{\sqrt{2}} \\ 0 & \sqrt{\frac{3}{2}}b_v & \frac{b_v}{\sqrt{2}} & 0 & -a_v & 0 \\ -\sqrt{\frac{3}{2}}b_v & 0 & 0 & -\frac{b_v}{\sqrt{2}} & 0 & -a_v \end{bmatrix} \tag{2.248}$$

$$D_{23} = \begin{bmatrix} 0 & 0 & -id_v & 0 & -i\frac{d_v}{\sqrt{2}} & 0 \\ 0 & 0 & 0 & -id_v & 0 & i\frac{d_v}{\sqrt{2}} \\ id_v & 0 & 0 & 0 & 0 & i\sqrt{\frac{3}{2}}d_v \\ 0 & id_v & 0 & 0 & -i\sqrt{\frac{3}{2}}d_v & 0 \\ i\frac{d_v}{\sqrt{2}} & 0 & 0 & i\sqrt{\frac{3}{2}}d_v & 0 & 0 \\ 0 & -i\frac{d_v}{\sqrt{2}} & -i\sqrt{\frac{3}{2}}d_v & 0 & 0 & 0 \end{bmatrix} \tag{2.249}$$

$$D_{33} = \begin{bmatrix} -(a_v - b_v) & 0 & 0 & 0 & 0 & 0 \\ 0 & -(a_v - b_v) & 0 & 0 & 0 & 0 \\ 0 & 0 & -(a_v + b_v) & 0 & -\sqrt{2}b_v & 0 \\ 0 & 0 & 0 & -(a_v + b_v) & 0 & \sqrt{2}b_v \\ 0 & 0 & -\sqrt{2}b_v & 0 & -a_v & 0 \\ 0 & 0 & 0 & \sqrt{2}b_v & 0 & -a_v \end{bmatrix} \tag{2.250}$$

In this way, our hole-phonon interaction Hamiltonian can be written as

$$H_{hp,\alpha} = \sum_{(i,j)} D_{ij}\varepsilon_{ij}\left[iq\sqrt{\frac{\hbar}{2\rho V\omega_\alpha}}\left(\hat{a}_{\alpha,\boldsymbol{q}}\exp(i\boldsymbol{q}\cdot\boldsymbol{x} - i\omega t) + \hat{a}^\dagger_{\alpha,-\boldsymbol{q}}\exp(i\boldsymbol{q}\cdot\boldsymbol{x} + i\omega t)\right)\right] \tag{2.251}$$

where (i, j) denotes the non-repeating index pairs such as xx, xy, xz, implying that pairs like yx, yz are excluded from the summation.

We only need to consider the hole-phonon interaction induced relaxation time, which is an advantage of semiconductor quantum dot hole spin qubits based on Group IV elements. In group III-V elements, we have to consider the piezo-electric effect induced phonons due to their non-polar nature of the crystal structure; the in-homogeneous distortion of the lattice can create an internal electric fields, which will further affect the carrier band structures.

2.6.3 Phonon induced docoherence time

The phonon-induced decoherence time, T_1, can be estimated from the hole-phonon interaction Hamiltonian using Fermi's golden rule. This estimation considers that the qubit interacts with the vibrations of the solid, or equivalently, with a thermal bath of bulk

acoustic phonons with energy $\hbar\omega_\alpha$. Qubit relaxation occurs when a phonon carries energy equal to the energy splitting between the qubit ground state and its first excited state. We denote the first excited state of the qubit as $|\mathbb{1}\rangle$ and the ground state as $|\mathbb{0}\rangle$. We will not specify the explicit form of these states, as they are device-specific. Examples will be provided in the following chapters.

First, we examine the phonon absorption process, wherein a phonon is absorbed by the qubit, facilitating the transition from the ground state $|0\rangle$ to the excited state $|1\rangle$:

$$\Gamma_+ = \frac{2\pi}{\hbar}\sum_\alpha \int \|\langle \mathbb{0}, N_\alpha(\boldsymbol{q})|H_{hp,\alpha}|\mathbb{1}, N_\alpha(\boldsymbol{q})+1\rangle\|^2 \delta(E_{\mathbb{1}} - E_{\mathbb{0}} - \hbar\omega_\alpha)\frac{V}{(2\pi)^2}\mathrm{d}^3q \tag{2.252}$$

where N_α represents the phonon occupation number along the polarization direction α, following the Bose-Einstein statistics; and $V/(2\pi)^3$ denotes the density of states in the reciprocal space. The relaxation rate for the phonon emission process can be expressed as follows:

$$\Gamma_- = \frac{2\pi}{\hbar}\sum_\alpha \int \|\langle \mathbb{1}, N_\alpha(\boldsymbol{q})+1|H_{hp,\alpha}|\mathbb{0}, N_\alpha(\boldsymbol{q})\rangle\|^2 \delta(E_{\mathbb{1}} - E_{\mathbb{0}} - \hbar\omega_\alpha)\frac{V}{(2\pi)^2}\mathrm{d}^3q \tag{2.253}$$

The total relaxation rate is given by:

$$\Gamma = \Gamma_+ + \Gamma_- \tag{2.254}$$

From these expressions, it is evident that the behavior of the phonon-induced relaxation time is quite complex. It depends on several factors: the shape of the qubit wave-functions ($|0\rangle$ and $|1\rangle$, which already incorporate spin-orbit physics), the temperature (as reflected in $N_\alpha(\boldsymbol{q})$), and the phonon propagation speeds (via $\omega_\alpha = qv_\alpha$). Additionally, it is important to note that our current formalism is based on bulk structures. For one-dimensional nanowires or two-dimensional thin films, we need to modify our expressions by applying the correct phonon boundary conditions and replacing the integrations with summations.

In recent experiments, long relaxation times 30 ms have been observed in Ref. [275], a germanium semiconductor quantum dot hole spin qubit system. Now, more scientisits are working on the long relaxation time in higher temperature regimes, which is the next stage for scalable quantum computations.

2.7 Charge dephasing

Hole spin qubits benefit from rapid electrical manipulation via spin-orbit couplings, however, they are also susceptible to electrical noise, leading to couplings between the qubit and stray fields and defects within the device [323, 55, 68]. In the last section, we focused on phonon relaxation time, treating our qubit states as a two-level system, and estimated the timescale of information loss in the qubit. Concurrently, there are two other important timescales: the dephasing times, commonly denoted as T_2 and T_2^* which have their roots in nuclear magnetic resonance experiments as we introduced in Section. 1.1.

In this section, we will analyze common dephasing mechanisms present in Group IV hole spin qubits based on SQDs. Initially, we introduce the fundamental concepts of T_2, known as the transverse dephasing time due to $\hat{z}$-noise, measurable via Hahn echo experiments. Subsequently, we will discuss T_2^*, which accounts for the spatial inhomogeneous broadening of the external field and can be measured using Ramsey experiments [430]. After introducing these concepts, our focus shifts to the T_2^* dephasing time, discussing its origins in SQD systems. Finally, we present the necessary formulas to estimate the dephasing time for Group IV hole spin qubits based on SQDs and comment on improving dephasing times guided by our formulations.

2.7.1 Transverse dephasing time

In our model developed in Sec. 2.5, we established that the spin polarization precesses with the Larmor frequency $\omega = -\gamma B_z$. An intriguing question arises when we consider adding a noise term, $\delta B_z(t)$, to the out-of-plane magnetic field (which serves as the quantization axis). This scenario is highly relevant in all semiconductor devices, with potential noise sources including paramagnetic impurities, surrounding nuclear spins, and temperature fluctuations [30, 415, 560, 387, 561, 344, 448]. To comprehend how this noise influences our precession dynamics, we need to incorporate a noise term like:

$$H = -\gamma\hbar(B_z + \delta B_z(t))\sigma_z \tag{2.255}$$

As the correction due to the noise term is linear, the results we derived in Sec. 2.5 will simply incorporate an additional noise term:

$$\omega_0 = -\gamma B_z \quad \delta\omega(t) = -\gamma \delta B_z(t) \tag{2.256}$$

To simplify the algebra, let us assume that we can prepare our state at $t = 0$ as follows:

$$|\Psi; t = 0\rangle = \frac{1}{\sqrt{2}} |\uparrow\rangle + \frac{1}{\sqrt{2}} |\downarrow\rangle \tag{2.257}$$

After free evolutions:

$$|\Psi; t\rangle = \frac{1}{\sqrt{2}} \left[\exp\left(-\frac{i}{2}\omega_0 t - \frac{i}{2} \int_0^t \delta\omega(t')\, \mathrm{d}t' \right) |\uparrow\rangle + \exp\left(\frac{i}{2}\omega_0 t + \frac{i}{2} \int_0^t \delta\omega(t')\, \mathrm{d}t' \right) |\downarrow\rangle \right] \tag{2.258}$$

Applying the frame of reference transformation techniques introduced in Sec. 2.5-2.5.3, we obtain the following result:

$$|\Psi; t\rangle = \frac{1}{\sqrt{2}} \left[\exp\left(-\frac{i}{2}\delta\Omega(t) \right) |\uparrow\rangle + \exp\left(\frac{i}{2}\delta\Omega(t) \right) |\downarrow\rangle \right] \tag{2.259}$$

where:

$$\delta\Omega(t) = \int_0^t \delta\omega(t')\, \mathrm{d}t' \tag{2.260}$$

Now, to gain a deeper understanding of the behaviors of the transverse dephasing time, it is necessary to specify a model for our noise spectrum, particularly defining how $\delta\omega(t)$ behaves. For a basic estimation, let us assume that $\delta\omega(t)$ possesses an infinitesimally short correlation time. Under this assumption, the noise spectrum $S_{\delta\omega(t)}$ would resemble random white noise. Consequently, the phase as described in Eq. (2.260) would undergo a non-stationary random walk diffusion, akin to the Wiener-Levy process shown in Fig. 2.6.

If our interest is confined to the correlations within a single gate operation time T, then we can deduce:

$$\langle \delta\Omega(t+\tau)\delta\Omega(t) \rangle = \int_0^{t+\tau} \int_0^t \langle \Delta\omega\left(t'\right) \Delta\omega\left(t''\right) \rangle \, dt' dt'' \tag{2.261}$$

To evaluate the correlation, we must utilize the properties of the noise, specifically its statistical stationarity and ergodicity. Consequently, we can express the correlation as a

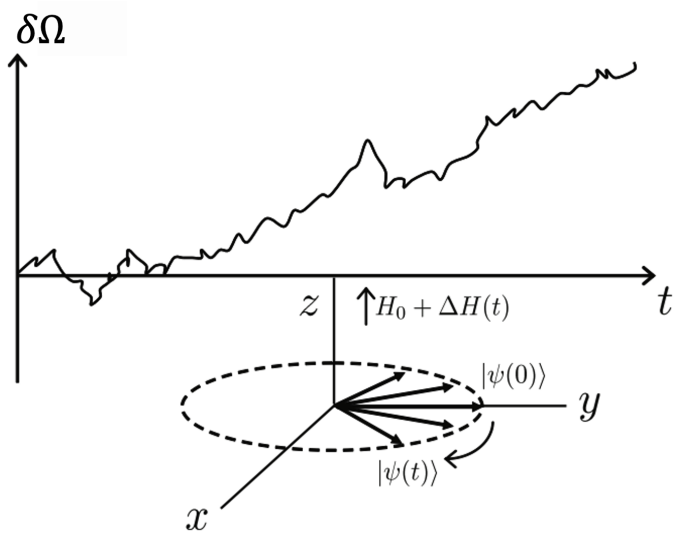

Figure 2.6: **Wiener-Levy process in dephasings**. A non-stationary random walk means that the mean value and the standard deviations can vary with time. In this white noise mode, the phase is increasing with time and the state will loss its coherence. The original source of this figure is Ref. [558].

time average:

$$\begin{aligned}\left\langle \delta\omega\left(t'\right)\delta\omega\left(t''\right)\right\rangle &= \lim_{T\to\infty}\frac{1}{T}\int_{-\frac{T}{2}}^{\frac{T}{2}}\delta\omega(t+\tau)\delta\omega(t)dt \\ &= \frac{1}{2\pi}\int_0^\infty S_{\delta\omega(t)}(\Lambda)\cos(\Lambda\tau)\,\mathrm{d}\Lambda\end{aligned} \tag{2.262}$$

Then we have:

$$\left\langle \delta\omega(t)^2\right\rangle = \frac{1}{\pi}S_{\delta\omega(t)}(\Lambda=0)\int_0^\infty\frac{1}{\Lambda^2}[1-\cos(\Lambda t)]\,\mathrm{d}\Lambda = \frac{1}{2}S_{\delta\omega(t)}(\Lambda=0)t \tag{2.263}$$

Again, we have assumed that $S_{\delta\omega}$ is a white noise so that only the zero-frequency spectral density will be relavant. If we introduce a phase diffusion constant $D_{\delta\Omega}$ by:

$$\left\langle \delta\Omega(t)^2\right\rangle = 2D_{\delta\Omega}t \Rightarrow D_{\delta\Omega} = \frac{1}{4}S_{\delta\omega}(\Lambda=0) \tag{2.264}$$

under the assumption that $S_{\delta(\omega)}$ represents white noise, only the zero-frequency spectral density is relevant. We can introduce a phase diffusion constant, $D_{\delta\Omega}$, defined as follows:

$$\langle\uparrow|\rho|\downarrow\rangle = \frac{1}{2}\left\langle e^{i\delta\Omega(t)}\right\rangle = \frac{1}{2}\exp(-D_{\delta\Omega}(t)) \tag{2.265}$$

which is a exponentially decaying term, with a time constant:

$$T_2 = \frac{1}{D_{\delta\Omega}} = \frac{4}{S_{\delta\omega}(\Lambda=0)} \tag{2.266}$$

This decay constant of time, based on the simplest white noise model, reveals the central idea of the transverse dephasing time T_2: the noise in the $\hat{z}$-direction will destroy the coherence of the phase. In our simple calculations, we have only considered a spatially homogeneous DC magnetic field B_z. However, if it becomes an inhomogeneous DC magnetic field in a system with multiple qubits, various Larmor frequencies will exist in the system, leading to another dephasing effect across the entire system. These spatial inhomogeneities in the DC field broadening are referred to as T_2^*, which will be the focus of our study, a difference between the two dephasing time constant can be demonstrated in Fig. 2.7.

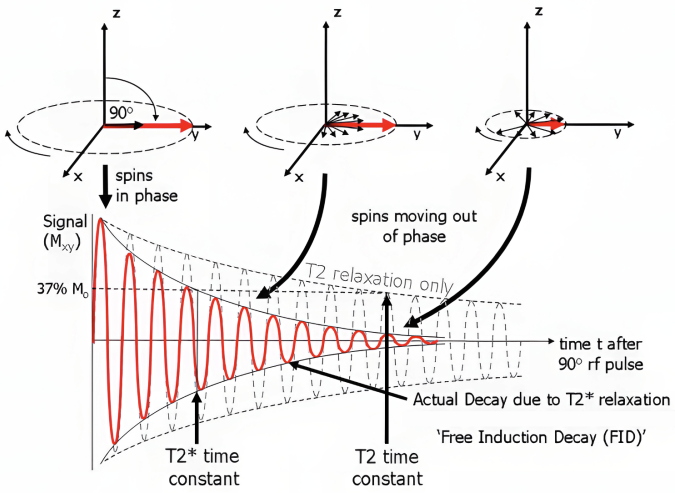

Figure 2.7: T_2 **dephasing time and** T_2^* **dephasing time.** When t=0, our system is in phase cempeletely, due to the coupling between the noise and the system, the dephasing start to appear. The original source of this figure is Ref. [418].

To estimate realistic dephasing times, several extra efforts can be made. Firstly, we can explore various other noise spectrum models to describe the magnetic environmental noise [540]. For example, $1/f$ noise will dominate at low frequencies due to random telegraph noise [141, 87, 409, 363]. At higher frequencies, quantum fluctuations become more significant. In the following sections, we will concentrate on the low-frequency random telegraph noise and delve into the specifics of this noise in Group IV hole spin qubits based on SQDs.

2.7.2 Random telegraph noise

In the semiconductor fabrication process, reducing charge defects remains a challenging task. This is particularly critical in devices with few carriers, such as silicon metal-oxide-semiconductor-field-effect transistors (MOSFETs), where defects can trap and subsequently re-emit carriers [514]. This discrete switching in the resistance of devices is known as random telegraph noise (RTN). Studies on RTN have demonstrated that it can be a microscopic origin of the low-frequency $1/f$ noise in these devices [21]. Recent experiments utilizing conductance techniques have identified two classes of interface defects: the first class includes those typically observed at the interface, characterized by a single time constant; the second class consists of defects residing in the oxide layer, exhibiting a wide range of time constants and contributing to the $1/f$ noise. For example, in Semiconductor Quantum Dots (SQDs), the dangling bond charge traps, often resulting from lattice parameter mismatches in heterostructure fabrication, can be a source of RTN. Similarly, dipole charge defects due to polar molecules, like in SiO_2, also contribute to RTN.

A standard RTN observed in devices will look like Fig. 2.8. We can model the high-current state of this spectrum as state 1, and the low-current state as 0. Now we demonstrate that the discrete switching of the resistance is a Poisson process [34, 176]. Firstly, we denote the transition probability from state 1 to 0 is given by $1/\tau_{1\to0}$, the transition probability from state 0 to 1 is given by $1/\tau_{0\to1}$. The transitions is instantaneous.

Consider the probability expressed as $p(t)\,\mathrm{d}t$, which corresponds to the scenario where the system remains in state 1 during the interval t and then transitions between t and $t+\mathrm{d}t$. Meanwhile, the probability denoted as $A(t)$ represents the case where the system experiences no transition during the time interval t. Therefore, the probability $p(t)$ can be described as the product of $A(t)$ and $\frac{1}{\tau_{1\to0}}$.

$$p_1(t) = \frac{A(t)}{\tau_{1\to0}} \tag{2.267}$$

The probability that there is no transition during the interval $t+\mathrm{d}t$ can be expressed as

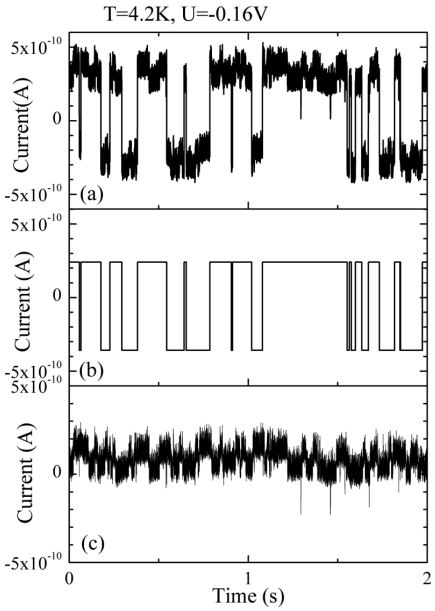

Figure 2.8: **Random telegraph noise signal measured in a MOS device**. **a)**. The signal measured from the device. **b)**. Time averaging of the signal. **c)**. The residual plot of the random telegraph noise signal. The original source of this figure is Ref. [402].

follows:

$$A(t+\mathrm{d}t) = A(t) \times \left(1 - \frac{\mathrm{d}t}{\tau_{1\to 0}}\right) \tag{2.268}$$

Namely, the product of not having transition in time interval t and not having transition sequentially in dt interval. We can rewrite Eq. (2.268) as:

$$\frac{\mathrm{d}A(t)}{\mathrm{d}t} = -\frac{A(t)}{\tau_{1\to 0}} \tag{2.269}$$

Solving this ordinary differential equation, we will have:

$$A(t) = \exp\left(-\frac{t}{\tau_{1\to 0}}\right) \tag{2.270}$$

With boundary condition $A(0) = 1$. Then we can solve for p_1:

$$p_1(t) = \frac{1}{\tau_{1\to 0}} \exp\left(-\frac{t}{\tau_{1\to 0}}\right) \tag{2.271}$$

From this result, it becomes evident that the switching time follows an exponential distribution. The mean time for which the system remains in state 1 can be calculated as:

$$\int_0^\infty t p_1(t)\,\mathrm{d}t = \frac{1}{\tau_{1\to 0}} \tag{2.272}$$

and the squared standard deviation is:

$$\int_0^\infty t^2 p_1(t)\,\mathrm{d}t - \tau_{1\to0}^2 = \tau_{1\to0}^2 \tag{2.273}$$

Repeating the whole derivation for the $0 \to 1$ process, we can obtain the same result. Therefore, we have demonstrated that the RTN switching process is Poisson distributed.

Next, we demonstrate that this Poisson-distributed RTN can generate a $1/f$-like spectrum. Consider a model where a carrier falls into a charge trap, as described by RTN. The probability of observing m RTN signals in the time interval T is given by:

$$p(m,T) = \frac{(rT)^m}{m!}\exp(-rT) \tag{2.274}$$

where r is the transition rate. Assuming $\tilde{t}_1$ and $\tilde{t}_0$ represent the mean times the system stays in state 1 and state 0, respectively, the probability density for the duration in state 1 is given by:

$$p(t_+) = \frac{1}{\tilde{t}_1}\exp\left(-\frac{t_1}{\tilde{t}_1}\right) \tag{2.275}$$

Now consider the waveform $x(t)$, which has an amplitude a. The product $x(t)x(t+\tau)$ will be a^2 when there is an even number of transitions, and $-a^2$ when there is an odd number of transitions in the time interval τ. Consequently, the auto-correlation function can be expressed as:

$$f_x(\tau) = a^2[p(0)+p(2)+...] - a^2[p(1)+p(3)+...] = a^2\exp(-2rT) \tag{2.276}$$

Then we can calculate the power spectrum, using the Wiener-Khintchine theorem:

$$S_x(\omega) = 4\int_0^\infty f_x(\tau)\cos(\omega t)\,\mathrm{d}\tau = a^2\frac{4r_0}{1+\omega^2 r_0^2} \tag{2.277}$$

where $r_0 = 1/2r$ is the time constant related to the charge trap. Then we can evaluate the total carrier number fluctuations:

$$S_n(\omega) = 4f_n(\tau=0)\int_0^\infty \frac{r_0 p(r_0)}{1+\omega^2 r_0^2}\,\mathrm{d}r_0 \tag{2.278}$$

Now we introduce a model that describe the time taken to arrive at the trap:

$$r_0 = A_0\exp(B_0 d) \tag{2.279}$$

where d is the distance between the conducting layer and the charge trap, located between d_1 and d_2. We can then express the probability as:

$$p(r_0) = \frac{1}{r_0} \frac{1}{\ln r_2/r_1} \quad r_1 < r_0 < r_2 \tag{2.280}$$

Now we can perform the integration of the total number fluctuations:

$$S_n(\omega) = \frac{4f_n(0)}{\ln r_2/r_1} \int_{r_1}^{r_2} \frac{1}{1+\omega^2 r_0^2} \, \mathrm{d}r_0 = \frac{4f_n(0)}{\ln r_2/r_1} \frac{\arctan(\omega r_2) - \arctan(\omega r_1)}{\omega} \tag{2.281}$$

2.7.3 Charge trap and dipole defects

Now that we have understood the significance of RTN and how it contributes to dephasing, our focus shifts to Group IV SQDs. In this subsection, we will delve into the properties of charge traps and dipole charge defects, as well as their formation mechanisms within SQDs.

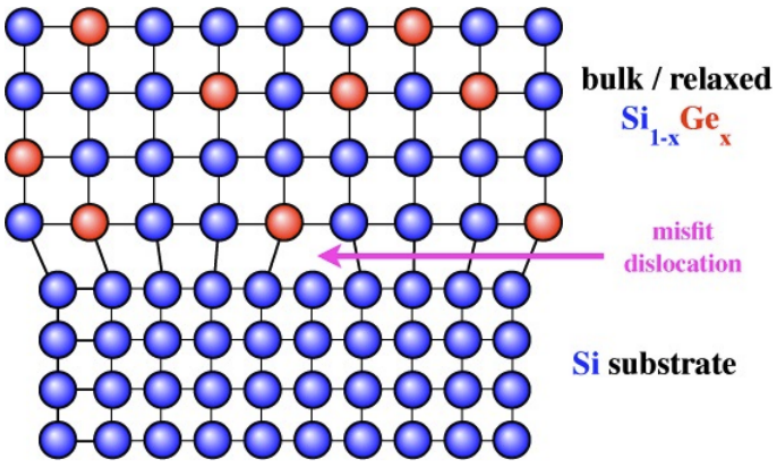

Figure 2.9: **Formations of a charge defect in SiGe-Si layer**. Misfit dislocations are due to missing or dangling bonds in the lattice between two layers with different lattice constant. The original source of this figure is Ref. [97].

During the fabrication of semiconductor samples, such as SiGe-Ge-SiGe heterostructures or silicon MOSFETs, a mismatch in lattice parameters is inevitable [168, 174, 492, 40, 39, 445]. This mismatch creates regions with missing bonds, which act as traps – these are practical examples of the traps considered in the previous sections. A demonstration of

the formation of the charge traps is shown in Fig. 2.9. These charge traps can capture carriers and then re-emit them, leading to what is known as a tunneling two-level system. Building on the theory established in the last subsection, we can describe this switching charge trap using an effective potential:

$$\boldsymbol{V}(t) = \boldsymbol{V}(-1)^{N(t)} \tag{2.282}$$

Where $N(t)$ is a Poisson variable, as we have demonstrated, taking values of either 0 or 1, with a switching time τ. The specific form of this potential is another critical topic in device modelling, which we will address in subsequent subsections. Notably, since this potential depends on position, a single charge trap can affect qubits differently within the system [104, 102, 33], playing a role analogous to the inhomogeneous magnetic field introduced in Sec. 2.7.1. Therefore, we will denote all the dephasing times calculated here as T_2^*. Furthermore, derivations from Eq. (2.278) to (2.281) indicate that the activated charge traps are typically situated close to the conduction channels, or in other words, near the interface and around the undepleted region.

The existence of dipole moments in many materials also contributes to charge noise, known as dipole charge defects [574, 534, 8, 321, 145, 369]. These defects arise from asymmetric bonding, material polarities, and sometimes the presence of defects and impurities. Such dipoles can randomly flip polarities. Similar to single charge traps, dipole charge defects are often located near the interface. The study of dipole charge defects remains an active area of research, particularly due to the complexity of their formation mechanisms.

2.7.4 Screened Coulomb potential

To estimate the T_2^* due to charge defects for semiconductor quantum dot hole spin qubits, we need to revise our derivations in Eq. (2.7.1), where the noise signals are replaced by charge defect-defined potentials V:

$$H = H_0 + \frac{1}{2}V(-1)^{N(t)}\sigma_z \tag{2.283}$$

with this model, we can evaluate the spin polarization expectations again:

$$\langle S_x(t)\rangle = \mathrm{Tr}\{\sigma_x \rho\} \tag{2.284}$$

where ρ is the density matrix describing the qubit-noise system. Using the similar techniques we mentioned in Sec. 2.7.1, we find:

$$\delta\Omega(t) = \frac{V}{\hbar}\int_0^t (-1)^{N(t)}\,\mathrm{d}t' \tag{2.285}$$

and

$$\langle S_x(t)\rangle = S_0\,\langle \cos\delta\Omega(t)\rangle \tag{2.286}$$

where we have:

$$\langle \cos\delta\Omega(t)\rangle = e^{-t/\tau}\left[\frac{\sinh\left((t/\hbar)\sqrt{(\hbar/\tau)^2 - V^2}\right)}{\frac{\tau}{\hbar}\sqrt{(\hbar/\tau)^2 - V^2}} + \cosh\left((t/\hbar)\sqrt{(\hbar/\tau)^2 - V^2}\right)\right] \tag{2.287}$$

If we assume the switching time τ is the largest time scale of the system, we have:

$$\sqrt{\left(\frac{\hbar}{\tau}\right)^2 - V^2} \approx \frac{\hbar}{\tau}\left(1 - \frac{V^2\tau^2}{2\hbar^2}\right) \tag{2.288}$$

which can give us:

$$\langle \cos h(t)\rangle = \exp\left(-\frac{V^2\tau}{2\hbar^2}t\right) \tag{2.289}$$

From here we can extract our motional narrowing dephasing time:

$$T_2^* = \frac{2\hbar^2}{V^2\tau} \tag{2.290}$$

Now the major task becomes to find a the best model for the defect potential V.

A first guess of a carrier in a charge trap is the standard Coulomb potential:

$$V_c = \frac{1}{4\pi\epsilon_0\epsilon_r}\frac{1}{\|\boldsymbol{r} - \boldsymbol{r}_D\|^2} \tag{2.291}$$

Where ϵ_0 is the vacuum permittivity, ϵ_r is the relative permittivity, and $\boldsymbol{r}_D$ denotes the location of the defect. Even though this model already reduces the magnitude of the Coulomb potential by a factor of ϵ_r in media, it still represents a long-range interaction due to the $1/r$ term. In semiconductors, the charge trap, buried within the stacking

materials at a distance d, is screened by the surrounding carriers. Particularly when focusing on the static response to long wavelengths, the Thomas-Fermi screened potential becomes a more apt model [211, 273, 293]:

$$U_{\mathrm{scr}}(q) = \frac{e^2}{2\epsilon_0\epsilon_r} e^{-qd} \left[\frac{\Theta\left(2k_{\mathrm{F}} - q\right)}{q + q_{\mathrm{TF}}} + \frac{\Theta\left(q - 2k_F\right)}{q + q_{\mathrm{TF}} \left(1 - \sqrt{1 - \left(\frac{2k_{\mathrm{F}}}{q}\right)^2}\right)} \right] \tag{2.292}$$

where d is distance between the carrier and the interface, q_{TF} is the Thomas-Fermi wave vector:

$$q_{\mathrm{TF}} = \frac{me^2}{2\pi\epsilon_0\epsilon_r\hbar^2} \tag{2.293}$$

k_F is the Fermi wave vector, Θ is the Heaviside step functions. As we only focus on the long wavelength limit, we can drop the second part:

$$U_{\mathrm{scr}}(q) = \frac{e^2}{2\epsilon_0\epsilon_r} e^{-qd} \frac{1}{q + q_{\mathrm{TF}}} \tag{2.294}$$

While the potential has a closed form in momentum space, its inverse Fourier transformation does not yield a closed form in real space. Therefore, to evaluate the potential magnitude, we can resort to either numerical schemes or asymptotic expansion:

$$U_{\mathrm{scr}}(\boldsymbol{r}) = \frac{e^2}{4\pi\epsilon_0\epsilon_r} \frac{1}{q_{\mathrm{TF}}^2} \frac{1}{\|\boldsymbol{r} - \boldsymbol{r}_D\|^3} + \frac{e^2}{4\pi\epsilon_0\epsilon_r} \frac{1}{q_{\mathrm{TF}}} \frac{d}{\|\boldsymbol{r} - \boldsymbol{r}_D\|^3} \tag{2.295}$$

Although this new model still represents a power potential without the exponential screening typically caused by carriers, it is important to note that we are dealing with a two-dimensional case [22, 69, 456, 15]. In such a scenario, electric field lines can exit the plane, resulting in less effective screening compared to what might be expected in three-dimensional problems.

For the dipole charge defects, we will use its unscreened form since it has only marginally small contribution:

$$U_{\mathrm{dip}}(\boldsymbol{r}) = \frac{\boldsymbol{p} \cdot (\boldsymbol{r} - \boldsymbol{r}_D)}{4\pi\epsilon_0\epsilon_{\mathrm{r}} \left(\boldsymbol{r} - \boldsymbol{r}_D\right)^3} \tag{2.296}$$

where $\boldsymbol{p} = e\boldsymbol{l}$ represents the magnitude of the dipole. Once we have determined these potentials, we can incorporate the defect potential terms into the total qubit Hamiltonian, thereby facilitating an estimation of the dephasing time.

2.7.5 Dephasing time

Once we have extracted the expression related to motional narrowing dephasing time:

$$T_2^* = \frac{2\hbar^2}{V^2\tau} \tag{2.297}$$

and the form of our potentials:

$$U_{\text{scr}}(\boldsymbol{r}) = \frac{e^2}{4\pi\epsilon_0\epsilon_r}\frac{1}{q_{\text{TF}}^2}\frac{1}{\|\boldsymbol{r}-\boldsymbol{r}_D\|^3} + \frac{e^2}{4\pi\epsilon_0\epsilon_r}\frac{1}{q_{\text{TF}}}\frac{d}{\|\boldsymbol{r}-\boldsymbol{r}_D\|^3} \tag{2.298}$$

and

$$U_{\text{dip}}\left(\boldsymbol{r}\right) = \frac{\boldsymbol{p}\cdot\left(\boldsymbol{r}-\boldsymbol{r}_D\right)}{4\pi\epsilon_0\epsilon_{\text{r}}\left(\boldsymbol{r}-\boldsymbol{r}_D\right)^3} \tag{2.299}$$

We can project these expressions onto our qubit wave-functions $|\mathbb{1}\rangle$ and $|\mathbb{0}\rangle$, as mentioned in Sec. 2.5. The resulting fluctuation in the qubit Larmor frequency, denoted as $\delta\omega$ (to distinguish it from the noise spectra), is given by:

$$V \equiv \hbar\,\delta\omega = \langle\mathbb{1}|U|\mathbb{1}\rangle - \langle\mathbb{0}|U|\mathbb{0}\rangle \tag{2.300}$$

The formula used to estimate dephasing time is referred to as the 'dephasing time in the motional narrowing limit', a concept originally developed in nuclear magnetic resonance studies. The core idea of the motional narrowing effect is that the carrier moves so quickly that the influence of the inhomogeneous field becomes less significant. In other words, the carrier relocates before the dephasing can significantly alter the system. Consequently, it is essential to extract the switching time τ from the noise spectrum using experimental data.

Another important time scale to consider is known as the dephasing time in the quasi-static limit. In this scenario, we do not account for any switching time but rather assume that the system exists in a quasi-static state:

$$T_2^* = \frac{\hbar}{V} \tag{2.301}$$

Experimentally, the dephasing time T_2^* can be determined by Ramsey experiments, and the dephasing time T_2 can be ascertained through Hahn echo experiments. Here, we briefly

outline their procedures to lay the foundation for discussions about our calculations in the following chapters.

In a Ramsey experiment, we first prepare the quantum state in a ground state, such as the spin-up state in our Larmor precession model. Then, a $\pi/2$ pulse (also known as a Rabi pulse) is applied to the system. The purpose of this pulse is to transform the state into a superposition state (e.g., $|x,+\rangle$ state):

$$|x,+\rangle = \frac{1}{\sqrt{2}}|\uparrow\rangle + \frac{1}{\sqrt{2}}|\downarrow\rangle \tag{2.302}$$

Next, the state is allowed to evolve freely for a certain period, during which the evolution Hamiltonian encompasses both the qubit system and all potential noise sources, not just the charge noise we've considered. During this period, environmental noise begins to cause dephasing. After this time, another $\pi/2$ pulse is sent to rotate the qubit state again, followed by a measurement. If there is no dephasing, the qubit should return to its original state; otherwise, the measurement signal will differ. By repeating this procedure several times, we can extract the dephasing time T_2^*, which describes the phase coherence decay due to overall noise.

In a Hahn echo experiment, the initial preparation is similar, with the spin oriented along the $|\uparrow\rangle$ direction. After applying the first $\pi/2$ pulse and allowing a period of free evolution, the spin acquires a phase shift due to noise, similar to the Ramsey experiment. The crucial difference is the introduction of a refocusing π pulse, which rotates the spin by π. Allowing the spin to precess freely for the same period again, any phase shifts are refocused onto the original direction. While magnetic resonance still disappears due to dephasing, the π pulse regenerates the signal. This second signal is the spin echo signal, known as T_2.

The dephasing problem in hole qubits presents a significant challenge in single-qubit operations, being the shortest time scale in such processes. Recent experiments have reported Ramsey dephasing times up to 8,μs and Hahn echo dephasing times up to 36,μs. When compared with the typical electric dipole spin resonance Rabi time of around 100 ns, this limits the number of feasible manipulations to only several hundreds. The complexities of dephasing include various aspects: firstly, the nature of the open quantum system itself

poses a challenge, as the various types of noise are difficult to capture accurately. Secondly, while specific dot geometries and external fields can be chosen to bring the qubit into a 'sweet spot' where noise is suppressed, this presents significant challenges in fabricating high-quality semiconductors. Recently, thanks to tremendous efforts by theorists and experimentalists, these obstacles are being gradually overcome. Several spin echo techniques have been proposed to refocus the spin state, and the quality of semiconductors has improved significantly [71]. All these accomplishments are bringing us closer to a new quantum world.

Chapter 3

Germanium hole spin qubit

The main content of this chapter is an adaption of a publication Ref. [532] by the candidate. I would like to express acknowledgement to all the co-authors: Elizabeth Marcellina, Alex R Hamilton, James H Cullen, Sven Rogger, Joe Salfi and Dimitrie Culcer.

Strong spin-orbit couplings position hole quantum dots at the forefront of electrical spin qubit manipulation, which is crucial for enabling fast, low-power, and scalable quantum computation. However, it is essential to determine the extent to which spin-orbit couplings make qubits vulnerable to electrical noise, potentially leading to increased decoherence. In this context, using germanium as an example, we demonstrate that group IV gate-defined hole spin qubits inherently exhibit optimal operation points. These points are determined by the top gate electric field, where the qubits are both rapid in operation and exhibit prolonged lifespans: the dephasing rate effectively vanishes to first order in electric field noise across all spatial directions, the electron dipole spin resonance strength reaches its maximum, and relaxation is significantly reduced at lower magnetic fields. The emergence of these optimal operation points can be attributed to the crystal symmetry of group IV elements and the unique properties of the Rashba spin-orbit interaction in spin-3/2 systems. Our findings challenge the traditional belief that faster operation necessarily leads to reduced lifetimes and position group IV hole spin qubits as prime candidates for

ultra-fast, highly coherent, and scalable quantum computing.

3.1 Introduction

Quantum computing architectures require reliable qubit initialization, robust single-qubit operations, long coherence times, and a clear pathway towards scaling up. Solid-state platforms are supported by the well-developed solid-state device industry, with mature micro-fabrication and miniaturization technologies. Among solid-state platforms, semiconductor quantum dot (QD) spin qubits have been actively pursued, with an energetic recent focus on hole spins in diamond and Zincblende nano-structures.

The primary motivation for this focus is the strong hole spin-orbit interaction, which enables qubit control via electric dipole spin resonance (EDSR), making quantum computing platforms faster, more power-efficient, and easier to operate. Electric fields are much easier to apply and localize than magnetic fields used in electron spin resonance. Only a global static magnetic field is required to split the qubit levels. In addition, the p-symmetry of the hole wave function causes the contact hyperfine interaction to vanish, and complications involving valley degrees of freedom are absent. Initial studies indicate that hole spins may possess sufficiently long coherence times for quantum computing. Meanwhile, much progress has been made in the initialization and read-out of hole spin qubits.

The existential question that will determine the future of hole QD spin qubits is: Does the strong spin-orbit interaction that allows fast qubit operation also enhance undesired couplings to stray fields such as phonons and charge noise leading to intractable relaxation and dephasing? In this chapter, we demonstrate theoretically that this is emphatically not the case for hole spin qubits in group IV materials taking germanium as the most prominent example.

In fact, the unique properties of the hole Rashba interaction overturn the conventional understanding of qubit coherence in spin-orbit coupled systems, which states that, as long as the qubit is described by an effective 2×2 Hamiltonian, holes behave in the same way as

electrons. That is, given that the EDSR rate is linear in the spin-orbit strength, while the relaxation and dephasing rates increase as the square of the spin-orbit strength, the Rabi ratio can be enhanced by operating the qubit at points at which the spin-orbit interaction is weaker. In contrast group IV hole qubits achieve the best coherence when the electrical driving rate is at its maximum. In all other systems, one has to choose between creating long-lived qubits by isolating them from the environment and accepting slower gate times, or designing fast qubits strongly coupled to the environment, but which decohere rapidly.

The key realization is that holes in group IV materials are qualitatively different from group III–V materials. They have tremendous potential for qubit coherence, with Germanium and Silicon possessing isotopes with no hyperfine interaction, as well as a near-inversion symmetry that eliminates piezo-electric phonons. This near-inversion symmetry will eliminate the Dresselhaus interaction, the interface inversion asymmetry terms are expected to be negligible in the system. Which enables spin resonance in group III–V materials. On the other hand, we show that strong cubic-symmetry terms enable a fully-tuneable Rashba coupling. Unlike the Dresselhaus interaction, and unlike electron systems, the hole Rashba interaction evolves nonlinearly as a function of the gate electric field, a fact traced to the hole spin-3/2. The qualitative difference between the Rashba and Dresselhaus interactions for holes is vital for qubit coherence. Thanks to this nonlinearity, dephasing due to electric field fluctuations in all spatial directions can be essentially eliminated at specific optimal operation points defined by the gate electric field. At these points electrical qubit rotations are at their most efficient, with the spin resonance Rabi gate time at a minimum. The relaxation rate due to phonons can be made as small as desired at small magnetic fields of the order of 0.1,T, which allows $10^6 - 10^7$ operations in one relaxation time for an in-plane alternating field $\mathrm{E_{AC}} \approx 10^3\,\mathrm{V/m}$.

3.2 Model and Methodology

Our focus in this chapter is on germanium, which has witnessed enormous recent progress. Holes in planar germanium quantum wells have a very large out of plane Landé g-factor,

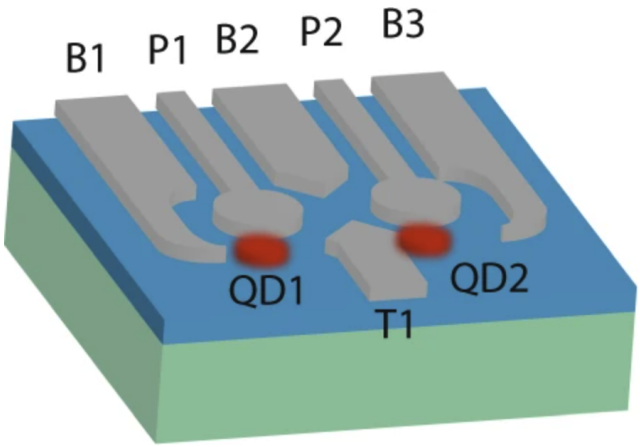

Figure 3.1: **Probability density distribution evaluated by evaluated by the norm square of the wave-function in $\hat{z}$-direction.** The probability density is plotted as a function of the $\hat{z}$-coordinate, in the main text, the quantum well width is 13 nm placed symmetrically. The shape of the probability density are very close if the number of sinusoidal wave-function used exceed seven.

$g \approx 20$, enabling operation at very small magnetic fields, which would not impede coupling to a superconducting resonator. The low resistivity of germanium when contacting with metals makes couplings between other devices such as superconductors easier. In the past decade some spectacular results have been reported, for example, EDSR detection techniques, structures of quantum confinement systems, the anisotropy of g-tensors, spin-orbit couplings, and transport phenomena in two-dimensional hole systems. We focus a on single dot throughout this work. A prototype device, including a neighbouring dot, is shown in Fig. 3.1. The Hamiltonian describing a single hole quantum dot has the general form

$$H = H_{\mathrm{LK}} + H_{\mathrm{BP}} + H_{\mathrm{Z}} + H_{\mathrm{PH}} + H_{\mathrm{conf}} \tag{3.1}$$

where H_{LK} represents the Luttinger-Kohn Hamiltonian, H_{Z} is the Zeeman interaction between the hole and an external magnetic field, and H_{ph} the hole-phonon interaction. H_{conf} is the confinement potential including the vertical and lateral confinement. The vertical confinement is achieved by applying a gate electric field F_z in the growth direction, leading to a term $eF_z z$ in the Hamiltonian; the lateral confinement is modelled as an in-plane parabolic potential well. The Bir-Pikus Hamiltonian H_{BP} represents strain, which appears naturally as part of the quantum well growth process. A typical configuration of

holes in germanium is achieved by growing a thin strained germanium layer (usually about 10 nm to 20 nm) between Si-Ge layers such that, if the barrier between the two layers is high enough, a quantum well can be formed. We consider Si_xGe_{1-x}, where $x = 0.15$.

We start from the bulk band structure of holes as derived by Luttinger and Kohn. The spinor basis is formed by the eigenstates of total angular momentum operators:

$$\left|\frac{3}{2},\frac{3}{2}\right\rangle \left|\frac{3}{2},-\frac{3}{2}\right\rangle \left|\frac{3}{2},\frac{1}{2}\right\rangle \left|\frac{3}{2},-\frac{1}{2}\right\rangle \tag{3.2}$$

We write the Luttinger-Kohn Hamiltonian as:

$$H_{\mathrm{LK}}\left(k^2,k_{\mathrm{z}}\right) = \begin{bmatrix} P+Q & 0 & L & M \\ 0 & P+Q & M^* & -L^* \\ L^* & M & P-Q & 0 \\ M^* & -L & 0 & P-Q \end{bmatrix}, \tag{3.3}$$

$$P+Q = \frac{\hbar^2}{2m_0}\left(\gamma_1-2\gamma_2\right)k_z^2 + \frac{\hbar^2}{2m_0}\left(\gamma_1+\gamma_2\right)\left(k_x^2+k_y^2\right) \tag{3.4}$$

$$P-Q = \frac{\hbar^2}{2m_0}\left(\gamma_1+2\gamma_2\right)k_z^2 + \frac{\hbar^2}{2m_0}\left(\gamma_1-\gamma_2\right)\left(k_x^2+k_y^2\right) \tag{3.5}$$

$$L = \sqrt{3}\frac{\hbar^2}{2m_0}\left[-\gamma_2\left(k_x^2-k_y^2\right)+2i\gamma_3 k_x k_y\right] \tag{3.6}$$

$$M = 2\sqrt{3}\frac{\hbar^2}{2m_0}\gamma_3\left(k_x k_z - i k_y k_z\right) \tag{3.7}$$

where m_0 is the free electron mass, $\gamma_1,\gamma_2,\gamma_3$ are Luttinger parameters which are determined by the band structure. The in-plane wave vectors are

$$k^2 = k_x^2+k_y^2 \quad k_\pm = k_x \pm i k_y\,. \tag{3.8}$$

In this manuscript, we use the symmetric gauge $\boldsymbol{A} = (B/2)(-y,x,0)$ so that $\mathbf{k} \to -i\nabla + e\mathbf{A}/\hbar$. We have also used $\bar{\gamma} = \left(\gamma_2+\gamma_3\right)/2$ and $\delta = \left(\gamma_3-\gamma_2\right)/2$ to simplify the algebra. In Ge $\delta/\bar{\gamma} < 0.15$, hence δ can be treated perturbatively, while bulk Dresselhaus terms are absent. Although interface inversion asymmetry terms with the same functional form may exist, at the strong gate fields considered here will be overwhelmed by the Rashba interaction and are not discussed in detail.

The strain is described by the Bir-Pikus Hamiltonian:

$$H_{\mathrm{BP}} = \begin{bmatrix} P_\varepsilon + Q_\varepsilon & 0 & -S_\varepsilon & R_\varepsilon \\ 0 & P_\varepsilon + Q_\varepsilon & R_\varepsilon^* & S_\varepsilon^* \\ -S_\varepsilon^* & R_\varepsilon & P_\varepsilon - Q_\varepsilon & 0 \\ R_\varepsilon^* & S_\varepsilon & 0 & P_\varepsilon - Q_\varepsilon \end{bmatrix} \tag{3.9}$$

where

$$P_\varepsilon = -a_v \left(\varepsilon_{xx} + \varepsilon_{yy} + \varepsilon_{zz}\right) \tag{3.10}$$

$$Q_\varepsilon = -\frac{b_v}{2} \left(\varepsilon_{xx} + \varepsilon_{yy} - 2\varepsilon_{zz}\right) \tag{3.11}$$

$$R_\varepsilon = \frac{\sqrt{3}}{2} b_v \left(\varepsilon_{xx} - \varepsilon_{yy}\right) - i d_v \varepsilon_{xy} \tag{3.12}$$

$$S_\varepsilon = -d_v \left(\varepsilon_{xz} - i\varepsilon_{yz}\right) \tag{3.13}$$

$$P_\varepsilon + Q_\varepsilon = -\left(a_v + \frac{b_v}{2}\right)\varepsilon_{xx} - \left(a_v + \frac{b_v}{2}\right)\varepsilon_{yy} - (a_v - b_v)\varepsilon_{zz} \tag{3.14}$$

$$P_\varepsilon - Q_\varepsilon = -\left(a_v - \frac{b_v}{2}\right)\varepsilon_{xx} - \left(a_v - \frac{b_v}{2}\right)\varepsilon_{yy} - (a_v + b_v)\varepsilon_{zz} \tag{3.15}$$

We added a subscript ϵ for strains. The material-specific parameters a_v, b_v, and d_v are known as the hydrostatic deformation potential constant, the uniaxial deformation potential constant, and the shear deformation potential constant, respectively. In our chosen configuration $\varepsilon_{\mathrm{xx}} = \varepsilon_{\mathrm{yy}} = -0.006$, the minus sign indicates that the germanium is compressed in xy-plane. In the $\hat{z}$-direction, the Ge layer will be stretched, and $\varepsilon_{zz} = (-2C_{12}/C_{11})\,\varepsilon_{xx} = 0.0042$, with $C_{12} = 44\mathrm{GPa}, C_{11} = 126\mathrm{GPa}$ for Ge. The diagonal terms of the strain-relaxed barrier configuration will change the $\mathrm{HH} - \mathrm{LH}$ energy splitting by a constant, which is approximately 50meV.

The growth direction provides the spin quantization axis, with the heavy hole states (HHs) representing the $|3/2, \pm 3/2\rangle$ angular momentum projection onto this axis, while the light hole states (LHs) represent $|3/2, \pm 1/2\rangle$. In 2D hole systems, the HHs are the ground state. To define a quantum dot a series of gates are added on top of the 2D hole gas confinement, as in Fig. 1, and we ultimately seek an effective Hamiltonian describing the two lowest-lying HH states in a quantum dot. Since we expect the HH LH splitting to be much larger than the quantum dot confinement energy, we proceed with the standard

assumptions of $\mathbf{k}\cdot\mathbf{p}$ theory, retaining at first only terms containing k_z with k_x and k_y initially set to zero. This determines the approximate eigenstates $\psi_{\mathrm{H,L}}(z)$ corresponding to the growth-direction. These are described by two variational Bastard wave functions ψ_H and ψ_L[48,66],

$$\psi_{\mathrm{H,L}}(z) = \sqrt{\frac{4\beta_{\mathrm{H,L}}\left(\pi^2+\beta_{\mathrm{H,L}}^2\right)}{\left(1-e^{-2\beta_{\mathrm{H,L}}}\right)d\pi^2}}\cos\left(\frac{\pi z}{d}\right)\exp\left[-\beta_{\mathrm{H,L}}\left(\frac{z}{d}+\frac{1}{2}\right)\right], \tag{3.16}$$

where the dimensionless variational parameters $\beta_{\mathrm{H,L}}$ are sensitive to the gate electric field due to the term $eF_z z$, and d is the width of the quantum well in the growth direction, which is an input parameter. The orthogonality of the HH and LH states is ensured by the spinors. This wave function is suitable for inversion layers, as well as accumulation layers, although our focus will be primarily on the latter. For inversion layers, the Bastard wave function will also be appropriate, because in experiments the electric field can be made large enough such that the hole gas sticks around the top of the quantum well.

In the xy-plane, we model the confinement potential using a harmonic oscillator

$$\left[\frac{\hbar^2}{2m_p}\left(-i\nabla_\parallel + e\mathbf{A}\right)^2 + \frac{1}{2}m_\mathrm{p}\omega_0^2\left(x^2+y^2\right)\right]\phi = \varepsilon\phi$$

where $m_\mathrm{p} = m_0/(\gamma_1+\gamma_2)$ is the in-plane effective mass of the heavy holes, the subscript $\parallel$ refers to the xy-plane, ω_0 is the oscillator frequency, a_0 the QD radius which satisfies, $a_0^2 = \hbar/(m_\mathrm{p}\omega_1)$ i.e., a magnetic field will narrow the QD radius. The solutions are the well-known Fock-Darwin wave functions $|\phi_{n_1,n_2}\rangle$ with eigenen-ergies $\varepsilon_{n_1,n_2} = \hbar(n_1+n_2+1)\omega_l + \frac{1}{2}\hbar(n_2-n_1)\omega_c$, where $\omega_1 = \sqrt{\omega_0^2+\omega_c^2/4}$, $\omega_c = eB/m_p$ is the cyclotron frequency. The Bastard wave functions account for the perpendicular confinement, in the $\hat{z}$-direction. The Fock-Darwin wave functions $|\phi_{n_1,n_2}\rangle$ account for the quantum dot confinement in the xy-plane. The Bastard and Fock-Darwin wave functions would be formally the same for electrons, while in a hole gas is that separate Bastard wave functions are required for the heavy and light holes.

Finally, the hole-phonon interaction is:

$$H_{\mathrm{i,j,s}} = \sum_{a,\beta=\mathrm{x,y,z}}\frac{1}{2}\sqrt{\frac{\hbar}{2NV_c\rho\omega_\mathrm{s}}}D_{a,\beta}^{\mathrm{i,j}}\left[\frac{q_a\hat{e}_{s,\beta}+q_\beta\hat{e}_{s,a}}{q}\right]q\left(e^{-i\mathbf{q}\cdot\mathrm{r}}\hat{a}_q^\dagger + e^{iq\cdot\mathrm{r}}\hat{a}_q\right) \tag{3.17}$$

where q is the phonon wave vector, V_c is the unit cell volume, NV_c is the crystal volume, $\hat{e}_s$ is the polarization direction vector. The density of the material is denoted by $\rho, D_{\alpha,\beta}$ represents the deformation potential matrix, and $\hat{a}^\dagger$ and $\hat{a}$ are the phonon creation and the annihilation operators.

Our approach is semi-analytical. To incorporate the contributions from the LHs, and the Rashba spin-orbit couplings, we start from the 4×4 Luttinger Hamiltonian and project it onto the product states of the out-of-plane sub-bands HH1, LH1, each with two spin projections, and the first four orbital levels of the in-plane confinement, such that our Hamiltonian matrix is 40×40. This refers to states $\left\{\left|\frac{3}{2}, S\right\rangle \otimes |\phi_{n,m}\rangle\right\}$, where $S = 3/2, -3/2, 1/2, -1/2$ represent the HHs or LHs, $n = 0, 1, 2, 3$ and $m = 0, \pm 1, 2, \pm 3$ denote the in-plane Fock-Darwin states. We have checked that addition of the HH2, LH2 sub-bands does not modify the results, this is attributed to the significant energy gaps separating them from HH1, LH1. Given the high computational cost of adding these sub-bands, we have not taken them into account in the results presented here. To obtain the matrix elements required for the dephasing and relaxation times, as well as for the EDSR Rabi frequency, we perform a 3rd order Schrieffer-Wolff transformation on the 40×40 Hamiltonian. This transformation takes into account all the spin-orbit terms that are not separable in the spatial coordinates, which are precisely the terms leading to the Rashba interaction. To ensure the accuracy of the Schrieffer-Wolff method we compare the results for the Larmor frequency with a full numerical diagonalization of the 40×40 matrix.

3.3 Result and discussion

3.3.1 Qubit Larmor frequency

The qubit Larmor frequency has been plotted in Fig. 3.2 as a function of the gate electric field. The Schrieffer-Wolff method agrees well with the numerical diagonalization: the location of the optimal operation point differs by only 2% in the two approaches. We note the non-monotonic behaviour as a function of the gate field, leading to an optimal

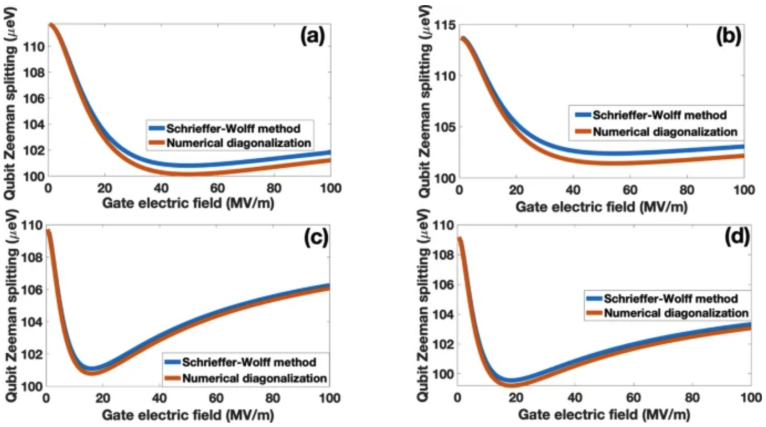

Figure 3.2: **Qubit Zeeman splitting.** Comparison of the qubit Zeeman splitting between Schrieffer-Wolff transformation (to the third order) and exact numerical diagonalization for four different configurations. When the gate electric field is turned off, the qubit Zeeman splitting $g_0\mu_B B \approx 110\mu$eV. In all these figures, the out-of-plane magnetic field is $B = 0.1$ T. We can notice that the sweet spot does not change much as a function of the quantum dot radius, but the size of the qubit Zeeman splitting will be smaller for a larger quantum dot size. In all of these plots, we have $\hbar\omega_l \gg g_0\mu_B B$. Numerical diagonalization is the red curve, Schrieffer-Wolff method is the blue curve. a.) $d = 11$ nm, $a_0 = 50$ nm. b.) d=11 nm, $a_0 = 60$ nm. c.) d=15 nm, $a_0 = 50$ nm.*d.*)$d = 15$ nm, $a_0 = 60$ nm.

operation point in the range of 30-50 MV/m. Electric fields of such magnitude are used routinely in quantum computing experiments. The non-monotonic behaviour is directly related to the behaviour of Rashba spin-orbit coupling discussed below. We note that the spatial dimensionality of the qubit is determined by the relevant energy scales, namely the $\hat{\mathbf{z}}$-sub-band energy spacing compared to the energy splitting of the lateral wave functions. The heavy hole-light hole splitting, given by the perpendicular confinement, is many times larger than the in-plane qubit confinement energy, determined by the in-plane confinement, so the system is in the quasi-2D limit. Nevertheless, our findings, such as trends with the top gate field, can be interpreted qualitatively by analogy with the Rashba interaction in the asymptotic 2D limit $d \to 0$. For a system with cubic symmetry this contains two terms with different rotational properties:

$$H_{\mathrm{SO}} = ia_2\left(k_+^3\hat{\sigma}_- - k_-^3\hat{\sigma}_+\right) + ia_3\left(k_+k_-k_+\hat{\sigma}_+ - k_-k_+k_-\hat{\sigma}_-\right),$$

where $\hat{\sigma}_\pm \equiv \left(\hat{\sigma}_x \pm i\hat{\sigma}_y\right)/2$. The coefficients are evaluated as:

$$a_2 = \frac{3}{2}\frac{\mu^2\bar{\gamma}\gamma_3}{E_{\mathrm{H}} - E_{\mathrm{L}}}\left\langle\psi_{\mathrm{H}} \mid \psi_{\mathrm{L}}\right\rangle\left[\left\langle\psi_{\mathrm{H}}\left|\hat{k}_{\mathrm{z}}\right|\psi_{\mathrm{L}}\right\rangle - \left\langle\psi_{\mathrm{L}}\left|\hat{k}_{\mathrm{z}}\right|\psi_{\mathrm{H}}\right\rangle\right] \tag{3.18}$$

$$a_3 = \frac{3}{2}\frac{\mu^2\delta\gamma_3}{E_{\mathrm{H}} - E_{\mathrm{L}}} \langle \psi_{\mathrm{H}} \mid \psi_{\mathrm{L}} \rangle \left[\left\langle \psi_{\mathrm{H}} \left| \hat{k}_{\mathrm{z}} \right| \psi_{\mathrm{L}} \right\rangle - \left\langle \psi_{\mathrm{L}} \left| \hat{k}_{\mathrm{z}} \right| \psi_{\mathrm{H}} \right\rangle \right], \tag{3.19}$$

where E_{H} and E_{L} are the energies of the lowest-lying HH and LH states, respectively, and are strong functions of the gate electric field. These formulas explain three main features.

Firstly, the optimal operation point reflects the interplay of the quadrupole degree of freedom with the gate electric field unique to spin-3/2 systems. The behaviour of the qubit Zeeman splitting and Rashba coefficients is understood by recalling that the Rashba effect for the HH sub-bands is primarily driven by the off-diagonal matrix element L connecting the HH and LH sub-bands. This term, which is $\alpha k_z k_+$, increases with the top gate field. At small gate fields, the Rashba spin-orbit constants increase monotonically due to the increase in the k_z overlap integral. This continues until a critical top gate field is reached at which the $\mathrm{HH} - \mathrm{LH}$ splittings, determined by the matrix element Q, begin to increase faster than the off-diagonal matrix element L.

The heavy hole-light hole splitting induced by the confinement potential and the gate electric field is traced to the different effective masses for heavy and light holes. This physics has been shown previously by Winkler and collaborators. Beyond this critical field, the Rashba terms decrease, resulting in a relatively broad optimal operation region at which the qubit is insensitive to background electric field fluctuations in the $\hat{z}$-direction and the dephasing rate vanishes to first order in the $\hat{z}$-electric field. As we show below, electric field fluctuations in the $\hat{z}$-direction are by far the most damaging to the qubit and are the key source of decoherence to be avoided. The breadth and smoothness of the extreme make the tuning of the electric field to reach the optimal operation point easier.

Secondly, the sweet spot shifts slightly with the dot radius, and this is fully captured by our Schrieffer-Wolff results. The reason for this is that, in a 2D system, while the angular form of the Rashba interaction is dictated by rotational symmetry, the Rashba coupling constants a_2 and a_3 are functions of the magnitude of the wave vector. This implies they are functions of the density, and this is vital at large densities. Hence a quantum dot can be envisaged as having Rashba parameters that are functions of the in-plane radius a_0, and their dependence is less pronounced at larger a_0, since this corresponds to smaller

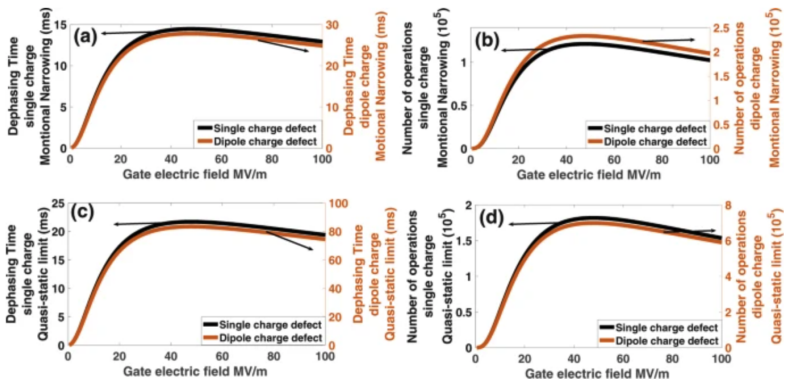

Figure 3.3: **Qubit dephasing time.** In all plots, the quantum well width is $d = 11\,\mathrm{nm}$ and dot radius $a_0 = 50\,\mathrm{nm}$. a) Dephasing time in the motional narrowing regime. b) The allowable number of single-qubit operations in one dephasing time in motional narrowing regime. c) Dephasing time in the quasi-static limit. d) The allowable number of single-qubit operations in one dephasing time in the quasi-static limit.

densities.

Thirdly, each of the two spin-orbit coupling terms can be envisaged as the interaction of the hole spin with an effective spin-orbit field that depends on the momentum. In the absence of a magnetic field, the a_2-Rashba spin-orbit field winds around the Fermi surface three times, whereas the a_3-Rashba spin-orbit field winds only once. In the strict 2D limit it is the a_3-term that enables EDSR. Although the quantum dot is not in the exact 2D limit, it still holds that EDSR is enabled by the cubic symmetry terms $\propto \delta$. Setting $\delta = 0$ in our calculations causes the EDSR frequency to vanish.

$$f_{\mathrm{EDSR}} = 24 g_0 \mu_{\mathrm{B}} B e E_{\mathrm{AC}} a_0^2 \delta m_{\mathrm{p}}^2 \times u \tag{3.20}$$

where u are a long expression can be found in Ref. [532]. A shorter similar expression obtained in the 2D limit is [484]:

$$|f_R| = \frac{e E_{\mathrm{AC}} \alpha_{R3} g_z \mu_B B_z m_x^2 a_0^2}{2\pi\hbar^5}\,. \tag{3.21}$$

3.3.2 Qubit dephasings

The main dephasing mechanisms are fluctuating electrical fields such as charge noise. We focus on random telegraph noise (RTN) due to charge defects, noting that a similar

discussion can be presented for $1/f$ noise, which is typically caused by an incoherent superposition of RTN sources. For this reason, we expect the trends for the two types of noise to be similar, while reliable numbers for $1/f$ noise must await the experimental determination of the noise spectral density $S(\omega)$ for hole qubits. To begin with, we estimate the dephasing time T_2^* , which is expected to be primarily determined by fluctuations in the Larmor frequency of the qubit induced by charge noise. The electric potential induced at the qubit by a defect located at r_D, which may give rise to RTN, can be modelled as a quasi-2D screened Coulomb potential:

$$U_{\mathrm{scr}} = \frac{e^2}{2\epsilon_0\epsilon_{\mathrm{r}}} \int_0^{2k_{\mathrm{F}}} \frac{e^{-i\mathbf{q}\cdot(\mathbf{r}-\mathbf{r}_{\mathrm{D}})}}{q+q_{\mathrm{TF}}} \frac{\mathrm{d}q}{(2\pi)^3} \tag{3.22}$$

where ϵ_0 is the vacuum permeability, ϵ_{r} is the relative permeability for Ge, q_{TF} is the Thomas-Fermi wave vector, and k_F is the Fermi wave vector. In a dilution refrigerator, the high energy modes of the Coulomb potential are negligible, therefore the $q > 2k_F$ part is ignored. Another source of dephasing is dipole defects due to the asymmetry in bond polarities.

$$U_{\mathrm{dip}}\left(\mathbf{R}_{\mathrm{D}}\right) = \frac{\mathbf{p}\cdot\mathbf{R}_{\mathrm{D}}}{4\pi\epsilon_0\epsilon_{\mathrm{r}}R_{\mathrm{D}}^3} \tag{3.23}$$

where $\mathbf{R}_D$ is the distance between the dot and the unscreened charge dipole. $\boldsymbol{p}$ is the dipole moment of the charge $\mathbf{p} = e\boldsymbol{l}$, the size of the dipole is about 1Å.

As a worst-case estimate of the dephasing time, we use the motional narrowing result, the dephasing time $T_2^{*-1} = (\delta\omega)^2\tau/2$, where $\delta\omega$ is the change in qubit Larmor frequency due to the fluctuator, and we consider $\tau = 10^3 t_{\mathrm{Rabi}}$ where t_{Rabi} is the single-qubit operation time (the inverse of the EDSR frequency), which can be found from Fig. 3.3-a. Because of the weak coupling between the spin degree of freedom and external reservoirs, slower fluctuators can be eliminated via pulse sequences and the spin-echo techniques. We consider two sample defects separately. One is a single-charge defect located 100 nm away from the quantum dot in the plane of the dot as a worst-case scenario for a charge trap. We use $r_D = 100$ nm since regions inside this range will be depleted by the top gate, and charge traps will not be active. We also consider a dipole defect immediately under the gate and above the dot, with $R_{\mathrm{D}} = 20$ nm in the $\hat{z}$ direction. This is because within the

depleted region the most relevant defects are charge dipoles, whose orientation fluctuates. To estimate the pure dephasing time at the optimal operation point due to such a defect, we first note that the in-plane electric field will not contribute to dephasing. An in-plane electric field enters the QD Hamiltonian as $\mathbf{E}_{\parallel} \cdot \mathbf{r}_{\parallel}$. This in-plane electric field term does not couple states with different spin orientations. When we consider the qubit Zeeman splittings, the corrections to the effective quantum dot levels due to the in-plane electric field will read the same for $H_{1,1}$ and $H_{2,2}$ up to the secondorder, therefore, fluctuations in qubit Zeeman splitting $H_{1,1} - H_{2,2}$ will not depend on the in-plane electric field. However, higher order terms in the expansion of the electrostatic potential of the defects will lead to dephasing, and these are responsible for dephasing at the optimal operation point itself. To determine their effect, we write the ground state energy as $E_{\mathrm{LK}} + E_0 + E_{\mathrm{z}} + v_0$ where E_0 is the lateral confinement energy, E_{z} is the Zeeman energy, and v_0 is the energy correction due to the defect.

We estimate the approximate qubit window of operation around the optimal operation point. Away from the optimal operation point, due to the fluctuating electric potential of the defect, the energy levels of the quantum dot will gain a correction, i.e., $\langle \phi_{n_1} | U_{sc} | \phi_{n_2} \rangle$. With these assumptions, the dephasing time is plotted as a function of the gate electric field in Fig. 3.3. At the optimal operation point, the dephasing time due to the out-of-plane fluctuations is calculated to the second-order, since the first-order fluctuation vanishes, the in-plane fluctuations will dominate the dephasing. Away from the optimal operation point, the motional narrowing result is much smaller than the quasi-static limit result. This is because the first-order variation of the qubit Zeeman splitting will weaken the correlation time, while the quasi-static limit does not consider any correlations. However, as the gate electric field approaches the optimal operation point, the variation of qubit Zeeman splitting decreases; at the optimal operation point, compared with the quasi-static limit result, a longer correlation time will lead to a larger dephasing time. We also determine the pure dephasing time in the quasi-static limit, where the switching time is the longest time scale in the system. This is essentially given by $T_2 = 2\pi/(\delta\omega)$, and is plotted in Fig. 3.3.

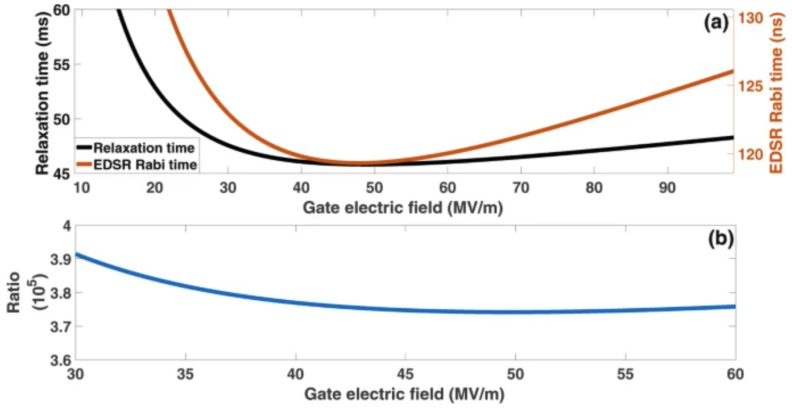

Figure 3.4: **Qubit phonon relaxation time and EDSR Rabi time.** In all plots $d = 11$ nm, $a_0 = 50$ nm, the external magnetic field is $B = 0.1$ T. The density of Ge $\rho = 5.33\times\ 10^3$ kg/m^3. The phonon propagation speed along the transverse direction is $v_t = 3.57 \times 10^3$ m/s, along the longitudinal direction it is $v_l = 4.85 \times 10^3$ m/s. a). Relaxation time and EDSR Rabi time as a function of the gate electric field. b.) The allowable number of single-qubit operations in one relaxation time.

3.3.3 Electric dipole spin resonance

We briefly discuss electrically driven spin resonance. An in-plane oscillating electric field represented in the Hamiltonian by $eE_{\mathrm{AC}}(t)x$ drives spin-conserving transitions between the QD states. For a multiple occupied hole dot, the excited state structure may be more complex but the argument above remains valid because the α_2 and α_3 Rashba terms couple the ground state to different excited states. The spin resonance Rabi time is the time taken to accomplish an operation. The Rabi frequency can be tuned by changing the gate electric field and with it the Rashba spin-orbit coupling constant. However, note that because the two Rashba terms directly determine the correction to the g-factor, the Rashba interaction and the g-factor cannot be tuned independently at present.

3.3.4 Phonon relaxation time

Given that the spin resonance frequency is a maximum at the optimal operation point, it follows that the qubit can be tuned to have maximum coherence and maximum electrical driving simultaneously. The nonlinearity in the hole Rashba interaction as a function of

the gate field that enables this feature has no counterpart in electron systems. In GaAs hole systems this nonlinearity does not lead to optimal operation points. This is because, firstly, the spin resonance Rabi frequency in GaAs hole qubits is driven by the Dresselhaus interaction, which is not tunable via the gate electric field, while α_3 is negligible in GaAs. Secondly, GaAs qubits are exposed to decoherence through the hyperfine interaction, piezoelectric phonons, and the Dresselhaus interaction, none of which can be mitigated.

Since the Rabi frequency is maximized at the optimal operation point, the relaxation time T_1 is minimized there. For the qubit to be operated efficiently it is vital to determine the ratio of the EDSR and relaxation rates. Hyperfine interactions and phonon-hole interactions are two major factors affecting the relaxation time, hence the quality of the qubit. However, the p-type symmetry of the valence band excludes the contact hyperfine interaction. There is no bulk inversion asymmetry in group IV elements; this leads to no Dresselhaus spin-orbit coupling. However, there is still the Rashba spin-orbit coupling due to the structure inversion asymmetry, which couples the heavy-hole states to the light-hole states. Neither the spin nor the orbital angular momentum will be a good quantum number, as the admixture of the spin-down and the spin-up states will modify the wave functions. We emphasize that, whereas EDSR comes only from the α_3-Rashba term, the qubit relaxation is caused by both the α_2- and the α_3-Rashba terms.

The relaxation time evaluated using Fermi's golden rule is shown in Fig. 3.4 . For completeness, we also consider two-phonon relaxation processes, which include virtual emission and absorption of a phonon between two heavy hole states, since in the first-order relaxation calculation there is no direct matrix element between the two heavy-hole states. However, the two-phonon process calculation returns a negligible relaxation rate, which will not contribute significantly to the relaxation time. The relaxation rate will depend on the external magnetic field as $1/T_1 \propto B^7$ for the α_3-Rashba term and $1/T_1 \propto B^9$ for the α_2-Rashba term.

We also plot the ratio between the relaxation time and the EDSR time, demonstrating that the system allows for a large number of operations. The allowable number of single-qubit

operations is calculated by evaluating the ratio of the relaxation time and the EDSR time, i.e., the Rabi ratio. The in-plane electric field we used is $E_{\mathrm{AC}} = 10^3 \mathrm{V/m}$. In Fig. 3.4, we plot the relaxation time, EDSR Rabi time, comparison of the magnitude of the relaxation time and EDSR time and an estimation of red the allowable number of single-qubit operations as the function of the gate electric field at a magnetic field $B = 0.1\,T$ which is parallel to the growth direction. Both the relaxation time and the EDSR time will depend on the spin-orbit coupling coefficients, therefore, their extrema coincide. The relaxation time increases for smaller dot sizes because that corresponds to larger confinement energy, while both the phonon and the spin-orbit coupling terms connect the orbital ground state to higher excited states. From Fig. 3.4, we can see that the Ge hole quantum dot has a long relaxation time and large Rabi ratio at dilution refrigerator temperatures. It is also useful to study the relaxation time at slightly higher temperatures, e.g., 4 K, at which both phonon absorption and emission must be taken into account. The phonon occupation number is given by the Bose-Einstein distribution, where N is the occupation number, $\omega = qv$, q is the phonon wave vector and v is the phonon propagation velocity, T is the temperature, k_B is the Boltzmann constant. For $T = 4\,K$, the relaxation time is 17 ms, suggesting that the qubit can easily be operated at this temperature.

Although we have used a simple parabolic model for the in-plane QD confinement, our conclusions are very general. Firstly, the dephasing optimal operation point will be present for potentials of arbitrary complexity (for example hut wire geometries), since it is due to the fundamental interplay between the HH and LH that gives rise to the Rashba spin-orbit coupling in the HH manifold. Secondly, we have examined the possibility that the insensitivity of the g-factor to in-plane electric fields is an artefact of the model. We have tested three deviations from parabolicity and found that none of them exposes the qubit to dephasing by fluctuating in-plane electric fields. This implies (i) that the dot does not have to be perfectly parabolic allowing for some flexibility in the gate structure; (ii) that in-plane electric field fluctuations generally have a negligible effect on the g-factor, while out-of-plane electric field fluctuations cause fluctuations in the Rashba spin-orbit coupling and affect the g-factor, therefore it is most important to avoid the effect of the out-of-plane

field; and (iii) that dephasing at the optimal operation point itself comes about primarily from higher-order terms in the electrical potential, i.e., electrical quadrupole and higher. Our results hold qualitatively in Si as well, where the spin-orbit interaction is weaker than in Ge, while δ is larger. However, the large δ and frequent failure of the Schrieffer-Wolff approximation in Si calls for fully numerical treatment.

3.4 Conclusion and Outlook

Experimentally, the configuration we describe requires a double-gated device with separate plunger gates and barrier gates allowing the number density and the gate electric-field (and spin-orbit coupling) to be controlled independently. The numerical estimates above suggest that, in general, a smooth and broad optimal operation point will enable the Ge hole qubit to work insensitively to the charge noise inside a large range of gate electric fields accessible to experiment. Exchange-based two-qubit gates should be possible for hole QDs, and their speed depends on the values of exchange obtained, which are expected to be tunable by gates. Moreover, it is likely to simplify the coupling between the two qubits since the valley degree of freedom is absent in hole systems. However, a two-qubit gate in the setup discussed here is not optimized for long-distance coupling, which leads to the two-qubit gate time is of the order of microseconds for dipole-dipole interactions and hundreds of microseconds for circuit QED, limited by the Ge Luttinger parameters. They can be sped up by enhancing the spin-orbit interaction, but we defer the discussion to a future publication.

A smaller g-factor will lead to a smaller Rabi frequency, a smaller change in the qubit Zeeman splitting due to the spin-orbit interaction, and a shorter dephasing time but a longer relaxation time and an improved Rabi ratio. The optimal operation point will not change its location, which is determined only by the effective mass and the width of the quantum well. A larger quantum dot radius would make the confinement energy smaller, increasing the effect of the spin-orbit interaction and resulting in a faster Rabi frequency, but also shorter T_1 and T_2^*. Nevertheless, the Rabi ratio decreases with increasing dot

radius. Moreover, since the confinement energy decreases as the square of the radius, it is preferable to work at smaller radii to ensure the thermal broadening is overcome. Increasing x increases the heavy hole - light hole splitting, leading to a reduced Rashba spin-orbit coupling and a smaller change in the qubit Zeeman splitting. The change in the Zeeman splitting will be large for smaller x e.g., 0.05-0.10, while at $x = 0.3$ it is essentially not noticeable.

We have demonstrated that electrostatically defined hole quantum dot spin qubits naturally exhibit an optimal operation point at which sensitivity to charge noise is minimized while the speed of electrical operation is maximized. The location of the optimal operation point can be determined from the width of the quantum well and the strain tensors applied. Relaxation times are long even at 4 K, while dephasing is determined by higher-order terms in the expansion of the electrostatic potential due to charge defects, but are expected to allow for a large window of operation around the optimal operation point. Our results provide a theoretical guideline for achieving fast, highly coherent, low-power electrically operated spin qubits experimentally. Future studies must consider in-plane magnetic fields, which interact much more weakly with HH spins and are more complicated to treat theoretically.

Chapter 4

Silicon hole spin qubit

The main content of this chapter is an adaption of a publication Ref. [533] by the candidate (accepted by Phys. Rev. B , waiting for publish [1]). I would like to express acknowledgement to all the co-authors: Abhikbrata Sarkar, S. D. Liles, Andre Saraiva, A. S. Dzurak, A. R. Hamilton, and Dimitrie Culcer.

Silicon hole quantum dots have been the subject of considerable attention thanks to their strong spin-orbit coupling enabling electrical control, a feature that has been demonstrated in recent experiments combined with the prospects for scalable fabrication in CMOS foundries. The physics of silicon holes is qualitatively different from germanium holes and requires a separate theoretical description, since many aspects differ substantially: the effective masses, cubic symmetry terms, spin-orbit energy scales, magnetic field response, and the role of the split-off band and strain. In this work, we theoretically study the electrical control and coherence properties of silicon hole dots with different magnetic field orientations, using a combined analytical and numerical approach. We discuss possible experimental configurations required to obtain a sweet spot in the qubit Larmor frequency, to optimize the electric dipole spin resonance Rabi time, the phonon relaxation time, and the dephasing due to random telegraph noise. Our main findings are: (i) The

[1] Online link: https://journals.aps.org/prb/accepted/4107dO4dWf512b4b87b942a39c3de0126130321a3

in-plane g-factor is strongly influenced by the presence of the split-off band, as well as by any shear strain that is typically present in the sample. The g-factor is a non-monotonic function of the top gate electric field, in agreement with recent experiments. This enables coherence sweet spots at specific values of the top gate field and specific magnetic field orientations. (ii) Even a small ellipticity (aspect ratios ~ 1.2) causes significant anisotropy in the in-plane g-factor, which can vary by $50\% - 100\%$ as the magnetic field is rotated in the plane. This is again consistent with experimental observations. (iii) electric dipole spin resonance Rabi frequencies are comparable to Ge, and the ratio between the relaxation time and the electric dipole spin resonance Rabi time $\sim 10^5$. For an out-of-plane magnetic field the electric dipole spin resonance Rabi frequency is anisotropic with respect to the orientation of the driving electric field, varying by $\approx 20\%$ as the driving field is rotated in the plane. Our work aims to stimulate experiments by providing guidelines on optimizing configurations and geometries to achieve robust, fast and long-lived hole spin qubits in silicon.

4.1 Introduction

Silicon quantum devices have emerged as an ideal platform for scalable quantum computation, with remarkable advancements both theoretically and experimentally in recent years [308, 236, 372, 270, 197, 358, 579, 234, 209, 434, 433, 508, 222, 56, 563, 499, 1, 244, 206, 205, 260, 274, 68, 256, 189, 76, 7, 151, 346, 438, 306, 49, 84, 264, 31]. Silicon devices offer several advantages, including weak hyperfine interaction with the possibility of isotopic purification to eliminate the hyperfine coupling altogether [493, 78, 398, 563, 392, 50, 368], absence of piezoelectric phonons [477, 283], and mature silicon microfabrication technology [172, 396, 334, 507, 335, 463, 535, 203, 483, 98, 165], making them competitive candidates to realize industrial-level scalable quantum computing architectures. Over the past few decades, numerous design proposals for qubits utilizing silicon quantum devices have been actively investigated, including the singlet-triplet transition qubit [334], single electron spin qubit [396, 243, 478], and acceptor or donor spin qubit

[61, 234, 432, 497, 434, 203]. Among the various platforms, silicon hole spin qubits exhibit additional desirable properties [425, 420, 577, 578, 489, 125, 320, 477, 208, 518, 376, 253, 333, 345, 169, 138, 323, 446]. Firstly, hole systems possess strong spin-orbit coupling [545, 546, 114, 103, 324, 251, 252, 79, 140, 356, 38, 347, 348, 329, 483, 2, 291, 412], which enables pure electrical manipulation of spin states via electric dipole spin resonance [188, 64, 413, 414], while the hole spin-3/2 is responsible for physics with no counterpart in electron systems [548, 103, 547, 302, 1, 110, 182, 152]. Secondly, the absence of valley degeneracy avoids complications associated with the increase in Hilbert space that occurs for electrons [190, 167, 106, 107, 166, 199, 432, 48, 56, 155, 519, 462, 520]. Thirdly, whereas the hyperfine interaction is a strong decoherence source in other materials such as III-V group semiconductors [226, 247, 90, 389, 271, 159, 89, 158, 77, 20, 78, 252, 398, 526], silicon can be isotopically purified [227, 493, 243, 478, 508, 222, 395]. Recent years have witnessed key experiments on silicon hole qubits, including successful demonstrations on industrial standard complementary metal-oxide-semiconductor (CMOS) technologies [214, 518, 508, 376, 266, 463, 222, 99, 285, 539, 461, 229], control of the number of holes and shell filling [578, 294], g-tensor manipulation in both nanowire and quantum dot systems [518, 99, 539, 295], qubit operation at 25 K in the few-hole regime [453], single qubit operation above 4 K [73], long coherence time up to 10 ms in Si:B acceptors [256], dispersive readout [376, 380, 98, 138, 148, 427], Pauli spin blockade [286, 46], coupling between photons and hole spins [564], and the demonstration of the coupling between two hole qubits via anisotropic exchange [181].

In parallel with developments in silicon, considerable attention has been devoted to hole spin qubits in germanium [394, 135, 521, 349, 204, 436, 305, 200, 275, 177, 556, 205, 484, 440, 230, 532, 207, 361, 52, 494, 301, 525, 331, 5, 525]. This includes spin state measurement and readout [420, 578, 569, 288, 241, 170], electrical control of spin states [400], g-tensor manipulation [17, 58, 46, 536, 312, 537, 349, 572], coupling to a superconducting microwave resonator [290], fast electric dipole spin resonance Rabi oscillations up to 540 MHz [530] and relaxation times of up to 32 ms [275, 276]. Nevertheless, the understanding gained from the study of germanium hole qubits cannot be directly translated to silicon. In silicon, the split-off energy is very small (44 meV) compared with gallium

arsenide (340 meV) and germanium (296 meV) [393, 74], necessitating the use of a full six-band Luttinger-Kohn model[315, 23, 24, 9, 309, 565, 63, 88, 450, 328]. Additionally, the larger effective mass of holes in silicon requires smaller dots to achieve the same orbital confinement energy splitting. The strength of the spin-orbit coupling in silicon is weaker than in germanium, while the cubic symmetry parameters are very strong and cannot be accounted for perturbatively. Moreover, previous studies have shown that, for silicon two-dimensional hole gases at experimentally relevant densities, the Schrieffer-Wolff transformation cannot be used to reduce the three-dimensional Hamiltonian to an effective two-dimensional one since the criteria for the applicability of the Schrieffer-Wolff transformation are not satisfied [328, 10]. Furthermore, the orbital magnetic field terms are not captured by such a Schrieffer-Wolff transformation, which will play an important role when the magnetic field is applied perpendicular to the gate electric field. Finally, strain effects in silicon are different from those in other materials, with axial and shear strains strongly affecting both spin dynamics and the in-plane g-factor in planar quantum dots. In particular, spatial strain gradients caused by thermal contraction of the gate electrodes have a very large effect in silicon due to the thin gate oxide [295].

Theoretical studies on silicon hole qubits have also advanced rapidly in line with experimental progress. The physics of spin-orbit coupling in silicon hole systems have been investigated with the aim of realizing fully electrically operated spin qubits [328, 253]. Studies have examined device geometry, dot orientation, and strain in the silicon quantum dot to optimize the quality of the electric dipole spin resonance Rabi frequency and qubit Larmor frequency. These studies have identified optimal operation points and the possibility of achieving fast electric dipole spin resonance Rabi oscillations even with small spin-orbit coupling in silicon hole systems [509, 345, 355, 53, 169, 406, 6, 54, 156]. Decoherence due to hyperfine interactions and dephasing due to charge noise have also been studied, identifying experimental configurations for ultra-fast and highly coherent silicon hole spin qubits [392, 50, 323, 446]. However, despite significant progress in both experiment and theory, a critical question remains unanswered: *When is it possible to minimize unwanted decoherence effects without reducing the efficiency of electric dipole spin resonance?*

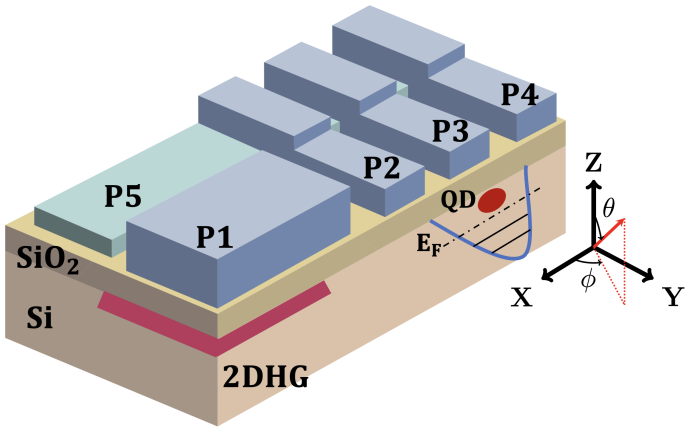

Figure 4.1: **Schematic planar silicon quantum dot**. In this specific design, we focus on a single hole quantum dot in the silicon layer. By applying a gate electric field F_z via gate P1, holes accumulate in silicon and are confined vertically against the silicon oxide (indicated at the location of the two-dimensional hole gas). The single quantum dot is formed using gates P2-P5. The gates P2 and P4 provide confinement in the $\hat{x}$-direction, while gate P5 provides confinement in the y direction. P3 is used as the top gate of the quantum dot, accumulating a single hole in the potential well beneath. The resulting potential is indicated schematically below the gates. On the right, we plot the coordinate system with an arbitrary vector colored in red. The vectors indicate the orientations of the polar and azimuthal angles.

In this chapter, we focus on electrically-driven single hole spin qubits in planar silicon quantum dots and describe qubit dynamics in both perpendicular and in-plane magnetic fields. We adopt a hybrid analytical and computational approach which enables us to treat quantum dots with arbitrary confinement in a magnetic field of arbitrary orientation. For a perpendicular magnetic field we show that coherence sweet spots exist at certain values of the top gate field, which reflect the coupling of heavy- and light-hole states by the gate electric field. The EDSR Rabi frequency exhibits a maximum as a function of the top gate field, as does the relaxation rate. The large Rabi ratios (the ratio between the phonon relaxation time and the EDSR Rabi time) can be achieved, in excess of 10^6 at very small in-plane driving electric fields of 1 kV/m. For an in-plane magnetic field, we demonstrate that the qubit Zeeman splitting exhibits a large modulation as a function of the top gate electric field. Although extrema in the qubit Zeeman splitting exist as a function of the top gate field, these do not protect against charge noise, and one cannot identify coherence sweet spots, since the qubit is exposed to all three components of the

noise electric field. At the same time, we find that the EDSR Rabi frequency reaches a maximum of about 100 MHz, with a minimum relaxation time of 1 ms, yielding a Rabi ratio of approximately 10^5 for an in-plane driving electric field of 1 kV/m. Importantly, the g-factor of elliptical dots is strongly anisotropic, with a very small aspect ratio (1.2) yielding a factor of 0.7-1.6 variation as the magnetic field is rotated in the plane. This is consistent with recent experimental observations [295]. Finally, we compare the properties and fabrication technologies of silicon and germanium and demonstrate that shear strain and axial strain are key factors leading to a large modulation of in-plane g-factors and the large Rabi ratio. The EDSR Rabi frequencies for a given in-plane driving electric field are comparable in the two materials, which may reflect the fact that, while Ge has stronger spin-orbit coupling, Si has larger cubic symmetry terms $\propto (\gamma_3 - \gamma_2)$, which enhance the effective spin-orbit coupling experienced by planar dots. Whereas we use characteristic values of the strain tensor components extracted from experiment, further investigation is needed to understand the role of strain and of the strain distribution throughout the sample.

The chapter is organized as follows. In Section 4.2, we introduce the Hamiltonian for the silicon hole quantum dot with an arbitrary magnetic field orientation, discuss the diagonalization technique, and outline the methodology used to determine the EDSR Rabi frequency, relaxation time due to phonons, and dephasing time due to random telegraph noise. In Section 4.3, we present the results in the presence of a perpendicular magnetic field as well as an in-plane magnetic field. We discuss the effect of ellipticity of the quantum dot and g-factor anisotropy in line with experimental observations. In Section 4.4, we compare the properties of silicon hole qubits with germanium hole qubits from the perspective of material parameters and fabrication details. We end with a summary and conclusions.

4.2 Model and Methodology

In this section, we elucidate the properties of a single silicon hole spin qubit by introducing the model device and relevant experimental parameters. Furthermore, we provide a detailed discussion on the physical origin of the strain Hamiltonian, confinement Hamiltonian, and Zeeman Hamiltonian, respectively, in the context of the envelope function approximation Hamiltonian H. We also introduce the details of the numerical diagonalization used to obtain the relevant energy levels and wave-functions of the system. Then, we present the formalism used to estimate the EDSR Rabi frequency, relaxation time, and dephasing time.

A schematic diagram of a possible realization of a silicon hole spin qubit is described in Fig. 4.1. The gate electric field is applied along the $\hat{z}$-direction, denoted by $\boldsymbol{F} = (0, 0, F_z)$. Our model is designed to describe a generic magnetic field $\boldsymbol{B} = (B_x, B_y, B_z)$ as illustrated in Fig. 4.1, using the vector potential $\boldsymbol{A} = -(B_z y, B_x z, B_y x)$. We consider magnetic fields either in the xy-plane or parallel to the $\hat{z}$-direction (perpendicular to the qubit plane); we do not consider magnetic fields tilted out of the plane in this work.

4.2.1 Diagonalization of silicon hole spin qubit Hamiltonian

The total Hamiltonian for a single silicon hole quantum dot qubit is given by:

$$H = H_{\text{LKBP}} + H_{\text{conf}} + H_{\text{gate}} + H_{\text{Zeeman}} \tag{4.1}$$

The perpendicular electric confinement potential is represented by $H_{\text{gate}} = eF_z z$ for z $\in [-L/2, L/2]$, where L denotes the width of the quantum well in the $\hat{z}$-direction. This gate field induces structural inversion asymmetry (SIA) in the silicon hole system, thereby leading to a Rashba spin-orbit coupling. Moreover, the symmetry of the diamond lattice ensures there is no Dresselhaus-type spin-orbit coupling [137, 173, 70, 192, 339, 357, 326]. Although interface misalignment may induce Dresselhaus-type spin-orbit coupling, it is expected to be negligible for the purposes of this chapter [328], and is therefore not

considered. In-plane confinement is modeled by a two-dimensional harmonic oscillator potential

$$H_{\text{conf}} = \frac{\hbar^2}{2m^* a_x^4} x^2 + \frac{\hbar^2}{2m^* a_y^4} y^2 \tag{4.2}$$

where m^* is the in-plane effective mass, and a_x and a_y are the two axes of an elliptical dot.

The Zeeman Hamiltonian can be written as:

$$H_{\text{Zeeman}} = -2\kappa_1 \mu_B \boldsymbol{J} \cdot \boldsymbol{B} - 2\kappa_2 \mu_B \boldsymbol{J}_3 \cdot \boldsymbol{B} \tag{4.3}$$

, where $\boldsymbol{J} = (J_x, J_y, J_z)$ represents the angular momentum matrices for the direct sum of the spin-3/2 and spin-1/2 systems. The explicit matrix form of expressions for $\boldsymbol{J}$ can be found in the supplementary material. Additionally, in the an-isotropic term in the Zeeman Hamiltonian, we have $\boldsymbol{J}_3 = (J_x^3, J_y^3, J_z^3)$. μ_B is the Bohr magneton, and $\kappa_1 = -0.42$, $\kappa_2 = 0.01$ for silicon.

The quantum dot studied in this chapter is produced by confining a two-dimensional hole gas in a metal-oxide-semiconductor structure grown along the $\hat{z} \parallel [001]$ direction. The strong heavy hole - light hole splitting results in angular momentum quantization perpendicular to the two-dimensional plane. The heavy-hole states are characterized by a $\hat{z}$-component of the angular momentum $|J = 3/2, M = \pm 3/2\rangle$, the light-hole states are characterized by $|J = 3/2, M = \pm 1/2\rangle$, while the split-off valence band has $|J = 1/2, M = \pm 1/2\rangle$. We orient the wave vectors k_x, k_y, k_z along [100], [010], and [001], respectively. The valence band and the effect of strain can be described by the Luttinger-Kohn-Bir-Pikus (LKBP) Hamiltonian in the basis of total angular momentum eigenstates:

$$\left|\frac{3}{2}, \frac{3}{2}\right\rangle, \left|\frac{3}{2}, -\frac{3}{2}\right\rangle, \left|\frac{3}{2}, \frac{1}{2}\right\rangle, \left|\frac{3}{2}, -\frac{1}{2}\right\rangle, \left|\frac{1}{2}, \frac{1}{2}\right\rangle, \left|\frac{1}{2}, -\frac{1}{2}\right\rangle \tag{4.4}$$

The six-band Luttinger-Kohn Hamiltonian is:

$$H_{\mathrm{LK}} = \begin{bmatrix} P+Q & 0 & -S & R & -\frac{1}{\sqrt{2}}S & \sqrt{2}R \\ 0 & P+Q & R^* & S^* & -\sqrt{2}R^* & -\frac{1}{\sqrt{2}}S^* \\ -S^* & R & P-Q & 0 & -\sqrt{2}Q & \sqrt{\frac{3}{2}}S \\ R^* & S & 0 & P-Q & \sqrt{\frac{3}{2}}S^* & \sqrt{2}Q \\ -\frac{1}{\sqrt{2}}S^* & -\sqrt{2}R & -\sqrt{2}Q^* & \sqrt{\frac{3}{2}}S & P+\Delta & 0 \\ \sqrt{2}R^* & -\frac{1}{\sqrt{2}}S & \sqrt{\frac{3}{2}}S^* & \sqrt{2}Q^* & 0 & P+\Delta \end{bmatrix} \tag{4.5}$$

$$P = \frac{\hbar^2}{2m_0}\gamma_1 k_z^2 + \frac{\hbar^2}{2m_0}\gamma_1(k_x^2+k_y^2) \tag{4.6}$$

$$Q = -2\frac{\hbar^2}{2m_0}\gamma_2 k_z^2 + \frac{\hbar^2}{2m_0}(k_x^2+k_y^2) \tag{4.7}$$

$$P+Q = \frac{\hbar^2}{2m_0}\left(\gamma_1-2\gamma_2\right)k_z^2 + \frac{\hbar^2}{2m_0}\left(\gamma_1+\gamma_2\right)\left(k_x^2+k_y^2\right) \tag{4.8}$$

$$P-Q = \frac{\hbar^2}{2m_0}\left(\gamma_1+2\gamma_2\right)k_z^2 + \frac{\hbar^2}{2m_0}\left(\gamma_1-\gamma_2\right)\left(k_x^2+k_y^2\right) \tag{4.9}$$

$$R = \sqrt{3}\frac{\hbar^2}{2m_0}\left[-\gamma_2\left(k_x^2-k_y^2\right)+2i\gamma_3 k_x k_y\right] \tag{4.10}$$

$$S = 2\sqrt{3}\frac{\hbar^2}{2m_0}\gamma_3\left(k_x k_z - i k_y k_z\right) \tag{4.11}$$

Here $\gamma_1 = 4.285, \gamma_2 = 0.339, \gamma_3 = 1.446$ are the Luttinger parameters for silicon [124, 417], m_0 is the bare electron mass and $\hbar$ is the Planck constant. Terms with subscripts ε are matrix elements from the Bir-Pikus (BP) Hamiltonian:

$$H_{\mathrm{BP}} = \begin{bmatrix} P_\varepsilon+Q_\varepsilon & 0 & -S_\varepsilon & R_\varepsilon & -\frac{1}{\sqrt{2}}S_\varepsilon & \sqrt{2}R_\varepsilon \\ 0 & P_\varepsilon+Q_\varepsilon & R_\varepsilon^* & S_\varepsilon^* & -\sqrt{2}R_\varepsilon^* & -\frac{1}{\sqrt{2}}S_\varepsilon^* \\ -S_\varepsilon^* & R_\varepsilon & P_\varepsilon-Q_\varepsilon & 0 & -\sqrt{2}Q_\varepsilon & \sqrt{\frac{3}{2}}S_\varepsilon \\ R_\varepsilon^* & S_\varepsilon & 0 & P_\varepsilon-Q_\varepsilon & \sqrt{\frac{3}{2}}S_\varepsilon^* & \sqrt{2}Q_\varepsilon \\ -\frac{1}{\sqrt{2}}S_\varepsilon^* & -\sqrt{2}R_\varepsilon & -\sqrt{2}Q_\varepsilon^* & \sqrt{\frac{3}{2}}S_\varepsilon & P_\varepsilon & 0 \\ \sqrt{2}R_\varepsilon^* & -\frac{1}{\sqrt{2}}S_\varepsilon & \sqrt{\frac{3}{2}}S_\varepsilon^* & \sqrt{2}Q_\varepsilon^* & 0 & P_\varepsilon \end{bmatrix} \tag{4.12}$$

where

$$P_\varepsilon = -a_v\left(\varepsilon_{xx}+\varepsilon_{yy}+\varepsilon_{zz}\right) \tag{4.13}$$

$$Q_\varepsilon = -\frac{b_v}{2}\left(\varepsilon_{xx}+\varepsilon_{yy}-2\varepsilon_{zz}\right) \tag{4.14}$$

$$R_\varepsilon = \frac{\sqrt{3}}{2}b_v\left(\varepsilon_{xx}-\varepsilon_{yy}\right) - id_v\varepsilon_{xy} \tag{4.15}$$

$$S_\varepsilon = -d_v\left(\varepsilon_{xz}-i\varepsilon_{yz}\right) \tag{4.16}$$

$$P_\varepsilon + Q_\varepsilon = -\left(a_v+\frac{b_v}{2}\right)\varepsilon_{xx} - \left(a_v+\frac{b_v}{2}\right)\varepsilon_{yy} - (a_v-b_v)\varepsilon_{zz} \tag{4.17}$$

$$P_\varepsilon - Q_\varepsilon = -\left(a_v-\frac{b_v}{2}\right)\varepsilon_{xx} - \left(a_v-\frac{b_v}{2}\right)\varepsilon_{yy} - (a_v+b_v)\varepsilon_{zz} \tag{4.18}$$

The material parameter $a_v = 2.38\,\text{eV}$ is the hydro-static deformation potential constant, $b_v = -2.10\,\text{eV}$ is the uni-axial deformation potential constant, $d_v = -4.85\,\text{eV}$ is the shear deformation potential constant [552, 213, 94]. The strain $\varepsilon_{i,j}$ where $i,j \in \{x,y,z\}$ is determined by experimental configurations and fabrication processes.

In a quantum dot placed in a magnetic field, the momentum operators in the Luttinger-Kohn Hamiltonian are modified by the gauge potentials. The new canonical conjugate momentum operators are given by $\boldsymbol{p}+e\boldsymbol{A}$. To numerically diagonalize the total Hamiltonian H, the wave functions we used are as follows:

$$\Psi_{n_x,n_y,n_z,i}(x,y,z) = \phi_{n_z}(z)\phi_{n_x}(x)\phi_{n_y}(y)\left|\chi_i\right\rangle \tag{4.19}$$

where n_x, n_y, n_z are the level numbers of the spatial wave functions and $|\chi_i\rangle$ is the i-th spinor.

The selection of wave functions depends on the shape of the confinement potentials, which necessitates the self-consistent solution of Poisson and Schrödinger equations to account for the density-dependent properties of a device. Previous studies have demonstrated the efficiency of the variational approach in gallium arsenide and germanium [328]. However, the numerical generalization of the variational method becomes challenging as the number of energy levels increases. Our approach is to determine a set of complete wave functions in all directions, using a sufficient number of energy levels to include the geometry of the quantum confinements.

For $\hat{z}$-direction, where our focus is on a triangular quantum well $eF_z z$, we select sinusoidal wave functions derived from an infinite square well positioned symmetrically between $z \in [-L/2, L/2]$. Incorporating the boundary conditions, these orthonormal complete set of wave functions are

$$\phi_{n_z}(z) = \sqrt{\frac{2}{L}} \cos\left(\frac{n_z \pi z}{L}\right) \quad \text{for } n_z = 1, 3, 5, \ldots \tag{4.20}$$

$$\phi_{n_z}(z) = \sqrt{\frac{2}{L}} \sin\left(\frac{n_z \pi z}{L}\right) \quad \text{for } n_z = 2, 4, 6, \ldots \tag{4.21}$$

The in-plane wave functions we use are eigenstates of the two-dimensional harmonic oscillator:

$$\phi_{n_x}(x) = \frac{\pi^{-1/4}}{\sqrt{2^n n!}} \frac{1}{\sqrt{a_x}} \exp\left(-\frac{x^2}{2a_x^2}\right) H_{n_x}\left(\frac{x}{a_x}\right), \tag{4.22}$$

$$\phi_{n_y}(y) = \frac{\pi^{-1/4}}{\sqrt{2^n n!}} \frac{1}{\sqrt{a_y}} \exp\left(-\frac{y^2}{2a_y^2}\right) H_{n_y}\left(\frac{y}{a_y}\right), \tag{4.23}$$

where the confinement frequency can be expressed as:

$$\omega_{x,y} = \frac{\hbar}{m^* a_{x,y}^2} \tag{4.24}$$

H_n represents Hermitian polynomials. To obtain high accuracy in numeric, we adopt 8 levels of Eq. 4.20, 14 levels of Eq.4.22, and 14 levels of 4.23. We can then diagonalize the Hamiltonian H for specific device geometries, strains, electric fields, and magnetic fields in the basis introduced in Eq. 4.19-4.23. After performing the diagonalization, the ground state of the qubit Hamiltonian will be denoted by $|\mathbb{0}\rangle$ with energy $E_{\mathbb{0}}$, the first excited state will be denoted by $|\mathbb{1}\rangle$ with energy $E_{\mathbb{1}}$ and the qubit Zeeman splitting will be defined by $\Delta E_z = E_{\mathbb{1}} - E_{\mathbb{0}}$.

4.2.2 EDSR frequency and phonon relaxation time

Electric dipole spin resonance (EDSR) methods are widely used to coherently drive transitions between spin states in silicon hole spin qubits. Within the ground state orbital, the spin of a hole qubit can be rotated by an alternating microwave signal (an alternating in-plane electric field), the frequency of this microwave signal should be matched with

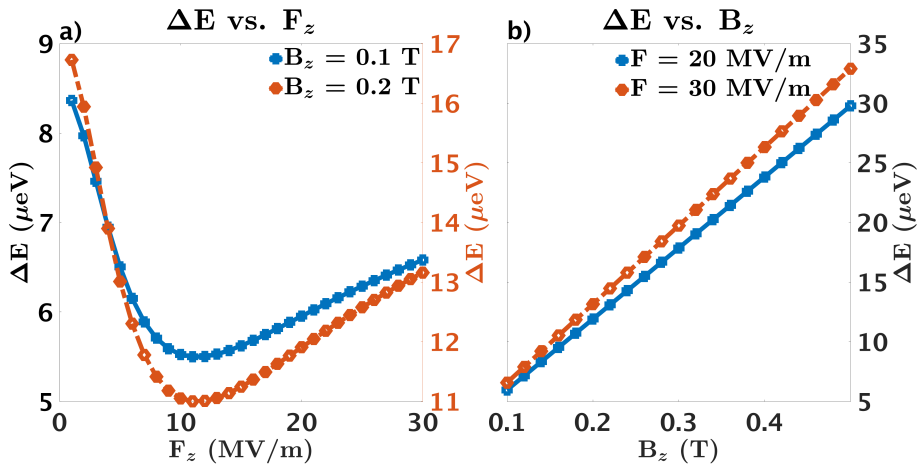

Figure 4.2: **Qubit Zeeman splitting for an out-of-plane magnetic field $\mathbf{B_z}$.** a) The qubit Zeeman splitting ΔE is plotted as a function of the gate electric field F_z for two different out-of-plane magnetic field strengths, B_z=0.1 T (solid line with square markers) and B_z=0.2 T (dashed line with diamond markers). A flat local minimum of the qubit Zeeman splitting is observed as a function of the gate electric field. b) The qubit Zeeman splitting ΔE is plotted as a function of the out-of-plane magnetic field B_z for two different top gate field strengths, F_z=20 MV/m (solid line with square markers) and F_z=30 MV/m (dashed line with diamond markers). The parameters used to generate all the figures in this chapter are provided in Table 4.1

the qubit Zeeman splitting ΔE_z. Therefore, the EDSR frequency can be calculated by evaluating the transition matrix element

$$f_{\text{Rabi}} = \frac{e}{h}\|\langle \mathbb{1}|\boldsymbol{r}\cdot\boldsymbol{E}_{\text{AC}}|\mathbb{0}\rangle\| \tag{4.25}$$

In our case, the in-plane alternating driving electric field E_{AC} is set to be 1 kV/m.

The phonon relaxation time can be calculated using the method detailed in numerous studies [245, 550, 565, 309, 476, 62, 63, 465, 489, 450, 218, 283]. Unlike III-V semiconductors, silicon and germanium do not have piezoelectric phonons due to their non-polar nature [477, 283]. We assume that the silicon hole spin qubit is coupled with a thermal bath of bulk acoustic phonons along the polarization direction $\alpha \in \ell, t_1, t_2$ (one longitudinal direction and two transverse directions), with phonon wave vectors denoted by $\boldsymbol{q}$. The energy of the acoustic phonons is $\hbar\omega_{\alpha,\boldsymbol{q}}$. To calculate the phonon relaxation time, we

consider the hole-phonon interaction Hamiltonian:

$$H_{\mathrm{hp}}^{\alpha}=\sum_{i,j}D_{i,j}\varepsilon_{i,j}^{\alpha}(\boldsymbol{r}) \tag{4.26}$$

for $i,j\in\{x,y,z\}$, where $D_{i,j}$ are deformation potential matrices. The detailed matrix elements can be found in the chapter. 2. The local strain $\varepsilon_{i,j}^{\alpha}(\boldsymbol{r})$ has the form

$$\varepsilon_{i,j}^{\alpha}=\frac{i}{2}q\sqrt{\frac{\hbar}{2\rho V_c\omega_{\alpha,\boldsymbol{q}}}}\epsilon_{i,j}^{\alpha}\left(e^{-i\boldsymbol{q}\cdot\boldsymbol{r}}\hat{a}_{\alpha,\boldsymbol{q}}^{\dagger}+e^{i\boldsymbol{q}\cdot\boldsymbol{r}}\hat{a}_{\alpha,\boldsymbol{q}}\right) \tag{4.27}$$

where

$$\epsilon_{i,j}^{\alpha}=\hat{e}_i^{\alpha}\frac{q_j}{q}+\hat{e}_j^{\alpha}\frac{q_i}{q} \tag{4.28}$$

is a symmetric 3×3 matrix, $\hat{e}$ is the unit vector in the direction of phonon propagation. The transition rate between the first excited state $E_{\mathbb{1}}$ and the ground state $E_{\mathbb{0}}$ due to spontaneous phonon emission can be obtained from Fermi's golden rule:

$$\Gamma^{\alpha}=\frac{2\pi}{\hbar}\int_0^{\infty}\int_0^{2\pi}\int_0^{\pi}\left\|\langle\mathbb{0},N_q+1|H_{\mathrm{hp}}^{\alpha}|\mathbb{1},N_q\rangle\right\|^2q^2\delta\left[\left(\frac{E_{\mathbb{1}}-E_{\mathbb{0}}}{\hbar v_{\alpha}}\right)-q\right]\sin\theta\frac{V_c}{(2\pi)^3}\,\mathrm{d}\theta\,\mathrm{d}\phi\,\mathrm{d}q \tag{4.29}$$

where $V_c/(2\pi)^3$ is the reciprocal space density of states, N_q^{α} is the phonon occupation number following Bose-Einstein statistics:

$$N_q^{\alpha}=\left[\exp\left(\hbar\omega_{\boldsymbol{q}}^{\alpha}/\beta\right)-1\right]^{-1}\quad\beta=k_BT \tag{4.30}$$

, where T=0.1 K, and k_B is the Boltzmann constant. The phonon propagation velocity is different for different polarization directions, with $v_{\ell}=9000\,\mathrm{m/s}$ for the longitudinal direction, $v_{t_1}=v_{t_2}=5400\,\mathrm{m/s}$ for the other two transversal directions [552, 198, 213]. Our calculations assume a three-dimensional phonon bath, a choice predicated on the observation that the confinement dimensions of our device are of the same order of magnitude. However, it is important to recognize that phonon models in strongly confined materials present sophisticated challenges and warrant more detailed scrutiny. The specific geometry of the device plays a critical role in defining the relationship between the magnetic field's order and the phonon relaxation rate. For a comprehensive treatment of phonons in various dimensions, readers are referred to Ref. [283].

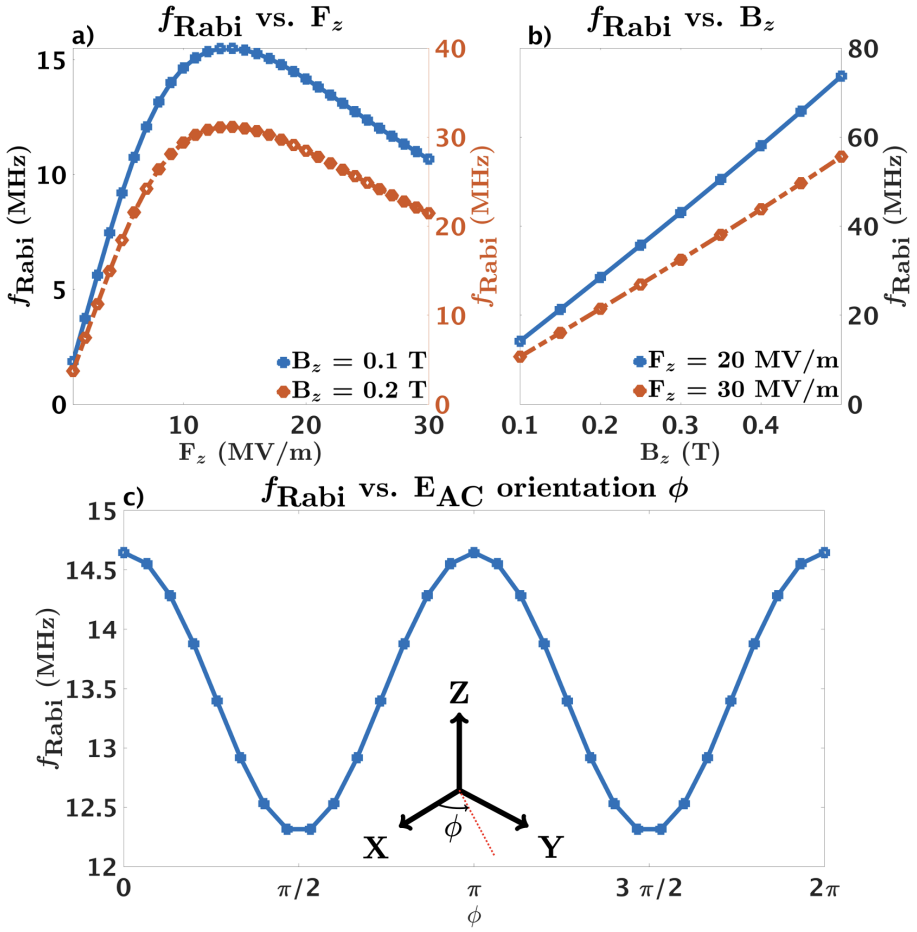

Figure 4.3: **EDSR Rabi frequency for an out-of-plane magnetic field $\mathbf{B}_z$.** a) The EDSR Rabi frequency f_{Rabi} is plotted as a function of the gate electric field F_z for two different out-of-plane magnetic field strengths: B_z=0.1 T (solid line with square markers) and B_z=0.2 T (dashed line with diamond markers). b) The EDSR Rabi frequency f_{Rabi} is shown as a function of the out-of-plane magnetic field B_z for two different gate electric field strengths: F_z=20 MV/m (solid line with square markers) and F_z=30 MV/m (dashed line with diamond markers). In this case, an in-plane AC electric field of 1 kV/m is applied along the $\hat{x}$-direction. c) The EDSR Rabi frequency f_{Rabi} is plotted as a function of the angle of the applied in-plane E_{AC} alternating driving electric field. The magnetic field is along the $\hat{z}$-direction with magnitude B_z=0.1 T. The top gate field is F_z=10 MV/m.

4.2.3 Random telegraph noise coherence time

In a silicon hole quantum dot system, the spin-orbit coupling induced by the top gate field exposes the hole spin qubit to charge noise, primarily from charge defects known as random telegraph noise (RTN) [496, 317]. The charge defects can lead to fluctuation in the qubit energy spectrum, resulting in qubit dephasing [104, 410, 102, 33, 424, 307, 323]. In our model, we particularly focus on two key sources of charge defects-induced dephasing: screened single charge defects and dipole charge defects.

For the purposes of this discussion we have chosen to focus on defects whose electric fields lie primarily in the plane of the qubit. This is because, as will emerge below, regardless of the orientation of the magnetic field, the qubit Larmor frequency exhibits extrema as a function of the top gate electric field. By operating the qubit at these extrema one can protect against fluctuations in the out-of-plane electric field. Thus fluctuations in the in-plane electric field are most detrimental to the qubit, and this is what our model focuses on.

The potential of a single defect can be modelled as [33, 532]:

$$U_{\text{scr}}(q) = \frac{e^2}{2\epsilon_0\epsilon_r} e^{-qd} \frac{\Theta\left(2k_F - q\right)}{q + q_{TF}}. \tag{4.31}$$

where q is the wave-vector, q_{TF} is the Thomas-Fermi wave-vector for silicon, which is independent of the density of holes, and k_F is the Fermi wave vector. The relevant values can be found in Table 4.1. Θ is the Heaviside step function. In position space, the single charge defect potential can be written as [118, 33].

$$U_{\text{scr}}(\boldsymbol{r}) = \frac{e^2}{4\pi\epsilon_0\epsilon_r} \frac{1}{q_{\text{TF}}^2} \left(\frac{1}{\|\boldsymbol{r} - \boldsymbol{r}_D\|^3} \right) \tag{4.32}$$

where $\boldsymbol{r}_D = (x_D, y_D, z_D)$ is the position vector of the single charge defect, taking the center of the quantum dot as the origin. For silicon, the relative electrical permeability is $\epsilon_r = 11.68$; ϵ_0 is the vacuum electrical permeability. The defect location x_D is set to be 30 nm from the center of the quantum dot. The resulting change in the dot's orbital splitting (the energy difference between the orbital ground state and first excited state)

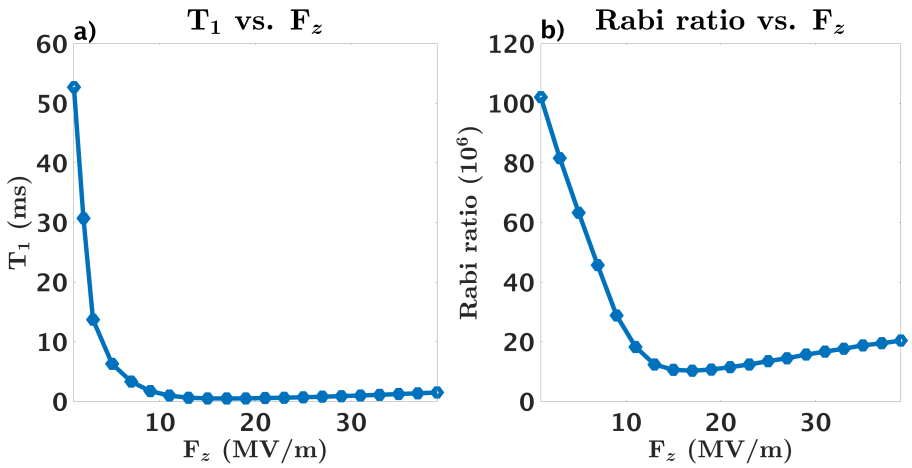

Figure 4.4: **Relaxation time and Rabi ratio for an out-of-plane magnetic field $\mathbf{B_z}$.** a) The single phonon relaxation time T_1 as a function of the gate electric field F_z is calculated for an out-of-plane magnetic field B_z=0.1 T. This relaxation time represents the characteristic time scale for the decay of the qubit due to phonon-hole interactions. b) The Rabi ratio is plotted as a function of the top gate electric field F_z when B_z=0.1 T. The Rabi ratio is around 10^6, which provides an indication of the efficiency of the qubit operation, with higher values indicating a stronger qubit coherence.

.

due to the defect is 1μeV at F_z=1 MV/m, consistent with Refs. [92, 93]. We also include dipole charge defects, with

$$U_{\text{dip}}(\boldsymbol{r}) = \frac{\boldsymbol{p}\cdot(\boldsymbol{r}-\boldsymbol{r}_D)}{4\pi\epsilon_0\epsilon_{\text{r}}(\boldsymbol{r}-\boldsymbol{r}_D)^3} \tag{4.33}$$

The dipole moment is $\boldsymbol{p} = e\boldsymbol{l}$, where $\boldsymbol{l}$ is the dipole vector. In our calculations, we assume the size of the dipole is 0.1 nm. The influence of the dipole charge defects on the dephasing time is typically much smaller than the influence due to single charge defects [102, 33, 304]. By considering both single charge defect and dipole charge defects, we can calculate the dephasing time in the quasi-static limit that estimates the upper bound of the dephasing time, denoted by:

$$T_2^* = \frac{2\pi}{\delta\omega} \tag{4.34}$$

In Silicon MOS devices, the single charge defects are the dominating source of noise leading to the qubit decoherence, however, the single charge defects are not active under the gate because there is no free electron to tunnel into, or out of the defect [102]. Dipole charge defects, which also grows naturally in amorphous solids, particularly in SiO_2 [113, 33]

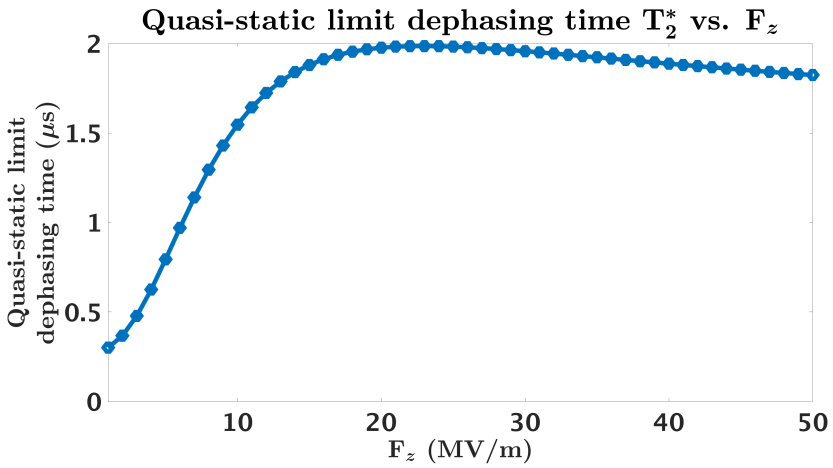

Figure 4.5: **Dephasing time in the quasi-static limit in an out-of-plane magnetic field B_z.** Both single charge defects and dipole charge defects are taken into account for an out-of-plane magnetic field B_z=0.1 T, but the dominant contribution to the dephasing potential comes from single charge defects. The dephasing time, which is estimated to be around 2 μs, exhibits a local maximum, suggesting the presence of an optimal operation point.

are active in the depleted region under the gate, but their electric field is much weaker than single charge defects. Hence for a qualitative understanding of planar hole qubit decoherence, we model a fluctuating single defect in the qubit plane situated further from the region under the gate.

However, the contribution to the regularization of the defect electric potential due to the gate-induced electric field screening can not be neglected. But it will require a device-specific modelling, which is outside the scope of this work. Furthermore, the potential of dipole charge defects tends to be static, which inherently limits the extent of screening [280, 523]. We note that single charge defects may in fact be active immediately under the gates if charges are able to tunnel into and out of the defect potential from the gate electrodes. This, however, does not change our model qualitatively, since the defect would still be modelled by a screened Coulomb potential. In our analysis we focus primarily on trends rather than absolute numbers (which will vary with the location of the defect) and we expect the physics to be qualitatively the same if the defect lies under the gate.

The single charge defects we considered is a description of the charge traps due to missing

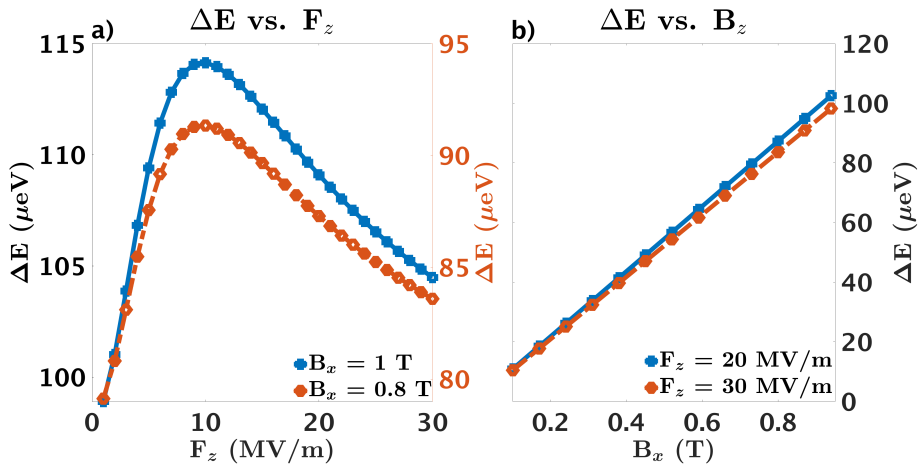

Figure 4.6: **Qubit Zeeman splitting for an in-plane magnetic field $\mathbf{B}_{\parallel}$.** a) The qubit Zeeman splitting ΔE is plotted as a function of the gate electric field F_z for two different in-plane magnetic field strengths: B_x=1 T (solid line with square markers) and B_x=0.8 T (dashed line with diamond markers). Notably, there is a flat local maximum observed around F_z=11 MV/m. b) The qubit Zeeman splitting is shown as a function of the in-plane magnetic field B_x=1 T for two different gate electric field strengths: F_z=20 MV/m (solid line with square markers) and F_z=30 MV/m (dashed line with diamond markers).

bonds during the growth of SiO_2 layer, the density of the single charge defects are highly temperature dependent depending on the method of fabrications [113]. In our calculations, we assume that the density of single charge defects are low enough that the electrical properties will not be altered. This local charge fluctuations due to charge traps is known as tunneling two-level system [381, 175, 330], which can be described by

$$V(t, \boldsymbol{r}) = (-1)^{N(t)} \times V(\boldsymbol{r}) \tag{4.35}$$

where $N(t)$ is a Poisson distribution taking value 0 or 1, with switching time τ. The random telegraph noise arises from isolated tunneling two-level system, leading to a dephasing [496, 317]. The Eq. 4.31 describes the potential that a hole will experienced in a trap. However, the real space expression does not have a closed analytical from [118], so an approximation form is used, which is Eq. 4.32 in our main text.

We note that this analysis is applicable only to a single defect giving rise to random telegraph noise. The realistic but more complicated case of $1/f$ noise for multiple defects will be considered in a forthcoming study.

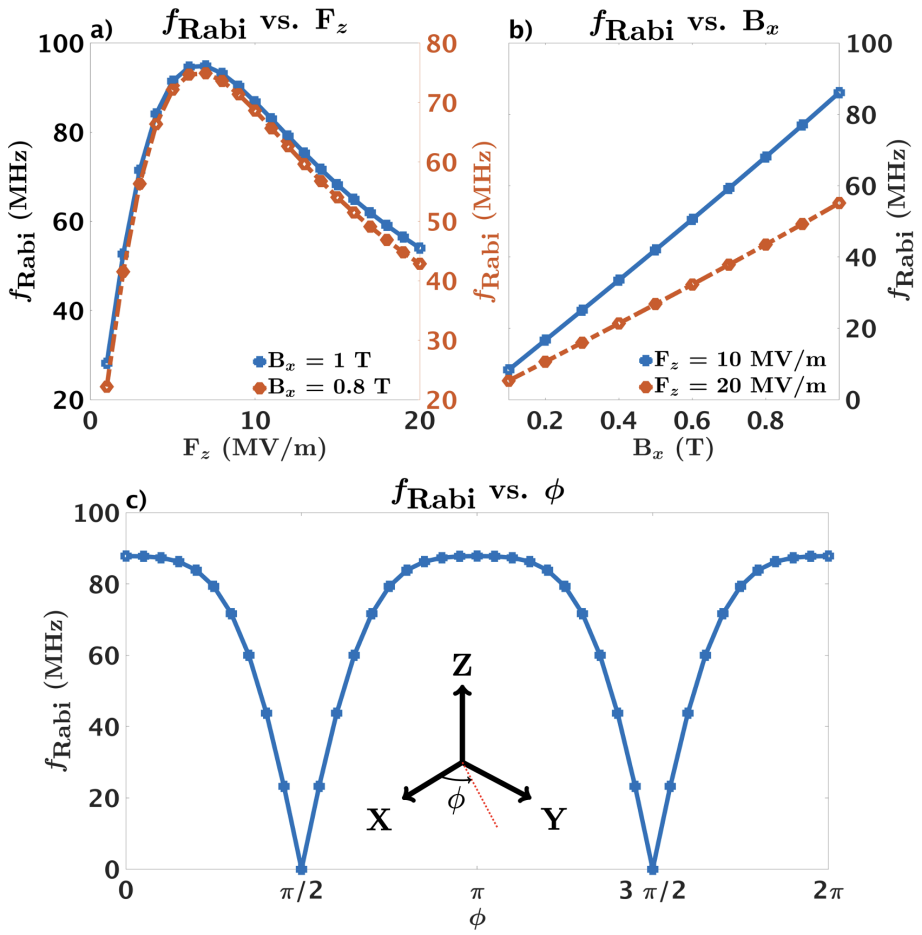

Figure 4.7: **EDSR Rabi frequency for an in-plane magnetic field $\mathbf{B}_{\parallel}$.** a) The EDSR Rabi frequency f_{Rabi} is plotted as a function of the gate electric field F_z for two different in-plane magnetic field strengths: B_x=1 T (solid line with square markers) and B_x=0.8 T (dashed line with diamond markers). b) The EDSR Rabi frequency f_{Rabi} is shown as a function of the in-plane magnetic field B_x=1 T for two different gate electric field strengths: F_z=10 MV/m (solid line with square markers) and F_z=20 MV/m (dashed line with diamond markers). c) The EDSR Rabi frequency f_{Rabi} is plotted as a function of the in-plane magnetic field orientation when B_x=1 T, F_z=10 MV/m, and the in-plane AC electric field remains at 1 kV/m along the $\hat{x}$-direction. The magnetic field is rotated through 2π in the xy-plane. Notably, the maximum EDSR Rabi frequency occurs when the magnetic field is aligned along the $\hat{x}$-direction, which coincides with the direction of the in-plane AC driving electric field.

4.3 Results and Discussion

In this section, we present the main findings of our numerical diagonalization. The section is divided into three parts, which focus on qubit dynamics in an out-of-plane magnetic field, dynamics in an in-plane magnetic field, and g-factor anisotropy respectively.

Our numerical model has identified extreme values of the qubit Zeeman splitting as a function of the top gate field for various parameters in different magnetic field orientations. This is because the vertical electric field creates two opposing Stark effects: it simultaneously increases the HH-LH gap and enhances the HH-LH coupling. The sweet spot is the point where these two sources of Stark shift cancel each other. At this point the variation of the qubit Zeeman splitting vanishes in the first order as a function of the gate electric field, as shown in Fig. 4.2 and Fig. 4.6. This non-linear behavior of the qubit Zeeman splitting leads to similar non-linearities in other important properties of the silicon hole spin qubits.

4.3.1 Out-of-plane magnetic field

The qubit Zeeman splitting ΔE_z as a function of the gate electric field F_z and the out-of-plane magnetic field B_z is plotted in Fig. 4.2. When B_z=0.1 T, the electric field can change the qubit Zeeman splitting by about 30%, and there is a local minimum in the qubit Zeeman splitting as a function of top gate field.

Next we discuss the EDSR Rabi frequency, shown in Fig. 4.3. We found that with an in-plane AC electric field of $\sim$ 1 kV/m applied along the $\hat{x}$-direction, the EDSR Rabi frequency is about 15 MHz at B_z=0.1 T. There also exists a local maximum of EDSR frequency as a function of the gate electric field, and the EDSR Rabi frequency is linear in B_z. With an out-of-plane field, the Zeeman splitting term is typically of the order of μeV, which can be treated perturbatively. Therefore, when B_z is small, the EDSR Rabi rate can be expanded as a function of B_z, with the leading order $\propto \mathrm{B}_z$, which is similar to the finding of Ref. [484] for Ge. Interestingly, as shown in Fig. 4.3c, the EDSR Rabi

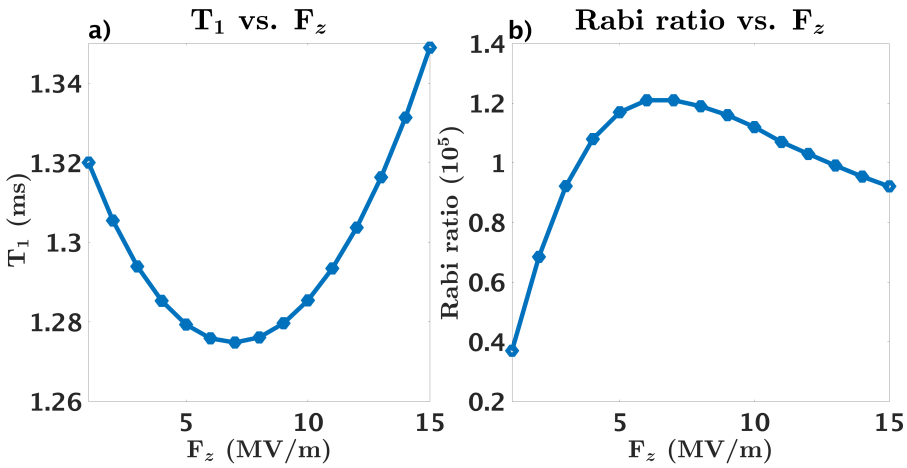

Figure 4.8: **Relaxation time and Rabi ratio for an in-plane magnetic field $\mathbf{B}_{\parallel}$.** a) The single phonon relaxation time T_1 as a function of the gate electric field F_z is calculated for an in-plane magnetic field B_x=1 T. b) The Rabi ratio is plotted as a function of the gate electric field F_z when B_x=1 T. The Rabi ratio is around 10^5.

frequency exhibits a slight anisotropy as the electric field is rotated in the plane, varying in magnitude by $\sim 20\%$. This is traced to the presence of the cubic-symmetry γ_3 terms in the Luttinger Hamiltonian. It is worth mentioning that the applied AC in-plane electric field E_{AC} will enhance the in-plane confinement. This enhancement distorts the parabolic shape of the confinement potential, thereby affecting the in-plane wave-functions. However, the E_{AC} value considered in this study are relatively small. Therefore, the distortion of the confinement potential and the subsequent impact on the in-plane wave-functions have been assumed to be negligible for our analysis. To study the number of operations allowed in one relaxation time, we plot the phonon-induced relaxation time and the Rabi ratio in Fig. 4.4. At B_z=0.1 T the relaxation time is several milliseconds, which allows $\sim 10^6$ operations. The long relaxation time reflects the weak hole-phonon interactions for silicon as a lighter material with a fast phonon propagation speed compared with germanium.

Our results Fig. 4.2 and Fig. 4.6 show that extrema in the qubit Zeeman splitting as a function of the top gate field F_z exist for all magnetic field orientations. Nevertheless, proper coherence sweet spots only exist for an out-of-plane magnetic field, as shown in Fig. 4.5. To understand this we must highlight the difference between extrema in the qubit Zeeman splitting and T_2^* sweet spots. The qubit states are Kramers conjugates.

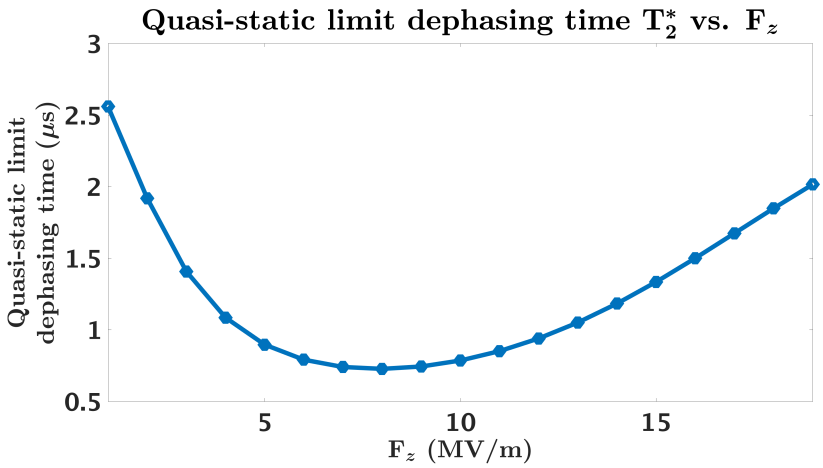

Figure 4.9: **Dephasing time in quasi-static limit for an in-plane magnetic field $\mathbf{B}_{\parallel}$.** Both single charge defects and dipole charge defects are taken into account for an in-plane magnetic field B_x=1 T, but the dominant contribution to the dephasing potential still comes from single charge defects. The dephasing time exhibits a local minimum, suggesting the absence of an optimal operation point.

Time-reversal symmetry implies that the matrix elements giving rise to pure dephasing, which represent an energy difference between the up and down spin states, must involve the magnetic field – they cannot come from charge noise and spin-orbit coupling alone. Because the magnetic field enters the qubit states both through the Zeeman and the orbital terms, the composition of the qubit states is different depending on the magnetic field orientation. For an out-of-plane magnetic field, the in-plane and out-of-plane dynamics can be approximately decoupled. The main effect of the gate electric field is to give rise to Rashba-like terms acting on the heavy hole spins. Unlike Ge, the Schrieffer-Wolff approximation is not applicable to Si as studied by [328] so this decomposition is not as easily visualized, although one can still envisage an effective spin-orbit Hamiltonian characterized by a Rashba constant. The Rashba term affects the qubit Zeeman splitting, and is directly susceptible to charge noise perpendicular to the interface, which is the main way a defect affects qubit spin dynamics. An in-plane electric field does not couple to the diagonal qubit matrix elements to leading order and can thus be disregarded in a first approximation.

4.3.2 In-plane magnetic field

When magnetic field is applied in the plane, our result (Fig. 4.6) shows a large qubit Zeeman splitting variations as a function of the top gate field, which is also observed in a recent experiments (Ref. [295]). A local minimum as a function of the gate electric field continues to exist, however, in an in-plane magnetic field the local minimum in the qubit Zeeman splitting does not protect the qubit from the single charge defect noise, as was emphasized above in the out-of-plane magnetic field case.

The EDSR Rabi frequency in an in-plane field contains a dominant term $\propto B_x$ as well as a small distortion $\propto B_x^2$ due to the orbital magnetic field terms. For an in-plane field, the orbital term in Luttinger-Kohn Hamiltonian can change the dispersion of holes significantly, away from the center of the Brillouin zone, the orbital term will distort the parabolicity of the dispersion. Therefore, an in-plane magnetic field will eventually result in stronger heavy-hole-light-hole mixing and significant modulation of the g-factor even when the amplitude of the field is small. Considering the transition matrix element in Eq. 4.25, this amplitude is determined by the in-plane AC electric field as well as the shapes of the ground state wave function $|\mathbb{0}\rangle$ and of the excited state wave function $|\mathbb{1}\rangle$. As a result, the EDSR Rabi frequency exhibits a non-linear behavior as a function of B_x due to the heavy-hole-light-hole admixture and due to the orbital magnetic field terms. We also observe a strong anisotropy in the EDSR Rabi frequency: applying the magnetic field parallel to the AC in-plane electric field results in an enhanced EDSR Rabi frequency, as shown in Fig. 4.7 c).

For an in-plane magnetic field, the orbital vector potential terms couple the in-plane and out-of-plane dynamics and no separation of the dynamics is possible. The net effect of this is that the qubit is sensitive to all components of the defect electric field, and an extremum in the qubit Zeeman splitting as a function of the perpendicular electric field does not translate into a coherence sweet spot for charge noise, as Fig. 4.9 shows. Notably, the existence of a sweet spot is feasible when the applied magnetic field is tilted, a concept that is supported by recent experimental and theoretical advancements [99, 295, 395, 524].

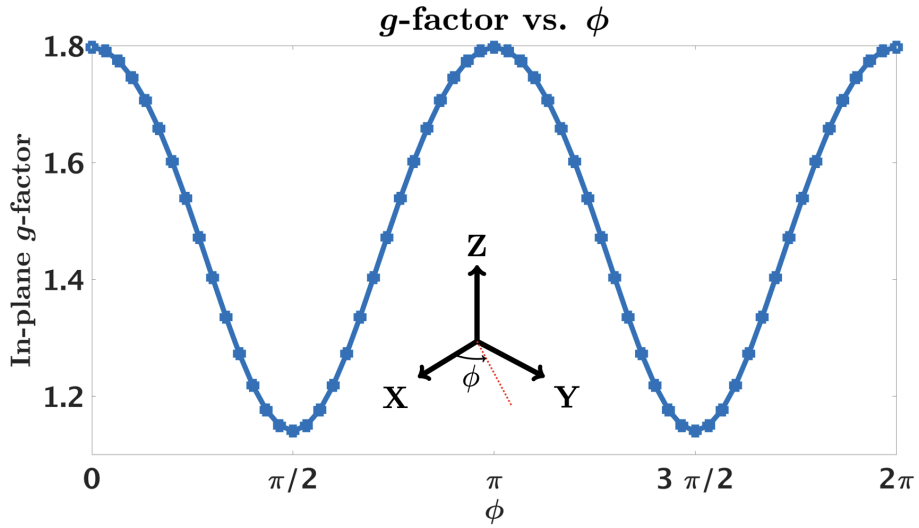

Figure 4.10: ***g*-factor anisotropy**. The variation of the g-factor is plotted as a function of the in-plane magnetic field orientation ϕ, representing the angle of the magnetic field with respect to the $\hat{x}$-direction. The magnitude of the applied magnetic field is 1 T. The semi-major axis of the dot is a_x=24 nm; the semi-minor axis of the dot is a_y=20 nm, giving the aspect ratio to be 1.2. When the magnetic field is parallel to the semi-major axis (ϕ=0°), the g-factor has a maximum value, which is also observed in Ref. [295].

A primary aspect of our investigations is to discern the distinctive dephasing responses when subjected to either out-of-plane or in-plane magnetic fields. The exploration of more complex magnetic field orientations and their associated dephasing characteristics will be considered in a future effort.

4.3.3 Ellipticity and in-plane *g*-factor anisotropy

In experimental studies, dots are often formed without explicitly attempting to remain circular, leading to a notable anisotropy in the effective g-factors, as depicted in Fig. 4.10. Despite the presence of an anisotropy term, denoted as κ_2 in the Zeeman Hamiltonian, it is important to note that κ_2 is typically smaller than κ_1 in both group IV and group III-V hole systems. Therefore, it has limited impact on the energy spectrum of the qubit. In contrast, the orbital term in H_{LK} and the effective mass will contribute more strongly to the anisotropy of the Rashba spin-orbit coupling and of the effective g-factors. Furthermore, we assume that hole qubit operation is governed by the k^3-Rashba spin-orbit coupling

[356], which consist of a 'linear' term that winds the Fermi surface once and a 'cubic' term which winds the Fermi surface three times. In the context of a circular dot, qubit operation is driven by the 'linear' Rashba term and the stronger 'cubic' Rashba term becomes activated in elliptical dots [328]. We discuss the origin and relevance of the different spin-orbit interactions in the language of quasi-degenerate perturbation theory in the Appendix B.

For possible experimental settings, the lateral confinement in the $\hat{x}$ and $\hat{y}$ directions can be independently adjusted using the electrostatic gates. This corresponds to in-situ control over $\omega_{x,y}$, which are defined in Eqs. 4.22-4.23. Previous work by Qvist and Danon (Ref. [406]) investigated lateral confinement potentials, providing an analytical study of effective mass anisotropy and the size of the confinement potential by taking the linear Rashba term as an example in a perturbative approach on the four-band Luttinger-Kohn Hamiltonian. In contrast, our numerical calculations include all Rashba terms, involving tracing all non-commutable canonical momentum operators in higher excited states, and accounting for the non-parabolic behaviors of the band structure based on a six-band Luttinger-Kohn Hamiltonian.

Our results indicate that the g-factor exhibits an oscillating pattern when we rotate a constant in-plane magnetic field in the xy-plane. For example, when the aspect ratio is 1.2, we observe a g-factor variation up to 50% as a function of the in-plane magnetic field angle. This substantial anisotropy in the in-plane g-factor is consistent with recent experimental observations (Ref. [295]).

4.4 Comparison between Germanium and Silicon

A promising competitor for silicon, in semiconductor quantum dot hole spin qubit area, is germanium. However, due to the fabrication details of silicon hole quantum dot and germanium hole quantum dot, the location of the sweet spot as a function of the top gate field, the strain in the sample, and the modulation of the in-plane and out-of-plane

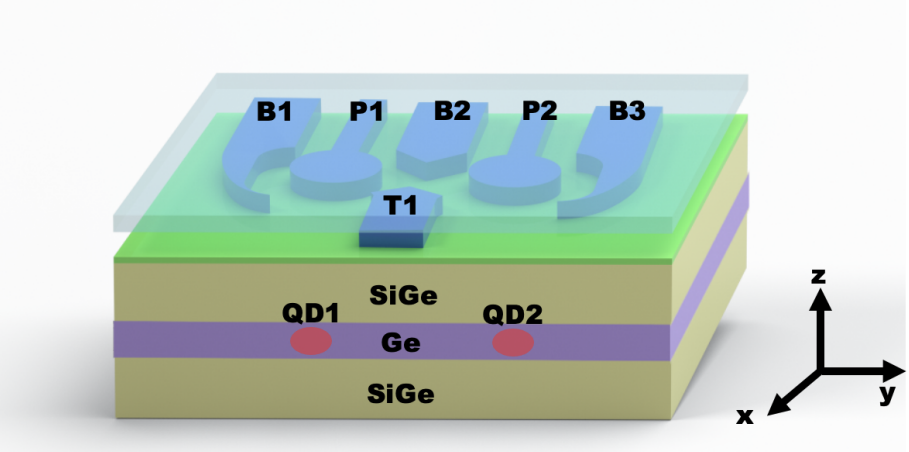

Figure 4.11: **A prototype double quantum dot in strained germanium hole system**. The substrate includes a fully strain-relaxed SiGe layer on the bottom. The middle of the heterostructure comprises an epitaxially grown layer of strained germanium, hosting the hole qubit, and another layer of relaxed SiGe atop the Ge layer. The concentration of Si atoms in Si_xGe_{1-x}, represented by the component fraction factor x, also determines the strain in the pure Ge layer via Vegard's law. The portion of the silicon in SiGe can be tuned experimentally, therefore, homogeneous axial strains can be controlled. Gate B1, P1, B2, P2, B3 are used to confine two quantum dots, while gate B2 and T1 can control the inter-dot tunneling. In this picture, we set the growth direction to be along the $\hat{z}$-direction.

Table 4.1: **Comparison of silicon and germanium material parameters**. The relevant parameters defining the silicon hole spin qubit and germanium hole spin qubits are collected from Ref. [552, 124, 213, 198, 417, 294, 206]. In the table, the out-of-plane heavy-hole band and light-hole band mass is defined as $m_{\mathrm{HH}} = m_0/(\gamma_1 - 2\gamma_2)$, $m_{\mathrm{LH}} = m_0/(\gamma_1 + 2\gamma_2)$; the in-plane heavy-hole band effective mass and the light-hole band effective mass is defined as $m_{\mathrm{HP}} = m_0/(\gamma_1 + \gamma_2)$, $m_{\mathrm{LP}} = m_0/(\gamma_1 - \gamma_2)$. m_0 is the bare electron mass, γ_1, γ_2, γ_3 are Luttinger parameters. The density ρ is the bulk density of isotropic silicon or germanium. v_ℓ, v_{t_1}, v_{t_2} are phonon propagation speeds along three different polarizations. a_v, b_v, d_v are the hydro-static deformation potential constant, uni-axial deformation potential constant, and shear deformation potential constant respectively. The split-off band gap is denoted by Δ_0. Throughout this chapter, unless specifically mentioned, the radius of the quantum dot is $a_x = a_y$ =20 nm, and the width of the quantum well is L=13 nm.

Parameters	Silicon	Germanium
γ_1	4.29	13.38
γ_2	0.34	4.24
γ_3	1.45	5.69
κ_1	-0.42	3.41
κ_2	0.01	0.06
m_{HH}	0.277 m_0	0.204 m_0
m_{LH}	0.201 m_0	0.046 m_0
m_{HP}	0.216 m_0	0.057 m_0
m_{HP}	0.253 m_0	0.109 m_0
ρ	2329 kg/m^3	5330 kg/m^3
v_ℓ	9000 m/s	3570 m/s
v_{t_1}	5400 m/s	4850 m/s
v_{t_2}	5400 m/s	4850 m/s
a_v	2.38 eV	2.00 eV
b_v	-2.10 eV	-2.16 eV
d_v	-4.85 eV	-6.06 eV
Δ_0	44 meV	296 meV
Hole density	10^{-2} nm^{-2}	3×10^{-3} nm^{-2}

g-factors are expected to be different. As a comparison of the material characters, we list important parameters, which is relevant in fabricating the hole spin qubit, of silicon and germanium in Table. 4.1.

The in-plane effective mass of a hole in silicon ($0.216m_0$) is much heavier than that in germanium ($0.057m_0$). As a consequence, the heavy-hole-light-hole energy splitting in silicon (around 5 meV) will be much smaller than that in germanium (around 50 meV). A direct outcome of a small heavy-hole-light-hole energy splitting is that, the presence of strains will efficiently lead to mixing between the light-hole and heavy-hole band, which will amplifies the Stark shift effect. Experimental evidence indicates that the in-plane g-factor for silicon varies from 1.5 to 2.5 [295]. Concurrently, germanium hole quantum dots have been observed to exhibit a g-factor range of 0.16 to 0.3 [205, 207]. Notably, both silicon and germanium demonstrate the potential for significant g-factor modulation, with variations reaching up to 50 %. Furthermore, the smaller effective mass in silicon imposes limitations on the splitting of quantum dot orbital levels, thereby restricting the size of silicon hole quantum dots, imposing a difficulty towards salable quantum computations.

The strain present in silicon and germanium hole quantum dots is another important feature. Engineering strains in semiconductor quantum dot hole spin qubits are receiving increased attention due to their potential in realizing significant g-factor modulations and accelerating EDSR Rabi oscillations. The axial strain terms commonly studied—namely, P_ε ,Q_ε, $P_\varepsilon + Q_\varepsilon$, and $P_\varepsilon - Q_\varepsilon$ in the H_{LKBP} Hamiltonian are directly responsible for adjusting the heavy-hole-light-hole energy splitting. Meanwhile, the role of shear strain terms, such as R_ε and S_ε in H_{LKBP}, which facilitate the intermixing of heavy-hole and light-hole states, is increasingly recognized for its importance. Recent theoretical studies have highlighted that in-homogeneous strain fields can activate linear Rashba spin-orbit interactions, leading to substantial g-factor modulations and potentially enhancing EDSR Rabi oscillations by an order of magnitude [2, 466, 421]. In MOS based silicon hole quantum dots, strains naturally arise due to the thermal contraction differences between the metal electrodes and the silicon substrate. Recent experimental findings, such as those documented in Ref. [295], have underscored the significance of in-homogeneous strains in

Table 4.2: **Possible configurations for optimal operation points**. We consider both in-plane and out-of-plane magnetic fields for silicon and germanium. The strains ε_{xx}, ε_{yy} and ε_{zz} have the relation $\varepsilon_{xx} = \varepsilon_{yy}{=}\varepsilon_{zz} = -\varepsilon_{xx}(2C_{12}/C_{11})$, the shear strain ε_{xz} is estimated from Ref. [295]. We use ΔE_{Z} to denote the qubit Zeeman splitting. Note that there exist many possible combinations of parameters to get an optimal operation point as a function of the gate electric field.

Confinements	Silicon	Germanium
Orbital energy splitting	0.3 meV	0.3 meV
HH-LH energy splitting	7 meV	100 meV
Typical ε_{xx}	0.001	0.01
Typical ε_{yy}	0.001	0.01
Typical ε_{zz}	-0.00077	-0.0077
Typical ε_{xz}	0.0008	0
ΔE_{Z} ($B_x = 1\mathrm{T}$)	100 μeV	15 μeV
Sweet spot ($B_x = 1\mathrm{T}$)	8 MV/m	18 MV/m
ΔE_{Z} ($B_z = 0.1\mathrm{T}$)	10 μeV	90 μeV
Sweet spot ($B_z = 0.1\mathrm{T}$)	13 MV/m	20 MV/m

explaining the non-monotonic behavior observed in qubit Zeeman splitting and other related properties. The existence of the shear strain can change the location of the sweet spot, the magnitude of the g-factor, and the magnitude of EDSR frequency. Using the parameter we used, the change of the magnitude of the in-plane g-factor is enhanced by around 5 %. In the germanium hole spin qubits, particularly those based on a uniformly strained germanium quantum well within a SiGe/Ge/SiGe heterostructure, the homogeneous axial strains are well defined Fig. 4.11. However, a mapping of the shear strain has been performed experimentally in Ref. [94] for Ge and Ref. [421] theoretically demonstrates the role of inhomogeneous strain for Ge planar hole qubit operations. To quantitatively compare the strain in the silicon and the germanium hole spin qubit devices, we use typical parameters as listed in Ref. [484, 439]. For instance, if the relaxed SiGe layer is $\mathrm{Si}_{0.25}\mathrm{Ge}_{0.75}$, ($x$=0.25) the axial compressive strain will be ϵ_{xx} =- 0.001, which is ~ 5 times larger than the strain present in the silicon metal-oxide-semiconductor quantum dot. In Table. 4.2, we summarize various typical configurations, including strains, top gate fields, magnetic fields, and geometries to reach the optimal operation points in different materials. We notice that the parameters used to fit experimental data, such as the dot geometry, shear strain, and axial strain, are estimates. It is crucial to include the non-uniform strain from

Table 4.3: **Comparison of the EDSR Rabi time, relaxation time and Rabi ratio between silicon and germanium with same orbital energy and qubit Zeeman splittings in an in-plane magnetic field**. The strain used in germanium is ε_{yy}=ε_{xx}=0.001, ε_{zz} =−$(2C_{12}/C_{11})\varepsilon_{xx}$. The strain used in silicon is ε_{xx}=ε_{yy}=0.1%, ε_{zz}=-0.077%, ε_{xz}=0.08%, ε_{xy}=ε_{yz}=0. One can always adjust the gate electric field and the magnetic field to ensure the qubit Zeeman splittings are the same in a silicon and a germanium hole qubit. For EDSR Rabi frequency, the in-plane AC electric field used is 1 kV/m. To have the same orbital confinement energy to be 0.3 meV, the silicon dot size is a_y=a_x=25 nm, L =13 nm, while the germanium dot size is a_y=a_x =50 nm, L =11 nm. The gate electric field is fixed to be 10 MV/m.

Confinements	Silicon	Germanium
Orbital energy splitting	0.3 meV	0.3 meV
$\Delta E_{\mathrm{Z}} = 25\,\mu$eV	$B_x = 0.3$ T	$B_x = 2$ T
EDSR Rabi time	80 ns	200 ns
Relaxation time	200 ms	4 ms
Rabi Ratio	2×10^6	2×10^4
Dephasing time	0.7 μs	10 μs

the gate electrodes, as shown in Ref. [295]. For more precise results, direct strain profilling as in Ref. [466], or device-specific modelling can be employed. Strain will be thoroughly investigated in future works. In this context, we note that we do not anticipate strain to change the existence of the optimal operation points of the qubits for fast EDSR Rabi ratio and minimized dephasing time as a function of the top gate field. Another important difference between Ge and Si concerns the applicability of the Schrieffer-Wolff transformation in analyzing qubit Hamiltonians. For Ge, a perturbative approach based on the Schrieffer-Wolff transformation is demonstrated to be effective for an out-of-plane magnetic field [532], which relies on the large heavy-hole-light-hole splitting in a low density Ge system. In Si the heavy-hole-light-hole splitting is much smaller than in Ge, while the cubic-symmetry term in the Luttinger Hamiltonian is very strong. As a result of this, the Schrieffer-Wolff transformation cannot account for full density-dependence (i.e., quantum dot radius dependence) of the hole states and split-off band correctly, and a full diagonalization of the Hamiltonian is needed to yield accurate results.

While Si and Ge are excellent hosts of planar hole spin qubits, both platforms have advantages and disadvantages. Silicon exhibits smaller sized quantum dots, which is highly compatible with the already existing advanced Si fabrication technologies. The intrinsic

spin-orbit coupling is weak in Si, evident from the fact that the split-off gap Δ_0 is 44 meV in Si compared to 325 meV in Ge. Yet the cubic-symmetry Rashba parameter α_3 is sizeable, resulting in a similar spin flip EDSR rate to Ge. On the other hand, the quantum dot size is large in Ge, providing great scope for potential scaling up of the technology. Although the spin-orbit coupling is larger in Ge than Si, the cubic term is not so strong. Lastly in terms of qubit coherence, experimentally noise is somewhat stronger in Si hole qubits, although if the qubit is operated at a sweet spot this may not matter.

4.5 Conclusions and Outlook

In this chapter, starting from the diagonalization of the Luttinger-Kohn-Bir-Pikus Hamiltonian, we have developed a numerical method to study the silicon hole spin qubits in different experimental configurations. We have shown that the gate electric field significantly modulates the qubit Zeeman splitting, EDSR Rabi frequency and relaxation time. We have shown that the dephasing time due to random telegraph noise stemming from single and dipole charge defects exhibits very different behaviors in in-plane and out-of-plane magnetic fields. We find that in an out-of-plane magnetic field coherence sweet spots can be identified as a function of the top gate field, at which random telegraph noise does not couple to the spin. However, in the case of in-plane fields the role of random telegraph noise can be reduced but not entirely removed, because the vector potential terms expose the qubit to all components of a defect's electric field. The numerical method we have developed in this work can be extended to many-hole spin qubits in other materials as well as to studies of several qubits required for entanglement.

Chapter 5

Helical Edge State

The main content of this independent chapter is an adaption of a publication Ref. [531] by the candidate. I would like to express acknowledgement to all the co-authors: Pankaj Bhalla, Mark Edmonds, Michael S. Fuhrer, and Dimitrie Culcer.

Quantum spin-Hall edges are envisaged as next-generation transistors, yet they exhibit dissipationless transport only over short distances. Here we show that in a diffusive sample, where charge puddles with odd spin cause back-scattering, a magnetic field drastically increases the mean free path and drives the system into the ballistic regime with a Landauer-Buttiker conductance. A strong non-linear non-reciprocal current emerges in the diffusive regime with opposite signs on each edge, and vanishes in the ballistic limit. We discuss its detection in state-of-the-art experiments.

5.1 Introduction

Quantum spin-Hall insulators are a novel class of materials hosting gapless, topologically protected, counter-propagating edge states. These have opposite spin polarizations and exhibit strong spin-momentum locking due to the dominant role of the spin-orbit interac-

tion [529, 284, 300, 201, 405, 404, 237, 327, 570]. Time-reversal symmetry ensures edge states come in Kramers doublets, which cannot be back-scattered by time-reversal invariant perturbations [269, 109, 384, 267, 553, 82, 491, 296]. Materials possessing topological edge states include topological insulators such as HgTe and Bi_2Se_3, Weyl semimetals such as WTe_2, and Dirac semimetals such as Na_3Bi [318, 452, 154, 482, 300, 573, 298, 35].

A ballistic edge has a longitudinal conductance of e^2/h at low temperature, a fact that has led to proposals for using topological edge states as building blocks for next-generation transistors, exploiting electrically tunable topological phase transitions [383]. Nevertheless, following the experimental discovery of topological edge states, it has emerged that puddles with odd numbers of charges, which exist inherently in the host materials due to doping disorder in fabrication, can act as effective magnetic impurities that back-scatter the edge states and significantly reduce their mobility [515, 384, 503, 267, 255, 506]. This may explain why ballistic conductance has only been observed over spatial scales of the order of 50 nm [154, 482, 515, 452, 262, 298, 299, 371]. Whereas initial studies focused on the Kondo effect, the Kondo temperature in current samples is expected to be negligibly small [528, 303, 527], while other aspects of transport remain poorly understood [300, 505, 468, 449, 311, 378, 284, 571, 296, 562]. The unexpectedly large resistance of topological edge states has emerged as a fundamental question and an obstacle in the development of topological transistors [543, 481]. Bearing in mind the role of magnetic impurities, the first step in overcoming this problem is understanding edge magneto-transport in the presence of puddles. This includes the identification of non-reciprocal currents, since non-linear response probes interactions that are difficult to access in linear response, due to constraints imposed by mirror symmetry and Onsager relations [257, 359, 281, 431, 452]. The rich physics underlying non-linear phenomena [486, 573, 238, 557, 36, 459] has been manifest in recent discoveries such as Hall effects in time-reversal invariant systems, as well as in unexpected features of topological edges, such as a large uni-directional magnetoresistance at zero magnetic field [154, 573, 431, 452].

In this article we demonstrate that a magnetic field has a drastic effect on both the linear and non-linear response of topological edge states: (i) It enhances the mean free

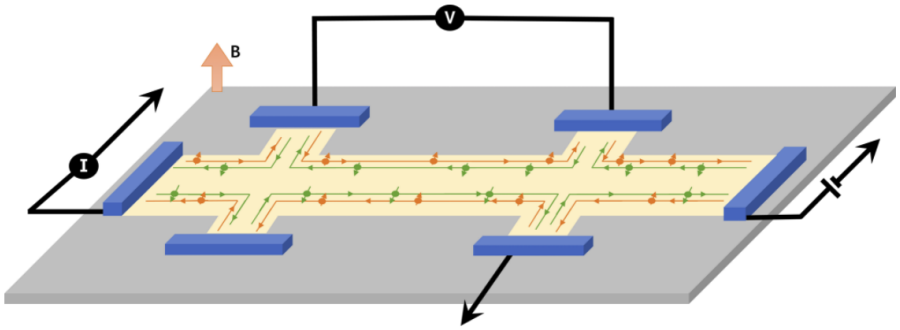

Figure 5.1: **Experimental setup in a perpendicular magnetic field B**. The current is measured across the sample, while the voltage can be measured at two different terminals along one side. On the opposite side one terminal is grounded. Spin-up electrons are shown in orange, spin-down electrons in green.

path l by orders of magnitude without opening a gap, eventually driving the system into the ballistic regime; (ii) By breaking mirror symmetry the magnetic field enables a strong unidirectional non-linear electrical response in the diffusive regime. The direction of the current is determined by the magnetic field and the spin quantization axis, and it has a different sign on each edge. Interestingly, the non-reciprocal current vanishes in the ballistic regime. This reflects the fact that, once magnetic impurity scattering is surmounted, the only remaining magnetic interaction is the Zeeman interaction with the out of plane field, which can be gauged away. Whereas a complete description of charge puddles is beyond the scope of this work, modelling the puddles as magnetic impurities is a simple way of capturing the physics that governs their magnetoresistance, which is in excellent agreement with experiment [299].

5.2 Model and Methodology

5.2.1 Material selections

We focus on Na_3Bi as a prototype material, motivated by the observations that ultra-thin films of Na_3Bi have a band-gap of $\geq$300 meV [127], much greater than k_BT at room temperature, are robust to layer-number fluctuations caused by imperfect growth [128],

exhibit an electrically driven topological phase transition[91], and show clear evidence of edge transport over millimetre distances, as well as a giant negative magneto-resistance [299]. Our model also applies to topological insulators with inversion symmetry such as Bi_2Se_3. Materials without inversion symmetry, such as WTe_2, exhibit a positive magneto-resistance and a position-dependent spin quantization axis, so they fall outside our scope.

5.2.2 Quantum kinetic equations

Considering a sample of finite size d a magnetic field $\boldsymbol{B} \parallel \hat{\boldsymbol{z}}$ is applied out of the plane. The full Hamiltonian H can be written as $H = H_0 + H_Z + V + U + U_Z$, where the band Hamiltonian $H_0 = \hbar v_F k_x \sigma_z$ represents the edge state dispersion of Na_3Bi; $H_Z = g_0 \mu_B B \sigma_z$ is the Zeeman interaction with the magnetic field. Since in the absence of warping terms the magnetic field does not open a gap in the dispersion the topological character of the states is preserved (the role of warping is discussed briefly below). $V(x)$ is the electrostatic potential, with the associated electric field $E = -\partial V/\partial x$, and $-e$ the electron charge. The random magnetic impurity potential $U = Js \cdot \sum_i S_i \delta(x - x_i')$ is the contact-like interaction term allowing spin-dependent scattering between an electron and effective magnetic impurities. s indicates the spin operators of the electron and S_i indicates the spin operators of impurities with spin-1/2 sited at position x_i. At the end we average over uncorrelated impurities which are all assumed to experience the same exchange interaction J with the mobile carriers. We choose the impurity density and exchange coupling to reproduce the mean free path observed experimentally in the diffusive regime. The local moments are in thermal equilibrium, relaxing their energy and angular momentum rapidly to an external bath [313], which corresponds to what is seen experimentally. If the local moments coupled only to the edges the moments on each edge would polarize quickly and the edges would become ballistic in a short amount of time: this is not observed in experiment. The Zeeman interaction between the impurities and the out-of-plane magnetic field $U_Z = g_1 \mu_B \sum_i S_i \cdot B$. The notation σ_z in the full Hamiltonian represents the z-component of the Pauli spin matrix for a spin-1/2 particle. We focus on the DC limit, where $\omega\tau \ll 1$.

We derive a quantum kinetic equation following the procedure of Refs. [504, 528], which ensures the Pauli blocking terms are correctly accounted for [504]. The system is described by the density matrix ρ, which satisfies the quantum Liouville equation $\partial\rho/\partial t + (i/\hbar)[H,\rho] = 0$. The explicit position dependence must be taken into account due to the finite size of the sample. Following a Wigner transformation [108, 105]

$$\frac{\partial\rho}{\partial t} + \frac{1}{2\hbar}\left\{\frac{\partial H_0}{\partial k_x}, \frac{\partial\rho}{\partial x}\right\} + J(\rho) = -\frac{e}{\hbar}\frac{\partial V}{\partial x}\frac{\partial\rho}{\partial k_x} \tag{5.1}$$

In Eq. (5.1), the single particle density matrix ρ takes the form $\mathrm{diag}\{f_\uparrow, f_\downarrow\}$. We write $f_\uparrow = f_\uparrow^{(0)} + g_\uparrow$ is the non-equilibrium distribution for the spin-up electrons composed of the equilibrium part $f_\uparrow^{(0)}$ and out-of-equilibrium part $g_\uparrow$; similarly, $f_\downarrow = f_\downarrow^{(0)} + g_\downarrow$ is the non-equilibrium distribution for the spin-down electrons, the equilibrium distribution have the form $f^{(0)}(\varepsilon) = [1+\exp(\beta(\varepsilon-\mu))]^{-1}$ where $\beta = (k_BT)^{-1}$. The last term in Eq. (5.1) is the scattering term in the Born approximation, which take the form

$$J(g_\uparrow) = \int \left[P_{k\downarrow,k'\uparrow} f'_\downarrow(1-f_\uparrow) - P_{k\uparrow,k'\downarrow} f_\uparrow(1-f'_\downarrow)\right]\frac{dk'}{2\pi} \tag{5.2}$$

$$J(g_\downarrow) = \int \left[P_{k\uparrow,k'\downarrow} f'_\uparrow(1-f_\downarrow) - P_{k\downarrow,k'\uparrow} f_\downarrow(1-f'_\uparrow)\right]\frac{dk'}{2\pi} \tag{5.3}$$

Here $P^i(k',\downarrow\to k,\uparrow)$ indicates the probability of spin-flip scattering between a spin-up electron at k and an impurity, ending with a spin-down electron at k'. Primed quantities indicate the final state following a scattering event. We obtain two coupled Boltzmann equations for the spin-up and spin-down electrons:

$$\frac{\partial g_\uparrow(\varepsilon)}{\partial x} + \Gamma_1(\varepsilon)g_\uparrow(\varepsilon) - \Gamma_2(\varepsilon)g_\downarrow(\varepsilon_-) = -e\frac{\partial V}{\partial x}\frac{\partial f_\uparrow^{(0)}(\varepsilon)}{\partial\varepsilon} \tag{5.4}$$

$$\frac{\partial g_\downarrow(\varepsilon)}{\partial x} - \Gamma_1(\varepsilon)g_\uparrow(\varepsilon_+) + \Gamma_2(\varepsilon_+)g_\downarrow(\varepsilon) = -e\frac{\partial V}{\partial x}\frac{\partial f_\downarrow^{(0)}(\varepsilon)}{\partial\varepsilon} \tag{5.5}$$

where $\varepsilon_- = \varepsilon - \varepsilon_Z$ and $\varepsilon_+ = \varepsilon + \varepsilon_Z$ The two scattering rates are defined as follows:

$$\Gamma_1(\varepsilon) = \frac{N_i J^2}{\hbar^2 v_F}\left[\frac{1}{1+e^{-\alpha}}\left[1-f_\downarrow^{(0)}(\varepsilon)\right] + \frac{1}{1+e^{\alpha}}f_\downarrow^{(0)}(\varepsilon)\right] \tag{5.6}$$

$$\Gamma_2(\varepsilon) = \frac{N_i J^2}{\hbar^2 v_F}\left[\frac{1}{1+e^{-\alpha}}f_\uparrow^{(0)}(\varepsilon) + \frac{1}{1+e^{\alpha}}\left[1-f_\uparrow^{(0)}(\varepsilon)\right]\right], \tag{5.7}$$

where N_i is the number of impurities, the dimensionless factor $\alpha = g_1\mu_B B/(k_BT)^{-1}$, and the change of the Zeeman energy during the spin-flipping interactions $\varepsilon_Z = g_1\mu_B B$. We solve the coupled Eq. (5.4) and Eq. (5.5) by integrating separately over left and right movers, which also ensures the correct solution in the ballistic regime:

$$g_\uparrow^{(1)} = -e\int_0^x \left[\frac{\Gamma_2}{\kappa} + \frac{\Gamma_1}{\kappa}\exp\left[\kappa(x-x')\right]\right]\frac{\partial V}{\partial x}\frac{\partial f_\uparrow^{(0)}}{\partial\varepsilon}dx' + e\int_d^x \left[\frac{\Gamma_2}{\kappa}\left(\exp\left[\kappa(x-x')\right]-1\right)\right]\frac{\partial V}{\partial x}\frac{\partial f_\downarrow^{(0)}}{\partial\varepsilon}dx' \tag{5.8}$$

$$g_{\downarrow}^{(1)} = -e\int_{d}^{x}\left[\frac{\Gamma_1}{\kappa}+\frac{\Gamma_2}{\kappa}\exp\left[\kappa(x-x')\right]\right]\frac{\partial V}{\partial x}\frac{\partial f_{\downarrow}^{(0)}}{\partial \varepsilon}dx' + e\int_{0}^{x}\left[\frac{\Gamma_1}{\kappa}\left(\exp\left[\kappa(x-x')\right]-1\right)\right]\frac{\partial V}{\partial x}\frac{\partial f_{\uparrow}^{(0)}}{\partial \varepsilon}dx' \quad (5.9)$$

where $\kappa = \Gamma_1 + \Gamma_2$, and the mean free path $l = \kappa^{-1} = (\Gamma_1 + \Gamma_2)^{-1}$. The current density $j = -e\mathrm{Tr}(v\rho)$, where $v = (1/\hbar)(\partial H_0/\partial k)$. For spin-up electrons the momentum integration is performed over $k > 0$, and for spin-down electrons over $k < 0$. For the second-order response the sign of the magnetic field in the scattering terms Eq. (5.6), (5.7) will change, yet Γ_1 and Γ_2 are symmetric in α; the sign of the driving term will change similarly to the band dispersion. The mean free path is unchanged and the formal solution to the differential equation is analogous to Eqs. 5.8-5.9, with the replacements

$$\frac{\partial f^{(0)}}{\partial \varepsilon} \rightarrow \frac{\partial g^{(1)}}{\partial \varepsilon} \quad (5.10)$$

These equations cannot be reduced to a simple closed form and are solved iteratively.

5.3 Result and Discussion

Referring to the set-up shown in Fig. 5.1, our main results are summarised in Fig. 5.2. The current in the channel will be denoted by I and the potentials of the left and right electrodes by V_L, V_R respectively. We define the conductance G and the non-linear electrical response function χ by $I = G(V_L - V_R) + \chi(V_L - V_R)^2$. In Fig. 5.2-(a) and Fig. 5.2-(b) we have plotted the conductance G as a function of the applied out-of-plane magnetic field B at small and large values of B, where small and large are quantified below. It is seen that G increases with B and eventually reaches the quantized Landauer-Buttiker value of e^2/h, indicating that the system reaches the ballistic limit. This opens up the exciting possibility of using a ferromagnet with an out-of-plane magnetization as a practical method to increase the mean free path and to study transport in the ballistic regime. The ferromagnet could couple to the impurities either via a magnetic field or through the exchange interaction. Next, Fig. 5.2-(c) and Fig. 5.2-(d) show the non-linear electrical response function χ at small and large magnetic fields respectively. At small B, χ increases with B, but in contrast to the Ohmic term the non-linear signal reaches a maximum beyond which it decreases, tending to zero as the system reaches the ballistic regime. This vanishing response is a

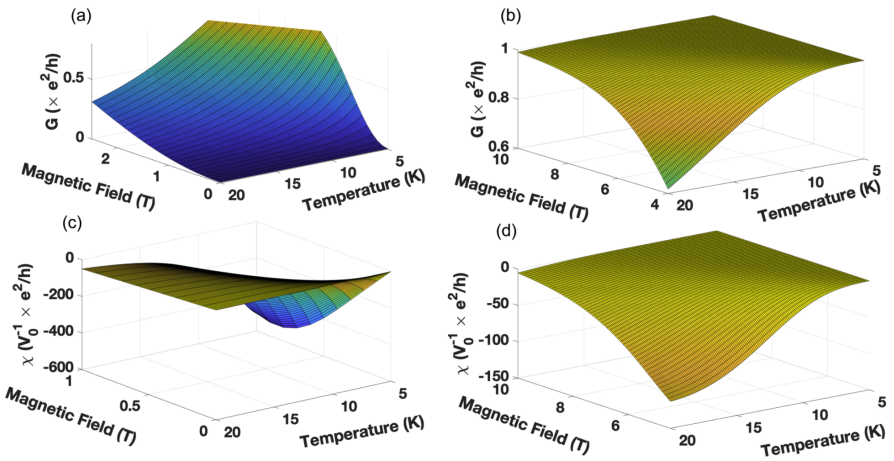

Figure 5.2: **Linear and non-linear response for a sample with** $d = 1000\text{nm}$**;** $v_0 = 10^3\text{V}$ **is a scaling factor.** (a) The conductance in the diffusive regime. When the magnetic field is small, the conductance increases as back-scattering is suppressed and the mean free path increases. (b) The conductance in the ballistic limit, when the mean free path is larger than the size of the sample, the conductance will not change, converging to to e^2/h. (c) The nonlinear response function χ in the diffusive regime. When the magnetic field is small, the mean free path is much shorter than the size of the sample, and the non-linear response increases as a function of B. (d) The nonlinear response function χ in the ballistic regime. At large magnetic fields the mean free path exceeds the size of the sample, causing χ to decrease in the ballistic regime and eventually vanish.

characteristic of the Dirac cone, indicating that the non-linear response is a probe of the edge state dispersion, and is a unique experimental signature reflecting chiral conduction in the TI. To generate and detect the second-order response at low-frequency it is sufficient to use an oscillator with angular frequency ω and read off the signal at 2ω.

The negative magneto-resistance in Fig. 5.2 is explained by the relationship between the magnetic field and the mean free path. Although conventional 1D systems are either ballistic or localised, the notion of a mean free path, defined explicitly below, can be applied meaningfully to 1D topological edge states, a diffusive system in which localisation is nevertheless not expected due to topological protection. We note that up and down spins have the same mean free path l. Figure 5.3 gives a diagrammatic example of spin-flip scattering, showing a spin-down electron being flipped to the spin-up channel due to scattering off an impurity. The energy required for this transition is set by the Zeeman splitting of the impurity spin states. As the magnetic field increases the energy cost likewise

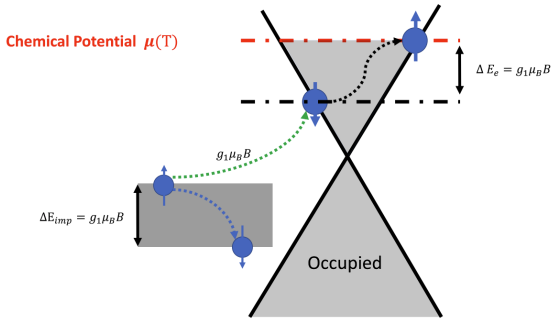

Figure 5.3: **Spin-flip scattering.** An electron with spin down is scattered into a spin-up state, which, due to spin-momentum locking, travels in the opposite direction; the energy change is given by the impurity Zeeman splitting $E_{1,Z} = g_1\mu_B B$.

increases and the transition is suppressed. Figure 5.4 shows the mean free path l increasing as a function of $\boldsymbol{B}$ until it exceeds the size d of the sample. Based on this we define the diffusive regime as $l \ll d$, and the ballistic regime as $l > d$. We focus on these two limiting cases, in which simplifying approximations can be made. Specifically, in the diffusive regime one may assume a constant electric field across the channel, and the conductance takes the simple general form $G = \frac{e^2}{h}\frac{l}{d}$, where the entire magnetic field dependence is contained in the mean free path $l(B)$. In the ballistic regime it is straightforward to express the current as a function of the potential difference between the source and drain electrodes, and the potential drop occurs overwhelmingly in the vicinity of the electrodes due to contact resistance, although the exact potential profile is immaterial [117, 116]. The conductance is obtained straightforwardly as $G = \frac{e^2}{h}$. The intermediate region is complicated by potential fluctuations, and is not a focus of current experimental efforts. A full treatment requires accounting for screening thoroughly [4, 115].

A perpendicular magnetic field breaks mirror symmetry and enables a second-order response, which increases as a function of the magnetic field in the diffusive regime due to the reduced efficiency of impurity scattering. Nevertheless, the non-linear response vanishes in the ballistic regime. Once transport becomes ballistic there is no more scattering and the impurities become irrelevant. The effective Hamiltonian becomes simply that of a Dirac cone, $H_0 + H_Z$, whence B can be removed by redefining the origin. The second-order response therefore probes the edge state dispersion: if a non-linear response is detected in

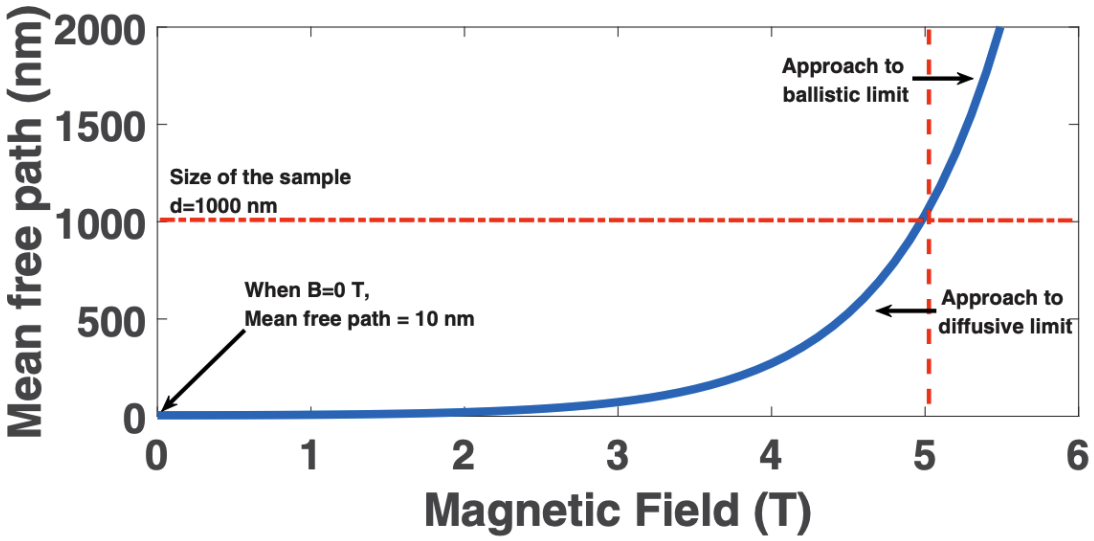

Figure 5.4: **The mean free path as a function of magnetic field.** The red dashed lines mark the size of the sample $d = 1000$nm compared with the mean free path the system. When the magnetic field is small, the system is diffusive, however a larger magnetic field will enhance the mean free path, driving the system into the ballistic regime, leading to a vanishing non-linear response. In all the plots, we have set the mean free path at zero magnetic field to be 10nm.

the ballistic regime it must come from band structure terms of higher order in the wave vector, which are challenging to calculate computationally for 1D systems. Although they can be determined by symmetry their magnitude is generally unknown [262] (the details are reserved for a future publication).

The response of the other edge can be found by reflecting the Hamiltonian in the xz-plane. The Hamiltonian describing the dispersion for the other edge reads $H_0 = -\hbar v_F k_x \sigma_z$. When the magnetic field is flipped the conductance G does not change, consistent with Onsager symmetry. But the direction of the non-linear response on each edge is set by the spin orientation with respect to the magnetic field and the solution to the second order quantum kinetic equation changes sign for the other edge. Hence χ changes sign, ensuring time reversal breaking in the non-linear response function [486].

5.4 Conclusion and Outlook

In this work we have not discussed dispersions beyond the linear case. In Bi_2Se_3 warping complicates the dispersion, and in the spin eigenstate basis $H_0 = Ak_x\sigma_y + C\sigma_z k_x^3$. A magnetic field $\parallel \hat{\boldsymbol{y}}$ yields a term of the form $\sigma_z B_y$ due to warping, which opens a small gap in the edge spectrum. However, warping only accounts for up to 10% of the Fermi energy, thus the gap is expected to be small, and will not influence the dynamics in the vicinity of the Fermi energy discussed here. Since the addition of warping complicates significantly the description of the interaction with the impurities, a further derivation is beyond the scope of this work.

In summary, we have shown that a magnetic field drastically enhances the conductivity of topological edge states and gives rise to an edge-dependent non-linear response which vanishes in the ballistic limit. The magnetic field, as well as proximity to a ferromagnet, can be used to drive the system into the ballistic regime, while the non-linear response probes the edge state dispersion. In the future the transport theory can be extended to the Kondo regime along the lines of Ref. [528].

Chapter 6

Conclusion and Outlook

This thesis aims to presented a comprehensive study on improving coherence in Group IV semiconductor quantum dot hole spin qubits. Starting from theoretical modelling of Group IV semiconductor quantum dots in $\boldsymbol{k}\cdot\boldsymbol{p}$ approach, we firstly examined the properties of the two-dimensional-hole-gas, and the effective Hamiltonians. Based on this effective model, we discussed the optimisation of the coherence in a fully electrically controlled hole spin qubits in germanium, where the higher order perturbative approach of the four-band Luttinger-Kohn Hamiltonian is adequte to capture the optimal operation points, verfied by simple numerical schemes. The electric dipole spin resonance Rabi time, and phonon induced relaxation time is discussed, resulting in a large Rabi ratios. In this project, the qubit dephasing time is over estimated due to the lack of experiment-relevant parameters to described defect potential models. However, the physics is expolored: the dephasing time will have a local maximum, which means at the optimal operational point, the charge defects induced dephasing time will vanish in the first order of the gate electric field, favoring the fast qubit manipulations, given the magnetic field is parallel to the gate electric field.

The second project on silicon hole spin qubits is a further extension of the germanium project. Silicon, as the main character in modern electronics, comes with various advantages along the developments of electronis. The state-of-art industry-level MOSFET

devices provides a natural platform for studying the p-type devices. However, the understanding of germanium hole spin qubits can not be translated into silicon directly due to the different band structure. Firstly, the smaller split-off band constant in silicon requires a six-band Luttinger-Kohn Hamiltonian, which will give further renormalization to the heavy-hole bands. This will impose a direct challenge using perturbative approach. Secondly, the planar quantum dot schemes are more attractive due to its potential of scalabity. These two resasons urged us to give the perturbative anslysis, and established a full numerical scheme for silicon hole qubits. In this project, we find that firstly the large modulation of g-factors can favours the electrical manipulations, agrees with some experiments. Secondly, we notice a difference between the different application of magneitc fields; when the magnetic field is applied perpendiculally to the quantum dot, there will still be a dephasing maximum, however it will vanish when we applied magnetic field parallely. This suggested further investigation will be required to fully understand the charge dephasing in semiconductor quantum dot systems.

Except the mysterious dephasing mechanisms in semiconductor quantum dot hole spin qubits, there are many aspects need to be further examined. One important issue is strain, which is a commonly used technique in semiconductor engineering. As we introduced in the thesis, there are already studies pointed out that strain can improve the Rabi oscillations by a order of magnitude. Therefore, how to incorperate the advanced strain engineering in modern electronics would be a challege in the near future.

In closing, the journey through *Optimising Coherence in Group IV Semiconductor Quantum Dot Hole Spin Qubits* not only aim to light on the intricate quantum computations, but also charts a path forward for the burgeoning field of semiconductor physics. As we stand on the brink of a new era, where quantum computing promises to redefine the boundaries of computation, communication, and encryption, this thesis is only a tentative step toward the achievements thus far and the vast possibilities that lie ahead. In this spirit of exploration and innovation, we look forward to the advancements that will emerge from this foundation, propelling us into a future quantum world.

Appendix A

Supplementary materials for chapter 4

A.1 Bastard variational wavefunction

Consider a particle with effective mass m^* in a triangular well:

$$-\frac{\hbar^2}{2m^*}\frac{\mathrm{d}^2\psi_z(z)}{\mathrm{d}z^2} + eFz\psi_z(z) = E\psi_z(z) \tag{A.1}$$

We can introduce the Bastard wavefunction:

$$\psi_H(z) = \sqrt{\frac{4\beta\left(\pi^2+\beta^2\right)}{\left(1-e^{-2\beta}\right)L\pi^2}}\cos\left(\frac{\pi z}{L}\right)\exp\left[-\beta\left(\frac{z}{L}+\frac{1}{2}\right)\right] \tag{A.2}$$

and its energy:

$$E = \left\langle \psi_z \left| -\frac{\hbar^2}{2m^*}\frac{\mathrm{d}^2}{\mathrm{d}z^2} + eFz \right| \psi_z \right\rangle = E_1^{(0)}\left[1+\frac{\beta^2}{4\pi^2}+\phi\left(\frac{1}{\beta}+\frac{2\beta}{4\pi^2+\beta^2}-\frac{1}{2}\coth\frac{\beta}{2}\right)\right], \tag{A.3}$$

where

$$\phi = \frac{eFL}{E_1^0} \quad E_1^0 = \frac{\hbar^2\pi^2}{2m^*L^2}\,. \tag{A.4}$$

The variational parameters is determined by:

$$\frac{\mathrm{d}E}{\mathrm{d}\beta} = \phi\left[-\frac{4\beta^2}{\left(\beta^2+4\pi^2\right)^2} - \frac{1}{\beta^2} + \frac{2}{\beta^2+4\pi^2} + \frac{1}{4}\operatorname{csch}^2\left(\frac{\beta}{2}\right)\right] + \frac{\beta}{2\pi^2} = 0\,. \tag{A.5}$$

Solving this equation, we will obtain a variational parameter β which is a function of F, therefore, the electric field dependency is implicit. Higher order Bastard wavefunctions are obtained by consider the basis:

$$u_n(z) = \sin\left[\frac{n\pi}{d}\left(z+\frac{L}{2}\right)\right] \times \exp\left[-\beta^n\left(\frac{z}{d}+\frac{1}{2}\right)\right]\,. \tag{A.6}$$

With this basis, we can construct the excited states via Gram-Schmidt process.

A.2 Distortion of the potential

In experiments, it is hard to establish a perfect parabolic confinement. To describe the distortions of the parabolic confinements, we study the following three models as new perturbation:

$$V_1' = \lambda|x|^3, \quad V_2' = \frac{1}{2}(\delta\omega)^2x^2, \quad V_3' = \xi|x| \tag{A.7}$$

For each of the distortion model, we set the perturbation parameters λ, δ, ξ to satisfy $2V'/\left(m_p\omega_0^2a_0^2\right) = 0.1$. If we consider regions close to the quantum dot, the energy correction due to the distortion $\langle\phi\,|V'|\,\phi\rangle$ will be small and we can treat it as off-diagonal terms and use the Schrieffer-Wolff transformation to evaluate the correction to the quantum dot energy levels. In this regime, the corrections to the first two effective quantum dot levels are the same, therefore will be no change in the qubit Zeeman splitting.

However, if we consider a larger region, the energy correction due to the distortion $\langle\phi\,|V'|\,\phi\rangle$ will be comparable to the confinement energy $\hbar\omega_0$, i.e, the new quantum dot energy levels will read $E = E_0 + E_z + \langle\phi_i\,|V'|\,\phi_i\rangle$. For example, when the quantum well width is $d = 11$ nm, $F = 4.6\times10^7$ V/m. The first model (cubic term) will change the qubit Zeeman splitting by 1.7%, and the second model (quadratic term) will change the qubit Zeeman splitting by 0.76% and the third model (linear term) will change the qubit Zeeman splitting by 0.83%.

Appendix B

Supplementary materials for chapter 5

B.1 Numerical diagonalization

In this section, we will discuss the details of the numerical diagonalization of the qubit Hamiltonian. In general, we can just project our qubit Hamiltonian onto the wave functions we are using up to as many levels as we want. However, performing integrals analytically over all the wave functions is time-consuming. However, due to the parity of the wave functions and the symmetry of our confinement potential, we can use the following relations to further simplify the integrals.

If ϕ is the simple Harmonic oscillator wave functions, we will have:

$$\int_{-\infty}^{\infty} \phi_n(x) \frac{d\phi_m}{dx} dx = \begin{cases} a\sqrt{\frac{n+1}{2}} & m = n+1 \\ -a\sqrt{\frac{n}{2}} & m = n-1 \\ 0 & \text{otherwise} \end{cases} \tag{B.1}$$

$$\int_{-\infty}^{\infty} \phi_m(x) x \phi_n(x) dx = \begin{cases} \frac{1}{a}\sqrt{\frac{n+1}{2}} & m = n+1 \\ \frac{1}{a}\sqrt{\frac{n}{2}} & m = n-1 \\ 0 & \text{otherwise} \end{cases} \tag{B.2}$$

$$\int_{-\infty}^{\infty} \phi_m(x) x^2 \phi_n(x) dx = \begin{cases} \frac{\sqrt{n(n-1)}}{2a^2} & m = n-2 \\ \frac{2n+1}{2a^2} & m = n \\ \frac{\sqrt{(n+1)(n+2)}}{2a^2} & m = n+2 \\ 0 & m \neq n \neq n \pm 2 \end{cases} \tag{B.3}$$

When we evaluating the integrals, we need to replace a by appropriate dot radius (a_x or a_y). The out-of-plane wave functions are derived from infinite square well, which are sinusoidal functions and easier to deal with in software. In general, this approach can be extended to as many levels as we want.

The number of levels used in $\hat{z}$-direction as described in the main text Eq. (3) - Eq. (4) are important to understand the convergence when electric field is large. The ground state wave-function can be written as $\langle x, y, z|\mathbb{0}\rangle$. In Fig. B.1, we plot several probability density curves of our $\hat{z}$-direction wave-functions using different number of sinusoidal wave-functions. We can see when we use more than seven sinusoidal wave-functions, the probability will not vary much along the $\hat{z}$-axis.

B.2 Rashba terms

In this section, we elaborate on the Rashba terms discussed in the main text, presenting their full expressions within the framework of a perturbative approach. The Rashba spin-orbit coupling Hamiltonian under our consideration comprises two distinct components: the α_2 terms, representing the 'cubic' k_+^3-type Rashba terms, and the 'linear' α_3 terms, corresponding to the $k_+k_-k_+$-type Rashba effect (where $k_+ = k_x + ik_y$, $k_- = k_x - ik_y$)

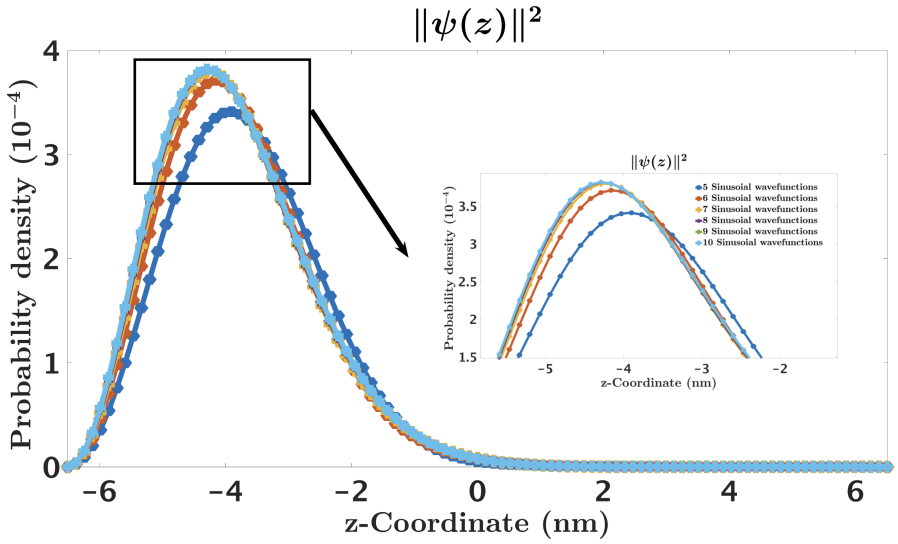

Figure B.1: **Probability density distribution evaluated by evaluated by the norm square of the wave-function in $\hat{z}$-direction.** The probability density is plotted as a function of the $\hat{z}$-coordinate, in the main text, the quantum well width is 13 nm placed symmetrically. The shape of the probability density are very close if the number of sinusoidal wave-function used exceed seven.

[328]. While the α_3 Rashba term winds the Fermi surface three times, enabling a $\Delta n = 3$ orbital transition; the α_3 Rashba term wind the Fermi surface once, inducing a $\Delta n = 1$ Rashba term. The possible k-linear term like $k_+\sigma_- - k_-\sigma_+$ are allowed by method of invariant, however, this term only have marginal contributions due to weak conduction band-valence band coupling [548, 328]. The form of our spin-orbital coupling Hamiltonian can be written as:

$$H_{\mathrm{SO}} = \alpha_2(k_+^3\sigma_- - k_-^3\sigma_+) + \alpha_3(\{k_+^2, k_-\}\sigma_+ - \{k_+, k_-^2\}\sigma_-) \tag{B.4}$$

As a example, consider the ground state and the two first excited states (one in x and one in y) we used in the main text

$$\phi_0 = \frac{1}{\sqrt{\pi}}\frac{1}{\sqrt{a_x a_y}}\exp\left(-\frac{x^2}{2a_x^2} - \frac{y^2}{2a_y^2}\right) \tag{B.5}$$

$$\phi_{1,x} = \frac{\sqrt{2}}{\sqrt{\pi a_x^3 a_y}} x \exp\left(-\frac{x^2}{2a_x^2} - \frac{y^2}{2a_y^2}\right) \tag{B.6}$$

$$\phi_{1,y} = \frac{\sqrt{2}}{\sqrt{\pi a_x a_y^3}} y \exp\left(-\frac{x^2}{2a_x^2} - \frac{y^2}{2a_y^2}\right) \tag{B.7}$$

We can realize that in a circular quantum dot case, there is no element between the ground states and the first excited for α_2 Rashba term:

$$\int_{-\infty}^{+\infty} \phi_0 \alpha_2 (k_+^3 \sigma_-) \phi_{1,y} = -i \frac{3\alpha_2}{2\sqrt{2} a_y^3} \left(1 - \frac{a_y^2}{a_x^2}\right) = 0 \tag{B.8}$$

while the α_3 Rashba term will be present:

$$\int_{-\infty}^{+\infty} \phi_0 \alpha_3 (k_+ k_- k_+ \sigma_+) \phi_{1,y} = i \frac{\alpha_3}{2\sqrt{2} a_y^3} \left(1 + 3\frac{a_y^2}{a_x^2}\right) \tag{B.9}$$

As our calculation shows, the α_3 'linear' terms can induce a transition between to adjacent levels, accompanied by spin flips in a circular dot case, while the α_2 'cubic' terms do not contribute to the EDSR unless in an elliptical dot.

References

[1] J C Abadillo-Uriel, Joe Salfi, Xuedong Hu, Sven Rogge, M J Calderon, and Dimitrie Culcer. Entanglement control and magic angles for acceptor qubits in si. *Appl. Phys. Lett.*, 113:12102, 2018. URL https://doi.org/10.1063/1.5036521.

[2] José Carlos Abadillo-Uriel, Esteban A. Rodríguez-Mena, Biel Martinez, and Yann-Michel Niquet. Hole-spin driving by strain-induced spin-orbit interactions. *Phys. Rev. Lett.*, 131:097002, Sep 2023. doi: 10.1103/PhysRevLett.131.097002. URL https://link.aps.org/doi/10.1103/PhysRevLett.131.097002.

[3] Dmitry A. Abanin, Ehud Altman, Immanuel Bloch, and Maksym Serbyn. Colloquium: Many-body localization, thermalization, and entanglement. *Rev. Mod. Phys.*, 91:021001, May 2019. doi: 10.1103/RevModPhys.91.021001. URL https://link.aps.org/doi/10.1103/RevModPhys.91.021001.

[4] S. Adam, E. H. Hwang, and S. Das Sarma. Two-dimensional transport and screening in topological insulator surface states. *Phys. Rev. B*, 85:235413, Jun 2012. doi: 10.1103/PhysRevB.85.235413. URL https://link.aps.org/doi/10.1103/PhysRevB.85.235413.

[5] Christoph Adelsberger, Mónica Benito, Stefano Bosco, Jelena Klinovaja, and Daniel Loss. Hole-spin qubits in ge nanowire quantum dots: Interplay of orbital magnetic field, strain, and growth direction. *Phys. Rev. B*, 105:075308, Feb 2022. doi: 10.1103/PhysRevB.105.075308. URL https://link.aps.org/doi/10.1103/PhysRevB.105.075308.

[6] Christoph Adelsberger, Stefano Bosco, Jelena Klinovaja, and Daniel Loss. Enhanced orbital magnetic field effects in ge hole nanowires. *Phys. Rev. B*, 106:235408, Dec 2022. doi: 10.1103/PhysRevB.106.235408. URL https://link.aps.org/doi/10.1103/PhysRevB.106.235408.

[7] Kushagra Aggarwal, Andrea Hofmann, Daniel Jirovec, Ivan Prieto, Amir Sammak, Marc Botifoll, Sara Martí-Sánchez, Menno Veldhorst, Jordi Arbiol, Giordano Scappucci, Jeroen Danon, and Georgios Katsaros. Enhancement of proximity-induced superconductivity in a planar ge hole gas. *Phys. Rev. Res.*, 3:L022005, Apr 2021. doi: 10.1103/PhysRevResearch.3.L022005. URL https://link.aps.org/doi/10.1103/PhysRevResearch.3.L022005.

[8] Rajeev Ahluwalia and Wenwu Cao. Influence of dipolar defects on switching behavior in ferroelectrics. *Phys. Rev. B*, 63:012103, Dec 2000. doi: 10.1103/PhysRevB.63.012103. URL https://link.aps.org/doi/10.1103/PhysRevB.63.012103.

[9] Doyeol Ahn, Sean J. Yoon, Shun Lien Chuang, and Chih-Sheng Chang. Theory of optical gain in strained-layer quantum wells within the 6×6 Luttinger–Kohn model. *Journal of Applied Physics*, 78(4):2489–2497, 08 1995. ISSN 0021-8979. doi: 10.1063/1.360103. URL https://doi.org/10.1063/1.360103.

[10] Golrokh Akhgar, Lothar Ley, Daniel L. Creedon, Alastair Stacey, Jeffrey C. McCallum, Alex R. Hamilton, and Christopher I. Pakes. g-factor and well-width fluctuations as a function of carrier density in the two-dimensional hole accumulation layer of transfer-doped diamond. *Phys. Rev. B*, 99:035159, Jan 2019. doi: 10.1103/PhysRevB.99.035159. URL https://link.aps.org/doi/10.1103/PhysRevB.99.035159.

[11] Tameem Albash and Daniel A. Lidar. Adiabatic quantum computation. *Rev. Mod. Phys.*, 90:015002, Jan 2018. doi: 10.1103/RevModPhys.90.015002. URL https://link.aps.org/doi/10.1103/RevModPhys.90.015002.

[12] Michael N. Alexadner and Donald F. Holcomb. Semiconductor-to-metal transition

in n-type group iv semiconductors. *Rev. Mod. Phys.*, 40:815–829, Oct 1968. doi: 10.1103/RevModPhys.40.815. URL https://link.aps.org/doi/10.1103/RevModPhys.40.815.

[13] Anian Altherr and Yuxiang Yang. Quantum metrology for non-markovian processes. *Physical Review Letters*, 127, 8 2021. ISSN 10797114. doi: 10.1103/PhysRevLett.127.060501. URL https://journals.aps.org/prl/abstract/10.1103/PhysRevLett.127.060501.

[14] S. Amasha, K. MacLean, Iuliana P. Radu, D. M. Zumbühl, M. A. Kastner, M. P. Hanson, and A. C. Gossard. Electrical control of spin relaxation in a quantum dot. *Phys. Rev. Lett.*, 100:046803, Jan 2008. doi: 10.1103/PhysRevLett.100.046803. URL https://link.aps.org/doi/10.1103/PhysRevLett.100.046803.

[15] Tsuneya Ando, Alan B. Fowler, and Frank Stern. Electronic properties of two-dimensional systems. *Rev. Mod. Phys.*, 54:437–672, Apr 1982. doi: 10.1103/RevModPhys.54.437. URL https://link.aps.org/doi/10.1103/RevModPhys.54.437.

[16] Markus Ansmann, H. Wang, Radoslaw C. Bialczak, Max Hofheinz, Erik Lucero, M. Neeley, A. D. O'Connell, D. Sank, M. Weides, J. Wenner, A. N. Cleland, and John M. Martinis. Violation of bell's inequality in josephson phase qubits. *Nature*, 461(7263):504–506, 2009. doi: 10.1038/nature08363. URL https://doi.org/10.1038/nature08363.

[17] N. Ares, V. N. Golovach, G. Katsaros, M. Stoffel, F. Fournel, L. I. Glazman, O. G. Schmidt, and S. De Franceschi. Nature of tunable hole g factors in quantum dots. *Phys. Rev. Lett.*, 110:046602, Jan 2013. doi: 10.1103/PhysRevLett.110.046602. URL https://link.aps.org/doi/10.1103/PhysRevLett.110.046602.

[18] C. A. Argüelles and B. J. P. Jones. Neutrino oscillations in a quantum processor. *Phys. Rev. Res.*, 1:033176, Dec 2019. doi: 10.1103/PhysRevResearch.1.033176. URL https://link.aps.org/doi/10.1103/PhysRevResearch.1.033176.

[19] E. Arimondo, M. Inguscio, and P. Violino. Experimental determinations of the hyperfine structure in the alkali atoms. *Rev. Mod. Phys.*, 49:31–75, Jan 1977. doi: 10.1103/RevModPhys.49.31. URL https://link.aps.org/doi/10.1103/RevModPhys.49.31.

[20] Lucy V. C. Assali, Helena M. Petrilli, Rodrigo B. Capaz, Belita Koiller, Xuedong Hu, and S. Das Sarma. Hyperfine interactions in silicon quantum dots. *Phys. Rev. B*, 83:165301, Apr 2011. doi: 10.1103/PhysRevB.83.165301. URL https://link.aps.org/doi/10.1103/PhysRevB.83.165301.

[21] A. Ayachi, W. Ben Chouikha, S. Jaziri, and R. Bennaceur. Telegraph noise effects on two charge qubits in double quantum dots. *Phys. Rev. A*, 89:012330, Jan 2014. doi: 10.1103/PhysRevA.89.012330. URL https://link.aps.org/doi/10.1103/PhysRevA.89.012330.

[22] Edward B. Baker. The application of the fermi-thomas statistical model to the calculation of potential distribution in positive ions. *Phys. Rev.*, 36:630–647, Aug 1930. doi: 10.1103/PhysRev.36.630. URL https://link.aps.org/doi/10.1103/PhysRev.36.630.

[23] A Baldereschi and Nunzio C Lipari. Energy levels of direct excitons in semiconductors with degenerate bands. *Phys. Rev. B*, 3:439–451, 1 1971. doi: 10.1103/PhysRevB.3.439. URL https://link.aps.org/doi/10.1103/PhysRevB.3.439.

[24] A Baldereschi and Nunzio O Lipari. Spherical model of shallow acceptor states in semiconductors. *Phys. Rev. B*, 8:2697–2709, 9 1973. doi: 10.1103/PhysRevB.8.2697. URL https://link.aps.org/doi/10.1103/PhysRevB.8.2697.

[25] Jeff P. Barnes and Warren S. Warren. Decoherence and programmable quantum computation. *Phys. Rev. A*, 60:4363–4374, Dec 1999. doi: 10.1103/PhysRevA.60.4363. URL https://link.aps.org/doi/10.1103/PhysRevA.60.4363.

[26] Stefano Baroni, Stefano de Gironcoli, Andrea Dal Corso, and Paolo Giannozzi. Phonons and related crystal properties from density-functional perturbation the-

ory. *Rev. Mod. Phys.*, 73:515–562, Jul 2001. doi: 10.1103/RevModPhys.73.515. URL https://link.aps.org/doi/10.1103/RevModPhys.73.515.

[27] John F. Barry, Jennifer M. Schloss, Erik Bauch, Matthew J. Turner, Connor A. Hart, Linh M. Pham, and Ronald L. Walsworth. Sensitivity optimization for nv-diamond magnetometry. *Rev. Mod. Phys.*, 92:015004, Mar 2020. doi: 10.1103/RevModPhys.92.015004. URL https://link.aps.org/doi/10.1103/RevModPhys.92.015004.

[28] R. H. Bartram, C. E. Swenberg, and J. T. Fournier. Theory of trapped-hole centers in aluminum oxide. *Phys. Rev.*, 139:A941–A951, Aug 1965. doi: 10.1103/PhysRev.139.A941. URL https://link.aps.org/doi/10.1103/PhysRev.139.A941.

[29] Christian W. Bauer, Zohreh Davoudi, A. Baha Balantekin, Tanmoy Bhattacharya, Marcela Carena, Wibe A. de Jong, Patrick Draper, Aida El-Khadra, Nate Gemelke, Masanori Hanada, Dmitri Kharzeev, Henry Lamm, Ying-Ying Li, Junyu Liu, Mikhail Lukin, Yannick Meurice, Christopher Monroe, Benjamin Nachman, Guido Pagano, John Preskill, Enrico Rinaldi, Alessandro Roggero, David I. Santiago, Martin J. Savage, Irfan Siddiqi, George Siopsis, David Van Zanten, Nathan Wiebe, Yukari Yamauchi, Kübra Yeter-Aydeniz, and Silvia Zorzetti. Quantum simulation for high-energy physics. *PRX Quantum*, 4, 4 2023. ISSN 26913399. doi: 10.1103/PRXQuantum.4.027001. URL https://journals.aps.org/prxquantum/abstract/10.1103/PRXQuantum.4.027001.

[30] Félix Beaudoin and W. A. Coish. Microscopic models for charge-noise-induced dephasing of solid-state qubits. *Phys. Rev. B*, 91:165432, Apr 2015. doi: 10.1103/PhysRevB.91.165432. URL https://link.aps.org/doi/10.1103/PhysRevB.91.165432.

[31] Christoph Becher, Weibo Gao, Swastik Kar, Christian Marciniak, Thomas Monz, John G Bartholomew, Philippe Goldner, Huanqian Loh, Elizabeth Marcellina, Kuan Eng Johnson Goh, Teck Seng Koh, Bent Weber, ZHAO MU, Jeng-Yuan Tsai, Qimin Yan, Tobias Huber, Sven Höfling, Samuel Gyger, Stephan Steinhauer, and Val

Zwiller. 2023 roadmap for materials for quantum technologies. *Materials for Quantum Technology*, 4 2022. ISSN 2633-4356. doi: 10.1088/2633-4356/aca3f2. URL https://iopscience.iop.org/article/10.1088/2633-4356/aca3f2.

[32] Paul Benioff. The computer as a physical system: A microscopic quantum mechanical hamiltonian model of computers as represented by turing machines. *Journal of Statistical Physics*, 22(5):563–591, 1980. doi: 10.1007/BF01011339. URL https://doi.org/10.1007/BF01011339.

[33] Adam Bermeister, Daniel Keith, and Dimitrie Culcer. Charge noise, spin-orbit coupling, and dephasing of single-spin qubits. *Applied Physics Letters*, 105(19):192102, 11 2014. ISSN 0003-6951. doi: 10.1063/1.4901162. URL https://doi.org/10.1063/1.4901162.

[34] WILLIAM BERNARD and HERBERT B. CALLEN. Irreversible thermodynamics of nonlinear processes and noise in driven systems. *Rev. Mod. Phys.*, 31:1017–1044, Oct 1959. doi: 10.1103/RevModPhys.31.1017. URL https://link.aps.org/doi/10.1103/RevModPhys.31.1017.

[35] B. Andrei Bernevig, Taylor L. Hughes, and Shou-Cheng Zhang. Quantum spin hall effect and topological phase transition in hgte quantum wells. *Science*, 314(5806):1757–1761, 2006. ISSN 0036-8075. doi: 10.1126/science.1133734. URL https://science.sciencemag.org/content/314/5806/1757.

[36] Pankaj Bhalla, Allan H. MacDonald, and Dimitrie Culcer. Resonant photovoltaic effect in doped magnetic semiconductors. *Phys. Rev. Lett.*, 124:087402, Feb 2020. doi: 10.1103/PhysRevLett.124.087402. URL https://link.aps.org/doi/10.1103/PhysRevLett.124.087402.

[37] Michael J. Biercuk, Hermann Uys, Aaron P. VanDevender, Nobuyasu Shiga, Wayne M. Itano, and John J. Bollinger. Optimized dynamical decoupling in a model quantum memory. *Nature*, 458(7241):996–1000, 2009. doi: 10.1038/nature07951. URL https://doi.org/10.1038/nature07951.

[38] G Bihlmayer, O Rader, and R Winkler. Focus on the rashba effect. *New Journal of Physics*, 17(5):050202, 2015. doi: 10.1088/1367-2630/17/5/050202. URL https://iopscience.iop.org/article/10.1088/1367-2630/17/5/050202/meta.

[39] Eliana Biolatti, Rita C. Iotti, Paolo Zanardi, and Fausto Rossi. Quantum information processing with semiconductor macroatoms. *Phys. Rev. Lett.*, 85:5647–5650, Dec 2000. doi: 10.1103/PhysRevLett.85.5647. URL https://link.aps.org/doi/10.1103/PhysRevLett.85.5647.

[40] J. L. Black and B. I. Halperin. Spectral diffusion, phonon echoes, and saturation recovery in glasses at low temperatures. *Phys. Rev. B*, 16:2879–2895, Sep 1977. doi: 10.1103/PhysRevB.16.2879. URL https://link.aps.org/doi/10.1103/PhysRevB.16.2879.

[41] Alexandre Blais, Arne L. Grimsmo, S. M. Girvin, and Andreas Wallraff. Circuit quantum electrodynamics. *Rev. Mod. Phys.*, 93:025005, May 2021. doi: 10.1103/RevModPhys.93.025005. URL https://link.aps.org/doi/10.1103/RevModPhys.93.025005.

[42] Rainer Blatt and David Wineland. Entangled states of trapped atomic ions. *Nature*, 453(7198):1008–1015, 2008. doi: 10.1038/nature07125. URL https://doi.org/10.1038/nature07125.

[43] F. Bloch. Nuclear induction. *Phys. Rev.*, 70:460–474, Oct 1946. doi: 10.1103/PhysRev.70.460. URL https://link.aps.org/doi/10.1103/PhysRev.70.460.

[44] N. Bloembergen, E. M. Purcell, and R. V. Pound. Relaxation effects in nuclear magnetic resonance absorption. *Phys. Rev.*, 73:679–712, Apr 1948. doi: 10.1103/PhysRev.73.679. URL https://link.aps.org/doi/10.1103/PhysRev.73.679.

[45] Karl W. Böer and Udo W. Pohl. *Bands and Bandgaps in Solids*, pages 257–317. Springer International Publishing, Cham, 2023. ISBN 978-3-031-18286-

0. doi: 10.1007/978-3-031-18286-0_8. URL https://doi.org/10.1007/978-3-031-18286-0_8.

[46] H. Bohuslavskyi, D. Kotekar-Patil, R. Maurand, A. Corna, S. Barraud, L. Bourdet, L. Hutin, Y.-M. Niquet, X. Jehl, S. De Franceschi, M. Vinet, and M. Sanquer. Pauli blockade in a few-hole PMOS double quantum dot limited by spin-orbit interaction. *Applied Physics Letters*, 109(19):193101, 11 2016. ISSN 0003-6951. doi: 10.1063/1.4966946. URL https://doi.org/10.1063/1.4966946.

[47] George Bool. *The Mathematical Analysis of Logic*. Project Gutenberg eBooks, New York, 1st edition, Jan 1850. doi: gutenberg.org.ebooks.36884. URL https://www.gutenberg.org/ebooks/36884.

[48] Péter Boross, Gábor Széchenyi, Dimitrie Culcer, and András Pályi. Control of valley dynamics in silicon quantum dots in the presence of an interface step. *Phys. Rev. B*, 94:035438, Jul 2016. doi: 10.1103/PhysRevB.94.035438. URL https://link.aps.org/doi/10.1103/PhysRevB.94.035438.

[49] Francesco Borsoi, Nico W. Hendrickx, Valentin John, Sayr Motz, Floor van Riggelen, Amir Sammak, Sander L. de Snoo, Giordano Scappucci, and Menno Veldhorst. Shared control of a 16 semiconductor quantum dot crossbar array. *Nature Nanotechnology*, 9 2022. ISSN 17483395. doi: 10.1038/s41565-023-01491-3. URL https://www.nature.com/articles/s41565-023-01491-3.

[50] Stefano Bosco and Daniel Loss. Fully tunable hyperfine interactions of hole spin qubits in si and ge quantum dots. *Phys. Rev. Lett.*, 127:190501, Nov 2021. doi: 10.1103/PhysRevLett.127.190501. URL https://link.aps.org/doi/10.1103/PhysRevLett.127.190501.

[51] Stefano Bosco and Daniel Loss. Hole spin qubits in thin curved quantum wells. *Phys. Rev. Appl.*, 18:044038, Oct 2022. doi: 10.1103/PhysRevApplied.18.044038. URL https://link.aps.org/doi/10.1103/PhysRevApplied.18.044038.

[52] Stefano Bosco, Mónica Benito, Christoph Adelsberger, and Daniel Loss. Squeezed hole spin qubits in ge quantum dots with ultrafast gates at low power. *Phys. Rev. B*,

104:115425, Sep 2021. doi: 10.1103/PhysRevB.104.115425. URL https://link.aps.org/doi/10.1103/PhysRevB.104.115425.

[53] Stefano Bosco, Bence Hetényi, and Daniel Loss. Hole spin qubits in si finfets with fully tunable spin-orbit coupling and sweet spots for charge noise. *PRX Quantum*, 2, 4 2021. ISSN 26913399. doi: 10.1103/PRXQuantum.2.010348. URL https://link.aps.org/doi/10.1103/PRXQuantum.2.010348.

[54] Stefano Bosco, Pasquale Scarlino, Jelena Klinovaja, and Daniel Loss. Fully tunable longitudinal spin-photon interactions in si and ge quantum dots. *Phys. Rev. Lett.*, 129:066801, Aug 2022. doi: 10.1103/PhysRevLett.129.066801. URL https://link.aps.org/doi/10.1103/PhysRevLett.129.066801.

[55] Stefano Bosco, Simon Geyer, Leon C. Camenzind, Rafael S. Eggli, Andreas Fuhrer, Richard J. Warburton, Dominik M. Zumbühl, J. Carlos Egues, Andreas V. Kuhlmann, and Daniel Loss. Phase-driving hole spin qubits. *Phys. Rev. Lett.*, 131:197001, Nov 2023. doi: 10.1103/PhysRevLett.131.197001. URL https://link.aps.org/doi/10.1103/PhysRevLett.131.197001.

[56] Léo Bourdet and Yann-Michel Niquet. All-electrical manipulation of silicon spin qubits with tunable spin-valley mixing. *Phys. Rev. B*, 97:155433, Apr 2018. doi: 10.1103/PhysRevB.97.155433. URL https://link.aps.org/doi/10.1103/PhysRevB.97.155433.

[57] Daniel Braun, Gerardo Adesso, Fabio Benatti, Roberto Floreanini, Ugo Marzolino, Morgan W. Mitchell, and Stefano Pirandola. Quantum-enhanced measurements without entanglement. *Rev. Mod. Phys.*, 90:035006, Sep 2018. doi: 10.1103/RevModPhys.90.035006. URL https://link.aps.org/doi/10.1103/RevModPhys.90.035006.

[58] Matthias Brauns, Joost Ridderbos, Ang Li, Erik P. A. M. Bakkers, Wilfred G. van der Wiel, and Floris A. Zwanenburg. Anisotropic pauli spin blockade in hole quantum dots. *Phys. Rev. B*, 94:041411, Jul 2016. doi:

10.1103/PhysRevB.94.041411. URL https://link.aps.org/doi/10.1103/PhysRevB.94.041411.

[59] S. L. Braunstein, C. M. Caves, R. Jozsa, N. Linden, S. Popescu, and R. Schack. Separability of very noisy mixed states and implications for nmr quantum computing. *Phys. Rev. Lett.*, 83:1054–1057, Aug 1999. doi: 10.1103/PhysRevLett.83.1054. URL https://link.aps.org/doi/10.1103/PhysRevLett.83.1054.

[60] Samuel L. Braunstein and Peter van Loock. Quantum information with continuous variables. *Rev. Mod. Phys.*, 77:513–577, Jun 2005. doi: 10.1103/RevModPhys.77.513. URL https://link.aps.org/doi/10.1103/RevModPhys.77.513.

[61] H Büch, S Mahapatra, R Rahman, A Morello, and M Y Simmons. Spin readout and addressability of phosphorus-donor clusters in silicon. *Nature Communications*, 4, 2013. ISSN 20411723. doi: 10.1038/ncomms3017. URL https://doi.org/10.1038/ncomms3017.

[62] Denis V. Bulaev and Daniel Loss. Spin relaxation and anticrossing in quantum dots: Rashba versus dresselhaus spin-orbit coupling. *Phys. Rev. B*, 71:205324, May 2005. doi: 10.1103/PhysRevB.71.205324. URL https://link.aps.org/doi/10.1103/PhysRevB.71.205324.

[63] Denis V. Bulaev and Daniel Loss. Spin relaxation and decoherence of holes in quantum dots. *Phys. Rev. Lett.*, 95:076805, Aug 2005. doi: 10.1103/PhysRevLett.95.076805. URL https://link.aps.org/doi/10.1103/PhysRevLett.95.076805.

[64] Denis V. Bulaev and Daniel Loss. Electric dipole spin resonance for heavy holes in quantum dots. *Phys. Rev. Lett.*, 98:097202, Feb 2007. doi: 10.1103/PhysRevLett.98.097202. URL https://link.aps.org/doi/10.1103/PhysRevLett.98.097202.

[65] Guido Burkard and Daniel Loss. Cancellation of spin-orbit effects in quantum gates based on the exchange coupling in quantum dots. *Phys. Rev. Lett.*, 88:047903,

Jan 2002. doi: 10.1103/PhysRevLett.88.047903. URL https://link.aps.org/doi/10.1103/PhysRevLett.88.047903.

[66] Guido Burkard, Daniel Loss, and David P. DiVincenzo. Coupled quantum dots as quantum gates. *Phys. Rev. B*, 59:2070–2078, Jan 1999. doi: 10.1103/PhysRevB.59.2070. URL https://link.aps.org/doi/10.1103/PhysRevB.59.2070.

[67] Guido Burkard, Daniel Loss, David P. DiVincenzo, and John A. Smolin. Physical optimization of quantum error correction circuits. *Phys. Rev. B*, 60:11404–11416, Oct 1999. doi: 10.1103/PhysRevB.60.11404. URL https://link.aps.org/doi/10.1103/PhysRevB.60.11404.

[68] Guido Burkard, Thaddeus D. Ladd, Andrew Pan, John M. Nichol, and Jason R. Petta. Semiconductor spin qubits. *Rev. Mod. Phys.*, 95:025003, Jun 2023. doi: 10.1103/RevModPhys.95.025003. URL https://link.aps.org/doi/10.1103/RevModPhys.95.025003.

[69] V. Bush and S. H. Caldwell. Thomas-fermi equation solution by the differential analyzer. *Phys. Rev.*, 38:1898–1902, Nov 1931. doi: 10.1103/PhysRev.38.1898. URL https://link.aps.org/doi/10.1103/PhysRev.38.1898.

[70] Yu A Bychkov and E I Rashba. Oscillatory effects and the magnetic susceptibility of carriers in inversion layers. *Journal of Physics C: Solid State Physics*, 17:6039, 11 1984. doi: 10.1088/0022-3719/17/33/015. URL https://dx.doi.org/10.1088/0022-3719/17/33/015.

[71] Zhenyu Cai, Ryan Babbush, Simon C. Benjamin, Suguru Endo, William J. Huggins, Ying Li, Jarrod R. McClean, and Thomas E. O'Brien. Quantum error mitigation. *Rev. Mod. Phys.*, 95:045005, Dec 2023. doi: 10.1103/RevModPhys.95.045005. URL https://link.aps.org/doi/10.1103/RevModPhys.95.045005.

[72] A. R. Calderbank and Peter W. Shor. Good quantum error-correcting codes exist. *Phys. Rev. A*, 54:1098–1105, Aug 1996. doi: 10.1103/PhysRevA.54.1098. URL https://link.aps.org/doi/10.1103/PhysRevA.54.1098.

[73] Leon C. Camenzind, Simon Geyer, Andreas Fuhrer, Richard J. Warburton, Dominik M. Zumbühl, and Andreas V. Kuhlmann. A hole spin qubit in a fin field-effect transistor above 4 kelvin. *Nature Electronics*, 5(3):178–183, 2022. doi: 10.1038/s41928-022-00722-0. URL https://doi.org/10.1038/s41928-022-00722-0.

[74] Manuel Cardona and Fred H Pollak. Energy-band structure of germanium and silicon: The k.p method. *Phys. Rev.*, 142:530–543, 2 1966. doi: 10.1103/PhysRev.142.530. URL https://link.aps.org/doi/10.1103/PhysRev.142.530.

[75] Matteo Carrega, Luca Chirolli, Stefan Heun, and Lucia Sorba. Anyons in quantum hall interferometry. *Nature Reviews Physics*, 3(10):698–711, 2021. doi: 10.1038/s42254-021-00351-0. URL https://doi.org/10.1038/s42254-021-00351-0.

[76] Anasua Chatterjee, Paul Stevenson, Silvano De Franceschi, Andrea Morello, Nathalie P de Leon, and Ferdinand Kuemmeth. Semiconductor qubits in practice. *Nature Reviews Physics*, 3:157–177, 2021. URL https://doi.org/10.1038/s42254-021-00283-9.

[77] E. A. Chekhovich, A. B. Krysa, M. S. Skolnick, and A. I. Tartakovskii. Direct measurement of the hole-nuclear spin interaction in single InP/GaInP quantum dots using photoluminescence spectroscopy. *Phys. Rev. Lett.*, 106:027402, Jan 2011. doi: 10.1103/PhysRevLett.106.027402. URL https://link.aps.org/doi/10.1103/PhysRevLett.106.027402.

[78] E A Chekhovich, M N Makhonin, A I Tartakovskii, A Yacoby, H Bluhm, K C Nowack, and L M K Vandersypen. Nuclear spin effects in semiconductor quantum dots. *Nature Materials*, 12:494–504, 4 2013. ISSN 14761122. doi: 10.1038/nmat3652. URL https://www.nature.com/articles/nmat3652.

[79] Stefano Chesi, Xiaoya Judy Wang, and W A Coish. Controlling hole spins in quantum dots and wells. *European Physical Journal Plus*, 129:1–16, 4 2014. ISSN 21905444. doi: 10.1140/epjp/i2014-14086-2.

[80] I. Chiorescu, Y. Nakamura, C. J. P. M. Harmans, and J. E. Mooij. Coherent quantum dynamics of a superconducting flux qubit. *Science*, 299(5614):1869–1871, 2003. doi: 10.1126/science.1081045. URL https://www.science.org/doi/abs/10.1126/science.1081045.

[81] Deung-Jang Choi, Nicolas Lorente, Jens Wiebe, Kirsten von Bergmann, Alexander F. Otte, and Andreas J. Heinrich. Colloquium: Atomic spin chains on surfaces. *Rev. Mod. Phys.*, 91:041001, Oct 2019. doi: 10.1103/RevModPhys.91.041001. URL https://link.aps.org/doi/10.1103/RevModPhys.91.041001.

[82] Rui-Lin Chu, Wen-Yu Shan, Jie Lu, and Shun-Qing Shen. Surface and edge states in topological semimetals. *Phys. Rev. B*, 83:075110, Feb 2011. doi: 10.1103/PhysRevB.83.075110. URL https://link.aps.org/doi/10.1103/PhysRevB.83.075110.

[83] Steven Chu. Laser manipulation of atoms and particles. *Science*, 253(5022):861–866, 1991. doi: 10.1126/science.253.5022.861. URL https://www.science.org/doi/abs/10.1126/science.253.5022.861.

[84] Ana Ciocoiu, Mohammad Khalifa, and Joe Salfi. Towards computer-assisted design of hole spin qubits in quantum dot devices. *arXiv preprint arXiv:2209.12026*, 2022. URL https://doi.org/10.48550/arXiv.2209.12026.

[85] J. I. Cirac and P. Zoller. Quantum computations with cold trapped ions. *Phys. Rev. Lett.*, 74:4091–4094, May 1995. doi: 10.1103/PhysRevLett.74.4091. URL https://link.aps.org/doi/10.1103/PhysRevLett.74.4091.

[86] J. I. Cirac, A. K. Ekert, S. F. Huelga, and C. Macchiavello. Distributed quantum computation over noisy channels. *Phys. Rev. A*, 59:4249–4254, Jun 1999. doi: 10.1103/PhysRevA.59.4249. URL https://link.aps.org/doi/10.1103/PhysRevA.59.4249.

[87] A. A. Clerk, M. H. Devoret, S. M. Girvin, Florian Marquardt, and R. J. Schoelkopf. Introduction to quantum noise, measurement, and amplification. *Rev. Mod. Phys.*,

82:1155–1208, Apr 2010. doi: 10.1103/RevModPhys.82.1155. URL https://link.aps.org/doi/10.1103/RevModPhys.82.1155.

[88] J I Climente, M Korkusinski, G Goldoni, and P Hawrylak. Theory of valence-band holes as luttinger spinors in vertically coupled quantum dots. *Physical Review B - Condensed Matter and Materials Physics*, 78, 4 2008. ISSN 10980121. doi: 10.1103/PhysRevB.78.115323.

[89] W A Coish and J Baugh. Nuclear spins in nanostructures. *physica status solidi (b)*, 246:2203–2215, 2009. doi: https://doi.org/10.1002/pssb.200945229. URL https://onlinelibrary.wiley.com/doi/abs/10.1002/pssb.200945229.

[90] W A Coish and Daniel Loss. Hyperfine interaction in a quantum dot: Non-markovian electron spin dynamics. *Phys. Rev. B*, 70:195340, 11 2004. doi: 10.1103/PhysRevB.70.195340. URL https://link.aps.org/doi/10.1103/PhysRevB.70.195340.

[91] James L. Collins, Anton Tadich, Weikang Wu, Lidia C. Gomes, Joao N. B. Rodrigues, Chang Liu, Jack Hellerstedt, Hyejin Ryu, Shujie Tang, Sung-Kwan Mo, Shaffique Adam, Shengyuan A. Yang, Michael S. Fuhrer, and Mark T. Edmonds. Electric-field-tuned topological phase transition in ultrathin na3bi. *Nature*, 564 (7736):390–394, Dec 2018. ISSN 1476-4687. doi: 10.1038/s41586-018-0788-5. URL https://doi.org/10.1038/s41586-018-0788-5.

[92] Elliot J. Connors, JJ Nelson, Haifeng Qiao, Lisa F. Edge, and John M. Nichol. Low-frequency charge noise in si/sige quantum dots. *Phys. Rev. B*, 100:165305, Oct 2019. doi: 10.1103/PhysRevB.100.165305. URL https://link.aps.org/doi/10.1103/PhysRevB.100.165305.

[93] Elliot J. Connors, J. Nelson, Lisa F. Edge, and John M. Nichol. Charge-noise spectroscopy of si/sige quantum dots via dynamically-decoupled exchange oscillations. *Nature Communications*, 13(1):940, 2022. doi: 10.1038/s41467-022-28519-x. URL https://doi.org/10.1038/s41467-022-28519-x.

[94] Cedric Corley-Wiciak, Carsten Richter, Marvin H. Zoellner, Ignatii Zaitsev, Costanza L. Manganelli, Edoardo Zatterin, Tobias U. Schülli, Agnieszka A. Corley-Wiciak, Jens Katzer, Felix Reichmann, Wolfgang M. Klesse, Nico W. Hendrickx, Amir Sammak, Menno Veldhorst, Giordano Scappucci, Michele Virgilio, and Giovanni Capellini. Nanoscale mapping of the 3d strain tensor in a germanium quantum well hosting a functional spin qubit device. *ACS Applied Materials & Interfaces*, 15(2):3119–3130, 01 2023. doi: 10.1021/acsami.2c17395. URL https://doi.org/10.1021/acsami.2c17395.

[95] David G. Cory, Amr F. Fahmy, and Timothy F. Havel. Ensemble quantum computing by nmr spectroscopy. *Proceedings of the National Academy of Sciences*, 94(5): 1634–1639, 1997. doi: 10.1073/pnas.94.5.1634. URL https://www.pnas.org/doi/abs/10.1073/pnas.94.5.1634.

[96] Jacob P. Covey, Harald Weinfurter, and Hannes Bernien. Quantum networks with neutral atom processing nodes. *npj Quantum Information*, 9(1):90, 2023. doi: 10.1038/s41534-023-00759-9. URL https://doi.org/10.1038/s41534-023-00759-9.

[97] John D. Cressler, editor. *Silicon Heterostructure Handbook: Materials, Fabrication, Devices, Circuits and Applications of SiGe and Si Strained-Layer Epitaxy*. CRC Press, 1st edition edition, 2005. doi: 10.1201/9781315221137. URL https://doi.org/10.1201/9781315221137.

[98] A Crippa, R Ezzouch, A Aprá, A Amisse, R Laviéville, L Hutin, B Bertrand, M Vinet, M Urdampilleta, T Meunier, M Sanquer, X Jehl, R Maurand, and S De Franceschi. Gate-reflectometry dispersive readout and coherent control of a spin qubit in silicon. *Nature Communications*, 10, 4 2019. ISSN 20411723. doi: 10.1038/s41467-019-10848-z. URL https://doi.org/10.1038/s41467-019-10848-z.

[99] Alessandro Crippa, Romain Maurand, Léo Bourdet, Dharmraj Kotekar-Patil, Anthony Amisse, Xavier Jehl, Marc Sanquer, Romain Laviéville, Heorhii Bohuslavskyi,

Louis Hutin, Sylvain Barraud, Maud Vinet, Yann-Michel Niquet, and Silvano De Franceschi. Electrical spin driving by g-matrix modulation in spin-orbit qubits. *Phys. Rev. Lett.*, 120:137702, Mar 2018. doi: 10.1103/PhysRevLett.120.137702. URL https://link.aps.org/doi/10.1103/PhysRevLett.120.137702.

[100] Sara M. Cronenwett, Tjerk H. Oosterkamp, and Leo P. Kouwenhoven. A tunable kondo effect in quantum dots. *Science*, 281(5376):540–544, 1998. doi: 10.1126/science.281.5376.540. URL https://www.science.org/doi/abs/10.1126/science.281.5376.540.

[101] S. A. Crooker, J. Brandt, C. Sandfort, A. Greilich, D. R. Yakovlev, D. Reuter, A. D. Wieck, and M. Bayer. Spin noise of electrons and holes in self-assembled quantum dots. *Phys. Rev. Lett.*, 104:036601, Jan 2010. doi: 10.1103/PhysRevLett.104.036601. URL https://link.aps.org/doi/10.1103/PhysRevLett.104.036601.

[102] Dimitrie Culcer and Neil M. Zimmerman. Dephasing of si singlet-triplet qubits due to charge and spin defects. *Applied Physics Letters*, 102(23):232108, 06 2013. ISSN 0003-6951. doi: 10.1063/1.4810911. URL https://doi.org/10.1063/1.4810911.

[103] Dimitrie Culcer, C. Lechner, and R. Winkler. Spin precession and alternating spin polarization in spin-3/2 hole systems. *Phys. Rev. Lett.*, 97:106601, Sep 2006. doi: 10.1103/PhysRevLett.97.106601. URL https://link.aps.org/doi/10.1103/PhysRevLett.97.106601.

[104] Dimitrie Culcer, Xuedong Hu, and S Das Sarma. Dephasing of si spin qubits due to charge noise. *Applied Physics Letters*, 95:73102, 2009. doi: 10.1063/1.3194778. URL https://doi.org/10.1063/1.3194778.

[105] Dimitrie Culcer, M. E. Lucassen, R. A. Duine, and R. Winkler. Current-induced spin torques in iii-v ferromagnetic semiconductors. *Phys. Rev. B*, 79:155208, Apr 2009. doi: 10.1103/PhysRevB.79.155208. URL https://link.aps.org/doi/10.1103/PhysRevB.79.155208.

[106] Dimitrie Culcer, Łukasz Cywiński, Qiuzi Li, Xuedong Hu, and S Das Sarma. Quantum dot spin qubits in silicon: Multivalley physics. *Physical Review B - Condensed Matter and Materials Physics*, 82, 4 2010. ISSN 10980121. doi: 10.1103/PhysRevB.82.155312. URL https://doi.org/10.1103/PhysRevB.82.155312.

[107] Dimitrie Culcer, Xuedong Hu, and S. Das Sarma. Interface roughness, valley-orbit coupling, and valley manipulation in quantum dots. *Phys. Rev. B*, 82:205315, Nov 2010. doi: 10.1103/PhysRevB.82.205315. URL https://link.aps.org/doi/10.1103/PhysRevB.82.205315.

[108] Dimitrie Culcer, Akihiko Sekine, and Allan H. MacDonald. Interband coherence response to electric fields in crystals: Berry-phase contributions and disorder effects. *Phys. Rev. B*, 96:035106, Jul 2017. doi: 10.1103/PhysRevB.96.035106. URL https://link.aps.org/doi/10.1103/PhysRevB.96.035106.

[109] Dimitrie Culcer, Aydın Cem Keser, Yongqing Li, and Grigory Tkachov. Transport in two-dimensional topological materials: recent developments in experiment and theory. *2D Materials*, 7(2):022007, mar 2020. doi: 10.1088/2053-1583/ab6ff7. URL https://doi.org/10.1088/2053-1583/ab6ff7.

[110] James H. Cullen, Pankaj Bhalla, E. Marcellina, A. R. Hamilton, and Dimitrie Culcer. Generating a topological anomalous hall effect in a nonmagnetic conductor: An in-plane magnetic field as a direct probe of the berry curvature. *Phys. Rev. Lett.*, 126:256601, Jun 2021. doi: 10.1103/PhysRevLett.126.256601. URL https://link.aps.org/doi/10.1103/PhysRevLett.126.256601.

[111] Łukasz Cywiński, Wayne M. Witzel, and S. Das Sarma. Electron spin dephasing due to hyperfine interactions with a nuclear spin bath. *Phys. Rev. Lett.*, 102:057601, Feb 2009. doi: 10.1103/PhysRevLett.102.057601. URL https://link.aps.org/doi/10.1103/PhysRevLett.102.057601.

[112] Ramin Dahbashi, Jens Hübner, Fabian Berski, Klaus Pierz, and Michael Oestreich. Optical spin noise of a single hole spin localized in an (inga)as quantum dot. *Phys.*

Rev. Lett., 112:156601, Apr 2014. doi: 10.1103/PhysRevLett.112.156601. URL https://link.aps.org/doi/10.1103/PhysRevLett.112.156601.

[113] Ronald D. Schrimpf Daniel M. Fleetwood, Sokrates T. Pantelides. *Defects in Microelectronic Materials and Devices*, volume 1. CRC Press, 1 edition, 11 2008. ISBN 9780429190919. doi: https://doi.org/10.1201/9781420043778. URL https://www.taylorfrancis.com/books/edit/10.1201/9781420043778/defects-microelectronic-materials-devices-ronald-schrimpf-daniel-flee

[114] R Danneau, O Klochan, W R Clarke, L H Ho, A P Micolich, M Y Simmons, A R Hamilton, M Pepper, D A Ritchie, and U Zülicke. Zeeman splitting in ballistic hole quantum wires. *Phys. Rev. Lett.*, 97:26403, 7 2006. doi: 10.1103/PhysRevLett.97.026403. URL https://link.aps.org/doi/10.1103/PhysRevLett.97.026403.

[115] S. Das Sarma, E. H. Hwang, and Hongki Min. Carrier screening, transport, and relaxation in three-dimensional dirac semimetals. *Phys. Rev. B*, 91:035201, Jan 2015. doi: 10.1103/PhysRevB.91.035201. URL https://link.aps.org/doi/10.1103/PhysRevB.91.035201.

[116] Supriyo Datta. *Electronic Transport in Mesoscopic Systems*. Cambridge Studies in Semiconductor Physics and Microelectronic Engineering. Cambridge University Press, 1995. doi: 10.1017/CBO9780511805776.

[117] Supriyo Datta. *Quantum Transport: Atom to Transistor*. Cambridge University Press, 2005. doi: 10.1017/CBO9781139164313.

[118] John H. Davies. *The Physics of Low-dimensional Semiconductors: An Introduction*. Cambridge University Press, 1997. doi: 10.1017/CBO9780511819070.

[119] M. Dawber, K. M. Rabe, and J. F. Scott. Physics of thin-film ferroelectric oxides. *Rev. Mod. Phys.*, 77:1083–1130, Oct 2005. doi: 10.1103/RevModPhys.77.1083. URL https://link.aps.org/doi/10.1103/RevModPhys.77.1083.

[120] Alberto de la Torre, Dante M. Kennes, Martin Claassen, Simon Gerber, James W. McIver, and Michael A. Sentef. Colloquium: Nonthermal pathways to ultrafast control in quantum materials. *Rev. Mod. Phys.*, 93:041002, Oct 2021. doi: 10.1103/RevModPhys.93.041002. URL https://link.aps.org/doi/10.1103/RevModPhys.93.041002.

[121] Rogerio de Sousa and S. Das Sarma. Gate control of spin dynamics in iii-v semiconductor quantum dots. *Phys. Rev. B*, 68:155330, Oct 2003. doi: 10.1103/PhysRevB.68.155330. URL https://link.aps.org/doi/10.1103/PhysRevB.68.155330.

[122] C. L. Degen, F. Reinhard, and P. Cappellaro. Quantum sensing. *Rev. Mod. Phys.*, 89:035002, Jul 2017. doi: 10.1103/RevModPhys.89.035002. URL https://link.aps.org/doi/10.1103/RevModPhys.89.035002.

[123] Patrick Del Vecchio and Oussama Moutanabbir. Light-hole gate-defined spin-orbit qubit. *Phys. Rev. B*, 107:L161406, Apr 2023. doi: 10.1103/PhysRevB.107.L161406. URL https://link.aps.org/doi/10.1103/PhysRevB.107.L161406.

[124] W Von der Osten, U Rossler, and ed. O. Madelung. *Semiconductors. Subvolume a : Intrinsic properties of group IV elements and III-V, II-VI and I-VII compounds*, volume 2. Springer, 1 edition, 4 1987. URL https://lib.ugent.be/catalog/rug01:000108491.

[125] Hanan Dery, Yang Song, Pengke Li, and Igor Zutic. Silicon spin communication. *Applied Physics Letters*, 99, 4 2011. ISSN 00036951. doi: 10.1063/1.3624923. URL https://doi.org/10.1063/1.3624923.

[126] David Deutsch and Roger Penrose. Quantum theory, the church–turing principle and the universal quantum computer. *Proceedings of the Royal Society of London. A. Mathematical and Physical Sciences*, 400(1818):97–117, 1985. doi: 10.1098/rspa.1985.0070. URL https://royalsocietypublishing.org/doi/abs/10.1098/rspa.1985.0070.

[127] I. Di Bernardo, J. Collins, W. Wu, Ju Zhou, Shengyuan A. Yang, Sheng Ju, M. T. Edmonds, and M. S. Fuhrer. Importance of interactions for the band structure of the topological dirac semimetal na_3Bi. *Phys. Rev. B*, 102:045124, Jul 2020. doi: 10.1103/PhysRevB.102.045124. URL https://link.aps.org/doi/10.1103/PhysRevB.102.045124.

[128] Iolanda Di Bernardo, Jack Hellerstedt, Chang Liu, Golrokh Akhgar, Weikang Wu, Shengyuan A. Yang, Dimitrie Culcer, Sung-Kwan Mo, Shaffique Adam, Mark T. Edmonds, and Michael S. Fuhrer. Progress in epitaxial thin-film na3bi as a topological electronic material. *Advanced Materials*, 33(11):2005897, 2019. doi: https://doi.org/10.1002/adma.202005897. URL https://onlinelibrary.wiley.com/doi/abs/10.1002/adma.202005897.

[129] L. DiCarlo, J. M. Chow, J. M. Gambetta, Lev S. Bishop, B. R. Johnson, D. I. Schuster, J. Majer, A. Blais, L. Frunzio, S. M. Girvin, and R. J. Schoelkopf. Demonstration of two-qubit algorithms with a superconducting quantum processor. *Nature*, 460(7252):240–244, 2009. doi: 10.1038/nature08121. URL https://doi.org/10.1038/nature08121.

[130] J. F. DiTusa, K. Lin, M. Park, M. S. Isaacson, and J. M. Parpia. Role of phonon dimensionality on electron-phonon scattering rates. *Phys. Rev. Lett.*, 68:1156–1159, Feb 1992. doi: 10.1103/PhysRevLett.68.1156. URL https://link.aps.org/doi/10.1103/PhysRevLett.68.1156.

[131] D. P. DiVincenzo, D. Bacon, J. Kempe, G. Burkard, and K. B. Whaley. Universal quantum computation with the exchange interaction. *Nature*, 408(6810):339–342, 2000. doi: 10.1038/35042541. URL https://doi.org/10.1038/35042541.

[132] David P. DiVincenzo. Quantum computation. *Science*, 270(5234):255–261, 1995. doi: 10.1126/science.270.5234.255. URL https://www.science.org/doi/abs/10.1126/science.270.5234.255.

[133] David P Divincenzo. Quantum gates and circuits. *Proceedings of the Royal Society of London. Series A: Mathematical, Physical and Engineering Sciences*, 454:261–276, 1

1998. doi: 10.1098/rspa.1998.0159. URL https://royalsocietypublishing.org/doi/abs/10.1098/rspa.1998.0159.

[134] David P. DiVincenzo. The physical implementation of quantum computation. *Fortschritte der Physik*, 48:771–783, 2000. ISSN 00158208. doi: 10.1002/1521-3978(200009)48:9/11<771::AID-PROP771>3.0.CO;2-E. URL https://onlinelibrary.wiley.com/doi/10.1002/1521-3978(200009)48:9/11%3C771::AID-PROP771%3E3.0.CO;2-E.

[135] A Dobbie, M Myronov, R J H Morris, A H A Hassan, M J Prest, V A Shah, E H C Parker, T E Whall, and D R Leadley. Ultra-high hole mobility exceeding one million in a strained germanium quantum well. *Applied Physics Letters*, 101:172108, 2012. URL https://doi.org/10.1063/1.4763476.

[136] Andrew C. Doherty and Matthew P. Wardrop. Two-qubit gates for resonant exchange qubits. *Phys. Rev. Lett.*, 111:050503, Jul 2013. doi: 10.1103/PhysRevLett.111.050503. URL https://link.aps.org/doi/10.1103/PhysRevLett.111.050503.

[137] G Dresselhaus. Spin-orbit coupling effects in zinc blende structures. *Phys. Rev.*, 100:580–586, 10 1955. doi: 10.1103/PhysRev.100.580. URL https://link.aps.org/doi/10.1103/PhysRev.100.580.

[138] Jingyu Duan, Janne S Lehtinen, Michael A Fogarty, Simon Schaal, Michelle M L Lam, Alberto Ronzani, Andrey Shchepetov, Panu Koppinen, Mika Prunnila, Fernando Gonzalez-Zalba, and John J L Morton. Dispersive readout of reconfigurable ambipolar quantum dots in a silicon-on-insulator nanowire. *Applied Physics Letters*, 118, 4 2021. ISSN 00036951. doi: 10.1063/5.0040259. URL https://doi.org/10.1063/5.0040259.

[139] L.-M. Duan and H. J. Kimble. Scalable photonic quantum computation through cavity-assisted interactions. *Phys. Rev. Lett.*, 92:127902, Mar 2004. doi: 10.1103/PhysRevLett.92.127902. URL https://link.aps.org/doi/10.1103/PhysRevLett.92.127902.

[140] M. V. Durnev, M. M. Glazov, and E. L. Ivchenko. Spin-orbit splitting of valence subbands in semiconductor nanostructures. *Phys. Rev. B*, 89:075430, Feb 2014. doi: 10.1103/PhysRevB.89.075430. URL https://link.aps.org/doi/10.1103/PhysRevB.89.075430.

[141] P. Dutta and P. M. Horn. Low-frequency fluctuations in solids: $\frac{1}{f}$ noise. *Rev. Mod. Phys.*, 53:497–516, Jul 1981. doi: 10.1103/RevModPhys.53.497. URL https://link.aps.org/doi/10.1103/RevModPhys.53.497.

[142] B. Eble, C. Testelin, P. Desfonds, F. Bernardot, A. Balocchi, T. Amand, A. Miard, A. Lemaître, X. Marie, and M. Chamarro. Hole–nuclear spin interaction in quantum dots. *Phys. Rev. Lett.*, 102:146601, Apr 2009. doi: 10.1103/PhysRevLett.102.146601. URL https://link.aps.org/doi/10.1103/PhysRevLett.102.146601.

[143] Sophia E. Economou, Juan I. Climente, Antonio Badolato, Allan S. Bracker, Daniel Gammon, and Matthew F. Doty. Scalable qubit architecture based on holes in quantum dot molecules. *Phys. Rev. B*, 86:085319, Aug 2012. doi: 10.1103/PhysRevB.86.085319. URL https://link.aps.org/doi/10.1103/PhysRevB.86.085319.

[144] Al. L. Efros and E. I. Rashba. Theory of electric dipole spin resonance in a parabolic quantum well. *Phys. Rev. B*, 73:165325, Apr 2006. doi: 10.1103/PhysRevB.73.165325. URL https://link.aps.org/doi/10.1103/PhysRevB.73.165325.

[145] Rüdiger-A. Eichel, Paul Erhart, Petra Träskelin, Karsten Albe, Hans Kungl, and Michael J. Hoffmann. Defect-dipole formation in copper-doped pbtio$_3$ ferroelectrics. *Phys. Rev. Lett.*, 100:095504, Mar 2008. doi: 10.1103/PhysRevLett.100.095504. URL https://link.aps.org/doi/10.1103/PhysRevLett.100.095504.

[146] J. M. Elzerman, R. Hanson, L. H. Willems van Beveren, B. Witkamp, L. M. K. Vandersypen, and L. P. Kouwenhoven. Single-shot read-out of an individual electron spin in a quantum dot. *Nature*, 430(6998):431–435, 2004. doi: 10.1038/nature02693. URL https://doi.org/10.1038/nature02693.

[147] Sigurdur I. Erlingsson and Yuli V. Nazarov. Hyperfine-mediated transitions between a zeeman split doublet in gaas quantum dots: The role of the internal field. *Phys. Rev. B*, 66:155327, Oct 2002. doi: 10.1103/PhysRevB.66.155327. URL https://link.aps.org/doi/10.1103/PhysRevB.66.155327.

[148] Rami Ezzouch, Simon Zihlmann, Vincent P Michal, Jing Li, Agostino Aprá, Benoit Bertrand, Louis Hutin, Maud Vinet, Matias Urdampilleta, Tristan Meunier, Xavier Jehl, Yann Michel Niquet, Marc Sanquer, Silvano De Franceschi, and Romain Maurand. Dispersively probed microwave spectroscopy of a silicon hole double quantum dot. *Physical Review Applied*, 16, 4 2021. ISSN 23317019. doi: 10.1103/PhysRevApplied.16.034031. URL https://doi.org/10.1103/PhysRevApplied.16.034031.

[149] Vladimir I. Fal'ko. Cyclotron and electric-dipole spin resonances in a two-dimensional electron gas in the vicinity of the crossing of spin-split landau levels. *Phys. Rev. B*, 46:4320–4323, Aug 1992. doi: 10.1103/PhysRevB.46.4320. URL https://link.aps.org/doi/10.1103/PhysRevB.46.4320.

[150] P. Fallahi, S. T. Y ılmaz, and A. Imamoğlu. Measurement of a heavy-hole hyperfine interaction in ingaas quantum dots using resonance fluorescence. *Phys. Rev. Lett.*, 105:257402, Dec 2010. doi: 10.1103/PhysRevLett.105.257402. URL https://link.aps.org/doi/10.1103/PhysRevLett.105.257402.

[151] Yinan Fang, Pericles Philippopoulos, Dimitrie Culcer, W A Coish, and Stefano Chesi. Recent advances in hole-spin qubits. *Materials for Quantum Technology*, 3 (1):012003, mar 2023. doi: 10.1088/2633-4356/acb87e. URL https://dx.doi.org/10.1088/2633-4356/acb87e.

[152] Mohsen Farokhnezhad, W. A. Coish, Reza Asgari, and Dimitrie Culcer. Quadrupolar photovoltaic effect in the terahertz range in a two-dimensional spin-$\frac{3}{2}$ hole system. *Phys. Rev. B*, 107:085405, Feb 2023. doi: 10.1103/PhysRevB.107.085405. URL https://link.aps.org/doi/10.1103/PhysRevB.107.085405.

[153] C. Fasth, A. Fuhrer, L. Samuelson, Vitaly N. Golovach, and Daniel Loss. Direct

measurement of the spin-orbit interaction in a two-electron inas nanowire quantum dot. *Phys. Rev. Lett.*, 98:266801, Jun 2007. doi: 10.1103/PhysRevLett.98.266801. URL https://link.aps.org/doi/10.1103/PhysRevLett.98.266801.

[154] Zaiyao Fei, Tauno Palomaki, Sanfeng Wu, Wenjin Zhao, Xinghan Cai, Bosong Sun, Paul Nguyen, Joseph Finney, Xiaodong Xu, and David H. Cobden. Edge conduction in monolayer WTe_2. *Nature Physics*, 13(7):677–682, Jul 2017. ISSN 1745-2481. doi: 10.1038/nphys4091. URL https://doi.org/10.1038/nphys4091.

[155] Rifat Ferdous, Erika Kawakami, Pasquale Scarlino, Michał P Nowak, D R Ward, D E Savage, M G Lagally, S N Coppersmith, Mark Friesen, Mark A Eriksson, Lieven M K Vandersypen, and Rajib Rahman. Valley dependent anisotropic spin splitting in silicon quantum dots. *npj Quantum Information*, 4, 4 2018. ISSN 20566387. doi: 10.1038/s41534-018-0075-1. URL https://doi.org/10.1038/s41534-018-0075-1.

[156] D. Fernández-Fernández, Yue Ban, and G. Platero. Quantum control of hole spin qubits in double quantum dots. *Phys. Rev. Appl.*, 18:054090, Nov 2022. doi: 10.1103/PhysRevApplied.18.054090. URL https://link.aps.org/doi/10.1103/PhysRevApplied.18.054090.

[157] Richard P Feynman. Simulating physics with computers. *International Journal of Theoretical Physics*, 21, 6 1982. doi: 10.1007/BF02650179. URL https://link.springer.com/article/10.1007/BF02650179.

[158] Jan Fischer and Daniel Loss. Hybridization and spin decoherence in heavy-hole quantum dots. *Phys. Rev. Lett.*, 105:266603, 12 2010. doi: 10.1103/PhysRevLett.105.266603. URL https://link.aps.org/doi/10.1103/PhysRevLett.105.266603.

[159] Jan Fischer, W A Coish, D V Bulaev, and Daniel Loss. Spin decoherence of a heavy hole coupled to nuclear spins in a quantum dot. *Physical Review B - Condensed Matter and Materials Physics*, 78, 4 2008. ISSN 10980121. doi: 10.1103/PhysRevB.78.155329. URL https://doi.org/10.1103/PhysRevB.78.155329.

[160] Michael Fleischhauer, Atac Imamoglu, and Jonathan P. Marangos. Electromagnetically induced transparency: Optics in coherent media. *Rev. Mod. Phys.*, 77: 633–673, Jul 2005. doi: 10.1103/RevModPhys.77.633. URL https://link.aps.org/doi/10.1103/RevModPhys.77.633.

[161] Christian Flindt, Anders S. Sørensen, and Karsten Flensberg. Spin-orbit mediated control of spin qubits. *Phys. Rev. Lett.*, 97:240501, Dec 2006. doi: 10.1103/PhysRevLett.97.240501. URL https://link.aps.org/doi/10.1103/PhysRevLett.97.240501.

[162] W. M. C. Foulkes, L. Mitas, R. J. Needs, and G. Rajagopal. Quantum monte carlo simulations of solids. *Rev. Mod. Phys.*, 73:33–83, Jan 2001. doi: 10.1103/RevModPhys.73.33. URL https://link.aps.org/doi/10.1103/RevModPhys.73.33.

[163] Akhil Francis, D. Zhu, C. Huerta Alderete, Sonika Johri, Xiao Xiao, J. K. Freericks, C. Monroe, N. M. Linke, and A. F. Kemper. Many body thermodynamics on quantum computers via partition function zeros, 2020. URL https://arxiv.org/abs/2009.04648.

[164] Christoph Freysoldt, Blazej Grabowski, Tilmann Hickel, Jörg Neugebauer, Georg Kresse, Anderson Janotti, and Chris G. Van de Walle. First-principles calculations for point defects in solids. *Rev. Mod. Phys.*, 86:253–305, Mar 2014. doi: 10.1103/RevModPhys.86.253. URL https://link.aps.org/doi/10.1103/RevModPhys.86.253.

[165] Lukas Fricke, Samuel J Hile, Ludwik Kranz, Yousun Chung, Yu He, Prasanna Pakkiam, Matthew G House, Joris G Keizer, and Michelle Y Simmons. Coherent control of a donor-molecule electron spin qubit in silicon. *Nature Communications*, 12, 4 2021. ISSN 20411723. doi: 10.1038/s41467-021-23662-3. URL https://doi.org/10.1038/s41467-021-23662-3.

[166] Mark Friesen and S N Coppersmith. Theory of valley-orbit coupling in a si/sige quantum dot. *Physical Review B - Condensed Matter and Materials Physics*, 81,

4 2010. ISSN 10980121. doi: 10.1103/PhysRevB.81.115324. URL https://doi.org/10.1103/PhysRevB.81.115324.

[167] Mark Friesen, Sucismita Chutia, Charles Tahan, and S N Coppersmith. Valley splitting theory of sige/si/sige quantum wells. *Physical Review B - Condensed Matter and Materials Physics*, 75, 4 2007. ISSN 10980121. doi: 10.1103/PhysRevB.75.115318. URL https://doi.org/10.1103/PhysRevB.75.115318.

[168] A. T. Fromhold and Earl L. Cook. Kinetics of oxide film growth on metal crystals: Electron tunneling and ionic diffusion. *Phys. Rev.*, 158:600–612, Jun 1967. doi: 10.1103/PhysRev.158.600. URL https://link.aps.org/doi/10.1103/PhysRev.158.600.

[169] F N M Froning, M J Rančić, B Hetényi, S Bosco, M K Rehmann, A Li, E P A M Bakkers, F A Zwanenburg, D Loss, D M Zumbühl, and F R Braakman. Strong spin-orbit interaction and g -factor renormalization of hole spins in ge/si nanowire quantum dots. *Physical Review Research*, 3, 4 2021. ISSN 26431564. doi: 10.1103/PhysRevResearch.3.013081. URL https://doi.org/10.1103/PhysRevResearch.3.013081.

[170] Florian N. M. Froning, Leon C. Camenzind, Orson A. H. van der Molen, Ang Li, Erik P. A. M. Bakkers, Dominik M. Zumbühl, and Floris R. Braakman. Ultrafast hole spin qubit with gate-tunable spin–orbit switch functionality. *Nature Nanotechnology*, 16(3):308–312, 2021. doi: 10.1038/s41565-020-00828-6. URL https://doi.org/10.1038/s41565-020-00828-6.

[171] Florian Fröwis, Pavel Sekatski, Wolfgang Dür, Nicolas Gisin, and Nicolas Sangouard. Macroscopic quantum states: Measures, fragility, and implementations. *Rev. Mod. Phys.*, 90:025004, May 2018. doi: 10.1103/RevModPhys.90.025004. URL https://link.aps.org/doi/10.1103/RevModPhys.90.025004.

[172] A Fuhrer, M Füchsle, T C G Reusch, B Weber, and M Y Simmons. Atomic-scale, all epitaxial in-plane gated donor quantum dot in silicon. *Nano Letters*, 9:707–710, 4 2009. ISSN 1530-6984. doi: 10.1021/nl803196f.

[173] J Ohkawa Fusayoshi and Uemura Yasutada. Quantized surface states of a narrow-gap semiconductor. *Journal of the Physical Society of Japan*, 37:1325–1333, 1974. doi: 10.1143/JPSJ.37.1325. URL https://doi.org/10.1143/JPSJ.37.1325.

[174] J. W. Gadzuk. Resonance-tunneling spectroscopy of atoms adsorbed on metal surfaces: Theory. *Phys. Rev. B*, 1:2110–2129, Mar 1970. doi: 10.1103/PhysRevB.1.2110. URL https://link.aps.org/doi/10.1103/PhysRevB.1.2110.

[175] Y. M. Galperin, B. L. Altshuler, J. Bergli, and D. V. Shantsev. Non-gaussian low-frequency noise as a source of qubit decoherence. *Phys. Rev. Lett.*, 96:097009, Mar 2006. doi: 10.1103/PhysRevLett.96.097009. URL https://link.aps.org/doi/10.1103/PhysRevLett.96.097009.

[176] Luca Gammaitoni, Peter Hänggi, Peter Jung, and Fabio Marchesoni. Stochastic resonance. *Rev. Mod. Phys.*, 70:223–287, Jan 1998. doi: 10.1103/RevModPhys.70.223. URL https://link.aps.org/doi/10.1103/RevModPhys.70.223.

[177] Fei Gao, Jian-Huan Wang, Hannes Watzinger, Hao Hu, Marko J Rančić, Jie-Yin Zhang, Ting Wang, Yuan Yao, Gui-Lei Wang, Josip Kukučka, et al. Site-controlled uniform ge/si hut wires with electrically tunable spin–orbit coupling. *Advanced Materials*, 32:1906523, 2020. URL https://doi.org/10.1002/adma.201906523.

[178] I. M. Georgescu, S. Ashhab, and Franco Nori. Quantum simulation. *Reviews of Modern Physics*, 86, 3 2014. ISSN 15390756. doi: 10.1103/RevModPhys.86.153. URL https://journals.aps.org/rmp/abstract/10.1103/RevModPhys.86.153.

[179] Brian D. Gerardot, Daniel Brunner, Paul A. Dalgarno, Patrik Öhberg, Stefan Seidl, Martin Kroner, Khaled Karrai, Nick G. Stoltz, Pierre M. Petroff, and Richard J. Warburton. Optical pumping of a single hole spin in a quantum dot. *Nature*, 451 (7177):441–444, 2008. doi: 10.1038/nature06472. URL https://doi.org/10.1038/nature06472.

[180] Neil A. Gershenfeld and Isaac L. Chuang. Bulk spin-resonance quantum computa-

tion. *Science*, 275(5298):350–356, 1997. doi: 10.1126/science.275.5298.350. URL https://www.science.org/doi/abs/10.1126/science.275.5298.350.

[181] Simon Geyer, Bence Hetényi, Stefano Bosco, Leon C Camenzind, Rafael S Eggli, Andreas Fuhrer, Daniel Loss, Richard J Warburton, Dominik M Zumbuhl, and Andreas V Kuhlmann. Two-qubit logic with anisotropic exchange in a fin field-effect transistor. *arXiv:2212.02308*, 2022. URL https://doi.org/10.48550/arXiv.2212.02308.

[182] Sina Gholizadeh, James H. Cullen, and Dimitrie Culcer. Nonlinear hall effect of magnetized two-dimensional spin-$\frac{3}{2}$ heavy holes. *Phys. Rev. B*, 107:L041301, Jan 2023. doi: 10.1103/PhysRevB.107.L041301. URL https://link.aps.org/doi/10.1103/PhysRevB.107.L041301.

[183] Vittorio Giovannetti, Seth Lloyd, and Lorenzo Maccone. Quantum metrology. *Phys. Rev. Lett.*, 96:010401, Jan 2006. doi: 10.1103/PhysRevLett.96.010401. URL https://link.aps.org/doi/10.1103/PhysRevLett.96.010401.

[184] Vittorio Giovannetti, Seth Lloyd, and Lorenzo MacCone. Advances in quantum metrology. *Nature Photonics*, 5:222–229, 4 2011. ISSN 17494885. doi: 10.1038/nphoton.2011.35. URL https://www.nature.com/articles/nphoton.2011.35.

[185] Nicolas Gisin, Grégoire Ribordy, Wolfgang Tittel, and Hugo Zbinden. Quantum cryptography. *Rev. Mod. Phys.*, 74:145–195, Mar 2002. doi: 10.1103/RevModPhys.74.145. URL https://link.aps.org/doi/10.1103/RevModPhys.74.145.

[186] T. M. Godden, J. H. Quilter, A. J. Ramsay, Yanwen Wu, P. Brereton, S. J. Boyle, I. J. Luxmoore, J. Puebla-Nunez, A. M. Fox, and M. S. Skolnick. Coherent optical control of the spin of a single hole in an InAs/GaAs quantum dot. *Phys. Rev. Lett.*, 108:017402, Jan 2012. doi: 10.1103/PhysRevLett.108.017402. URL https://link.aps.org/doi/10.1103/PhysRevLett.108.017402.

[187] Vitaly N. Golovach, Alexander Khaetskii, and Daniel Loss. Phonon-induced decay of the electron spin in quantum dots. *Phys. Rev. Lett.*, 93:016601, Jun 2004.

doi: 10.1103/PhysRevLett.93.016601. URL https://link.aps.org/doi/10.1103/PhysRevLett.93.016601.

[188] Vitaly N. Golovach, Massoud Borhani, and Daniel Loss. Electric-dipole-induced spin resonance in quantum dots. *Phys. Rev. B*, 74:165319, Oct 2006. doi: 10.1103/PhysRevB.74.165319. URL https://link.aps.org/doi/10.1103/PhysRevB.74.165319.

[189] M F Gonzalez-Zalba, S de Franceschi, E Charbon, T Meunier, M Vinet, and A S Dzurak. Scaling silicon-based quantum computing using cmos technology. *Nature Electronics*, 4:872–884, 4 2021. ISSN 25201131. doi: 10.1038/s41928-021-00681-y. URL https://doi.org/10.1038/s41928-021-00681-y.

[190] Srijit Goswami, K A Slinker, Mark Friesen, L M McGuire, J L Truitt, Charles Tahan, L J Klein, J O Chu, P M Mooney, D W Van Der Weide, Robert Joynt, S N Coppersmith, and Mark A Eriksson. Controllable valley splitting in silicon quantum devices. *Nature Physics*, 3:41–45, 4 2007. ISSN 17452481. doi: 10.1038/nphys475. URL https://doi.org/10.1038/nphys475.

[191] Hayato Goto. Double-transmon coupler: Fast two-qubit gate with no residual coupling for highly detuned superconducting qubits. *Phys. Rev. Appl.*, 18:034038, Sep 2022. doi: 10.1103/PhysRevApplied.18.034038. URL https://link.aps.org/doi/10.1103/PhysRevApplied.18.034038.

[192] M Governale. Quantum dots with rashba spin-orbit coupling. *Physical Review Letters*, 89, 2002. ISSN 10797114. doi: 10.1103/PhysRevLett.89.206802. URL https://doi.org/10.1103/PhysRevLett.89.206802.

[193] Otfried Gühne, Erkka Haapasalo, Tristan Kraft, Juha-Pekka Pellonpää, and Roope Uola. Colloquium: Incompatible measurements in quantum information science. *Rev. Mod. Phys.*, 95:011003, Feb 2023. doi: 10.1103/RevModPhys.95.011003. URL https://link.aps.org/doi/10.1103/RevModPhys.95.011003.

[194] J. A. Gupta, D. D. Awschalom, X. Peng, and A. P. Alivisatos. Spin coherence in semiconductor quantum dots. *Phys. Rev. B*, 59:R10421–R10424, Apr 1999. doi:

10.1103/PhysRevB.59.R10421. URL https://link.aps.org/doi/10.1103/PhysRevB.59.R10421.

[195] J. A. Gupta, R. Knobel, N. Samarth, and D. D. Awschalom. Ultrafast manipulation of electron spin coherence. *Science*, 292(5526):2458–2461, 2001. doi: 10.1126/science.1061169. URL https://www.science.org/doi/abs/10.1126/science.1061169.

[196] R. Hanson, B. Witkamp, L. M. K. Vandersypen, L. H. Willems van Beveren, J. M. Elzerman, and L. P. Kouwenhoven. Zeeman energy and spin relaxation in a one-electron quantum dot. *Phys. Rev. Lett.*, 91:196802, Nov 2003. doi: 10.1103/PhysRevLett.91.196802. URL https://link.aps.org/doi/10.1103/PhysRevLett.91.196802.

[197] R. Hanson, L. P. Kouwenhoven, J. R. Petta, S. Tarucha, and L. M. K. Vandersypen. Spins in few-electron quantum dots. *Rev. Mod. Phys.*, 79:1217–1265, Oct 2007. doi: 10.1103/RevModPhys.79.1217. URL https://link.aps.org/doi/10.1103/RevModPhys.79.1217.

[198] H.-Y. Hao and H J Maris. Study of phonon dispersion in silicon and germanium at long wavelengths using picosecond ultrasonics. *Phys. Rev. Lett.*, 84:5556–5559, 6 2000. doi: 10.1103/PhysRevLett.84.5556. URL https://link.aps.org/doi/10.1103/PhysRevLett.84.5556.

[199] Xiaojie Hao, Rusko Ruskov, Ming Xiao, Charles Tahan, and Hongwen Jiang. Electron spin resonance and spin-valley physics in a silicon double quantum dot. *Nature Communications*, 5, 4 2014. ISSN 20411723. doi: 10.1038/ncomms4860. URL https://doi.org/10.1038/ncomms4860.

[200] Will J Hardy, C Thomas Harris, Yi Hsin Su, Yen Chuang, Jonathan Moussa, Leon N Maurer, Jiun Yun Li, Tzu Ming Lu, and Dwight R Luhman. Single and double hole quantum dots in strained ge/sige quantum wells. *Nanotechnology*, 30, 4 2019. ISSN 13616528. doi: 10.1088/1361-6528/ab061e. URL https://doi.org/10.1088/1361-6528/ab061e.

[201] M. Z. Hasan and C. L. Kane. Colloquium: Topological insulators. *Rev. Mod. Phys.*, 82:3045–3067, Nov 2010. doi: 10.1103/RevModPhys.82.3045. URL https://link.aps.org/doi/10.1103/RevModPhys.82.3045.

[202] T. Hatano, M. Stopa, and S. Tarucha. Single-electron delocalization in hybrid vertical-lateral double quantum dots. *Science*, 309(5732):268–271, 2005. doi: 10.1126/science.1111205. URL https://www.science.org/doi/abs/10.1126/science.1111205.

[203] Y. He, S. K. Gorman, D. Keith, L. Kranz, J. G. Keizer, and M. Y. Simmons. A two-qubit gate between phosphorus donor electrons in silicon. *Nature*, 571(7765):371–375, 2019. doi: 10.1038/s41586-019-1381-2. URL https://doi.org/10.1038/s41586-019-1381-2.

[204] N W Hendrickx, D P Franke, A Sammak, M Kouwenhoven, D Sabbagh, L Yeoh, Roy Li, M L V Tagliaferri, M Virgilio, G Capellini, et al. Gate-controlled quantum dots and superconductivity in planar germanium. *Nature communications*, 9:1–7, 2018. URL https://www.nature.com/articles/s41467-018-05299-x.

[205] N W Hendrickx, D P Franke, A Sammak, G Scappucci, and M Veldhorst. Fast two-qubit logic with holes in germanium. *Nature*, 577:487–491, 2020. URL https://www.nature.com/articles/s41586-019-1919-3.

[206] N W Hendrickx, W I L Lawrie, L Petit, A Sammak, G Scappucci, and M Veldhorst. A single-hole spin qubit. *Nature Communications*, 11, 4 2020. ISSN 20411723. doi: 10.1038/s41467-020-17211-7. URL https://doi.org/10.1038/s41467-020-17211-7.

[207] Nico W Hendrickx, William I L Lawrie, Maximilian Russ, Floor van Riggelen, Sander L de Snoo, Raymond N Schouten, Amir Sammak, Giordano Scappucci, and Menno Veldhorst. A four-qubit germanium quantum processor. *Nature*, 591:580–585, 2021. URL https://www.nature.com/articles/s41586-021-03332-6.

[208] A P Higginbotham, T W Larsen, J Yao, H Yan, C M Lieber, C M Marcus, and F Kuemmeth. Hole spin coherence in a ge/si heterostructure nanowire. *Nano*

Letters, 14:3582–3586, 2014. URL https://pubs.acs.org/doi/10.1021/nl501242b.

[209] Charles D Hill, Eldad Peretz, Samuel J Hile, Matthew G House, Martin Fuechsle, Sven Rogge, Michelle Y Simmons, and Lloyd C L Hollenberg. Quantum computing: A surface code quantum computer in silicon. *Science Advances*, 1, 4 2015. ISSN 23752548. doi: 10.1126/sciadv.1500707. URL https://doi.org/10.1126/sciadv.1500707.

[210] Armin Hochrainer, Mayukh Lahiri, Manuel Erhard, Mario Krenn, and Anton Zeilinger. Quantum indistinguishability by path identity and with undetected photons. *Rev. Mod. Phys.*, 94:025007, Jun 2022. doi: 10.1103/RevModPhys.94.025007. URL https://link.aps.org/doi/10.1103/RevModPhys.94.025007.

[211] P. Hohenberg and W. Kohn. Inhomogeneous electron gas. *Phys. Rev.*, 136:B864–B871, Nov 1964. doi: 10.1103/PhysRev.136.B864. URL https://link.aps.org/doi/10.1103/PhysRev.136.B864.

[212] Jonathan P. Home, David Hanneke, John D. Jost, Jason M. Amini, Dietrich Leibfried, and David J. Wineland. Complete methods set for scalable ion trap quantum information processing. *Science*, 325(5945):1227–1230, 2009. doi: 10.1126/science.1177077. URL https://www.science.org/doi/abs/10.1126/science.1177077.

[213] Matthew A Hopcroft, William D Nix, and Thomas W Kenny. What is the young's modulus of silicon? *Journal of Microelectromechanical Systems*, 19:229–238, 2010. doi: 10.1109/JMEMS.2009.2039697. URL https://doi.org/10.1109/JMEMS.2009.2039697.

[214] Kosuke Horibe, Tetsuo Kodera, and Shunri Oda. Lithographically defined few-electron silicon quantum dots based on a silicon-on-insulator substrate. *Applied Physics Letters*, 106, 4 2015. ISSN 00036951. doi: 10.1063/1.4913321. URL https://doi.org/10.1063/1.4913321.

[215] Ryszard Horodecki, Paweł Horodecki, Michał Horodecki, and Karol Horodecki. Quantum entanglement. *Rev. Mod. Phys.*, 81:865–942, Jun 2009. doi: 10.1103/RevModPhys.81.865. URL https://link.aps.org/doi/10.1103/RevModPhys.81.865.

[216] C. Y. Hu, A. Young, J. L. O'Brien, W. J. Munro, and J. G. Rarity. Giant optical faraday rotation induced by a single-electron spin in a quantum dot: Applications to entangling remote spins via a single photon. *Phys. Rev. B*, 78:085307, Aug 2008. doi: 10.1103/PhysRevB.78.085307. URL https://link.aps.org/doi/10.1103/PhysRevB.78.085307.

[217] Xuedong Hu and S. Das Sarma. Hilbert-space structure of a solid-state quantum computer: Two-electron states of a double-quantum-dot artificial molecule. *Phys. Rev. A*, 61:062301, May 2000. doi: 10.1103/PhysRevA.61.062301. URL https://link.aps.org/doi/10.1103/PhysRevA.61.062301.

[218] Yongjie Hu, Ferdinand Kuemmeth, Charles M Lieber, and Charles M Marcus. Hole spin relaxation in ge-si core-shell nanowire qubits. *Nature Nanotechnology*, 7:47–50, 2012. ISSN 17483395. doi: 10.1038/nnano.2011.234. URL https://doi.org/10.1038/nnano.2011.234.

[219] C. Huerta Alderete, Shivani Singh, Nhung H. Nguyen, Daiwei Zhu, Radhakrishnan Balu, Christopher Monroe, C. M. Chandrashekar, and Norbert M. Linke. Quantum walks and dirac cellular automata on a programmable trapped-ion quantum computer. *Nature Communications*, 11(1):3720, 2020. doi: 10.1038/s41467-020-17519-4. URL https://doi.org/10.1038/s41467-020-17519-4.

[220] Richard J. Hughes, Daniel F. V. James, Emanuel H. Knill, Raymond Laflamme, and Albert G. Petschek. Decoherence bounds on quantum computation with trapped ions. *Phys. Rev. Lett.*, 77:3240–3243, Oct 1996. doi: 10.1103/PhysRevLett.77.3240. URL https://link.aps.org/doi/10.1103/PhysRevLett.77.3240.

[221] L. Huthmacher, R. Stockill, E. Clarke, M. Hugues, C. Le Gall, and M. Atatüre. Coherence of a dynamically decoupled quantum-dot hole spin. *Phys. Rev. B*, 97:

241413, Jun 2018. doi: 10.1103/PhysRevB.97.241413. URL https://link.aps.org/doi/10.1103/PhysRevB.97.241413.

[222] L Hutin, B Bertrand, R Maurand, A Crippa, M Urdampilleta, Y J Kim, A Amisse, H Bohuslavskyi, L Bourdet, S Barraud, X Jeh, Y M Niquet, M Sanquer, C Bauerle, T Meunier, S De Franceschi, and M Vinet. Si mos technology for spin-based quantum computing. *European Solid-State Device Research Conference*, 2018-September:12–17, 4 2018. ISSN 19308876. doi: 10.1109/ESSDERC.2018.8486863. URL https://doi.org/10.1109/ESSDERC.2018.8486863.

[223] T. Hyart, B. van Heck, I. C. Fulga, M. Burrello, A. R. Akhmerov, and C. W. J. Beenakker. Flux-controlled quantum computation with majorana fermions. *Phys. Rev. B*, 88:035121, Jul 2013. doi: 10.1103/PhysRevB.88.035121. URL https://link.aps.org/doi/10.1103/PhysRevB.88.035121.

[224] Igor Žutić, Jaroslav Fabian, and S. Das Sarma. Spintronics: Fundamentals and applications. *Rev. Mod. Phys.*, 76:323–410, Apr 2004. doi: 10.1103/RevModPhys.76.323. URL https://link.aps.org/doi/10.1103/RevModPhys.76.323.

[225] A. Imamog¯lu, D. D. Awschalom, G. Burkard, D. P. DiVincenzo, D. Loss, M. Sherwin, and A. Small. Quantum information processing using quantum dot spins and cavity qed. *Phys. Rev. Lett.*, 83:4204–4207, Nov 1999. doi: 10.1103/PhysRevLett.83.4204. URL https://link.aps.org/doi/10.1103/PhysRevLett.83.4204.

[226] Kohei Itoh, W L Hansen, E E Haller, J W Farmer, V I Ozhogin, A Rudnev, and A Tikhomirov. High purity isotopically enriched 70ge and 74ge single crystals: Isotope separation, growth, and properties. *Journal of Materials Research*, 8:1341–1347, 1993. URL https://link.springer.com/article/10.1557/JMR.1993.1341.

[227] Kohei M Itoh, Jiro Kato, Masafumi Uemura, Alexey K Kaliteevskii, Oleg N Godisov, Grigori G Devyatych, Andrey D Bulanov, Anatoli V Gusev, Igor D Kovalev, Pyotr G Sennikov, Hans-J. Pohl, Nikolai V Abrosimov, and Helge Riemann. High purity isotopically enriched 29si and 30si single crystals: Isotope separation, purification,

and growth. *Jpn. J. Appl. Phys.*, 42:6248, 2003. URL https://iopscience.iop.org/article/10.1143/JJAP.42.6248.

[228] H. Jeong, A. M. Chang, and M. R. Melloch. The kondo effect in an artificial quantum dot molecule. *Science*, 293(5538):2221–2223, 2001. doi: 10.1126/science.1063182. URL https://www.science.org/doi/abs/10.1126/science.1063182.

[229] Ik Kyeong Jin, Krittika Kumar, Matthew J. Rendell, Jonathan Yue Huang, Chris C. Escott, Fay E. Hudson, Wee Han Lim, Andrew S. Dzurak, Alexander R. Hamilton, and Scott D. Liles. Combining n-mos charge sensing with p-mos silicon hole double quantum dots in a cmos platform. *Nano Letters*, 23(4):1261–1266, 2023. doi: 10.1021/acs.nanolett.2c04417. URL https://doi.org/10.1021/acs.nanolett.2c04417. PMID: 36748989.

[230] Daniel Jirovec, Andrea Hofmann, Andrea Ballabio, Philipp M Mutter, Giulio Tavani, Marc Botifoll, Alessandro Crippa, Josip Kukucka, Oliver Sagi, Frederico Martins, Jaime Saez-Mollejo, Ivan Prieto, Maksim Borovkov, Jordi Arbiol, Daniel Chrastina, Giovanni Isella, and Georgios Katsaros. A singlet-triplet hole spin qubit in planar ge. *Nature Materials*, 20:1106–1112, 4 2021. ISSN 14764660. doi: 10.1038/s41563-021-01022-2. URL https://doi.org/10.1038/s41563-021-01022-2.

[231] Daniel Jirovec, Philipp M. Mutter, Andrea Hofmann, Alessandro Crippa, Marek Rychetsky, David L. Craig, Josip Kukucka, Frederico Martins, Andrea Ballabio, Natalia Ares, Daniel Chrastina, Giovanni Isella, Guido Burkard, and Georgios Katsaros. Dynamics of hole singlet-triplet qubits with large g-factor differences. *Phys. Rev. Lett.*, 128:126803, Mar 2022. doi: 10.1103/PhysRevLett.128.126803. URL https://link.aps.org/doi/10.1103/PhysRevLett.128.126803.

[232] A. C. Johnson, J. R. Petta, J. M. Taylor, A. Yacoby, M. D. Lukin, C. M. Marcus, M. P. Hanson, and A. C. Gossard. Triplet–singlet spin relaxation via nuclei in a double quantum dot. *Nature*, 435(7044):925–928, 2005. doi: 10.1038/nature03815. URL https://doi.org/10.1038/nature03815.

[233] R. O. Jones. Density functional theory: Its origins, rise to prominence, and future. *Rev. Mod. Phys.*, 87:897–923, Aug 2015. doi: 10.1103/RevModPhys.87.897. URL https://link.aps.org/doi/10.1103/RevModPhys.87.897.

[234] Rachpon Kalra, Arne Laucht, Charles D. Hill, and Andrea Morello. Robust two-qubit gates for donors in silicon controlled by hyperfine interactions. *Phys. Rev. X*, 4:021044, Jun 2014. doi: 10.1103/PhysRevX.4.021044. URL https://link.aps.org/doi/10.1103/PhysRevX.4.021044.

[235] Yoshiki Kamata. High-k/ge mosfets for future nanoelectronics. *Materials today*, 11: 30–38, 2008. URL https://www.sciencedirect.com/science/article/pii/S1369702107703504.

[236] B. E. Kane. A silicon-based nuclear spin quantum computer. *Nature*, 393(6681): 133–137, 1998. doi: 10.1038/30156. URL https://doi.org/10.1038/30156.

[237] C. L. Kane and E. J. Mele. Quantum spin hall effect in graphene. *Phys. Rev. Lett.*, 95:226801, Nov 2005. doi: 10.1103/PhysRevLett.95.226801. URL https://link.aps.org/doi/10.1103/PhysRevLett.95.226801.

[238] Kaifei Kang, Tingxin Li, Egon Sohn, Jie Shan, and Kin Fai Mak. Nonlinear anomalous hall effect in few-layer wte2. *Nature Materials*, 18(4):324–328, Apr 2019. ISSN 1476-4660. doi: 10.1038/s41563-019-0294-7. URL https://doi.org/10.1038/s41563-019-0294-7.

[239] Marc A. Kastner. Artificial atoms. *Physics Today*, 46(1):24–31, 01 1993. ISSN 0031-9228. doi: 10.1063/1.881393. URL https://doi.org/10.1063/1.881393.

[240] Y. Kato, R. C. Myers, A. C. Gossard, and D. D. Awschalom. Coherent spin manipulation without magnetic fields in strained semiconductors. *Nature*, 427(6969): 50–53, 2004. doi: 10.1038/nature02202. URL https://doi.org/10.1038/nature02202.

[241] Georgios Katsaros, Josip Kukucka, Lada Vukusic, Hannes Watzinger, Fei Gao, Ting Wang, Jian-Jun Zhang, and Karsten Held. Zero field splitting of heavy-hole states

in quantum dots. *Nano. Lett.*, 20:5201, 2020. URL https://pubs.acs.org/doi/10.1021/acs.nanolett.0c01466.

[242] K. V. Kavokin. Anisotropic exchange interaction of localized conduction-band electrons in semiconductors. *Phys. Rev. B*, 64:075305, Jul 2001. doi: 10.1103/PhysRevB.64.075305. URL https://link.aps.org/doi/10.1103/PhysRevB.64.075305.

[243] E. Kawakami, P. Scarlino, D. R. Ward, F. R. Braakman, D. E. Savage, M. G. Lagally, Mark Friesen, S. N. Coppersmith, M. A. Eriksson, and L. M. K. Vandersypen. Electrical control of a long-lived spin qubit in a si/sige quantum dot. *Nature Nanotechnology*, 9(9):666–670, 2014. doi: 10.1038/nnano.2014.153. URL https://doi.org/10.1038/nnano.2014.153.

[244] D Keith, S K Gorman, L Kranz, Y He, J G Keizer, M A Broome, and M Y Simmons. Benchmarking high fidelity single-shot readout of semiconductor qubits. *New Journal of Physics*, 21, 4 2019. ISSN 13672630. doi: 10.1088/1367-2630/ab242c.

[245] Alexander V Khaetskii and Yuli V Nazarov. Spin relaxation in semiconductor quantum dots. *Physical Review B*, 15:12639–12643, 2000. URL https://journals.aps.org/prb/abstract/10.1103/PhysRevB.61.12639.

[246] Alexander V. Khaetskii and Yuli V. Nazarov. Spin-flip transitions between zeeman sublevels in semiconductor quantum dots. *Phys. Rev. B*, 64:125316, Sep 2001. doi: 10.1103/PhysRevB.64.125316. URL https://link.aps.org/doi/10.1103/PhysRevB.64.125316.

[247] Alexander V. Khaetskii, Daniel Loss, and Leonid Glazman. Electron spin decoherence in quantum dots due to interaction with nuclei. *Phys. Rev. Lett.*, 88:186802, Apr 2002. doi: 10.1103/PhysRevLett.88.186802. URL https://link.aps.org/doi/10.1103/PhysRevLett.88.186802.

[248] K. Khodjasteh and D. A. Lidar. Fault-tolerant quantum dynamical decoupling. *Phys. Rev. Lett.*, 95:180501, Oct 2005. doi: 10.1103/PhysRevLett.95.180501. URL https://link.aps.org/doi/10.1103/PhysRevLett.95.180501.

[249] Scott Kirkpatrick. Percolation and conduction. *Rev. Mod. Phys.*, 45:574–588, Oct 1973. doi: 10.1103/RevModPhys.45.574. URL https://link.aps.org/doi/10.1103/RevModPhys.45.574.

[250] A Yu Kitaev. Quantum computations: algorithms and error correction. *Russian Mathematical Surveys*, 52(6):1191, dec 1997. doi: 10.1070/RM1997v052n06ABEH002155. URL https://dx.doi.org/10.1070/RM1997v052n06ABEH002155.

[251] Christoph Kloeffel, Mircea Trif, and Daniel Loss. Strong spin-orbit interaction and helical hole states in ge/si nanowires. *Phys. Rev. B*, 84:195314, Nov 2011. doi: 10.1103/PhysRevB.84.195314. URL https://link.aps.org/doi/10.1103/PhysRevB.84.195314.

[252] Christoph Kloeffel, Mircea Trif, Peter Stano, and Daniel Loss. Circuit qed with hole-spin qubits in ge/si nanowire quantum dots. *Phys. Rev. B*, 88:241405, Dec 2013. doi: 10.1103/PhysRevB.88.241405. URL https://link.aps.org/doi/10.1103/PhysRevB.88.241405.

[253] Christoph Kloeffel, Marko J Rančić, and Daniel Loss. Direct rashba spin-orbit interaction in si and ge nanowires with different growth directions. *Physical Review B*, 97, 4 2018. ISSN 24699969. doi: 10.1103/PhysRevB.97.235422. URL https://doi.org/10.1103/PhysRevB.97.235422.

[254] E. Knill, R. Laflamme, and G. J. Milburn. A scheme for efficient quantum computation with linear optics. *Nature*, 409(6816):46–52, 2001. doi: 10.1038/35051009. URL https://doi.org/10.1038/35051009.

[255] T. Knispel, W. Jolie, N. Borgwardt, J. Lux, Zhiwei Wang, Yoichi Ando, A. Rosch, T. Michely, and M. Grüninger. Charge puddles in the bulk and on the surface of the topological insulator bisbtese$_2$ studied by scanning tunneling microscopy and optical spectroscopy. *Phys. Rev. B*, 96:195135, Nov 2017. doi: 10.1103/PhysRevB.96.195135. URL https://link.aps.org/doi/10.1103/PhysRevB.96.195135.

[256] Takashi Kobayashi, Joseph Salfi, Cassandra Chua, Joost van der Heijden, Matthew G House, Dimitrie Culcer, Wayne D Hutchison, Brett C Johnson, Jeff C McCallum, Helge Riemann, Nikolay V Abrosimov, Peter Becker, Hans Joachim Pohl, Michelle Y Simmons, and Sven Rogge. Engineering long spin coherence times of spin–orbit qubits in silicon. *Nature Materials*, 20:38–42, 4 2021. ISSN 14764660. doi: 10.1038/s41563-020-0743-3. URL https://doi.org/10.1038/s41563-020-0743-3.

[257] Takuro Kobayashi, Taiki Matsushita, Takeshi Mizushima, Atsushi Tsuruta, and Satoshi Fujimoto. Negative thermal magnetoresistivity as a signature of a chiral anomaly in weyl superconductors. *Phys. Rev. Lett.*, 121:207002, Nov 2018. doi: 10.1103/PhysRevLett.121.207002. URL https://link.aps.org/doi/10.1103/PhysRevLett.121.207002.

[258] Christiane P. Koch, Mikhail Lemeshko, and Dominique Sugny. Quantum control of molecular rotation. *Rev. Mod. Phys.*, 91:035005, Sep 2019. doi: 10.1103/RevModPhys.91.035005. URL https://link.aps.org/doi/10.1103/RevModPhys.91.035005.

[259] Jens Koch, Terri M. Yu, Jay Gambetta, A. A. Houck, D. I. Schuster, J. Majer, Alexandre Blais, M. H. Devoret, S. M. Girvin, and R. J. Schoelkopf. Charge-insensitive qubit design derived from the cooper pair box. *Phys. Rev. A*, 76:042319, Oct 2007. doi: 10.1103/PhysRevA.76.042319. URL https://link.aps.org/doi/10.1103/PhysRevA.76.042319.

[260] Tetsuo Kodera. Silicon quantum dot devices for spin-based quantum computing. *2020 IEEE Silicon Nanoelectronics Workshop, SNW 2020*, pages 31–32, 4 2020. doi: 10.1109/SNW50361.2020.9131665. URL https://doi.org/10.1109/SNW50361.2020.9131665.

[261] Pieter Kok, W. J. Munro, Kae Nemoto, T. C. Ralph, Jonathan P. Dowling, and G. J. Milburn. Linear optical quantum computing with photonic qubits. *Rev. Mod.*

Phys., 79:135–174, Jan 2007. doi: 10.1103/RevModPhys.79.135. URL https://link.aps.org/doi/10.1103/RevModPhys.79.135.

[262] Artem Kononov, Gulibusitan Abulizi, Kejian Qu, Jiaqiang Yan, David Mandrus, Kenji Watanabe, Takashi Taniguchi, and Christian Schönenberger. One-dimensional edge transport in few-layer WTe_2. *Nano Letters*, 20(6):4228–4233, 2020. doi: 10.1021/acs.nanolett.0c00658. URL https://doi.org/10.1021/acs.nanolett.0c00658.

[263] F. H. L. Koppens, K. C. Nowack, and L. M. K. Vandersypen. Spin echo of a single electron spin in a quantum dot. *Phys. Rev. Lett.*, 100:236802, Jun 2008. doi: 10.1103/PhysRevLett.100.236802. URL https://link.aps.org/doi/10.1103/PhysRevLett.100.236802.

[264] F.N. Krauth, S.K. Gorman, Y. He, M.T. Jones, P. Macha, S. Kocsis, C. Chua, B. Voisin, S. Rogge, R. Rahman, Y. Chung, and M.Y. Simmons. Flopping-mode electric dipole spin resonance in phosphorus donor qubits in silicon. *Phys. Rev. Appl.*, 17:054006, May 2022. doi: 10.1103/PhysRevApplied.17.054006. URL https://link.aps.org/doi/10.1103/PhysRevApplied.17.054006.

[265] Miro Kroutvar, Yann Ducommun, Dominik Heiss, Max Bichler, Dieter Schuh, Gerhard Abstreiter, and Jonathan J. Finley. Optically programmable electron spin memory using semiconductor quantum dots. *Nature*, 432(7013):81–84, 2004. doi: 10.1038/nature03008. URL https://doi.org/10.1038/nature03008.

[266] Andreas V Kuhlmann, Veeresh Deshpande, Leon C Camenzind, Dominik M Zumbühl, and Andreas Fuhrer. Ambipolar quantum dots in undoped silicon fin field-effect transistors. *Applied Physics Letters*, 113, 4 2018. ISSN 00036951. doi: 10.1063/1.5048097. URL https://doi.org/10.1063/1.5048097.

[267] Vladislav D. Kurilovich, Pavel D. Kurilovich, Igor S. Burmistrov, and Moshe Goldstein. Helical edge transport in the presence of a magnetic impurity: The role of local anisotropy. *Phys. Rev. B*, 99:085407, Feb 2019. doi: 10.1103/PhysRevB.99.085407. URL https://link.aps.org/doi/10.1103/PhysRevB.99.085407.

[268] Jordan Kyriakidis, M. Pioro-Ladriere, M. Ciorga, A. S. Sachrajda, and P. Hawrylak. Voltage-tunable singlet-triplet transition in lateral quantum dots. *Phys. Rev. B*, 66: 035320, Jul 2002. doi: 10.1103/PhysRevB.66.035320. URL https://link.aps.org/doi/10.1103/PhysRevB.66.035320.

[269] Markus König, Hartmut Buhmann, Laurens W. Molenkamp, Taylor Hughes, Chao-Xing Liu, Xiao-Liang Qi, and Shou-Cheng Zhang. The quantum spin hall effect: Theory and experiment. *Journal of the Physical Society of Japan*, 77(3):031007, 2008. doi: 10.1143/JPSJ.77.031007. URL https://doi.org/10.1143/JPSJ.77.031007.

[270] T D Ladd, J R Goldman, F Yamaguchi, Y Yamamoto, E Abe, and K M Itoh. All-silicon quantum computer. *Physical Review Letters*, 89:179011–179014, 4 2002. ISSN 00319007. doi: 10.1103/PhysRevLett.89.017901. URL https://doi.org/10.1103/PhysRevLett.89.017901.

[271] E. A. Laird, C. Barthel, E. I. Rashba, C. M. Marcus, M. P. Hanson, and A. C. Gossard. Hyperfine-mediated gate-driven electron spin resonance. *Phys. Rev. Lett.*, 99:246601, Dec 2007. doi: 10.1103/PhysRevLett.99.246601. URL https://link.aps.org/doi/10.1103/PhysRevLett.99.246601.

[272] Gabriel T. Landi and Mauro Paternostro. Irreversible entropy production: From classical to quantum. *Rev. Mod. Phys.*, 93:035008, Sep 2021. doi: 10.1103/RevModPhys.93.035008. URL https://link.aps.org/doi/10.1103/RevModPhys.93.035008.

[273] Richard Latter. Atomic energy levels for the thomas-fermi and thomas-fermi-dirac potential. *Phys. Rev.*, 99:510–519, Jul 1955. doi: 10.1103/PhysRev.99.510. URL https://link.aps.org/doi/10.1103/PhysRev.99.510.

[274] Arne Laucht, Frank Hohls, Niels Ubbelohde, M Fernando Gonzalez-Zalba, David J Reilly, Søren Stobbe, Tim Schröder, Pasquale Scarlino, Jonne V Koski, Andrew Dzurak, Chih Hwan Yang, Jun Yoneda, Ferdinand Kuemmeth, Hendrik Bluhm, Jarryd Pla, Charles Hill, Joe Salfi, Akira Oiwa, Juha T Muhonen, Ewold Verhagen, M D

LaHaye, Hyun Ho Kim, Adam W Tsen, Dimitrie Culcer, Attila Geresdi, Jan A Mol, Varun Mohan, Prashant K Jain, and Jonathan Baugh. Roadmap on quantum nanotechnologies. *Nanotechnology*, 32, 4 2021. ISSN 13616528. doi: 10.1088/1361-6528/abb333. URL https://doi.org/10.1088/1361-6528/abb333.

[275] W I L Lawrie, H G J Eenink, N W Hendrickx, J M Boter, L Petit, S V Amitonov, M Lodari, B Paquelet Wuetz, C Volk, S G J Philips, G Droulers, N Kalhor, F Van Riggelen, D Brousse, A Sammak, L M K Vandersypen, G Scappucci, and M Veldhorst. Quantum dot arrays in silicon and germanium. *Applied Physics Letters*, 116, 4 2020. ISSN 00036951. doi: 10.1063/5.0002013. URL https://doi.org/10.1063/5.0002013.

[276] W I L Lawrie, N W Hendrickx, F Van Riggelen, M Russ, L Petit, A Sammak, G Scappucci, and M Veldhorst. Spin relaxation benchmarks and individual qubit addressability for holes in quantum dots. *Nano Letters*, 20:7237–7242, 4 2020. ISSN 15306992. doi: 10.1021/acs.nanolett.0c02589. URL https://doi.org/10.1021/acs.nanolett.0c02589.

[277] W. I. L. Lawrie, M. Rimbach-Russ, F. van Riggelen, N. W. Hendrickx, S. L. de Snoo, A. Sammak, G. Scappucci, J. Helsen, and M. Veldhorst. Simultaneous single-qubit driving of semiconductor spin qubits at the fault-tolerant threshold. *Nature Communications*, 14(1):3617, 2023. doi: 10.1038/s41467-023-39334-3. URL https://doi.org/10.1038/s41467-023-39334-3.

[278] Patrick A. Lee and T. V. Ramakrishnan. Disordered electronic systems. *Rev. Mod. Phys.*, 57:287–337, Apr 1985. doi: 10.1103/RevModPhys.57.287. URL https://link.aps.org/doi/10.1103/RevModPhys.57.287.

[279] D. Leibfried, R. Blatt, C. Monroe, and D. Wineland. Quantum dynamics of single trapped ions. *Rev. Mod. Phys.*, 75:281–324, Mar 2003. doi: 10.1103/RevModPhys.75.281. URL https://link.aps.org/doi/10.1103/RevModPhys.75.281.

[280] M Leslie and N J Gillan. The energy and elastic dipole tensor of defects in ionic crystals calculated by the supercell method. *Journal of Physics C: Solid State*

Physics, 18(5):973, feb 1985. doi: 10.1088/0022-3719/18/5/005. URL https://dx.doi.org/10.1088/0022-3719/18/5/005.

[281] B. A. Levitan and T. Pereg-Barnea. Second-order topological insulator under strong magnetic field: Landau levels, zeeman effect, and magnetotransport. *Phys. Rev. Research*, 2:033327, Aug 2020. doi: 10.1103/PhysRevResearch.2.033327. URL https://link.aps.org/doi/10.1103/PhysRevResearch.2.033327.

[282] Jeremy Levy. Universal quantum computation with spin-1/2 pairs and heisenberg exchange. *Phys. Rev. Lett.*, 89:147902, Sep 2002. doi: 10.1103/PhysRevLett.89.147902. URL https://link.aps.org/doi/10.1103/PhysRevLett.89.147902.

[283] Jing Li, Benjamin Venitucci, and Yann-Michel Niquet. Hole-phonon interactions in quantum dots: Effects of phonon confinement and encapsulation materials on spin-orbit qubits. *Phys. Rev. B*, 102:075415, Aug 2020. doi: 10.1103/PhysRevB.102.075415. URL https://link.aps.org/doi/10.1103/PhysRevB.102.075415.

[284] Pengke Li and Ian Appelbaum. Interpreting current-induced spin polarization in topological insulator surface states. *Phys. Rev. B*, 93:220404, Jun 2016. doi: 10.1103/PhysRevB.93.220404. URL https://link.aps.org/doi/10.1103/PhysRevB.93.220404.

[285] R Li, N I.Dumoulin Stuyck, S Kubicek, J Jussot, B T Chan, F A Mohiyaddin, A Elsayed, M Shehata, G Simion, C Godfrin, Y Canvel, Ts Ivanov, L Goux, B Govoreanu, and I P Radu. A flexible 300 mm integrated si mos platform for electron- and hole-spin qubits exploration. *Technical Digest - International Electron Devices Meeting, IEDM*, 2020-December:38.3.1–38.3.4, 4 2020. ISSN 01631918. doi: 10.1109/IEDM13553.2020.9371956. URL https://imec-publications.be/handle/20.500.12860/38560.2?show=full.

[286] Ruoyu Li, Fay E Hudson, Andrew S Dzurak, and Alexander R Hamilton. Pauli spin blockade of heavy holes in a silicon double quantum dot. *Nano letters*, 15:7314–

7318, 2015. URL https://pubs.acs.org/doi/10.1021/acs.nanolett.5b02561.

[287] Ruoyu Li, Fay E. Hudson, Andrew S. Dzurak, and Alexander R. Hamilton. Pauli spin blockade of heavy holes in a silicon double quantum dot. *Nano Letters*, 15(11): 7314–7318, 11 2015. doi: 10.1021/acs.nanolett.5b02561. URL https://doi.org/10.1021/acs.nanolett.5b02561.

[288] Shu Xiao Li, Yan Li, Fei Gao, Gang Xu, Hai Ou Li, Gang Cao, Ming Xiao, Ting Wang, Jian Jun Zhang, and Guo Ping Guo. Measuring hole spin states of single quantum dot in germanium hut wire. *Applied Physics Letters*, 110, 4 2017. ISSN 00036951. doi: 10.1063/1.4979521. URL https://doi.org/10.1063/1.4979521.

[289] Yan Li, Shu-Xiao Li, Fei Gao, Hai-Ou Li, Gang Xu, Ke Wang, Di Liu, Gang Cao, Ming Xiao, Ting Wang, Jian-Jun Zhang, Guang-Can Guo, and Guo-Ping Guo. Coupling a germanium hut wire hole quantum dot to a superconducting microwave resonator. *Nano Letters*, 18(3):2091–2097, 03 2018. doi: 10.1021/acs.nanolett.8b00272. URL https://doi.org/10.1021/acs.nanolett.8b00272.

[290] Yan Li, Shu-Xiao Li, Fei Gao, Hai-Ou Li, Gang Xu, Ke Wang, Di Liu, Gang Cao, Ming Xiao, Ting Wang, et al. Coupling a germanium hut wire hole quantum dot to a superconducting microwave resonator. *Nano Letters*, 18:2091–2097, 2018. URL https://pubs.acs.org/doi/10.1021/acs.nanolett.8b00272.

[291] Jonas Lidal and Jeroen Danon. Effects of spin-orbit coupling and in-plane zeeman fields on the critical current in two-dimensional hole gas sns junctions. *Phys. Rev. B*, 107:085303, Feb 2023. doi: 10.1103/PhysRevB.107.085303. URL https://link.aps.org/doi/10.1103/PhysRevB.107.085303.

[292] D. A. Lidar, I. L. Chuang, and K. B. Whaley. Decoherence-free subspaces for quantum computation. *Phys. Rev. Lett.*, 81:2594–2597, Sep 1998. doi: 10.1103/PhysRevLett.81.2594. URL https://link.aps.org/doi/10.1103/PhysRevLett.81.2594.

[293] Elliott H. Lieb and Barry Simon. Thomas-fermi theory revisited. *Phys. Rev. Lett.*, 31:681–683, Sep 1973. doi: 10.1103/PhysRevLett.31.681. URL https://link.aps.org/doi/10.1103/PhysRevLett.31.681.

[294] S D Liles, R Li, C H Yang, F E Hudson, M Veldhorst, A S Dzurak, and A R Hamilton. Spin and orbital structure of the first six holes in a silicon metal-oxide-semiconductor quantum dot. *Nature Communications*, 9, 4 2018. ISSN 20411723. doi: 10.1038/s41467-018-05700-9. URL https://doi.org/10.1038/s41467-018-05700-9.

[295] S D Liles, F Martins, D S Miserev, A A Kiselev, I D Thorvaldson, M J Rendell, I K Jin, F E Hudson, M Veldhorst, K M Itoh, O P Sushkov, T D Ladd, A S Dzurak, and A R Hamilton. Electrical control of the g tensor of the first hole in a silicon mos quantum dot. *Physical Review B*, 104, 4 2021. ISSN 24699969. doi: 10.1103/PhysRevB.104.235303. URL https://doi.org/10.1103/PhysRevB.104.235303.

[296] Jacob Linder, Yukio Tanaka, Takehito Yokoyama, Asle Sudbø, and Naoto Nagaosa. Unconventional superconductivity on a topological insulator. *Phys. Rev. Lett.*, 104: 067001, Feb 2010. doi: 10.1103/PhysRevLett.104.067001. URL https://link.aps.org/doi/10.1103/PhysRevLett.104.067001.

[297] Joanna W. Lis, Aruku Senoo, William F. McGrew, Felix Rönchen, Alec Jenkins, and Adam M. Kaufman. Midcircuit operations using the omg architecture in neutral atom arrays. *Phys. Rev. X*, 13:041035, Nov 2023. doi: 10.1103/PhysRevX.13.041035. URL https://link.aps.org/doi/10.1103/PhysRevX.13.041035.

[298] Chang Liu, Golrokh Akhgar, James L. Collins, Jack Hellerstedt, Cheng Tan, Lan Wang, Shaffique Adam, Michael S. Fuhrer, and Mark T. Edmonds. Quantum transport in air-stable na3bi thin films. *ACS Applied Materials & Interfaces*, 12(31): 35542–35546, 2020. doi: 10.1021/acsami.0c05832. URL https://doi.org/10.1021/acsami.0c05832.

[299] Chang Liu, Dimitrie Culcer, Zhanning Wang, Mark T. Edmonds, and Michael S.

Fuhrer. Helical edge transport in millimeter-scale thin films of na3bi. *Nano Letters*, 20(9):6306–6312, 2020. doi: 10.1021/acs.nanolett.0c01649. URL https://doi.org/10.1021/acs.nanolett.0c01649.

[300] Chao-Xing Liu, Xiao-Liang Qi, HaiJun Zhang, Xi Dai, Zhong Fang, and Shou-Cheng Zhang. Model hamiltonian for topological insulators. *Phys. Rev. B*, 82:045122, Jul 2010. doi: 10.1103/PhysRevB.82.045122. URL https://link.aps.org/doi/10.1103/PhysRevB.82.045122.

[301] He Liu, Ting Zhang, Ke Wang, Fei Gao, Gang Xu, Xin Zhang, Shu Xiao Li, Gang Cao, Ting Wang, Jianjun Zhang, Xuedong Hu, Hai Ou Li, and Guo Ping Guo. Gate-tunable spin-orbit coupling in a germanium hole double quantum dot. *Physical Review Applied*, 17, 4 2022. ISSN 23317019. doi: 10.1103/PhysRevApplied.17.044052. URL https://doi.org/10.1103/PhysRevApplied.17.044052.

[302] Hong Liu, E Marcellina, A R Hamilton, and Dimitrie Culcer. Strong spin-orbit contribution to the hall coefficient of two-dimensional hole systems. *Phys. Rev. Lett.*, 121:87701, 8 2018. doi: 10.1103/PhysRevLett.121.087701. URL https://link.aps.org/doi/10.1103/PhysRevLett.121.087701.

[303] Qin Liu, Chao-Xing Liu, Cenke Xu, Xiao-Liang Qi, and Shou-Cheng Zhang. Magnetic impurities on the surface of a topological insulator. *Phys. Rev. Lett.*, 102:156603, Apr 2009. doi: 10.1103/PhysRevLett.102.156603. URL https://link.aps.org/doi/10.1103/PhysRevLett.102.156603.

[304] Shi Liu and R. E. Cohen. Multiscale simulations of defect dipole–enhanced electromechanical coupling at dilute defect concentrations. *Applied Physics Letters*, 111(8):082903, 08 2017. ISSN 0003-6951. doi: 10.1063/1.4989670. URL https://doi.org/10.1063/1.4989670.

[305] M. Lodari, A. Tosato, D. Sabbagh, M. A. Schubert, G. Capellini, A. Sammak, M. Veldhorst, and G. Scappucci. Light effective hole mass in undoped ge/sige quantum wells. *Phys. Rev. B*, 100:041304, Jul 2019. doi: 10.1103/PhysRevB.100.041304. URL https://link.aps.org/doi/10.1103/PhysRevB.100.041304.

[306] M Lodari, O Kong, M Rendell, A Tosato, A Sammak, M Veldhorst, A R Hamilton, and G Scappucci. Lightly strained germanium quantum wells with hole mobility exceeding one million. *Applied Physics Letters*, 120:122104, 2022. URL https://doi.org/10.1063/5.0083161.

[307] Mario Lodari, Nico W Hendrickx, William I L Lawrie, Tzu-Kan Hsiao, Lieven M K Vandersypen, Amir Sammak, Menno Veldhorst, and Giordano Scappucci. Low percolation density and charge noise with holes in germanium. *Materials for Quantum Technology*, 1:11002, 2021. URL https://iopscience.iop.org/article/10.1088/2633-4356/abcd82.

[308] Daniel Loss and David P. DiVincenzo. Quantum computation with quantum dots. *Phys. Rev. A*, 57:120–126, Jan 1998. doi: 10.1103/PhysRevA.57.120. URL https://link.aps.org/doi/10.1103/PhysRevA.57.120.

[309] C Lü, J L Cheng, and M W Wu. Hole spin relaxation in semiconductor quantum dots. *Physical Review B - Condensed Matter and Materials Physics*, 71, 4 2005. ISSN 10980121. doi: 10.1103/PhysRevB.71.075308. URL https://doi.org/10.1103/PhysRevB.71.075308.

[310] Chao-Yang Lu, Yuan Cao, Cheng-Zhi Peng, and Jian-Wei Pan. Micius quantum experiments in space. *Rev. Mod. Phys.*, 94:035001, Jul 2022. doi: 10.1103/RevModPhys.94.035001. URL https://link.aps.org/doi/10.1103/RevModPhys.94.035001.

[311] Hai-Zhou Lu and Shun-Qing Shen. Finite-temperature conductivity and magnetoconductivity of topological insulators. *Phys. Rev. Lett.*, 112:146601, Apr 2014. doi: 10.1103/PhysRevLett.112.146601. URL https://link.aps.org/doi/10.1103/PhysRevLett.112.146601.

[312] T M Lu, C T Harris, S-H Huang, Y Chuang, J-Y Li, and C W Liu. Effective g factor of low-density two-dimensional holes in a ge quantum well. *Applied Physics Letters*, 111:102108, 2017. URL https://doi.org/10.1063/1.4990569.

[313] Anders Mathias Lunde and Gloria Platero. Helical edge states coupled to a spin bath: Current-induced magnetization. *Phys. Rev. B*, 86:035112, Jul 2012. doi: 10.1103/PhysRevB.86.035112. URL https://link.aps.org/doi/10.1103/PhysRevB.86.035112.

[314] A. Lupaşcu, S. Saito, T. Picot, P. C. de Groot, C. J. P. M. Harmans, and J. E. Mooij. Quantum non-demolition measurement of a superconducting two-level system. *Nature Physics*, 3(2):119–123, 2007. doi: 10.1038/nphys509. URL https://doi.org/10.1038/nphys509.

[315] J M Luttinger and W Kohn. Motion of electrons and holes in perturbed periodic fields. *Phys. Rev.*, 97:869–883, 2 1955. doi: 10.1103/PhysRev.97.869. URL https://link.aps.org/doi/10.1103/PhysRev.97.869.

[316] Xiao-song Ma, Johannes Kofler, and Anton Zeilinger. Delayed-choice gedanken experiments and their realizations. *Rev. Mod. Phys.*, 88:015005, Mar 2016. doi: 10.1103/RevModPhys.88.015005. URL https://link.aps.org/doi/10.1103/RevModPhys.88.015005.

[317] Stefan Machlup. Noise in semiconductors: Spectrum of a two-parameter random signal. *Journal of Applied Physics*, 25(3):341–343, 05 2004. ISSN 0021-8979. doi: 10.1063/1.1721637. URL https://doi.org/10.1063/1.1721637.

[318] Joseph Maciejko, Taylor L. Hughes, and Shou-Cheng Zhang. The quantum spin hall effect. *Annual Review of Condensed Matter Physics*, 2(1):31–53, 2011. doi: 10.1146/annurev-conmatphys-062910-140538. URL https://doi.org/10.1146/annurev-conmatphys-062910-140538.

[319] Mateusz T. Madzik, Arne Laucht, Fay E. Hudson, Alexander M. Jakob, Brett C. Johnson, David N. Jamieson, Kohei M. Itoh, Andrew S. Dzurak, and Andrea Morello. Conditional quantum operation of two exchange-coupled single-donor spin qubits in a mos-compatible silicon device. *Nature Communications*, 12(1):181, 2021. doi: 10.1038/s41467-020-20424-5. URL https://doi.org/10.1038/s41467-020-20424-5.

[320] Franziska Maier, Christoph Kloeffel, and Daniel Loss. Tunable g factor and phonon-mediated hole spin relaxation in ge/si nanowire quantum dots. *Physical Review B - Condensed Matter and Materials Physics*, 87, 4 2013. ISSN 10980121. doi: 10.1103/PhysRevB.87.161305. URL https://doi.org/10.1103/PhysRevB.87.161305.

[321] Yuriy Makhlin and Alexander Shnirman. Dephasing of solid-state qubits at optimal points. *Phys. Rev. Lett.*, 92:178301, Apr 2004. doi: 10.1103/PhysRevLett.92.178301. URL https://link.aps.org/doi/10.1103/PhysRevLett.92.178301.

[322] Yuriy Makhlin, Gerd Schön, and Alexander Shnirman. Quantum-state engineering with josephson-junction devices. *Rev. Mod. Phys.*, 73:357–400, May 2001. doi: 10.1103/RevModPhys.73.357. URL https://link.aps.org/doi/10.1103/RevModPhys.73.357.

[323] Ognjen Malkoc, Peter Stano, and Daniel Loss. Charge-noise induced dephasing in silicon hole-spin qubits. *Physical Review Letters*, 129:247701–247708, 4 2022. ISSN 10797114. doi: 10.1103/PhysRevLett.129.247701. URL https://journals.aps.org/prl/abstract/10.1103/PhysRevLett.129.247701.

[324] A Manaselyan and T Chakraborty. Enhanced rashba effect for hole states in a quantum dot. *EPL*, 88, 2009. ISSN 02955075. doi: 10.1209/0295-5075/88/17003. URL https://doi.org/10.1209/0295-5075/88/17003.

[325] A. Manaselyan and T. Chakraborty. Enhanced rashba effect for hole states in a quantum dot. *Europhysics Letters*, 88(1):17003, oct 2009. doi: 10.1209/0295-5075/88/17003. URL https://dx.doi.org/10.1209/0295-5075/88/17003.

[326] A Manchon, H C Koo, J Nitta, S M Frolov, and R A Duine. New perspectives for rashba spin-orbit coupling. *Nature Materials*, 14:871–882, 4 2015. ISSN 14764660. doi: 10.1038/nmat4360. URL https://doi.org/10.1038/nmat4360.

[327] Arjun Mani and Colin Benjamin. Probing helicity and the topological origins of helicity via non-local hanbury-brown and twiss correlations. *Scientific Reports*, 7(1):

6954, Jul 2017. ISSN 2045-2322. doi: 10.1038/s41598-017-06820-w. URL https://doi.org/10.1038/s41598-017-06820-w.

[328] E Marcellina, A R Hamilton, R Winkler, and Dimitrie Culcer. Spin-orbit interactions in inversion-asymmetric two-dimensional hole systems: A variational analysis. *Physical Review B*, 95, 4 2017. ISSN 24699969. doi: 10.1103/PhysRevB.95.075305. URL https://doi.org/10.1103/PhysRevB.95.075305.

[329] E. Marcellina, A. Srinivasan, D. S. Miserev, A. F. Croxall, D. A. Ritchie, I. Farrer, O. P. Sushkov, Dimitrie Culcer, and A. R. Hamilton. Electrical control of the zeeman spin splitting in two-dimensional hole systems. *Phys. Rev. Lett.*, 121:077701, Aug 2018. doi: 10.1103/PhysRevLett.121.077701. URL https://link.aps.org/doi/10.1103/PhysRevLett.121.077701.

[330] I. Martin and Y. M. Galperin. Loss of quantum coherence due to nonstationary glass fluctuations. *Phys. Rev. B*, 73:180201, May 2006. doi: 10.1103/PhysRevB.73.180201. URL https://link.aps.org/doi/10.1103/PhysRevB.73.180201.

[331] Biel Martinez, José Carlos Abadillo-Uriel, Esteban A. Rodríguez-Mena, and Yann-Michel Niquet. Hole spin manipulation in inhomogeneous and nonseparable electric fields. *Phys. Rev. B*, 106:235426, Dec 2022. doi: 10.1103/PhysRevB.106.235426. URL https://link.aps.org/doi/10.1103/PhysRevB.106.235426.

[332] John M. Martinis, S. Nam, J. Aumentado, and C. Urbina. Rabi oscillations in a large josephson-junction qubit. *Phys. Rev. Lett.*, 89:117901, Aug 2002. doi: 10.1103/PhysRevLett.89.117901. URL https://link.aps.org/doi/10.1103/PhysRevLett.89.117901.

[333] Marian Marx, Jun Yoneda, Tomohiro Otsuka, Kenta Takeda, Yu Yamaoka, Takashi Nakajima, Sen Li, Akito Noiri, Tetsuo Kodera, and Seigo Tarucha. Spin–orbit assisted spin funnels in dc transport through a physically defined pmos double quantum dot. *Japanese Journal of Applied Physics*, 58(SB):SBBI07, apr 2019. doi: 10.7567/1347-4065/ab01d6. URL https://dx.doi.org/10.7567/1347-4065/ab01d6.

[334] B M Maune, M G Borselli, B Huang, T D Ladd, P W Deelman, K S Holabird, A A Kiselev, I Alvarado-Rodriguez, R S Ross, A E Schmitz, M Sokolich, C A Watson, M F Gyure, and A T Hunter. Coherent singlet-triplet oscillations in a silicon-based double quantum dot. *Nature*, 481:344–347, 4 2012. ISSN 00280836. doi: 10.1038/nature10707. URL https://doi.org/10.1038/nature10707.

[335] R Maurand, X Jehl, D Kotekar-Patil, A Corna, H Bohuslavskyi, R Laviéville, L Hutin, S Barraud, M Vinet, M Sanquer, and S De Franceschi. A cmos silicon spin qubit. *Nature Communications*, 7, 4 2016. ISSN 20411723. URL https://www.nature.com/articles/ncomms13575.

[336] Sam McArdle, Suguru Endo, Alán Aspuru-Guzik, Simon C. Benjamin, and Xiao Yuan. Quantum computational chemistry. *Reviews of Modern Physics*, 92, 3 2020. ISSN 15390756. doi: 10.1103/RevModPhys.92.015003. URL https://journals.aps.org/rmp/abstract/10.1103/RevModPhys.92.015003.

[337] J. Medford, J. Beil, J. M. Taylor, E. I. Rashba, H. Lu, A. C. Gossard, and C. M. Marcus. Quantum-dot-based resonant exchange qubit. *Phys. Rev. Lett.*, 111:050501, Jul 2013. doi: 10.1103/PhysRevLett.111.050501. URL https://link.aps.org/doi/10.1103/PhysRevLett.111.050501.

[338] M. Mehring, J. Mende, and W. Scherer. Entanglement between an electron and a nuclear spin $\frac{1}{2}$. *Phys. Rev. Lett.*, 90:153001, Apr 2003. doi: 10.1103/PhysRevLett.90.153001. URL https://link.aps.org/doi/10.1103/PhysRevLett.90.153001.

[339] Lorenz Meier, Gian Salis, Ivan Shorubalko, Emilio Gini, Silke Schön, and Klaus Ensslin. Measurement of rashba and dresselhaus spin-orbit magnetic fields. *Nature Physics*, 3:650–654, 2007. ISSN 17452481. doi: 10.1038/nphys675. URL https://doi.org/10.1038/nphys675.

[340] I. A. Merkulov, Al. L. Efros, and M. Rosen. Electron spin relaxation by nuclei in semiconductor quantum dots. *Phys. Rev. B*, 65:205309, Apr 2002. doi:

10.1103/PhysRevB.65.205309. URL https://link.aps.org/doi/10.1103/PhysRevB.65.205309.

[341] X. Mi, J. V. Cady, D. M. Zajac, J. Stehlik, L. F. Edge, and J. R. Petta. Circuit quantum electrodynamics architecture for gate-defined quantum dots in silicon. *Applied Physics Letters*, 110(4):043502, 01 2017. ISSN 0003-6951. doi: 10.1063/1.4974536. URL https://doi.org/10.1063/1.4974536.

[342] X. Mi, M. Benito, S. Putz, D. M. Zajac, J. M. Taylor, Guido Burkard, and J. R. Petta. A coherent spin–photon interface in silicon. *Nature*, 555(7698):599–603, 2018. doi: 10.1038/nature25769. URL https://doi.org/10.1038/nature25769.

[343] V. P. Michal, J. C. Abadillo-Uriel, S. Zihlmann, R. Maurand, Y.-M. Niquet, and M. Filippone. Tunable hole spin-photon interaction based on g-matrix modulation. *Phys. Rev. B*, 107:L041303, Jan 2023. doi: 10.1103/PhysRevB.107.L041303. URL https://link.aps.org/doi/10.1103/PhysRevB.107.L041303.

[344] D. L. Mickelsen, Hervé M. Carruzzo, S. N. Coppersmith, and Clare C. Yu. Effects of temperature fluctuations on charge noise in quantum dot qubits. *Phys. Rev. B*, 108:075303, Aug 2023. doi: 10.1103/PhysRevB.108.075303. URL https://link.aps.org/doi/10.1103/PhysRevB.108.075303.

[345] Marko Milivojević. Electrical control of the hole spin qubit in si and ge nanowire quantum dots. *Physical Review B*, 104, 4 2021. ISSN 24699969. doi: 10.1103/PhysRevB.104.235304. URL https://doi.org/10.1103/PhysRevB.104.235304.

[346] Adam R Mills, Charles R Guinn, Michael J Gullans, Anthony J Sigillito, Mayer M Feldman, Erik Nielsen, and Jason R Petta. Two-qubit silicon quantum processor with operation fidelity exceeding 99%. *Sci. Adv*, 8:5130, 2022. doi: 10.1126/sciadv.abn5130. URL https://www.science.org/doi/10.1126/sciadv.abn5130.

[347] D. S. Miserev and O. P. Sushkov. Dimensional reduction of the luttinger hamiltonian and g-factors of holes in symmetric two-dimensional semiconductor heterostruc-

tures. *Phys. Rev. B*, 95:085431, Feb 2017. doi: 10.1103/PhysRevB.95.085431. URL https://link.aps.org/doi/10.1103/PhysRevB.95.085431.

[348] D. S. Miserev, A. Srinivasan, O. A. Tkachenko, V. A. Tkachenko, I. Farrer, D. A. Ritchie, A. R. Hamilton, and O. P. Sushkov. Mechanisms for strong anisotropy of in-plane g-factors in hole based quantum point contacts. *Phys. Rev. Lett.*, 119: 116803, Sep 2017. doi: 10.1103/PhysRevLett.119.116803. URL https://link.aps.org/doi/10.1103/PhysRevLett.119.116803.

[349] R Mizokuchi, R Maurand, F Vigneau, M Myronov, and S De Franceschi. Ballistic one-dimensional holes with strong g-factor anisotropy in germanium. *Nano letters*, 18:4861–4865, 2018. URL https://pubs.acs.org/doi/10.1021/acs.nanolett.8b01457.

[350] P. Mohanty and R. A. Webb. Decoherence and quantum fluctuations. *Phys. Rev. B*, 55:R13452–R13455, May 1997. doi: 10.1103/PhysRevB.55.R13452. URL https://link.aps.org/doi/10.1103/PhysRevB.55.R13452.

[351] P. Mohanty, E. M. Q. Jariwala, and R. A. Webb. Intrinsic decoherence in mesoscopic systems. *Phys. Rev. Lett.*, 78:3366–3369, Apr 1997. doi: 10.1103/PhysRevLett.78.3366. URL https://link.aps.org/doi/10.1103/PhysRevLett.78.3366.

[352] C. Monroe, D. M. Meekhof, B. E. King, W. M. Itano, and D. J. Wineland. Demonstration of a fundamental quantum logic gate. *Phys. Rev. Lett.*, 75:4714–4717, Dec 1995. doi: 10.1103/PhysRevLett.75.4714. URL https://link.aps.org/doi/10.1103/PhysRevLett.75.4714.

[353] C. Monroe, W. C. Campbell, L.-M. Duan, Z.-X. Gong, A. V. Gorshkov, P. W. Hess, R. Islam, K. Kim, N. M. Linke, G. Pagano, P. Richerme, C. Senko, and N. Y. Yao. Programmable quantum simulations of spin systems with trapped ions. *Rev. Mod. Phys.*, 93:025001, Apr 2021. doi: 10.1103/RevModPhys.93.025001. URL https://link.aps.org/doi/10.1103/RevModPhys.93.025001.

[354] KISHIN MOORJANI and CHARLES FELDMAN. Electrical properties of amorphous semiconductors. *Rev. Mod. Phys.*, 36:1042–1049, Oct 1964. doi: 10.

1103/RevModPhys.36.1042. URL https://link.aps.org/doi/10.1103/RevModPhys.36.1042.

[355] K Moratis, J Cibert, D Ferrand, and Y M Niquet. Light hole states in a strained quantum dot: Numerical calculation and phenomenological models. *Physical Review B*, 103, 4 2021. ISSN 24699969. doi: 10.1103/PhysRevB.103.245304. URL https://doi.org/10.1103/PhysRevB.103.245304.

[356] Rai Moriya, Kentarou Sawano, Yusuke Hoshi, Satoru Masubuchi, Yasuhiro Shiraki, Andreas Wild, Christian Neumann, Gerhard Abstreiter, Dominique Bougeard, Takaaki Koga, and Tomoki Machida. Cubic rashba spin-orbit interaction of a two-dimensional hole gas in a strained- ge/sige quantum well. *Physical Review Letters*, 113, 4 2014. ISSN 10797114. doi: 10.1103/PhysRevLett.113.086601. URL https://doi.org/10.1103/PhysRevLett.113.086601.

[357] C Morrison, P Wiśniewski, S D Rhead, J Foronda, D R Leadley, and M Myronov. Observation of rashba zero-field spin splitting in a strained germanium 2d hole gas. *Applied Physics Letters*, 105, 4 2014. ISSN 00036951. doi: 10.1063/1.4901107. URL https://doi.org/10.1063/1.4901107.

[358] John J L Morton, Dane R McCamey, Mark A Eriksson, and Stephen A Lyon. Embracing the quantum limit in silicon computing. *Nature*, 479:345–353, 4 2011. ISSN 00280836. doi: 10.1038/nature10681. URL https://doi.org/10.1038/nature10681.

[359] Shuichi Murakami. Quantum spin hall effect and enhanced magnetic response by spin-orbit coupling. *Phys. Rev. Lett.*, 97:236805, Dec 2006. doi: 10.1103/PhysRevLett.97.236805. URL https://link.aps.org/doi/10.1103/PhysRevLett.97.236805.

[360] Philipp M. Mutter and Guido Burkard. Cavity control over heavy-hole spin qubits in inversion-symmetric crystals. *Phys. Rev. B*, 102:205412, Nov 2020. doi: 10.1103/PhysRevB.102.205412. URL https://link.aps.org/doi/10.1103/PhysRevB.102.205412.

[361] Philipp M Mutter and Guido Burkard. Natural heavy-hole flopping mode qubit in germanium. *Physical Review Research*, 3, 4 2021. ISSN 26431564. doi: 10.1103/PhysRevResearch.3.013194. URL https://doi.org/10.1103/PhysRevResearch.3.013194.

[362] S. Nadj-Perge, S. M. Frolov, E. P. A. M. Bakkers, and L. P. Kouwenhoven. Spin–orbit qubit in a semiconductor nanowire. *Nature*, 468(7327):1084–1087, 2010. doi: 10.1038/nature09682. URL https://doi.org/10.1038/nature09682.

[363] Takashi Nakajima, Akito Noiri, Kento Kawasaki, Jun Yoneda, Peter Stano, Shinichi Amaha, Tomohiro Otsuka, Kenta Takeda, Matthieu R. Delbecq, Giles Allison, Arne Ludwig, Andreas D. Wieck, Daniel Loss, and Seigo Tarucha. Coherence of a driven electron spin qubit actively decoupled from quasistatic noise. *Phys. Rev. X*, 10: 011060, Mar 2020. doi: 10.1103/PhysRevX.10.011060. URL https://link.aps.org/doi/10.1103/PhysRevX.10.011060.

[364] Y. Nakamura, Yu. A. Pashkin, and J. S. Tsai. Coherent control of macroscopic quantum states in a single-cooper-pair box. *Nature*, 398(6730):786–788, 1999. doi: 10.1038/19718. URL https://doi.org/10.1038/19718.

[365] Chetan Nayak, Steven H. Simon, Ady Stern, Michael Freedman, and Sankar Das Sarma. Non-abelian anyons and topological quantum computation. *Rev. Mod. Phys.*, 80:1083–1159, Sep 2008. doi: 10.1103/RevModPhys.80.1083. URL https://link.aps.org/doi/10.1103/RevModPhys.80.1083.

[366] C. Negrevergne, T. S. Mahesh, C. A. Ryan, M. Ditty, F. Cyr-Racine, W. Power, N. Boulant, T. Havel, D. G. Cory, and R. Laflamme. Benchmarking quantum control methods on a 12-qubit system. *Phys. Rev. Lett.*, 96:170501, May 2006. doi: 10.1103/PhysRevLett.96.170501. URL https://link.aps.org/doi/10.1103/PhysRevLett.96.170501.

[367] A. O. Niskanen, K. Harrabi, F. Yoshihara, Y. Nakamura, S. Lloyd, and J. S. Tsai. Quantum coherent tunable coupling of superconducting qubits. *Science*, 316(5825):

723–726, 2007. doi: 10.1126/science.1141324. URL https://www.science.org/doi/abs/10.1126/science.1141324.

[368] Akito Noiri, Kenta Takeda, Takashi Nakajima, Takashi Kobayashi, Amir Sammak, Giordano Scappucci, and Seigo Tarucha. Fast universal quantum gate above the fault-tolerance threshold in silicon. *Nature*, 601:338–342, 2022. URL https://doi.org/10.1038/s41586-021-04182-y.

[369] Leigh M. Norris, Gerardo A. Paz-Silva, and Lorenza Viola. Qubit noise spectroscopy for non-gaussian dephasing environments. *Phys. Rev. Lett.*, 116:150503, Apr 2016. doi: 10.1103/PhysRevLett.116.150503. URL https://link.aps.org/doi/10.1103/PhysRevLett.116.150503.

[370] G. A. Northrop. Phonon focusing of dispersive phonons in ge. *Phys. Rev. B*, 26: 903–911, Jul 1982. doi: 10.1103/PhysRevB.26.903. URL https://link.aps.org/doi/10.1103/PhysRevB.26.903.

[371] Pietro Novelli, Fabio Taddei, Andre K. Geim, and Marco Polini. Failure of conductance quantization in two-dimensional topological insulators due to nonmagnetic impurities. *Phys. Rev. Lett.*, 122:016601, Jan 2019. doi: 10.1103/PhysRevLett.122.016601. URL https://link.aps.org/doi/10.1103/PhysRevLett.122.016601.

[372] J L O'Brien, S R Schofield, M Y Simmons, R G Clark, A S Dzurak, B E Kane, N S McAlpine, M E Hawley, and G W Brown. Towards the fabrication of phosphorus qubits for a silicon quantum computer. *Physical Review B - Condensed Matter and Materials Physics*, 64:1614011–1614014, 4 2001. ISSN 01631829. doi: 10.1103/PhysRevB.64.161401. URL https://doi.org/10.1103/PhysRevB.64.161401.

[373] Jeremy L. O'Brien. Optical quantum computing. *Science*, 318(5856):1567–1570, 2007. doi: 10.1126/science.1142892. URL https://www.science.org/doi/abs/10.1126/science.1142892.

[374] Nissim Ofek, Andrei Petrenko, Reinier Heeres, Philip Reinhold, Zaki Leghtas, Brian Vlastakis, Yehan Liu, Luigi Frunzio, S. M. Girvin, L. Jiang, Mazyar Mirrahimi, M. H. Devoret, and R. J. Schoelkopf. Extending the lifetime of a quantum bit with error correction in superconducting circuits. *Nature*, 536(7617):441–445, 2016. doi: 10.1038/nature18949. URL https://doi.org/10.1038/nature18949.

[375] K. Ono, G. Giavaras, T. Tanamoto, T. Ohguro, X. Hu, and F. Nori. Hole spin resonance and spin-orbit coupling in a silicon metal-oxide-semiconductor field-effect transistor. *Phys. Rev. Lett.*, 119:156802, Oct 2017. doi: 10.1103/PhysRevLett.119.156802. URL https://link.aps.org/doi/10.1103/PhysRevLett.119.156802.

[376] K Ono, G Giavaras, T Tanamoto, T Ohguro, X Hu, and F Nori. Hole spin resonance and spin-orbit coupling in a silicon metal-oxide-semiconductor field-effect transistor. *Physical Review Letters*, 119, 4 2017. ISSN 10797114. doi: 10.1103/PhysRevLett.119.156802. URL https://doi.org/10.1103/PhysRevLett.119.156802.

[377] T. P. Orlando, J. E. Mooij, Lin Tian, Caspar H. van der Wal, L. S. Levitov, Seth Lloyd, and J. J. Mazo. Superconducting persistent-current qubit. *Phys. Rev. B*, 60:15398–15413, Dec 1999. doi: 10.1103/PhysRevB.60.15398. URL https://link.aps.org/doi/10.1103/PhysRevB.60.15398.

[378] T Ozturk, R L Field, Y S Eo, S Wolgast, K Sun, and C Kurdak. Influence of helical spin structure on the magnetoresistance of an ideal topological insulator. *Journal of Physics Communications*, 1(3):035005, oct 2017. doi: 10.1088/2399-6528/aa8cfb. URL https://doi.org/10.1088/2399-6528/aa8cfb.

[379] C. Padurariu and Yu. V. Nazarov. Theoretical proposal for superconducting spin qubits. *Phys. Rev. B*, 81:144519, Apr 2010. doi: 10.1103/PhysRevB.81.144519. URL https://link.aps.org/doi/10.1103/PhysRevB.81.144519.

[380] P Pakkiam, A V Timofeev, M G House, M R Hogg, T Kobayashi, M Koch, S Rogge, and M Y Simmons. Single-shot single-gate rf spin readout in silicon. *Physical*

Review X, 8, 4 2018. ISSN 21603308. doi: 10.1103/PhysRevX.8.041032. URL https://doi.org/10.1103/PhysRevX.8.041032.

[381] E. Paladino, L. Faoro, G. Falci, and Rosario Fazio. Decoherence and $1/f$ noise in josephson qubits. *Phys. Rev. Lett.*, 88:228304, May 2002. doi: 10.1103/PhysRevLett.88.228304. URL https://link.aps.org/doi/10.1103/PhysRevLett.88.228304.

[382] Arthur G. III Palmer. Nmr characterization of the dynamics of biomacromolecules. *Chemical Reviews*, 104(8):3623–3640, 2004. doi: 10.1021/cr030413t. URL https://doi.org/10.1021/cr030413t. PMID: 15303831.

[383] Hui Pan, Meimei Wu, Ying Liu, and Shengyuan A. Yang. Electric control of topological phase transitions in dirac semimetal thin films. *Scientific Reports*, 5 (1):14639, Sep 2015. ISSN 2045-2322. doi: 10.1038/srep14639. URL https://doi.org/10.1038/srep14639.

[384] B. V. Pashinsky, M. Goldstein, and I. S. Burmistrov. Finite frequency backscattering current noise at a helical edge. *Phys. Rev. B*, 102:125309, Sep 2020. doi: 10.1103/PhysRevB.102.125309. URL https://link.aps.org/doi/10.1103/PhysRevB.102.125309.

[385] Maurizio Pellecchia, Daniel S. Sem, and Kurt Wüthrich. Nmr in drug discovery. *Nature Reviews Drug Discovery*, 1(3):211–219, 2002. doi: 10.1038/nrd748. URL https://doi.org/10.1038/nrd748.

[386] Asher Peres. Reversible logic and quantum computers. *Phys. Rev. A*, 32:3266–3276, Dec 1985. doi: 10.1103/PhysRevA.32.3266. URL https://link.aps.org/doi/10.1103/PhysRevA.32.3266.

[387] L. Petit, J. M. Boter, H. G. J. Eenink, G. Droulers, M. L. V. Tagliaferri, R. Li, D. P. Franke, K. J. Singh, J. S. Clarke, R. N. Schouten, V. V. Dobrovitski, L. M. K. Vandersypen, and M. Veldhorst. Spin lifetime and charge noise in hot silicon quantum dot qubits. *Phys. Rev. Lett.*, 121:076801, Aug 2018. doi: 10.1103/PhysRevLett.121.

076801. URL https://link.aps.org/doi/10.1103/PhysRevLett.121.076801.

[388] J. R. Petta and D. C. Ralph. Measurements of strongly anisotropic g factors for spins in single quantum states. *Phys. Rev. Lett.*, 89:156802, Sep 2002. doi: 10.1103/PhysRevLett.89.156802. URL https://link.aps.org/doi/10.1103/PhysRevLett.89.156802.

[389] J. R. Petta, A. C. Johnson, J. M. Taylor, E. A. Laird, A. Yacoby, M. D. Lukin, C. M. Marcus, M. P. Hanson, and A. C. Gossard. Coherent manipulation of coupled electron spins in semiconductor quantum dots. *Science*, 309(5744):2180–2184, 2005. doi: 10.1126/science.1116955. URL https://www.science.org/doi/abs/10.1126/science.1116955.

[390] J. R. Petta, J. M. Taylor, A. C. Johnson, A. Yacoby, M. D. Lukin, C. M. Marcus, M. P. Hanson, and A. C. Gossard. Dynamic nuclear polarization with single electron spins. *Phys. Rev. Lett.*, 100:067601, Feb 2008. doi: 10.1103/PhysRevLett.100.067601. URL https://link.aps.org/doi/10.1103/PhysRevLett.100.067601.

[391] Luca Pezzè, Augusto Smerzi, Markus K. Oberthaler, Roman Schmied, and Philipp Treutlein. Quantum metrology with nonclassical states of atomic ensembles. *Rev. Mod. Phys.*, 90:035005, Sep 2018. doi: 10.1103/RevModPhys.90.035005. URL https://link.aps.org/doi/10.1103/RevModPhys.90.035005.

[392] Pericles Philippopoulos, Stefano Chesi, and W A Coish. First-principles hyperfine tensors for electrons and holes in gaas and silicon. *Physical Review B*, 101, 4 2020. ISSN 24699969. doi: 10.1103/PhysRevB.101.115302. URL https://doi.org/10.1103/PhysRevB.101.115302.

[393] J C Phillips. Band structure of silicon, germanium, and related semiconductors. *Phys. Rev.*, 125:1931–1936, 3 1962. doi: 10.1103/PhysRev.125.1931. URL https://link.aps.org/doi/10.1103/PhysRev.125.1931.

[394] Ravi Pillarisetty. Academic and industry research progress in germanium nanodevices. *Nature*, 479:324–328, 2011. URL https://www.nature.com/articles/nature10678.

[395] N Piot, B Brun, V Schmitt, S Zihlmann, V P Michal, A Apra, J C Abadillo-Uriel, X Jehl, B Bertrand, H Niebojewski, L Hutin, M Vinet, M Urdampilleta, T Meunier, Y M Niquet, R Maurand, and S De Franceschi. A single hole spin with enhanced coherence in natural silicon. *Nature Nanotechnology*, 17:1072–1077, 4 2022. ISSN 17483395. doi: 10.1038/s41565-022-01196-z. URL https://doi.org/10.1038/s41565-022-01196-z.

[396] Jarryd J Pla, Kuan Y Tan, Juan P Dehollain, Wee H Lim, John J L Morton, David N Jamieson, Andrew S Dzurak, and Andrea Morello. A single-atom electron spin qubit in silicon. *Nature*, 489:541–544, 4 2012. ISSN 00280836. doi: 10.1038/nature11449.

[397] Christopher Portmann and Renato Renner. Security in quantum cryptography. *Rev. Mod. Phys.*, 94:025008, Jun 2022. doi: 10.1103/RevModPhys.94.025008. URL https://link.aps.org/doi/10.1103/RevModPhys.94.025008.

[398] Jonathan H Prechtel, Andreas V Kuhlmann, Julien Houel, Arne Ludwig, Sascha R Valentin, Andreas D Wieck, and Richard J Warburton. Decoupling a hole spin qubit from the nuclear spins. *Nature Materials*, 15:981–986, 4 2016. ISSN 14764660. doi: 10.1038/nmat4704. URL https://doi.org/10.1038/nmat4704.

[399] John Preskill. Quantum computing: pro and con. *Proceedings of the Royal Society of London. Series A: Mathematical, Physical and Engineering Sciences*, 454(1969):469–486, 1998. doi: 10.1098/rspa.1998.0171. URL https://royalsocietypublishing.org/doi/abs/10.1098/rspa.1998.0171.

[400] V S Pribiag, S Nadj-Perge, S M Frolov, J W G Van Den Berg, I Van Weperen, S R Plissard, EPAM Bakkers, and L P Kouwenhoven. Electrical control of single hole spins in nanowire quantum dots. *Nature nanotechnology*, 8:170–174, 2013. URL https://www.nature.com/articles/nnano.2013.5.

[401] Craig E. Pryor and Michael E. Flatté. Landé g factors and orbital momentum quenching in semiconductor quantum dots. *Phys. Rev. Lett.*, 96:026804, Jan 2006. doi: 10.1103/PhysRevLett.96.026804. URL https://link.aps.org/doi/10.1103/PhysRevLett.96.026804.

[402] J Przybytek, R Stankiewicz, M Gryglas-Borysiewicz, M Baj, A Cavanna, and G Faini. Observation of thermally-activated electron traps in gaas/alas/gaas heterostructures in low-frequency noise measurements. *Acta Physica Polonica A*, 119(5), 2011. URL http://przyrbwn.icm.edu.pl/APP/PDF/119/a119z5p47.pdf.

[403] Michael Pustilnik and Leonid Glazman. Kondo effect in quantum dots. *Journal of Physics: Condensed Matter*, 16(16):R513, apr 2004. doi: 10.1088/0953-8984/16/16/R01. URL https://dx.doi.org/10.1088/0953-8984/16/16/R01.

[404] Xiao-Liang Qi and Shou-Cheng Zhang. Topological insulators and superconductors. *Rev. Mod. Phys.*, 83:1057–1110, Oct 2011. doi: 10.1103/RevModPhys.83.1057. URL https://link.aps.org/doi/10.1103/RevModPhys.83.1057.

[405] Xiao-Liang Qi, Taylor L. Hughes, and Shou-Cheng Zhang. Topological field theory of time-reversal invariant insulators. *Phys. Rev. B*, 78:195424, Nov 2008. doi: 10.1103/PhysRevB.78.195424. URL https://link.aps.org/doi/10.1103/PhysRevB.78.195424.

[406] Jørgen Holme Qvist and Jeroen Danon. Anisotropic formula presented-tensors in hole quantum dots: Role of transverse confinement direction. *Physical Review B*, 105, 4 2022. ISSN 24699969. doi: 10.1103/PhysRevB.105.075303.

[407] I. I. Rabi, J. R. Zacharias, S. Millman, and P. Kusch. A new method of measuring nuclear magnetic moment. *Phys. Rev.*, 53:318–318, Feb 1938. doi: 10.1103/PhysRev.53.318. URL https://link.aps.org/doi/10.1103/PhysRev.53.318.

[408] J. M. Raimond, M. Brune, and S. Haroche. Manipulating quantum entanglement with atoms and photons in a cavity. *Rev. Mod. Phys.*, 73:565–582, Aug 2001. doi: 10.1103/RevModPhys.73.565. URL https://link.aps.org/doi/10.1103/RevModPhys.73.565.

[409] Guy Ramon. Non-gaussian signatures and collective effects in charge noise affecting a dynamically decoupled qubit. *Phys. Rev. B*, 92:155422, Oct 2015. doi: 10.1103/PhysRevB.92.155422. URL https://link.aps.org/doi/10.1103/PhysRevB.92.155422.

[410] Guy Ramon and Xuedong Hu. Decoherence of spin qubits due to a nearby charge fluctuator in gate-defined double dots. *Phys. Rev. B*, 81:45304, 1 2010. doi: 10.1103/PhysRevB.81.045304. URL https://link.aps.org/doi/10.1103/PhysRevB.81.045304.

[411] E. I. Rashba and Al. L. Efros. Orbital mechanisms of electron-spin manipulation by an electric field. *Phys. Rev. Lett.*, 91:126405, Sep 2003. doi: 10.1103/PhysRevLett.91.126405. URL https://link.aps.org/doi/10.1103/PhysRevLett.91.126405.

[412] E.I. Rashba and E.Ya. Sherman. Spin-orbital band splitting in symmetric quantum wells. *Physics Letters A*, 129(3):175–179, 1988. ISSN 0375-9601. doi: https://doi.org/10.1016/0375-9601(88)90140-5. URL https://www.sciencedirect.com/science/article/pii/0375960188901405.

[413] Emmanuel I. Rashba. Theory of electric dipole spin resonance in quantum dots: Mean field theory with gaussian fluctuations and beyond. *Phys. Rev. B*, 78:195302, Nov 2008. doi: 10.1103/PhysRevB.78.195302. URL https://link.aps.org/doi/10.1103/PhysRevB.78.195302.

[414] Emmanuel I Rashba. Quantum nanostructures in strongly spin-orbit coupled two-dimensional systems. *Phys. Rev. B*, 86:125319, 9 2012. doi: 10.1103/PhysRevB.86.125319. URL https://link.aps.org/doi/10.1103/PhysRevB.86.125319.

[415] M. D. Reed, B. M. Maune, R. W. Andrews, M. G. Borselli, K. Eng, M. P. Jura, A. A. Kiselev, T. D. Ladd, S. T. Merkel, I. Milosavljevic, E. J. Pritchett, M. T. Rakher, R. S. Ross, A. E. Schmitz, A. Smith, J. A. Wright, M. F.

Gyure, and A. T. Hunter. Reduced sensitivity to charge noise in semiconductor spin qubits via symmetric operation. *Phys. Rev. Lett.*, 116:110402, Mar 2016. doi: 10.1103/PhysRevLett.116.110402. URL https://link.aps.org/doi/10.1103/PhysRevLett.116.110402.

[416] Bernd Reif, Sharon E. Ashbrook, Lyndon Emsley, and Mei Hong. Solid-state nmr spectroscopy. *Nature Reviews Methods Primers*, 1(1):2, 2021. doi: 10.1038/s43586-020-00002-1. URL https://doi.org/10.1038/s43586-020-00002-1.

[417] Soline Richard, Frédéric Aniel, and Guy Fishman. Energy band structure of ge si and gaas a thirty band k p method. *Phys. Rev. B*, 70:235204, 12 2004. doi: 10.1103/PhysRevB.70.235204. URL https://link.aps.org/doi/10.1103/PhysRevB.70.235204.

[418] John P. Ridgway. Cardiovascular magnetic resonance physics for clinicians: part i. *Journal of Cardiovascular Magnetic Resonance*, 12(1):71, 2010. doi: 10.1186/1532-429X-12-71. URL https://doi.org/10.1186/1532-429X-12-71.

[419] Hans Riesel. *Prime Numbers and Computer Methods for Factorization*. Birkhäuser, Boston, Nov 2011. ISBN 978-0-8176-8297-2. doi: 10.1007/978-0-8176-8298-9. URL https://doi.org/10.1007/978-0-8176-8298-9.

[420] S Roddaro, A Fuhrer, P Brusheim, C Fasth, H Q Xu, L Samuelson, J Xiang, and C M Lieber. Spin states of holes in ge/si nanowire quantum dots. *Phys. Rev. Lett.*, 101:186802, 10 2008. doi: 10.1103/PhysRevLett.101.186802. URL https://link.aps.org/doi/10.1103/PhysRevLett.101.186802.

[421] Esteban A. Rodríguez-Mena, José Carlos Abadillo-Uriel, Gaëtan Veste, Biel Martinez, Jing Li, Benoît Sklénard, and Yann-Michel Niquet. Linear-in-momentum spin orbit interactions in planar ge/gesi heterostructures and spin qubits. *Phys. Rev. B*, 108:205416, Nov 2023. doi: 10.1103/PhysRevB.108.205416. URL https://link.aps.org/doi/10.1103/PhysRevB.108.205416.

[422] Alessandro Roggero, Andy C. Y. Li, Joseph Carlson, Rajan Gupta, and Gabriel N. Perdue. Quantum computing for neutrino-nucleus scattering. *Phys. Rev. D*, 101: 074038, Apr 2020. doi: 10.1103/PhysRevD.101.074038. URL https://link.aps.org/doi/10.1103/PhysRevD.101.074038.

[423] Robert Roloff, Thomas Eissfeller, Peter Vogl, and Walter Pötz. Electric g tensor control and spin echo of a hole-spin qubit in a quantum dot molecule. *New Journal of Physics*, 12(9):093012, sep 2010. doi: 10.1088/1367-2630/12/9/093012. URL https://dx.doi.org/10.1088/1367-2630/12/9/093012.

[424] Katarzyna Roszak, Damian Kwiatkowski, and Łukasz Cywiński. How to detect qubit-environment entanglement generated during qubit dephasing. *Phys. Rev. A*, 100:022318, Aug 2019. doi: 10.1103/PhysRevA.100.022318. URL https://link.aps.org/doi/10.1103/PhysRevA.100.022318.

[425] Frank J Ruess, Lars Oberbeck, Michelle Y Simmons, Kuan Eng J Goh, Alex R Hamilton, Toby Hallam, Steven R Schofield, Neil J Curson, and Robert G Clark. Toward atomic-scale device fabrication in silicon using scanning probe microscopy. *Nano Letters*, 4:1969–1973, 4 2004. ISSN 15306984. doi: 10.1021/nl048808v. URL https://doi.org/10.1021/nl048808v.

[426] Maximilian Russ and Guido Burkard. Asymmetric resonant exchange qubit under the influence of electrical noise. *Phys. Rev. B*, 91:235411, Jun 2015. doi: 10.1103/PhysRevB.91.235411. URL https://link.aps.org/doi/10.1103/PhysRevB.91.235411.

[427] Angus Russell, Alexander Zotov, Ruichen Zhao, Andrew S. Dzurak, M. Fernando Gonzalez-Zalba, and Alessandro Rossi. Gate-based spin readout of hole quantum dots with site-dependent g-factors. *Phys. Rev. Appl.*, 19:044039, Apr 2023. doi: 10.1103/PhysRevApplied.19.044039. URL https://link.aps.org/doi/10.1103/PhysRevApplied.19.044039.

[428] C. A. Ryan, O. Moussa, J. Baugh, and R. Laflamme. Spin based heat engine: Demonstration of multiple rounds of algorithmic cooling. *Phys. Rev. Lett.*, 100:

140501, Apr 2008. doi: 10.1103/PhysRevLett.100.140501. URL https://link.aps.org/doi/10.1103/PhysRevLett.100.140501.

[429] M. Saffman, T. G. Walker, and K. Mølmer. Quantum information with rydberg atoms. *Rev. Mod. Phys.*, 82:2313–2363, Aug 2010. doi: 10.1103/RevModPhys.82.2313. URL https://link.aps.org/doi/10.1103/RevModPhys.82.2313.

[430] Francesc Sagués, José M. Sancho, and Jordi García-Ojalvo. Spatiotemporal order out of noise. *Rev. Mod. Phys.*, 79:829–882, Jul 2007. doi: 10.1103/RevModPhys.79.829. URL https://link.aps.org/doi/10.1103/RevModPhys.79.829.

[431] Ebrahim Sajadi, Tauno Palomaki, Zaiyao Fei, Wenjin Zhao, Philip Bement, Christian Olsen, Silvia Luescher, Xiaodong Xu, Joshua A. Folk, and David H. Cobden. Gate-induced superconductivity in a monolayer topological insulator. *Science*, 362(6417):922–925, 2018. ISSN 0036-8075. doi: 10.1126/science.aar4426. URL https://science.sciencemag.org/content/362/6417/922.

[432] J Salfi, J A Mol, R Rahman, G Klimeck, M Y Simmons, L C L Hollenberg, and S Rogge. Spatially resolving valley quantum interference of a donor in silicon. *Nature Materials*, 13:605–610, 2014. ISSN 14764660. doi: 10.1038/nmat3941. URL https://doi.org/10.1038/nmat3941.

[433] Joe Salfi, Jan A Mol, Dimitrie Culcer, and Sven Rogge. Charge-insensitive single-atom spin-orbit qubit in silicon. *Physical Review Letters*, 116, 4 2016. ISSN 10797114. doi: 10.1103/PhysRevLett.116.246801. URL https://doi.org/10.1103/PhysRevLett.116.246801.

[434] Joe Salfi, Mengyang Tong, Sven Rogge, and Dimitrie Culcer. Quantum computing with acceptor spins in silicon. *Nanotechnology*, 27, 4 2016. ISSN 13616528. doi: 10.1088/0957-4484/27/24/244001. URL https://doi.org/10.1088/0957-4484/27/24/244001.

[435] G. Salis, Y. Kato, K. Ensslin, D. C. Driscoll, A. C. Gossard, and D. D. Awschalom. Electrical control of spin coherence in semiconductor nanostructures. *Nature*, 414

(6864):619–622, 2001. doi: 10.1038/414619a. URL https://doi.org/10.1038/414619a.

[436] Amir Sammak, Diego Sabbagh, Nico W Hendrickx, Mario Lodari, Brian Paquelet Wuetz, Alberto Tosato, LaReine Yeoh, Monica Bollani, Michele Virgilio, Markus Andreas Schubert, et al. Shallow and undoped germanium quantum wells: a playground for spin and hybrid quantum technology. *Advanced Functional Materials*, 29:1807613, 2019. URL https://doi.org/10.1002/adfm.201807613.

[437] Pablo San-Jose, Gergely Zarand, Alexander Shnirman, and Gerd Schön. Geometrical spin dephasing in quantum dots. *Phys. Rev. Lett.*, 97:076803, Aug 2006. doi: 10.1103/PhysRevLett.97.076803. URL https://link.aps.org/doi/10.1103/PhysRevLett.97.076803.

[438] Abhikbrata Sarkar, Joel Hochstetter, Allen Kha, Xuedong Hu, Michelle Y Simmons, Rajib Rahman, and Dimitrie Culcer. Optimisation of electron spin qubits in electrically driven multi-donor quantum dots. *npj Quantum Information*, 8, 4 2022. ISSN 20566387. doi: 10.1038/s41534-022-00646-9. URL https://doi.org/10.1038/s41534-022-00646-9.

[439] Abhikbrata Sarkar, Zhanning Wang, Matthew Rendell, Nico W. Hendrickx, Menno Veldhorst, Giordano Scappucci, Mohammad Khalifa, Joe Salfi, Andre Saraiva, A. S. Dzurak, A. R. Hamilton, and Dimitrie Culcer. Electrical operation of planar ge hole spin qubits in an in-plane magnetic field. *Phys. Rev. B*, 108:245301, Dec 2023. doi: 10.1103/PhysRevB.108.245301. URL https://link.aps.org/doi/10.1103/PhysRevB.108.245301.

[440] Giordano Scappucci, Christoph Kloeffel, Floris A Zwanenburg, Daniel Loss, Maksym Myronov, Jian Jun Zhang, Silvano De Franceschi, Georgios Katsaros, and Menno Veldhorst. The germanium quantum information route. *Nature Reviews Materials*, 6:926–943, 4 2021. ISSN 20588437. doi: 10.1038/s41578-020-00262-z. URL https://doi.org/10.1038/s41578-020-00262-z.

[441] John Schliemann. Colloquium: Persistent spin textures in semiconductor nanostructures. *Rev. Mod. Phys.*, 89:011001, Jan 2017. doi: 10.1103/RevModPhys.89.011001. URL https://link.aps.org/doi/10.1103/RevModPhys.89.011001.

[442] John Schliemann, Alexander Khaetskii, and Daniel Loss. Electron spin dynamics in quantum dots and related nanostructures due to hyperfine interaction with nuclei. *Journal of Physics: Condensed Matter*, 15(50):R1809, dec 2003. doi: 10.1088/0953-8984/15/50/R01. URL https://dx.doi.org/10.1088/0953-8984/15/50/R01.

[443] H. Schmidt and A. Imamoglu. Giant kerr nonlinearities obtained by electromagnetically induced transparency. *Opt. Lett.*, 21(23):1936–1938, Dec 1996. doi: 10.1364/OL.21.001936. URL https://opg.optica.org/ol/abstract.cfm?URI=ol-21-23-1936.

[444] Charles Schwartz. Theory of hyperfine structure. *Phys. Rev.*, 97:380–395, Jan 1955. doi: 10.1103/PhysRev.97.380. URL https://link.aps.org/doi/10.1103/PhysRev.97.380.

[445] M. S. Shahriar, P. R. Hemmer, S. Lloyd, P. S. Bhatia, and A. E. Craig. Solid-state quantum computing using spectral holes. *Phys. Rev. A*, 66:032301, Sep 2002. doi: 10.1103/PhysRevA.66.032301. URL https://link.aps.org/doi/10.1103/PhysRevA.66.032301.

[446] Baker Shalak, Christophe Delerue, and Yann-Michel Niquet. Modeling of spin decoherence in a si hole qubit perturbed by a single charge fluctuator. *Phys. Rev. B*, 107:125415, Mar 2023. doi: 10.1103/PhysRevB.107.125415. URL https://link.aps.org/doi/10.1103/PhysRevB.107.125415.

[447] Claude Elwood Shannon. A mathematical theory of communication. *The Bell System Technical Journal*, 27(3):379–423, 1948. doi: 10.1002/j.1538-7305.1948.tb01338.x. URL https://ieeexplore.ieee.org/document/6773024.

[448] M. Mohamed El Kordy Shehata, George Simion, Ruoyu Li, Fahd A. Mohiyaddin, Danny Wan, Massimo Mongillo, Bogdan Govoreanu, Iuliana Radu, Kristiaan

De Greve, and Pol Van Dorpe. Modeling semiconductor spin qubits and their charge noise environment for quantum gate fidelity estimation. *Phys. Rev. B*, 108:045305, Jul 2023. doi: 10.1103/PhysRevB.108.045305. URL https://link.aps.org/doi/10.1103/PhysRevB.108.045305.

[449] H. Z. Shen, M. Qin, X. Q. Shao, and X. X. Yi. General response formula and application to topological insulator in quantum open system. *Phys. Rev. E*, 92: 052122, Nov 2015. doi: 10.1103/PhysRevE.92.052122. URL https://link.aps.org/doi/10.1103/PhysRevE.92.052122.

[450] K Shen and M W Wu. Hole spin relaxation in intrinsic and p -type bulk gaas. *Physical Review B - Condensed Matter and Materials Physics*, 82, 4 2010. ISSN 10980121. doi: 10.1103/PhysRevB.82.115205. URL https://doi.org/10.1103/PhysRevB.82.115205.

[451] Mark S. Sherwin, Atac Imamoglu, and Thomas Montroy. Quantum computation with quantum dots and terahertz cavity quantum electrodynamics. *Phys. Rev. A*, 60:3508–3514, Nov 1999. doi: 10.1103/PhysRevA.60.3508. URL https://link.aps.org/doi/10.1103/PhysRevA.60.3508.

[452] Yanmeng Shi, Joshua Kahn, Ben Niu, Zaiyao Fei, Bosong Sun, Xinghan Cai, Brian A. Francisco, Di Wu, Zhi-Xun Shen, Xiaodong Xu, David H. Cobden, and Yong-Tao Cui. Imaging quantum spin hall edges in monolayer WTe_2. *Science Advances*, 5(2), 2019. doi: 10.1126/sciadv.aat8799. URL https://advances.sciencemag.org/content/5/2/eaat8799.

[453] N Shimatani, Y Yamaoka, R Ishihara, A Andreev, D A Williams, S Oda, and T Kodera. Temperature dependence of hole transport properties through physically defined silicon quantum dots. *Applied Physics Letters*, 117:94001, 2020. doi: 10.1063/5.0010981. URL https://doi.org/10.1063/5.0010981.

[454] Peter W. Shor. Scheme for reducing decoherence in quantum computer memory. *Phys. Rev. A*, 52:R2493–R2496, Oct 1995. doi: 10.1103/PhysRevA.52.R2493. URL https://link.aps.org/doi/10.1103/PhysRevA.52.R2493.

[455] Peter W Shor. Polynomial-time algorithms for prime factorization and discrete logarithms on a quantum computer. *Society for Industrial and Applied Mathematics*, 41:303–332, 1999. doi: 10.1137/S0097539795293172. URL http://www.siam.org/journals/sirev/41-2/34701.html.

[456] J. C. Slater. The electronic structure of metals. *Rev. Mod. Phys.*, 6:209–280, Oct 1934. doi: 10.1103/RevModPhys.6.209. URL https://link.aps.org/doi/10.1103/RevModPhys.6.209.

[457] J. C. Slater. A simplification of the hartree-fock method. *Phys. Rev.*, 81:385–390, Feb 1951. doi: 10.1103/PhysRev.81.385. URL https://link.aps.org/doi/10.1103/PhysRev.81.385.

[458] Darin Sleiter and W. F. Brinkman. Using holes in gaas as qubits: An estimate of the rabi frequency in the presence of an external rf field. *Phys. Rev. B*, 74:153312, Oct 2006. doi: 10.1103/PhysRevB.74.153312. URL https://link.aps.org/doi/10.1103/PhysRevB.74.153312.

[459] Inti Sodemann and Liang Fu. Quantum nonlinear hall effect induced by berry curvature dipole in time-reversal invariant materials. *Phys. Rev. Lett.*, 115:216806, Nov 2015. doi: 10.1103/PhysRevLett.115.216806. URL https://link.aps.org/doi/10.1103/PhysRevLett.115.216806.

[460] Aaron Somoroff, Quentin Ficheux, Raymond A. Mencia, Haonan Xiong, Roman Kuzmin, and Vladimir E. Manucharyan. Millisecond coherence in a superconducting qubit. *Phys. Rev. Lett.*, 130:267001, Jun 2023. doi: 10.1103/PhysRevLett.130.267001. URL https://link.aps.org/doi/10.1103/PhysRevLett.130.267001.

[461] Cameron Spence, Bruna Cardoso Paz, Bernhard Klemt, Emmanuel Chanrion, David J Niegemann, Baptiste Jadot, Vivien Thiney, Benoit Bertrand, Heimanu Niebojewski, Pierre André Mortemousque, Xavier Jehl, Romain Maurand, Silvano De Franceschi, Maud Vinet, Franck Balestro, Christopher Bäuerle, Yann Michel Niquet, Tristan Meunier, and Matias Urdampilleta. Spin-valley coupling anisotropy

and noise in cmos quantum dots. *Physical Review Applied*, 17, 4 2022. ISSN 23317019. doi: 10.1103/PhysRevApplied.17.034047. URL https://doi.org/10.1103/PhysRevApplied.17.034047.

[462] Cameron Spence, Bruna Cardoso Paz, Vincent Michal, Emmanuel Chanrion, David J. Niegemann, Baptiste Jadot, Pierre-André Mortemousque, Bernhard Klemt, Vivien Thiney, Benoit Bertrand, Louis Hutin, Christopher Bäuerle, Maud Vinet, Yann-Michel Niquet, Tristan Meunier, and Matias Urdampilleta. Probing low-frequency charge noise in few-electron cmos quantum dots. *Phys. Rev. Appl.*, 19:044010, Apr 2023. doi: 10.1103/PhysRevApplied.19.044010. URL https://link.aps.org/doi/10.1103/PhysRevApplied.19.044010.

[463] Paul C Spruijtenburg, Sergey V Amitonov, Wilfred G.Van Der Wiel, and Floris A Zwanenburg. A fabrication guide for planar silicon quantum dot heterostructures. *Nanotechnology*, 29, 4 2018. ISSN 13616528. doi: 10.1088/1361-6528/aaabf5. URL https://doi.org/10.1088/1361-6528/aaabf5.

[464] Peter Stano and Jaroslav Fabian. Spin-orbit effects in single-electron states in coupled quantum dots. *Phys. Rev. B*, 72:155410, Oct 2005. doi: 10.1103/PhysRevB.72.155410. URL https://link.aps.org/doi/10.1103/PhysRevB.72.155410.

[465] Peter Stano and Jaroslav Fabian. Theory of phonon-induced spin relaxation in laterally coupled quantum dots. *Physical Review Letters*, 96, 2006. ISSN 00319007. doi: 10.1103/PhysRevLett.96.186602.

[466] Lucas E. A. Stehouwer, Alberto Tosato, Davide Degli Esposti, Davide Costa, Menno Veldhorst, Amir Sammak, and Giordano Scappucci. Germanium wafers for strained quantum wells with low disorder. *Applied Physics Letters*, 123(9):092101, 08 2023. ISSN 0003-6951. doi: 10.1063/5.0158262. URL https://doi.org/10.1063/5.0158262.

[467] Dimitrije Stepanenko, Guido Burkard, Geza Giedke, and Atac Imamoglu. Enhancement of electron spin coherence by optical preparation of nuclear spins. *Phys.*

Rev. Lett., 96:136401, Apr 2006. doi: 10.1103/PhysRevLett.96.136401. URL https://link.aps.org/doi/10.1103/PhysRevLett.96.136401.

[468] Doru Sticlet and Jérôme Cayssol. Dynamical response of dissipative helical edge states. *Phys. Rev. B*, 90:201303, Nov 2014. doi: 10.1103/PhysRevB.90.201303. URL https://link.aps.org/doi/10.1103/PhysRevB.90.201303.

[469] Alexander Streltsov, Gerardo Adesso, and Martin B. Plenio. Colloquium: Quantum coherence as a resource. *Rev. Mod. Phys.*, 89:041003, Oct 2017. doi: 10.1103/RevModPhys.89.041003. URL https://link.aps.org/doi/10.1103/RevModPhys.89.041003.

[470] C. P. Sun, H. Zhan, and X. F. Liu. Decoherence and relevant universality in quantum algorithms via a dynamic theory for quantum measurement. *Phys. Rev. A*, 58:1810–1821, Sep 1998. doi: 10.1103/PhysRevA.58.1810. URL https://link.aps.org/doi/10.1103/PhysRevA.58.1810.

[471] G. Sun, L. Friedman, and R. A. Soref. Light-hole to heavy-hole acoustic phonon scattering rate. *Phys. Rev. B*, 62:8114–8119, Sep 2000. doi: 10.1103/PhysRevB.62.8114. URL https://link.aps.org/doi/10.1103/PhysRevB.62.8114.

[472] L. Sun, A. Petrenko, Z. Leghtas, B. Vlastakis, G. Kirchmair, K. M. Sliwa, A. Narla, M. Hatridge, S. Shankar, J. Blumoff, L. Frunzio, M. Mirrahimi, M. H. Devoret, and R. J. Schoelkopf. Tracking photon jumps with repeated quantum non-demolition parity measurements. *Nature*, 511(7510):444–448, 2014. doi: 10.1038/nature13436. URL https://doi.org/10.1038/nature13436.

[473] Yongke Sun, Scott E. Thompson, and Toshikazu Nishida. *Strain Effect in Semiconductors*. Springer New York, NY, 1 edition, 2009. doi: 10.1007/978-1-4419-0552-9. URL https://link.springer.com/book/10.1007/978-1-4419-0552-9.

[474] Dieter Suter and Gonzalo A. Álvarez. Colloquium: Protecting quantum information against environmental noise. *Rev. Mod. Phys.*, 88:041001, Oct 2016. doi: 10.1103/RevModPhys.88.041001. URL https://link.aps.org/doi/10.1103/RevModPhys.88.041001.

[475] P. Szumniak, S. Bednarek, B. Partoens, and F. M. Peeters. Spin-orbit-mediated manipulation of heavy-hole spin qubits in gated semiconductor nanodevices. *Phys. Rev. Lett.*, 109:107201, Sep 2012. doi: 10.1103/PhysRevLett.109.107201. URL https://link.aps.org/doi/10.1103/PhysRevLett.109.107201.

[476] Charles Tahan and Robert Joynt. Rashba spin-orbit coupling and spin relaxation in silicon quantum wells. *Physical Review B - Condensed Matter and Materials Physics*, 71, 4 2005. ISSN 10980121. doi: 10.1103/PhysRevB.71.075315. URL https://doi.org/10.1103/PhysRevB.71.075315.

[477] Charles Tahan and Robert Joynt. Relaxation of excited spin, orbital, and valley qubit states in ideal silicon quantum dots. *Physical Review B - Condensed Matter and Materials Physics*, 89, 4 2014. ISSN 10980121. doi: 10.1103/PhysRevB.89.075302.

[478] Kenta Takeda, Jun Kamioka, Tomohiro Otsuka, Jun Yoneda, Takashi Nakajima, Matthieu R. Delbecq, Shinichi Amaha, Giles Allison, Tetsuo Kodera, Shunri Oda, and Seigo Tarucha. A fault-tolerant addressable spin qubit in a natural silicon quantum dot. *Science Advances*, 2(8):e1600694, 2016. doi: 10.1126/sciadv.1600694. URL https://www.science.org/doi/abs/10.1126/sciadv.1600694.

[479] Takeji Takui, Lawrence Berliner, and Graeme Hanson, editors. *Electron Spin Resonance (ESR) Based Quantum Computing*. Biological Magnetic Resonance. Springer New York, NY, New York, 1 edition, 2016. ISBN 978-1-4939-3656-4. doi: 10.1007/978-1-4939-3658-8. URL https://doi.org/10.1007/978-1-4939-3658-8. Hardcover published: 12 October 2016; Softcover ISBN: 978-1-4939-8108-3, published: 14 June 2018; eBook ISBN: 978-1-4939-3658-8, published: 12 October 2016.

[480] Jan Talpe and Lieven Van Gerven. Dispersion, a most useful tool in paramagnetic resonance. *Phys. Rev.*, 145:718–726, May 1966. doi: 10.1103/PhysRev.145.718. URL https://link.aps.org/doi/10.1103/PhysRev.145.718.

[481] Yoichi Tanaka, A. Furusaki, and K. A. Matveev. Conductance of a helical edge liquid coupled to a magnetic impurity. *Phys. Rev. Lett.*, 106:236402, Jun 2011.

doi: 10.1103/PhysRevLett.106.236402. URL https://link.aps.org/doi/10.1103/PhysRevLett.106.236402.

[482] Shujie Tang, Chaofan Zhang, Dillon Wong, Zahra Pedramrazi, Hsin-Zon Tsai, Chunjing Jia, Brian Moritz, Martin Claassen, Hyejin Ryu, Salman Kahn, Juan Jiang, Hao Yan, Makoto Hashimoto, Donghui Lu, Robert G. Moore, Chan-Cuk Hwang, Choongyu Hwang, Zahid Hussain, Yulin Chen, Miguel M. Ugeda, Zhi Liu, Xiaoming Xie, Thomas P. Devereaux, Michael F. Crommie, Sung-Kwan Mo, and Zhi-Xun Shen. Quantum spin hall state in monolayer 1t'-wte2. *Nature Physics*, 13 (7):683–687, Jul 2017. ISSN 1745-2481. doi: 10.1038/nphys4174. URL https://doi.org/10.1038/nphys4174.

[483] Tuomo Tanttu, Bas Hensen, Kok Wai Chan, Chih Hwan Yang, Wister Wei Huang, Michael Fogarty, Fay Hudson, Kohei Itoh, Dimitrie Culcer, Arne Laucht, Andrea Morello, and Andrew Dzurak. Controlling spin-orbit interactions in silicon quantum dots using magnetic field direction. *Phys. Rev. X*, 9:021028, May 2019. doi: 10.1103/PhysRevX.9.021028. URL https://link.aps.org/doi/10.1103/PhysRevX.9.021028.

[484] L. A. Terrazos, E. Marcellina, Zhanning Wang, S. N. Coppersmith, Mark Friesen, A. R. Hamilton, Xuedong Hu, Belita Koiller, A. L. Saraiva, Dimitrie Culcer, and Rodrigo B. Capaz. Theory of hole-spin qubits in strained germanium quantum dots. *Phys. Rev. B*, 103:125201, Mar 2021. doi: 10.1103/PhysRevB.103.125201. URL https://link.aps.org/doi/10.1103/PhysRevB.103.125201.

[485] C. Testelin, F. Bernardot, B. Eble, and M. Chamarro. Hole–spin dephasing time associated with hyperfine interaction in quantum dots. *Phys. Rev. B*, 79:195440, May 2009. doi: 10.1103/PhysRevB.79.195440. URL https://link.aps.org/doi/10.1103/PhysRevB.79.195440.

[486] Yoshinori Tokura and Naoto Nagaosa. Nonreciprocal responses from non-centrosymmetric quantum materials. *Nature Communications*, 9(1):3740, Sep 2018.

ISSN 2041-1723. doi: 10.1038/s41467-018-05759-4. URL https://doi.org/10.1038/s41467-018-05759-4.

[487] Daniel D. Traficante. Relaxation: Can t2 be longer than t1? *Concepts in Magnetic Resonance*, 3(3):171–177, 1991. doi: https://doi.org/10.1002/cmr.1820030305. URL https://onlinelibrary.wiley.com/doi/abs/10.1002/cmr.1820030305.

[488] Mircea Trif, Vitaly N. Golovach, and Daniel Loss. Spin dynamics in inas nanowire quantum dots coupled to a transmission line. *Phys. Rev. B*, 77:045434, Jan 2008. doi: 10.1103/PhysRevB.77.045434. URL https://link.aps.org/doi/10.1103/PhysRevB.77.045434.

[489] Mircea Trif, Pascal Simon, and Daniel Loss. Relaxation of hole spins in quantum dots via two-phonon processes. *Physical Review Letters*, 103, 4 2009. ISSN 00319007. doi: 10.1103/PhysRevLett.103.106601. URL https://doi.org/10.1103/PhysRevLett.103.106601.

[490] Mircea Trif, Pascal Simon, and Daniel Loss. Relaxation of hole spins in quantum dots via two-phonon processes. *Phys. Rev. Lett.*, 103:106601, Sep 2009. doi: 10.1103/PhysRevLett.103.106601. URL https://link.aps.org/doi/10.1103/PhysRevLett.103.106601.

[491] Wang-Kong Tse and A. H. MacDonald. Magneto-optical and magnetoelectric effects of topological insulators in quantizing magnetic fields. *Phys. Rev. B*, 82:161104, Oct 2010. doi: 10.1103/PhysRevB.82.161104. URL https://link.aps.org/doi/10.1103/PhysRevB.82.161104.

[492] D. C. Tsui. Electron-tunneling studies of a quantized surface accumulation layer. *Phys. Rev. B*, 4:4438–4449, Dec 1971. doi: 10.1103/PhysRevB.4.4438. URL https://link.aps.org/doi/10.1103/PhysRevB.4.4438.

[493] Alexei M Tyryshkin, Shinichi Tojo, John J L Morton, Helge Riemann, Nikolai V Abrosimov, Peter Becker, Hans Joachim Pohl, Thomas Schenkel, Michael L W Thewalt, Kohei M Itoh, and S A Lyon. Electron spin coherence exceeding seconds

in high-purity silicon. *Nature Materials*, 11:143–147, 2012. ISSN 14764660. doi: 10.1038/nmat3182. URL https://www.nature.com/articles/nmat3182.

[494] J H Ungerer, P Chevalier Kwon, T Patlatiuk, J Ridderbos, A Kononov, D Sarmah, E P A M Bakkers, D Zumbühl, and C Schönenberger. Charge-sensing of a ge/si core/shell nanowire double quantum dot using a high-impedance superconducting resonator. *Materials for Quantum Technology*, 3(3):031001, jul 2023. doi: 10.1088/2633-4356/ace2a6. URL https://dx.doi.org/10.1088/2633-4356/ace2a6.

[495] Roope Uola, Ana C. S. Costa, H. Chau Nguyen, and Otfried Gühne. Quantum steering. *Rev. Mod. Phys.*, 92:015001, Mar 2020. doi: 10.1103/RevModPhys.92.015001. URL https://link.aps.org/doi/10.1103/RevModPhys.92.015001.

[496] M. J. Uren, D. J. Day, and M. J. Kirton. 1/f and random telegraph noise in silicon metal-oxide-semiconductor field-effect transistors. *Applied Physics Letters*, 47(11): 1195–1197, 12 1985. ISSN 0003-6951. doi: 10.1063/1.96325. URL https://doi.org/10.1063/1.96325.

[497] M Usman, C D Hill, R Rahman, G Klimeck, M Y Simmons, S Rogge, and L C L Hollenberg. Strain and electric field control of hyperfine interactions for donor spin qubits in silicon. *Physical Review B - Condensed Matter and Materials Physics*, 91, 4 2015. ISSN 1550235X. doi: 10.1103/PhysRevB.91.245209. URL https://doi.org/10.1103/PhysRevB.91.245209.

[498] E. Vahapoglu, J. P. Slack-Smith, R. C. C. Leon, W. H. Lim, F. E. Hudson, T. Day, J. D. Cifuentes, T. Tanttu, C. H. Yang, A. Saraiva, N. V. Abrosimov, H. J. Pohl, M. L. W. Thewalt, A. Laucht, A. S. Dzurak, and J. J. Pla. Coherent control of electron spin qubits in silicon using a global field. *npj Quantum Information*, 8 (1):126, 2022. doi: 10.1038/s41534-022-00645-w. URL https://doi.org/10.1038/s41534-022-00645-w.

[499] Joost van Der Heijden, Takashi Kobayashi, Matthew G House, Joe Salfi, Sylvain Barraud, Romain Laviéville, Michelle Y Simmons, and Sven Rogge. Readout and

control of the spin-orbit states of two coupled acceptor atoms in a silicon transistor. *Science advances*, 4, 2018. URL https://www.science.org/doi/abs/10.1126/sciadv.aat9199.

[500] Caspar H. van der Wal, A. C. J. ter Haar, F. K. Wilhelm, R. N. Schouten, C. J. P. M. Harmans, T. P. Orlando, Seth Lloyd, and J. E. Mooij. Quantum superposition of macroscopic persistent-current states. *Science*, 290(5492):773–777, 2000. doi: 10.1126/science.290.5492.773. URL https://www.science.org/doi/abs/10.1126/science.290.5492.773.

[501] W. G. van der Wiel, S. De Franceschi, J. M. Elzerman, T. Fujisawa, S. Tarucha, and L. P. Kouwenhoven. Electron transport through double quantum dots. *Rev. Mod. Phys.*, 75:1–22, Dec 2002. doi: 10.1103/RevModPhys.75.1. URL https://link.aps.org/doi/10.1103/RevModPhys.75.1.

[502] Lieven M. K. Vandersypen, Matthias Steffen, Gregory Breyta, Costantino S. Yannoni, Mark H. Sherwood, and Isaac L. Chuang. Experimental realization of shor's quantum factoring algorithm using nuclear magnetic resonance. *Nature*, 414(6866):883–887, 2001. doi: 10.1038/414883a. URL https://doi.org/10.1038/414883a.

[503] Luca Vannucci, Thomas Olsen, and Kristian S. Thygesen. Conductance of quantum spin hall edge states from first principles: The critical role of magnetic impurities and inter-edge scattering. *Phys. Rev. B*, 101:155404, Apr 2020. doi: 10.1103/PhysRevB.101.155404. URL https://link.aps.org/doi/10.1103/PhysRevB.101.155404.

[504] F. T. Vasko and V. V. Mitin. Generation and recombination processes via acoustic phonons in disordered graphene. *Phys. Rev. B*, 84:155445, Oct 2011. doi: 10.1103/PhysRevB.84.155445. URL https://link.aps.org/doi/10.1103/PhysRevB.84.155445.

[505] Jukka I. Väyrynen and Leonid I. Glazman. Current noise from a magnetic moment in a helical edge. *Phys. Rev. Lett.*, 118:106802, Mar 2017. doi: 10.

1103/PhysRevLett.118.106802. URL https://link.aps.org/doi/10.1103/PhysRevLett.118.106802.

[506] Jukka I. Väyrynen, Moshe Goldstein, Yuval Gefen, and Leonid I. Glazman. Resistance of helical edges formed in a semiconductor heterostructure. *Phys. Rev. B*, 90: 115309, Sep 2014. doi: 10.1103/PhysRevB.90.115309. URL https://link.aps.org/doi/10.1103/PhysRevB.90.115309.

[507] M. Veldhorst, C. H. Yang, J. C. C. Hwang, W. Huang, J. P. Dehollain, J. T. Muhonen, S. Simmons, A. Laucht, F. E. Hudson, K. M. Itoh, A. Morello, and A. S. Dzurak. A two-qubit logic gate in silicon. *Nature*, 526(7573):410–414, 2015. doi: 10.1038/nature15263. URL https://doi.org/10.1038/nature15263.

[508] M Veldhorst, H G J Eenink, C H Yang, and A S Dzurak. Silicon cmos architecture for a spin-based quantum computer. *Nature Communications*, 8, 4 2017. ISSN 20411723. doi: 10.1038/s41467-017-01905-6. URL https://doi.org/10.1038/s41467-017-01905-6.

[509] Benjamin Venitucci and Yann Michel Niquet. Simple model for electrical hole spin manipulation in semiconductor quantum dots: Impact of dot material and orientation. *Physical Review B*, 99, 4 2019. ISSN 24699969. doi: 10.1103/PhysRevB.99.115317. URL https://doi.org/10.1103/PhysRevB.99.115317.

[510] Benjamin Venitucci, Léo Bourdet, Daniel Pouzada, and Yann-Michel Niquet. Electrical manipulation of semiconductor spin qubits within the g-matrix formalism. *Phys. Rev. B*, 98:155319, Oct 2018. doi: 10.1103/PhysRevB.98.155319. URL https://link.aps.org/doi/10.1103/PhysRevB.98.155319.

[511] Maurizio Verde, Christian T. Schmiegelow, Ulrich Poschinger, and Ferdinand Schmidt-Kaler. Trapped atoms in spatially-structured vector light fields. *Scientific Reports*, 13(1):21283, 2023. doi: 10.1038/s41598-023-48589-1. URL https://doi.org/10.1038/s41598-023-48589-1.

[512] F. Verstraete, J. Dehaene, B. De Moor, and H. Verschelde. Four qubits can be entangled in nine different ways. *Phys. Rev. A*, 65:052112, Apr 2002. doi:

10.1103/PhysRevA.65.052112. URL https://link.aps.org/doi/10.1103/PhysRevA.65.052112.

[513] Sagar Vijay, Timothy H. Hsieh, and Liang Fu. Majorana fermion surface code for universal quantum computation. *Phys. Rev. X*, 5:041038, Dec 2015. doi: 10.1103/PhysRevX.5.041038. URL https://link.aps.org/doi/10.1103/PhysRevX.5.041038.

[514] J. M. G. Vilar and J. M. Rubí. Noise suppression by noise. *Phys. Rev. Lett.*, 86: 950–953, Feb 2001. doi: 10.1103/PhysRevLett.86.950. URL https://link.aps.org/doi/10.1103/PhysRevLett.86.950.

[515] Yuval Vinkler-Aviv, Daniel May, and Frithjof B. Anders. Analytical and numerical study of the out-of-equilibrium current through a helical edge coupled to a magnetic impurity. *Phys. Rev. B*, 101:165112, Apr 2020. doi: 10.1103/PhysRevB.101.165112. URL https://link.aps.org/doi/10.1103/PhysRevB.101.165112.

[516] Lorenza Viola and Seth Lloyd. Dynamical suppression of decoherence in two-state quantum systems. *Phys. Rev. A*, 58:2733–2744, Oct 1998. doi: 10.1103/PhysRevA.58.2733. URL https://link.aps.org/doi/10.1103/PhysRevA.58.2733.

[517] Lorenza Viola, Emanuel Knill, and Seth Lloyd. Dynamical decoupling of open quantum systems. *Phys. Rev. Lett.*, 82:2417–2421, Mar 1999. doi: 10.1103/PhysRevLett.82.2417. URL https://link.aps.org/doi/10.1103/PhysRevLett.82.2417.

[518] B Voisin, R Maurand, S Barraud, M Vinet, X Jehl, M Sanquer, J Renard, and S De Franceschi. Electrical control of g-factor in a few-hole silicon nanowire mosfet. *Nano Letters*, 16:88–92, 2016. doi: 10.1021/acs.nanolett.5b02920. URL https://doi.org/10.1021/acs.nanolett.5b02920. PMID: 26599868.

[519] B Voisin, J Bocquel, A Tankasala, M Usman, J Salfi, R Rahman, M Y Simmons, L C L Hollenberg, and S Rogge. Valley interference and spin exchange at the atomic scale in silicon. *Nature Communications*, 11, 4 2020. ISSN

20411723. doi: 10.1038/s41467-020-19835-1. URL https://doi.org/10.1038/s41467-020-19835-1.

[520] B Voisin, K S H Ng, J Salfi, M Usman, J C Wong, A Tankasala, B C Johnson, J C McCallum, L Hutin, B Bertrand, M Vinet, N Valanoor, M Y Simmons, R Rahman, L C L Hollenberg, and S Rogge. Valley population of donor states in highly strained silicon. *Materials for Quantum Technology*, 2:25002, 4 2022. doi: 10.1088/2633-4356/ac5d1d. URL https://doi.org/10.1088/2633-4356/ac5d1d.

[521] Lada Vukušić, Josip Kukučka, Hannes Watzinger, Joshua Michael Milem, Friedrich Schäffler, and Georgios Katsaros. Single-shot readout of hole spins in ge. *Nano letters*, 18:7141–7145, 2018. URL https://pubs.acs.org/doi/10.1021/acs.nanolett.8b03217.

[522] A. Wallraff, D. I. Schuster, A. Blais, L. Frunzio, R. S. Huang, J. Majer, S. Kumar, S. M. Girvin, and R. J. Schoelkopf. Strong coupling of a single photon to a superconducting qubit using circuit quantum electrodynamics. *Nature*, 431(7005): 162–167, 2004. doi: 10.1038/nature02851. URL https://doi.org/10.1038/nature02851.

[523] Aron Walsh. Correcting the corrections for charged defects in crystals. *npj Computational Materials*, 7(1):72, 2021. doi: 10.1038/s41524-021-00546-0. URL https://doi.org/10.1038/s41524-021-00546-0.

[524] Chien-An Wang, Giordano Scappucci, Menno Veldhorst, and Maximilian Russ. Modelling of planar germanium hole qubits in electric and magnetic fields. *arXiv preprint arXiv:2208.04795*, 2022. URL https://doi.org/10.48550/arXiv.2208.04795.

[525] Chien An Wang, Corentin Déprez, Hanifa Tidjani, William I.L. Lawrie, Nico W. Hendrickx, Amir Sammak, Giordano Scappucci, and Menno Veldhorst. Probing resonating valence bonds on a programmable germanium quantum simulator. *npj Quantum Information*, 9, 12 2023. ISSN 20566387. doi: 10.1038/s41534-023-00727-3. URL https://doi.org/10.1038/s41534-023-00727-3.

[526] Daisy Q Wang, Oleh Klochan, Jo-Tzu Hung, Dimitrie Culcer, Ian Farrer, David A Ritchie, and Alex R Hamilton. Anisotropic pauli spin blockade of holes in a gaas double quantum dot. *Nano Letters*, 16:7685–7689, 2016. URL https://pubs.acs.org/doi/10.1021/acs.nanolett.6b03752.

[527] Huan-Wen Wang, Bo Fu, and Shun-Qing Shen. Intrinsic magnetoresistance in three-dimensional dirac materials with low carrier density. *Phys. Rev. B*, 98:081202, Aug 2018. doi: 10.1103/PhysRevB.98.081202. URL https://link.aps.org/doi/10.1103/PhysRevB.98.081202.

[528] Jie Wang and Dimitrie Culcer. Suppression of the kondo resistivity minimum in topological insulators. *Phys. Rev. B*, 88:125140, Sep 2013. doi: 10.1103/PhysRevB.88.125140. URL https://link.aps.org/doi/10.1103/PhysRevB.88.125140.

[529] Jing Wang and Shou-Cheng Zhang. Topological states of condensed matter. *Nature Materials*, 16(11):1062–1067, Nov 2017. ISSN 1476-4660. doi: 10.1038/nmat5012. URL https://doi.org/10.1038/nmat5012.

[530] Ke Wang, Gang Xu, Fei Gao, He Liu, Rong-Long Ma, Xin Zhang, Zhanning Wang, Gang Cao, Ting Wang, Jian-Jun Zhang, Dimitrie Culcer, Xuedong Hu, Hong-Wen Jiang, Hai-Ou Li, Guang-Can Guo, and Guo-Ping Guo. Ultrafast coherent control of a hole spin qubit in a germanium quantum dot. *Nature Communications*, 13(1): 206, 2022. doi: 10.1038/s41467-021-27880-7. URL https://doi.org/10.1038/s41467-021-27880-7.

[531] Zhanning Wang, Pankaj Bhalla, Mark Edmonds, Michael S. Fuhrer, and Dimitrie Culcer. Unidirectional magnetotransport of linearly dispersing topological edge states. *Phys. Rev. B*, 104:L081406, Aug 2021. doi: 10.1103/PhysRevB.104.L081406. URL https://link.aps.org/doi/10.1103/PhysRevB.104.L081406.

[532] Zhanning Wang, Elizabeth Marcellina, Alex R Hamilton, James H Cullen, Sven Rogge, Joe Salfi, and Dimitrie Culcer. Optimal operation points for ultrafast, highly coherent ge hole spin-orbit qubits. *npj Quantum Information*, 7, 4 2021. ISSN

20566387. doi: 10.1038/s41534-021-00386-2. URL https://doi.org/10.1038/s41534-021-00386-2.

[533] Zhanning Wang, Abhikbrata Sarkar, S. D. Liles, Andre Saraiva, A. S. Dzurak, A. R. Hamilton, and Dimitrie Culcer. Electrical operation of hole spin qubits in planar mos silicon quantum dots, 2023.

[534] W. L. Warren, G. E. Pike, K. Vanheusden, D. Dimos, B. A. Tuttle, and J. Robertson. Defect-dipole alignment and tetragonal strain in ferroelectrics. *Journal of Applied Physics*, 79(12):9250–9257, 06 1996. ISSN 0021-8979. doi: 10.1063/1.362600. URL https://doi.org/10.1063/1.362600.

[535] T F Watson, S G J Philips, E Kawakami, D R Ward, P Scarlino, M Veldhorst, D E Savage, M G Lagally, Mark Friesen, S N Coppersmith, M A Eriksson, and L M K Vandersypen. A programmable two-qubit quantum processor in silicon. *Nature*, 555:633–637, 4 2018. ISSN 14764687. doi: 10.1038/nature25766. URL https://doi.org/10.1038/nature25766.

[536] Hannes Watzinger, Christoph Kloeffel, Lada Vukusic, Marta D Rossell, Violetta Sessi, Josip Kukucka, Raimund Kirchschlager, Elisabeth Lausecker, Alisha Truhlar, Martin Glaser, et al. Heavy-hole states in germanium hut wires. *Nano letters*, 16:6879–6885, 2016. URL https://pubs.acs.org/doi/full/10.1021/acs.nanolett.6b02715.

[537] Hannes Watzinger, Josip Kukučka, Lada Vukušić, Fei Gao, Ting Wang, Friedrich Schäffler, Jian-Jun Zhang, and Georgios Katsaros. A germanium hole spin qubit. *Nature Communications*, 9(1):3902, 2018. doi: 10.1038/s41467-018-06418-4. URL https://doi.org/10.1038/s41467-018-06418-4.

[538] Christian Weedbrook, Stefano Pirandola, Raúl García-Patrón, Nicolas J. Cerf, Timothy C. Ralph, Jeffrey H. Shapiro, and Seth Lloyd. Gaussian quantum information. *Rev. Mod. Phys.*, 84:621–669, May 2012. doi: 10.1103/RevModPhys.84.621. URL https://link.aps.org/doi/10.1103/RevModPhys.84.621.

[539] Henan Wei, Seiya Mizoguchi, Raisei Mizokuchi, and Tetsuo Kodera. Estimation of hole spin g-factors in p-channel silicon single and double quantum dots towards spin manipulation. *Japanese Journal of Applied Physics*, 59:SGGI10, 2 2020. doi: 10.35848/1347-4065/ab6b7e. URL https://dx.doi.org/10.35848/1347-4065/ab6b7e.

[540] M. B. Weissman. $\frac{1}{f}$ noise and other slow, nonexponential kinetics in condensed matter. *Rev. Mod. Phys.*, 60:537–571, Apr 1988. doi: 10.1103/RevModPhys.60.537. URL https://link.aps.org/doi/10.1103/RevModPhys.60.537.

[541] John E. Wertz, Peteris Auzins, R. A. Weeks, and R. H. Silsbee. Electron spin resonance of f centers in magnesium oxide; confirmation of the spin of magnesium-25. *Phys. Rev.*, 107:1535–1537, Sep 1957. doi: 10.1103/PhysRev.107.1535. URL https://link.aps.org/doi/10.1103/PhysRev.107.1535.

[542] H. H. Wickman, A. M. Trozzolo, H. J. Williams, G. W. Hull, and F. R. Merritt. Spin-3/2 iron ferromagnet: Its mössbauer and magnetic properties. *Phys. Rev.*, 155:563–566, Mar 1967. doi: 10.1103/PhysRev.155.563. URL https://link.aps.org/doi/10.1103/PhysRev.155.563.

[543] S. Wiedmann, A. Jost, B. Fauqué, J. van Dijk, M. J. Meijer, T. Khouri, S. Pezzini, S. Grauer, S. Schreyeck, C. Brüne, H. Buhmann, L. W. Molenkamp, and N. E. Hussey. Anisotropic and strong negative magnetoresistance in the three-dimensional topological insulator bi_2se_3. *Phys. Rev. B*, 94:081302, Aug 2016. doi: 10.1103/PhysRevB.94.081302. URL https://link.aps.org/doi/10.1103/PhysRevB.94.081302.

[544] Patrick Winkel, Kiril Borisov, Lukas Grünhaupt, Dennis Rieger, Martin Spiecker, Francesco Valenti, Alexey V. Ustinov, Wolfgang Wernsdorfer, and Ioan M. Pop. Implementation of a transmon qubit using superconducting granular aluminum. *Phys. Rev. X*, 10:031032, Aug 2020. doi: 10.1103/PhysRevX.10.031032. URL https://link.aps.org/doi/10.1103/PhysRevX.10.031032.

[545] R Winkler. Rashba spin splitting in two-dimensional electron and hole systems.

Physical Review B, 62:4245–4248, 2000. URL https://journals.aps.org/prb/abstract/10.1103/PhysRevB.62.4245.

[546] R Winkler, H Noh, E Tutuc, and M Shayegan. Anomalous rashba spin splitting in two-dimensional hole systems. *Physical Review B*, 65:155303–155307, 2002. doi: 10.1103/PhysRevB.65.1553XX. URL https://journals.aps.org/prb/abstract/10.1103/PhysRevB.65.155303.

[547] R Winkler, Dimitrie Culcer, S J Papadakis, B Habib, and M Shayegan. Spin orientation of holes in quantum wells. *Semiconductor science and technology*, 23:114017, 2008. URL https://iopscience.iop.org/article/10.1088/0268-1242/23/11/114017.

[548] Roland Winkler. *Spin-orbit coupling effects in two-dimensional electron and hole systems*, volume 191. Springer, 1 edition, 1 2003. ISBN 978-3-540-01187-3. doi: https://doi.org/10.1007/b13586. URL https://link.springer.com/book/10.1007/b13586.

[549] W. M. Witzel and S. Das Sarma. Quantum theory for electron spin decoherence induced by nuclear spin dynamics in semiconductor quantum computer architectures: Spectral diffusion of localized electron spins in the nuclear solid-state environment. *Phys. Rev. B*, 74:035322, Jul 2006. doi: 10.1103/PhysRevB.74.035322. URL https://link.aps.org/doi/10.1103/PhysRevB.74.035322.

[550] L. M. Woods, T. L. Reinecke, and Y. Lyanda-Geller. Spin relaxation in quantum dots. *Phys. Rev. B*, 66:161318, Oct 2002. doi: 10.1103/PhysRevB.66.161318. URL https://link.aps.org/doi/10.1103/PhysRevB.66.161318.

[551] L. M. Woods, T. L. Reinecke, and R. Kotlyar. Hole spin relaxation in quantum dots. *Phys. Rev. B*, 69:125330, Mar 2004. doi: 10.1103/PhysRevB.69.125330. URL https://link.aps.org/doi/10.1103/PhysRevB.69.125330.

[552] J J Wortman and R A Evans. Young's modulus, shear modulus, and poisson's ratio in silicon and germanium. *Journal of Applied Physics*, 36:153–156, 1965. doi: 10.1063/1.1713863. URL https://doi.org/10.1063/1.1713863.

[553] Congjun Wu, B. Andrei Bernevig, and Shou-Cheng Zhang. Helical liquid and the edge of quantum spin hall systems. *Phys. Rev. Lett.*, 96:106401, Mar 2006. doi: 10.1103/PhysRevLett.96.106401. URL https://link.aps.org/doi/10.1103/PhysRevLett.96.106401.

[554] Ya-Jie Wu, Jing He, and Su-Peng Kou. Realizing universal majorana fermionic quantum computation. *Phys. Rev. A*, 90:022324, Aug 2014. doi: 10.1103/PhysRevA.90.022324. URL https://link.aps.org/doi/10.1103/PhysRevA.90.022324.

[555] Feihu Xu, Xiongfeng Ma, Qiang Zhang, Hoi-Kwong Lo, and Jian-Wei Pan. Secure quantum key distribution with realistic devices. *Rev. Mod. Phys.*, 92:025002, May 2020. doi: 10.1103/RevModPhys.92.025002. URL https://link.aps.org/doi/10.1103/RevModPhys.92.025002.

[556] Gang Xu, Yan Li, Fei Gao, Hai-Ou Li, He Liu, Ke Wang, Gang Cao, Ting Wang, Jian-Jun Zhang, Guang-Can Guo, et al. Dipole coupling of a hole double quantum dot in germanium hut wire to a microwave resonator. *New Journal of Physics*, 22:83068, 2020. URL https://iopscience.iop.org/article/10.1088/1367-2630/aba85a.

[557] Su-Yang Xu, Qiong Ma, Huitao Shen, Valla Fatemi, Sanfeng Wu, Tay-Rong Chang, Guoqing Chang, Andrés M. Mier Valdivia, Ching-Kit Chan, Quinn D. Gibson, Jiadong Zhou, Zheng Liu, Kenji Watanabe, Takashi Taniguchi, Hsin Lin, Robert J. Cava, Liang Fu, Nuh Gedik, and Pablo Jarillo-Herrero. Electrically switchable berry curvature dipole in the monolayer topological insulator wte2. *Nature Physics*, 14 (9):900–906, Sep 2018. ISSN 1745-2481. doi: 10.1038/s41567-018-0189-6. URL https://doi.org/10.1038/s41567-018-0189-6.

[558] Yoshihisa Yamamoto. Quantum information processing. *NII lecture sereies: Quantum Information Processing*, 2024. URL https://www.nii.ac.jp/qis/first-quantum/e/forStudents/lecture/.

[559] Jia-An Yan, W. Y. Ruan, and M. Y. Chou. Phonon dispersions and vibrational properties of monolayer, bilayer, and trilayer graphene: Density-functional perturbation theory. *Phys. Rev. B*, 77:125401, Mar 2008. doi: 10.1103/PhysRevB.77.125401. URL https://link.aps.org/doi/10.1103/PhysRevB.77.125401.

[560] Xu-Chen Yang and Xin Wang. Suppression of charge noise using barrier control of a singlet-triplet qubit. *Phys. Rev. A*, 96:012318, Jul 2017. doi: 10.1103/PhysRevA.96.012318. URL https://link.aps.org/doi/10.1103/PhysRevA.96.012318.

[561] Yuan-Chi Yang, S. N. Coppersmith, and Mark Friesen. High-fidelity single-qubit gates in a strongly driven quantum-dot hybrid qubit with $1/f$ charge noise. *Phys. Rev. A*, 100:022337, Aug 2019. doi: 10.1103/PhysRevA.100.022337. URL https://link.aps.org/doi/10.1103/PhysRevA.100.022337.

[562] Hong Yao and Dung-Hai Lee. Topological insulators and topological nonlinear σ models. *Phys. Rev. B*, 82:245117, Dec 2010. doi: 10.1103/PhysRevB.82.245117. URL https://link.aps.org/doi/10.1103/PhysRevB.82.245117.

[563] Jun Yoneda, Kenta Takeda, Tomohiro Otsuka, Takashi Nakajima, Matthieu R Delbecq, Giles Allison, Takumu Honda, Tetsuo Kodera, Shunri Oda, Yusuke Hoshi, Noritaka Usami, Kohei M Itoh, and Seigo Tarucha. A quantum-dot spin qubit with coherence limited by charge noise and fidelity higher than 99.9%. *Nature Nanotechnology*, 13:102–106, 4 2018. ISSN 17483395. doi: 10.1038/s41565-017-0014-x. URL https://doi.org/10.1038/s41565-017-0014-x.

[564] Cécile X. Yu, Simon Zihlmann, José C. Abadillo-Uriel, Vincent P. Michal, Nils Rambal, Heimanu Niebojewski, Thomas Bedecarrats, Maud Vinet, Étienne Dumur, Michele Filippone, Benoit Bertrand, Silvano De Franceschi, Yann Michel Niquet, and Romain Maurand. Strong coupling between a photon and a hole spin in silicon. *Nature Nanotechnology*, 7 2023. ISSN 17483395. doi: 10.1038/s41565-023-01332-3. URL https://doi.org/10.1038/s41565-023-01332-3.

[565] Z G Yu, S Krishnamurthy, Mark Van Schilfgaarde, and N Newman. Spin relaxation

of electrons and holes in zinc-blende semiconductors. *Physical Review B - Condensed Matter and Materials Physics*, 71, 4 2005. ISSN 10980121. doi: 10.1103/PhysRevB.71.245312. URL https://doi.org/10.1103/PhysRevB.71.245312.

[566] D. M. Zajac, T. M. Hazard, X. Mi, K. Wang, and J. R. Petta. A reconfigurable gate architecture for si/sige quantum dots. *Applied Physics Letters*, 106(22):223507, 06 2015. ISSN 0003-6951. doi: 10.1063/1.4922249. URL https://doi.org/10.1063/1.4922249.

[567] D. M. Zajac, A. J. Sigillito, M. Russ, F. Borjans, J. M. Taylor, G. Burkard, and J. R. Petta. Resonantly driven cnot gate for electron spins. *Science*, 359(6374):439–442, 2018. doi: 10.1126/science.aao5965. URL https://www.science.org/doi/abs/10.1126/science.aao5965.

[568] Paolo Zanardi. Dissipation and decoherence in a quantum register. *Phys. Rev. A*, 57:3276–3284, May 1998. doi: 10.1103/PhysRevA.57.3276. URL https://link.aps.org/doi/10.1103/PhysRevA.57.3276.

[569] A. Zarassi, Z. Su, J. Danon, J. Schwenderling, M. Hocevar, B. M. Nguyen, J. Yoo, S. A. Dayeh, and S. M. Frolov. Magnetic field evolution of spin blockade in ge/si nanowire double quantum dots. *Phys. Rev. B*, 95:155416, Apr 2017. doi: 10.1103/PhysRevB.95.155416. URL https://link.aps.org/doi/10.1103/PhysRevB.95.155416.

[570] S. Zhang and A. Fert. Conversion between spin and charge currents with topological insulators. *Phys. Rev. B*, 94:184423, Nov 2016. doi: 10.1103/PhysRevB.94.184423. URL https://link.aps.org/doi/10.1103/PhysRevB.94.184423.

[571] S. X. Zhang, R. D. McDonald, A. Shekhter, Z. X. Bi, Y. Li, Q. X. Jia, and S. T. Picraux. Magneto-resistance up to 60 tesla in topological insulator bi2te3 thin films. *Applied Physics Letters*, 101(20):202403, 2012. doi: 10.1063/1.4766739. URL https://doi.org/10.1063/1.4766739.

[572] Ting Zhang, He Liu, Fei Gao, Gang Xu, Ke Wang, Xin Zhang, Gang Cao, Ting Wang, Jianjun Zhang, Xuedong Hu, Hai-Ou Li, and Guo-Ping Guo. Anisotropic

g-factor and spin–orbit field in a germanium hut wire double quantum dot. *Nano Letters*, 21(9):3835–3842, 05 2021. doi: 10.1021/acs.nanolett.1c00263. URL https://doi.org/10.1021/acs.nanolett.1c00263.

[573] Wenjin Zhao, Zaiyao Fei, Tiancheng Song, Han Kyou Choi, Tauno Palomaki, Bosong Sun, Paul Malinowski, Michael A. McGuire, Jiun-Haw Chu, Xiaodong Xu, and David H. Cobden. Magnetic proximity and nonreciprocal current switching in a monolayer wte2 helical edge. *Nature Materials*, 19(5):503–507, May 2020. ISSN 1476-4660. doi: 10.1038/s41563-020-0620-0. URL https://doi.org/10.1038/s41563-020-0620-0.

[574] A. Zur, T.C. McGill, and D.L. Smith. Dipoles, defects and interfaces. *Surface Science*, 132(1):456–464, 1983. ISSN 0039-6028. doi: https://doi.org/10.1016/0039-6028(83)90552-6. URL https://www.sciencedirect.com/science/article/pii/0039602883905526.

[575] Wojciech H. Zurek, Salman Habib, and Juan Pablo Paz. Coherent states via decoherence. *Phys. Rev. Lett.*, 70:1187–1190, Mar 1993. doi: 10.1103/PhysRevLett.70.1187. URL https://link.aps.org/doi/10.1103/PhysRevLett.70.1187.

[576] Wojciech Hubert Zurek. Decoherence, einselection, and the quantum origins of the classical. *Rev. Mod. Phys.*, 75:715–775, May 2003. doi: 10.1103/RevModPhys.75.715. URL https://link.aps.org/doi/10.1103/RevModPhys.75.715.

[577] F A Zwanenburg, A A Van Loon, G A Steele, C E W M Van Rijmenam, T Balder, Y Fang, C M Lieber, and L P Kouwenhoven. Ultrasmall silicon quantum dots. *Journal of Applied Physics*, 105, 2009. ISSN 00218979. doi: 10.1063/1.3155854. URL https://doi.org/10.1063/1.3155854.

[578] Floris A Zwanenburg, Cathalijn E W M Van Rijmenam, Ying Fang, Charles M Lieber, and Leo P Kouwenhoven. Spin states of the first four holes in a silicon nanowire quantum dot. *Nano Letters*, 9:1071–1079, 4 2009. ISSN 15306984. doi: 10.1021/nl803440s. URL https://doi.org/10.1021/nl803440s.

[579] Floris A Zwanenburg, Andrew S Dzurak, Andrea Morello, Michelle Y Simmons, Lloyd C L Hollenberg, Gerhard Klimeck, Sven Rogge, Susan N Coppersmith, and Mark A Eriksson. Silicon quantum electronics. *Reviews of Modern Physics*, 85:961–1019, 4 2013. ISSN 00346861. doi: 10.1103/RevModPhys.85.961. URL https://doi.org/10.1103/RevModPhys.85.961.

[580] Justyna P. Zwolak and Jacob M. Taylor. Colloquium: Advances in automation of quantum dot devices control. *Rev. Mod. Phys.*, 95:011006, Feb 2023. doi: 10.1103/RevModPhys.95.011006. URL https://link.aps.org/doi/10.1103/RevModPhys.95.011006.